

GRAN SASSO SCIENCE INSTITUTE  
ASTROPARTICLE PHYSICS DOCTORAL PROGRAMME  
CYCLE XXXIII  
2017-2020

NEWTONIAN NOISE STUDIES IN  $2^{ND}$  AND  $3^{RD}$   
GENERATION GRAVITATIONAL-WAVE  
INTERFEROMETRIC DETECTORS

PhD CANDIDATE:  
Francesca Badaracco

SUPERVISOR:  
Jan Harms





NEWTONIAN NOISE STUDIES IN  $2^{ND}$  AND  $3^{RD}$   
GENERATION GRAVITATIONAL-WAVE  
INTERFEROMETRIC DETECTORS

*Author:*

Francesca Badaracco

*Supervisor:*

Jan Harms

A thesis submitted for the degree of  
Doctor of Philosophy

October 2020

*To my family and Alessio*

## List of acronyms

**AdV+** Advanced Virgo Plus

**ASD** Amplitude Spectral Density

**BH** Basin Hopping

**BNS** Binary Neutron Star

**BS** Beam Splitter

**CPSD** Cross Power Spectral Density

**DE** Differential Evolution

**DOA** Direction Of Arrival

**ELGAR** European Laboratory for Gravitational wave and Atom-interferometry  
Research

**ET** Einstein Telescope

**FIR** Finite Impulse Response

**FPC** Fabry-Perot Cavity

**GPR** Gaussian Process Regression

**GR** General Relativity

**GW** Gravitational Wave

**IMC** Input Mode Cleaner

**KAGRA** KAmioka GRAvitational-wave detector

**LGWA** Lunar Gravitational Wave Antenna

**LIGO** Laser Interferometer Gravitational-wave Observatory

**LISA** Laser Interferometer Space Antenna

**NHNM** New High Noise Model

**NLNM** New Low Noise Model

**NN** Newtonian Noise

**OMC** Output Mode Cleaner

**PRC** Power Recycling Cavity

**PSD** Power Spectral Density

**PSO** Particle Swarm Optimization

**SNR** Signal to Noise Ratio

**SOGRO** Superconducting Omni-directional Gravitational Radiation Observatory

**SQL** Standard Quantum Limit

**SRC** Signal Recycling Cavity

**TOBA** Torsion Bar Antenna

**WF** Wiener Filter

# Contents

INTRODUCTION	1
<b>I</b>	<b>5</b>
1 GRAVITATIONAL WAVES AND DETECTION THEORY	7
1.1 A brief historical introduction	8
1.1.1 <i>Milestones in gravitational wave astronomy</i>	10
1.2 General relativity for gravitational waves	12
1.2.1 <i>Linearisation of Einstein equations and wave equation</i>	13
1.2.2 <i>TT gauge and polarization of gravitational waves</i>	14
1.2.3 <i>Energy and momentum carried by gravitational waves</i>	14
1.2.4 <i>Principle of measurement</i>	16
1.3 Gravitational wave interaction with the interferometric detector	17
1.3.1 <i>Proper reference frame</i>	19
2 ADVANCED DETECTORS	23
2.1 Required sensitivity	24
2.2 The optical design	25
2.2.1 <i>Michelson layout</i>	25
2.2.2 <i>Fabry-Perot cavities</i>	25
2.2.3 <i>Signal and power recycling mirrors</i>	26
2.2.4 <i>Additional optics</i>	28
2.2.5 <i>Signal detection and strain reconstruction</i>	28
2.3 Suspension system	29
3 NOISES	33
3.1 Seismic noise	35
3.2 Newtonian noises	35
3.3 Thermal noise	37
3.4 Quantum noise	38
3.4.1 <i>Squeezing</i>	39

## CONTENTS

---

4	CONCEPTS FOR FUTURE GW-DETECTORS	41
4.1	Introduction	42
4.2	ET - Einstein Telescope	42
4.3	LISA - Laser Interferometer Space Antenna	45
4.4	Low frequency Terrestrial GW detectors	45
4.4.1	<i>ELGAR - European Laboratory for Gravitational wave and Atom-interferometry Research</i>	45
4.4.2	<i>TOBA: Torsion Bar Antenna</i>	46
4.4.3	<i>SOGRO: Superconducting Omni-directional Gravitational Radiation Observatory</i>	47
4.5	LGWA: Lunar Gravitational Wave Antenna	48
<b>II</b>		<b>49</b>
5	ALGORITHMIC TOOLS	51
5.1	Global optimization algorithms	52
5.1.1	<i>Basin hopping optimization</i>	52
5.1.2	<i>Evolutionary algorithms for optimization</i>	53
5.1.3	<i>Particle swarm optimization</i>	54
5.2	Gaussian Process Regression	55
5.3	Wiener filter for NN cancellation	57
5.3.1	<i>Could the Wiener filter also cancel part of the GW signal?</i>	63
5.3.2	<i>Stationarity of the seismic data</i>	64
5.3.3	<i>SNR limiting curve</i>	64
6	SEISMIC NEWTONIAN NOISE CANCELLATION	67
6.1	Introduction	68
6.2	Seismic fields generating NN	69
6.3	Required Newtonian noise suppression in GW interferometers	72
6.4	NN in ELGAR	74
6.5	NN from body waves	76
6.6	NN from surface waves	81
6.7	Active NN cancellation	84
6.8	Two point spatial correlation for the NN cancellation	84
6.8.1	<i>Isotropic and homogeneous seismic field</i>	86
6.8.2	<i>Two point spatial correlation for isotropic and homogeneous body waves field</i>	87
6.8.3	<i>Two point spatial correlation for isotropic and homogeneous Rayleigh waves field</i>	89
6.8.4	<i>Two point spatial correlation for a generic seismic field</i>	92

## CONTENTS

---

<b>7</b>	<b>OPTIMIZED ARRAYS FOR UNDERGROUND NN CANCELLATION</b>	<b>95</b>
7.1	Introduction	96
7.2	Wiener filters for underground NN cancellation	97
7.3	Optimization of seismic arrays for NN cancellation	100
7.3.1	<i>Validation of algorithms using the case of surface isotropic and homogeneous Rayleigh waves</i>	100
7.3.2	<i>Cancellation of NN from body waves</i>	101
7.4	Conclusion	110
<b>8</b>	<b>ARRAY SEISMOMETER OPTIMIZATION FOR ADV</b>	<b>115</b>
8.1	Introduction	116
8.2	Instruments and positioning	119
8.3	Surrogate model of the Wiener filter	120
8.4	Array optimization	125
8.5	Conclusion	132
<b>9</b>	<b>SEISMIC AND NEWTONIAN NOISE ESTIMATES AT KAGRA</b>	<b>137</b>
9.1	KAGRA mine as a probe for 3rd generation underground detectors	138
9.2	Instrumentation and measurements	138
9.3	Underground seismic noise	140
9.4	Seismic array processing	141
9.4.1	<i>Introduction to the method</i>	141
9.4.2	<i>Velocity estimation in KAGRA</i>	145
9.5	NN estimate in KAGRA	149
<b>10</b>	<b>CONCLUSION</b>	<b>155</b>
<b>A</b>	<b>APPENDIX</b>	<b>159</b>
A.1	Bessel functions	160
A.2	Calculations of Equation 6.53	160
A.3	Calculations of Equation 6.56 and Equation 6.57	161
<b>B</b>	<b>APPENDIX</b>	<b>163</b>
B.1	Reduced SNR for sum of incoherent signals	164
	<b>BIBLIOGRAPHY</b>	<b>165</b>



# INTRODUCTION

Gravitational waves have been theorized by the general theory of relativity and they proved to be a great tool to study the Universe. Nowadays, gravitational waves observation is becoming a routinely task in astronomy. To detect these ripples in space and time, huge interferometers have been constructed. They work together in a global network composed by LIGO Hanford and LIGO Livingston in the US [1], Virgo in Italy [2] and KAGRA in Japan [3]. LIGO-India will be also constructed in the near future and it will join the network [4].

Since gravitational wave detections proved to be practicable [5, 6, 7] new projects, aimed to develop more sensitive detectors, are now being planned for the next future.

Interferometric gravitational-wave detectors are very interesting from the physical point of view: they suffer from a huge variety of background noises [8], each one arising from different physical processes. These noises produce unwanted displacements on the detector's *test masses*, which are the probes that, through the use of coherent light, measure the gravitational field distortions due to gravitational waves.

The so called Newtonian Noise (NN) arises from the density fluctuations of the materials which, in turn, cause unwanted perturbations in the gravity field that surrounds the test masses. These *gravitational noises* cannot be physically shielded, neither reduced, without forcing severe modifications to the already existing infrastructure [9, 10]. The best approach to suppress this noise is therefore through its *active cancellation* from the data stream, which can also be done offline. Techniques of this kind have already been implemented in gravitational-wave detectors to reduce other noises [11, 12, 13, 14]. Already in 1998, with the contemporaneous works of Beccaria et al. [15] and Hughes and Thorne [9], it was predicted that NN would have been a limiting noise in the lower frequency band (below 10 Hz) of ground-based interferometric detectors. In the next observing run (O4) Advanced Virgo+ (AdV+) sensitivity will be enhanced enough that NN will become the dominant noise below the few tens of Hz. For this reason it

## CONTENTS

---

will be important to be able to reduce it as well.

Addressing the NN problem will be a crucial task also for 3<sup>rd</sup> generation gravitational-wave detectors, like the Einstein Telescope (ET) [16]. In spite of the fact that ET will be constructed underground, it will still be very important to find ways to reduce NN. [17].

The active noise cancellation is based on the idea that the NN affecting a test mass can be reconstructed by simply monitoring nearby density fluctuations by means of many auxiliary sensors and then use a Wiener filter to cancel out the noise. Optimizing the positions of the sensors in the array is a very important thing that we need to do in order to maximize the Wiener filter performances.

The NN arises mainly from atmospheric fluctuations and seismic displacements. In this thesis work I focused on the NN of seismic origin but the same techniques can also be applied to the atmospheric NN.

As mentioned before, the problem of finding the optimized array is a crucial step for implementing the NN cancellation system. Some attempts were already made for 2<sup>nd</sup> generation gravitational-wave detectors, in particular for LIGO [18]. LIGO has a seismic noise that is nearly homogeneous, and thus the optimization was made assuming a homogeneous seismic field. This is sufficient for the NN cancellation in LIGO, but not for AdV+: here we know that the seismic field is far from being homogeneous and isotropic [19].

The optimization of seismic arrays for underground detectors is instead a problem that has not yet been accomplished. This is also important to understand the feasibility of NN cancellation in ET, but also, potentially, in KAGRA.

My work can be divided into three main tasks: the optimization of a seismic array for the NN cancellation in underground detectors (Chapter 7), the optimization of a seismic array for AdV+ (Chapter 8), which required a more advanced approach with respect to the former, and the evaluation of the NN and the seismic field in the KAGRA site (Chapter 9).

The structure of this thesis is organised in two parts: Part I is a broad introduction to the gravitational wave physics but mainly focused on the detection techniques. Chapter 1 explains what gravitational waves are, how they arise from the general relativity framework and the major breakthroughs of the 2<sup>nd</sup> generation gravitational-wave detectors. Chapter 2 presents the general components of Advanced Virgo+ and how they work. Chapter 3 describes the contributions to the noise given by intrinsic limitations arising from the physics upon which the detector is based on. Some of the techniques used to suppress them up to the edge of the available technology are also presented. Chapter 4 introduces con-

## CONTENTS

---

cepts for future gravitational-wave detectors, in particular the Einstein Telescope and ELGAR: an interferometric detector that will exploit atom interferometers. Part II presents and describes my PhD work. Chapter 6 is a self consistent introduction to the NN field with particular attention to all the equations needed in the following chapters. Chapter 7 will present the published results regarding the optimization of seismic arrays in underground detectors, while Chapter 8 will present my other second work on the optimization of seismic arrays for AdV+. Finally, Chapter 9 will explain the work I have made to characterize the Newtonian and seismic noises budget in KAGRA.

## CONTENTS

---

# Part I



# 1

## GRAVITATIONAL WAVES AND DETECTION THEORY

### Contents

---

1.1	A brief historical introduction	8
1.1.1	<i>Milestones in gravitational wave astronomy</i>	10
1.2	General relativity for gravitational waves	12
1.2.1	<i>Linearisation of Einstein equations and wave equation</i>	13
1.2.2	<i>TT gauge and polarization of gravitational waves</i>	14
1.2.3	<i>Energy and momentum carried by gravitational waves</i>	14
1.2.4	<i>Principle of measurement</i>	16
1.3	Gravitational wave interaction with the interferometric detector	17
1.3.1	<i>Proper reference frame</i>	19

---

## 1.1 A brief historical introduction

The theory of gravitation has an interesting history: it starts from the gravitational law of Newton and ends (at least for now) with the General Relativity (GR) theory of Einstein which, in the weak field limit, can be reduced to the classical gravity theory.

Einstein was not the first one to propose the concept of gravitational waves (GWs), but eventually, his GR theory was the only one which was able to predict phenomena in the right way [20].

In the beginning (with Newton), gravity was treated like an instantaneous force, but later (1805) Laplace made a first attempt to consider a finite speed for the propagation of gravity and concluded - wrongly - that it had to be million times larger than the speed of light. Later (end of 1800), Gerber obtained a gravity speed very close to that of light using the perihelion shift of Mercury's orbit (even though his results were controversial due to some errors). In the meantime (1865), Maxwell, in his paper on electromagnetism [21], made a first attempt to understand gravity as something that could *propagate* into some medium. Even Heaviside attempted to write an analogue of the Maxwell theory for gravitation, showing that gravity could produce waves ("A gravitational and electromagnetic analogy, Oliver Heaviside, 1893"). On 5 July 1905 Poincaré published a work in which he assumed that gravitational forces could propagate at the speed of light by means of GWs. Many were, in the end, the attempts to explain gravity as some signal propagating with finite speed. Indeed, Special Relativity (published some months after Poincaré's paper, on 26 September 1905) and Classical Gravity theory were incompatible precisely because Classical Gravity assumed an instantaneous transmission of the gravity force. It was with GR that gravity and Special Relativity found an agreement. The development of GR started with the Einstein conception of the equivalence principle, which implies the necessity of considering the gravity as a manifestation of a curved space-time rather than a force. Indeed, GR reduces to Special Relativity in the case of a flat space-time (which means in absence of gravity - or in absence of energy which can curve the space-time).

In that period other scientists, like Max Abraham and Gustav Mie, developed unified theories of gravitation and electromagnetism, but these were scalar theories and the predicted GWs that arose from those theories were polarised longitudinally (which we know now to be wrong). Gunnar Nordström then developed the *very first* theory (1913) that can be considered predating GR: he treated for the first time gravitation as a pure effect of the space curvature, but his theory was not in agreement with observations (Mercury perihelion shift and light bending) while, as we know, GR is.



## 1. GRAVITATIONAL WAVES AND DETECTION THEORY

---

After his paper on GR, Einstein came to the conclusion that GWs should exist in three different types: longitudinal–longitudinal, transverse–longitudinal, and transverse–transverse. However, later, Eddington showed that two types were due to coordinate system artifacts and that only one (the transverse-transverse type) was really physical. In 1956 Felix Pirani [22] reformulated the GWs theory relying on the Riemann tensor and leading then to an invariant formulation of the theory.

GWs are the solution to the *linearised* Einstein equations (which otherwise are not linear), so they are the result of an approximation (Equation 1.1). For this reason, it is important to prove that the Einstein equations can have a gravitational radiation as a solution and that, in the far field approximation, this radiation can be written as the GWs obtained from the linearised Einstein equations. Indeed, there exist a planar wave solution to the non-linear equations (see [23]) which also carries energy, but it was only after the works of Trautman, Bondi, Pirani, Robinson [24, 25], and others (early 60s) that the theoretical arguments supporting the existence of gravitational radiation became solid and well accepted.

The first attempt to measure GWs was made by Weber in the 60s with a resonance bar, but, despite the claim of a detection, no convincing evidences were found and GWs remained something to be yet proven experimentally. Meanwhile, the very first paper concerning the possibility of building a gravitational-wave detector was written in the Soviet Union by Gertsenshtein and Pustovoi in 1963 [26]. Eight years later, Robert L. Forward, a student of Weber, constructed the first interferometric detector which was only 8.5 meters long [27]. The following year Weiss wrote the historical paper where he described how to construct an interferometric detector and its sensitivity limits [28]: for this reason Weiss can be regarded as the father of the LIGO detectors.

Virgo instead, the interferometric detector placed in Italy, was devised primarily by A. Giazotto and A. Brillet: the proposal was submitted in 1989 [29] and its construction started in 1996.

The first (indirect) experimental evidence of GWs was related to the discovery of the binary pulsar PSR B1913+16 by Hulse and Taylor [30]: indeed it was evident from the data that an orbital decay happened and that it was completely in agreement with the GWs energetic loss predicted by GR.

It was then in 2016 that the first direct gravitational wave detection was announced by the LIGO collaboration. This was the beginning of the gravitational wave astronomy.

### 1.1.1 Milestones in gravitational wave astronomy

On September 14, 2015 at 09:50:45 UTC, the LIGO Hanford (WA) and the LIGO Livingston (LA) observatories detected the GW150914 event [5]: the first direct detection of a GW! This signal marked the beginning of GW astronomy. GW observations are important because they can provide a direct access to the space-time behavior in the strong gravity field regime. This signal belonged to a binary black hole system with masses of  $36_{-4}^{+5} M_{\odot}$  and  $29_{-4}^{+4} M_{\odot}$ . Already with the first detection, it was possible to understand some important astrophysical implications: heavy ( $>25 M_{\odot}$ ) black holes do exist, binary black hole systems do form and they can merge within the Hubble time [5, 6].

Another important event is GW170817 [31]: it marked the beginning of a new era of multi-messenger astronomy [32]. Its signal was recorded 2 sec before the GRB 170817A [33], which turned out to be linked with the GW signal. GW170817 lasted for  $\sim 100$  s and its sky localization was significantly better compared to that of GW150914:  $28 \text{ deg}^2$  (see Figure 1.1) compared to the  $600 \text{ deg}^2$  of the first detection. This improved precision was the result of the presence of Virgo, a third detector, in the observing run (O2). This allowed the electromagnetic follow-up campaign to discover the electromagnetic counterpart of GW170817: it was located in the near galaxy NGC 4993. It is worth mentioning also the event GW190521 [34], discovered during the third observing run of LIGO and Virgo. This was related to the detection of a  $142 M_{\odot}$  black hole resulted from the merging of two black holes of  $66$  and  $85 M_{\odot}$ . It is of particular importance because both the remnants and the biggest progenitor lie in the *upper mass gap*, where no black holes should be found according to the current black hole formation theories. Indeed, according to the current theories, in very massive stars (in the  $130 M_{\odot}$  -  $250 M_{\odot}$  range) a pair-instability supernovae should occur: as a result of a particular mechanism the star would be completely blown apart with no remnant left. For this reason, the detection of black holes in this gap is so important: it opens new insights into the study of the death of massive stars and the supernovae mechanism, even though, it might be that black holes in the gap are simply formed by the merging of lighter black holes (like in the case of the the product of GW190521) or from the collision of massive stars (or other exotic processes).

These are few of the new discoveries allowed by this new field: we expect many other exciting detections with future GW detectors (see Chapter 4).

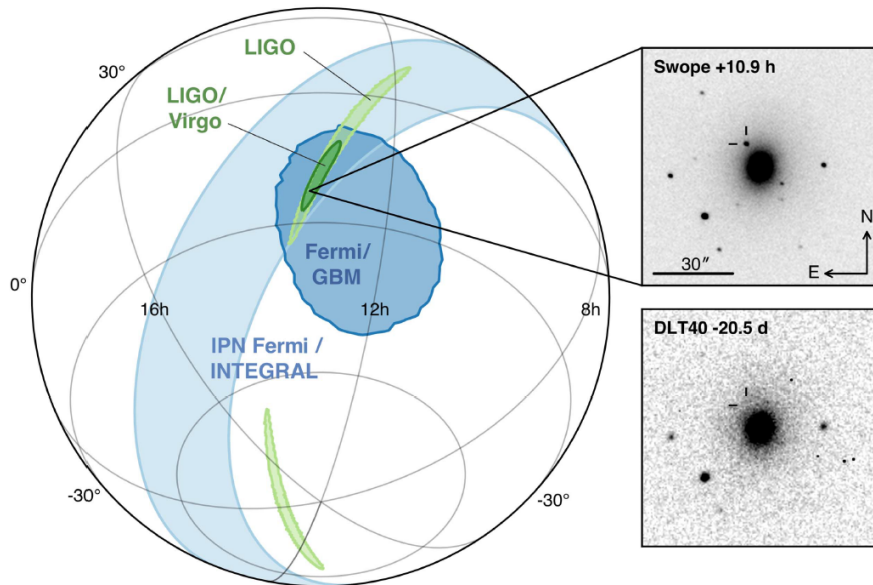


Figure 1.1: Localization of GW170817. The light green represents the 90% credible region of localization using only LIGO data, the dark green is instead obtained using also data from Virgo. The other colors come from Fermi and INTEGRAL detector localizations. The inset on the right shows the pre-discovery image of the apparent host galaxy NGC 4993 20.5 days prior the GW signal (*bottom*) and the image of the same galaxy 10.9 hours after the discovery (*top*) [6].

## 1.2 General relativity for gravitational waves

With Einstein (but already before him, with Nordström, see section 1.1), the concept of gravitational force passed from being an instantaneous force to being an effect due to the geometry of the four dimensional space-time.

The Einstein equations Equation 1.1 are a set of non-linear partial differential equations whose solutions represent the geometry of the space-time. This equations can be summarized with a citation from J.A. Wheeler: *"Space acts on matter, telling it how to move. In turn, matter reacts back on space telling it how to curve."* This mutual effect is a consequence of the non-linearity of these equations. Moreover, this leads to a big difference with respect to the electromagnetic field (which is a linear theory): the source of the electromagnetic potential,  $A^\alpha$ , is a conserved 4-current,  $J^\alpha$ , which doesn't depend on  $A^\alpha$  itself, this means that the electromagnetic field is not "charged". The source of the gravitational field, the energy-momentum tensor  $T_{\mu\nu}$ , instead does depend also on the gravitational field; this means that the field itself carries energy and momentum from which it is also generated [35].

$$R_{\mu\nu} - \frac{1}{2}Rg_{\mu\nu} = \frac{8\pi G}{c^4}T_{\mu\nu} \quad (1.1)$$

Here  $T_{\mu\nu}$  is the energy-momentum tensor which describes the matter distribution in space-time and  $g_{\mu\nu}$  is the metric: a tensor which describes the geometry of the space-time and allows to calculate distances between points ( $ds^2 = g_{\mu\nu}dx^\mu dx^\nu$ ).  $R_{\mu\nu}$  is called Ricci tensor and it can be obtained by contraction of the Riemann curvature tensor:  $R^\rho_{\mu\nu\rho} = R_{\mu\nu}$ , while  $R$ , the Ricci scalar, is obtained from:  $g^{\mu\nu}R_{\mu\nu}$ . The curvature tensor,  $R^\sigma_{\mu\nu\rho}$ , represents the physics of the gravitational field and a good understanding of this comes from the *geodesic deviation equation* [36]

$$\frac{D^2\xi^\mu}{Du^2} = -R^\mu_{\rho\nu\sigma}\xi^\rho\dot{x}^\nu\dot{x}^\sigma \quad (1.2)$$

Here  $x^\nu$  and  $x^\sigma$  represent the points belonging to two nearby geodesics that are separated by a distance  $\xi^\mu$ .  $\frac{D^2\xi^\mu}{Du^2}$  is the covariant derivative of the geodesics deviation took along a geodesic of reference (and parametrized by  $u$ ), while  $\dot{x}^\nu = dx^\nu/du$ . We can now understand the meaning of  $R^\mu_{\rho\nu\sigma}$ : if it is zero then:  $\xi^\mu(u) = A^\mu u + B^\mu$ , which means that the geodesics are straight lines, and so the geometry is flat. In a curved geometry instead, like a sphere or a saddle, two initial parallel geodesics will converge or diverge and  $D^2\xi^\mu/Du^2$  can be regarded as the tidal force that push/pull the points on the two geodesics. We can deduce that we have to look at the curvature tensor if we want to understand the physics of the gravitational field. Even if  $g_{\mu\nu}$  describes the geometry, it depends on the

coordinate system, so that a very complicate metric could still represent a flat geometry.  $R^\mu_{\rho\nu\sigma} = 0$ , on the other side, represents the physics of a constant gravitational field (which, for the *principle of equivalence* is the same as an absent gravitational field) and, being a relation between tensors, it holds in any system of coordinates (zero remains zero in all coordinate systems).

### 1.2.1 Linearisation of Einstein equations and wave equation

The theory of gravity is not linear, but we can turn it into a linear one under the approximation of weak fields:

$$g_{\mu\nu} = \eta_{\mu\nu} + h_{\mu\nu}, \quad |h_{\mu\nu}| \ll 1 \quad (1.3)$$

Here  $\eta_{\mu\nu}$  represents the metric corresponding to a flat space-time and  $h_{\mu\nu}$  can be regarded as a small deviation from this flatness. If we restrict ourselves to a coordinate system where Equation 1.3 still holds, we can expand Equation 1.1 in powers of  $h_{\mu\nu}$  and then keep only the linear terms in  $h_{\mu\nu}$ , thus obtaining a linearised theory of gravitation. The expansion in linear terms of  $h_{\mu\nu}$  is not enough to retrieve the wave equation for GWs:  $h_{\mu\nu}$  should be redefined as  $\bar{h}_{\mu\nu} \equiv h_{\mu\nu} - \frac{1}{2}\eta_{\mu\nu}h$ , where  $h = \eta^{\mu\nu}h_{\mu\nu}$ . The equations that we obtain by linearising and defining  $\bar{h}_{\mu\nu}$  are valid only in systems of coordinate in which Equation 1.3 remains valid, but, in this way, we are breaking the general covariance that characterizes GR (that means that the *form* of the physical laws remains invariant under general coordinate transformations). This implies that the linearised theory of gravity remains covariant solely for two kind of coordinate transformations: *Lorentz transformations* and *infinitesimal transformations*. By transforming our coordinate system with a Lorentz transformation,  $\Lambda^\nu_\mu$ , we can see that  $g_{\mu\nu} \rightarrow g'_{\mu\nu} = \eta_{\mu\nu} + h'_{\mu\nu}$  with  $h'_{\mu\nu} = \Lambda^\rho_\mu \Lambda^\sigma_\nu h_{\rho\sigma}$ . So, in the context of the linearised theory, we can look at  $h_{\mu\nu}$  in Equation 1.3 as a tensor living in the flat space-time. This is equivalent to have a gravitational field defined in a special-relativistic context. Infinitesimal coordinate transformations, instead, allow us to rewrite Equation 1.1 in a convenient way: under this transformations we have that  $x^\mu \rightarrow x^\mu + \xi^\mu(x)$  with  $\partial_\mu \xi_\nu(x)$  of the order of  $h_{\mu\nu}$  and so:

$$g_{\mu\nu} \rightarrow g'_{\mu\nu} = \eta_{\mu\nu} + h'_{\mu\nu}, \quad h'_{\mu\nu} = h_{\mu\nu} - \partial_\mu \xi_\nu - \partial_\nu \xi_\mu \quad (1.4)$$

In the viewpoint where  $h_{\mu\nu}$  is a tensor defined on the flat space-time, Equation 1.4 can be regarded as the analogous of the gauge transformation in electromagnetism. We can exploit this *gauge freedom* by choosing  $\xi^\mu$  in order to have  $\partial_\rho \bar{h}^{\mu\rho} = 0$  (called *Lorenz gauge*), this leads to the the wave equation for the

gravity field (for an extended treatment see [23, 35, 36]):

$$\partial_\rho \partial^\rho \bar{h}_{\mu\nu} = -\frac{16\pi G}{c^4} T_{\mu\nu} \quad (1.5)$$

### 1.2.2 TT gauge and polarization of gravitational waves

The simplest solution to Equation 1.5 is the monochromatic plane wave:  $\bar{h}_{\mu\nu} = \Re\{A_{\mu\nu} \exp(ik_\rho x^\rho)\}$ . The amplitude symmetric tensor,  $A_{\mu\nu}$ , has 6 independent components: 10 less 4 constraints coming from the Lorenz gauge (that implies:  $A_{\mu\nu} k^\mu = 0$ ). Actually, we still have 4 degrees of freedom because the Lorenz gauge is preserved for any *further* infinitesimal transformation that satisfy:  $\partial_\alpha \partial^\alpha \xi^\mu = 0$ . We can see ([23, 36]) that only 2 degrees of freedom survive if we *fix the Lorenz gauge*. For a particular choice of  $\xi^\mu$  (called the *Transverse-Traceless gauge* - or *TT gauge*) it is possible to write  $h_{\mu\nu}$  in the simplest way possible (where summation is intended over repeated indexes):

$$h_{TT}^{0\mu} = 0, \quad \partial_j h_{TT}^{ij} = 0 \text{ (transverse)}, \quad h_{TT_i}^i = 0 \text{ (traceless)} \quad (1.6)$$

where i and j represent the spatial indexes. Note that in this gauge there is no distinction between  $h_{\mu\nu}$  and  $\bar{h}_{\mu\nu}$  (indeed the trace is zero  $h_{TT} = \bar{h}_{TT_i}^i = 0$ ). In this case the only non vanishing components of  $h_{TT}^{\mu\nu}$  are  $h_{TT}^{11}$ ,  $h_{TT}^{22}$ ,  $h_{TT}^{12} = h_{TT}^{21}$ :

$$\begin{aligned} h_{TT}^+ &\equiv h_{TT}^{xx} = -h_{TT}^{yy} = \Re\{A^+ e^{-i\omega(t-z/c)}\} \\ h_{TT}^\times &\equiv h_{TT}^{xy} = +h_{TT}^{yx} = \Re\{A^\times e^{-i\omega(t-z/c)}\} \end{aligned} \quad (1.7)$$

Using the geodesic deviation equation (Equation 1.2) in the TT gauge, it can be shown that a particle, initially at rest, will remain so, despite the passage of a GW. This is due to the fact that the position of the particle is calculated in the TT gauge, which can be seen as a *breathing frame*: that is a coordinate frame which expands and squeezes following the wave expansion/squeeze. We fixed the Lorenz gauge by choosing  $\xi^\mu$  such that the TT gauge was satisfied, but  $\xi^\mu$  had to satisfy also  $\partial_\alpha \partial^\alpha \xi^\mu = 0$ , in order to preserve the Lorenz gauge. This means that the TT gauge forces the new coordinates to move according with the GW. If instead of looking at the coordinate position in the TT frame of reference, we look at the distance between two point coordinates ( $ds^2 = g_{\mu\nu} dx^\mu dx^\nu$ ), we find that polarized GWs indeed move particles with respect to each other, in the way shown in Figure 1.2.

### 1.2.3 Energy and momentum carried by gravitational waves

GWs do carry energy and momentum, because otherwise they could not even be detected and no forces (Newtonian approach) would be applied to the detector. The problem is that this energy is not localized. Indeed, we know from the

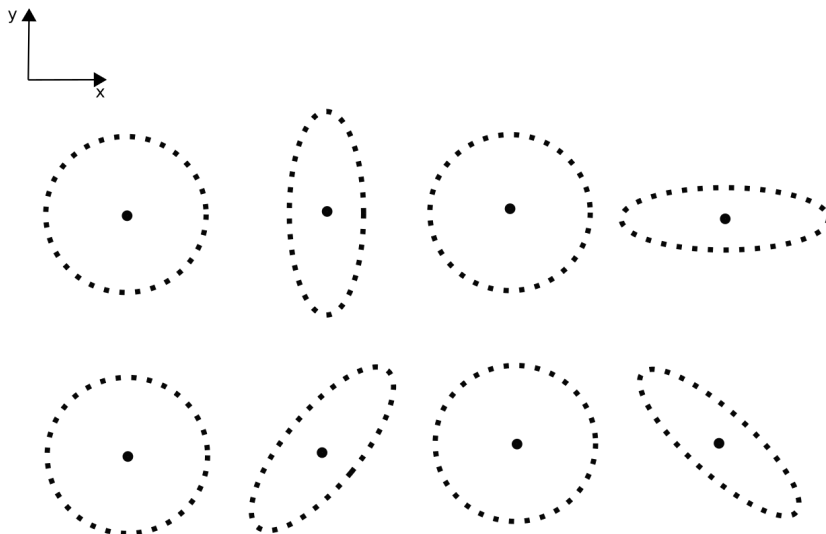


Figure 1.2: Effects induced by polarized GWs travelling along  $z$  on a circle composed by free falling test masses. ”+” polarization effects ( $h_{TT}^{xx}$ ) are shown on the top and ” $\times$ ” polarization effects ( $h_{TT}^{xy}$ ) are shown on the bottom.

principle of equivalence that we can find a local frame in which all local gravitational fields disappear (local flat coordinate system). Moreover, in the linearised theory we look at  $h_{\mu\nu}$  as a tensor living in a flat space-time: a zero space-time curvature, as supposed in the linearised theory, means no energy-momentum (see Equation 1.1). So, in order to understand the energy-momentum tensor of the GWs, we need to go beyond the linearised theory and, in particular, we cannot any more consider a flat background metric. In this regard, we need to use the *shortwave approximation* [37, 23], where the GWs are considered as short-wave fluctuations over a much more coarse grained metric (no longer flat):  $g_{\mu\nu} = g_{\mu\nu}^{coarse} + h_{\mu\nu}$ . However, close to a GW source,  $h_{\mu\nu}$  will become comparable to its background metric, so that speaking of the latter will become meaningless. However, far from it, on the Earth, we can still use the short-wave approximation and obtain:

$$\left\langle R_{\mu\nu} - \frac{1}{2}g_{\mu\nu}R \right\rangle = \left\langle \frac{8\pi G}{c^4} (T_{\mu\nu} + t_{\mu\nu}) \right\rangle \quad (1.8)$$

Where the mean is intended over lengths of the order of the background metric ( $g_{\mu\nu}^{coarse}$ ),  $T_{\mu\nu}$  is the energy-momentum tensor associated with any presence of matter and  $t_{\mu\nu}$  is the energy-momentum associated to the GWs and is meant to be quadratic in  $h_{\mu\nu}$ . Only quadratic terms of  $h_{\mu\nu}$  can indeed contribute to a coarse-grained energy-momentum tensor. It is through this non-linearity that

## 1. GRAVITATIONAL WAVES AND DETECTION THEORY

---

the GWs can act back on the space-time and curve it. The averaging process is important because we know that for a suitable coordinate choice we can make disappear the gravity field locally and so the energy of the GW cannot be defined locally, but only in a coarse-grained sense.

We can explicitly compute  $t_{\mu\nu}$  far from the source (at the detector location), where the background can be thought again as flat ( $g_{\mu\nu} \rightarrow \eta_{\mu\nu}$ ) and covariant derivatives become simple derivatives:

$$t_{\mu\nu} = \frac{c^2}{32\pi G} \langle \partial_\mu h_{TT}{}^{\rho\sigma} \partial_\nu h_{TT\rho\sigma} \rangle \quad (1.9)$$

Moreover, we can calculate the energy flux of the emitted gravitational radiation of very far sources with velocities  $v \ll c$ :

$$\frac{dE}{dt} = \frac{G}{5c^5} \langle \ddot{I}_{ij} \ddot{I}^{ij} \rangle \quad (1.10)$$

Where  $i, j$  are the spatial components,  $I^{ij} \equiv \int d^3x \rho(t, \mathbf{x})(x^i x^j - 1/3 r^2 \delta^{ij})$  is the quadrupole moment (with  $\rho(t, \mathbf{x})$  the mass density distribution of the source and  $x^i$  the  $i^{\text{th}}$  spatial coordinate of the mass element). The quadrupole moment is non-zero only for asymmetric systems with mass density which varies in time. This equation is only valid for nearly Newtonian sources; fast sources in strong fields, instead, need to rely on a complete field equations treatment [Equation 1.1](#).

Possible sources that can radiate are [\[38, 23\]](#): *binary systems* (composed by black holes, neutron stars, or both), *supernovae* and, possibly, a *stochastic background* composed by the all unresolved astrophysical sources. At very low frequencies we can also hope to find a cosmological stochastic background arising from early universe sources.

### 1.2.4 Principle of measurement

Let us consider a ”+” polarized GW propagating along  $z$ . Then, if we consider the distance between two points at  $(t, 0, 0, 0)$  and  $(t, L_x, 0, 0)$ , we can see that a GW modifies their distance in the following way:  $L'_x \equiv ds = (1 + h_+(t))^{1/2} L_x \simeq (1 + (1/2)h_+(t))L_x$  and so we can write:

$$\Delta L = \frac{1}{2} h_+(t) L_x \quad (1.11)$$

We can make the same simple calculation along the  $y$  direction, the result will be the same but with reversed sign (see [Equation 1.7](#)). So, if we want to measure  $h_+(t)$ , we just need to find a way to measure  $\Delta L$ . One way of doing this is measuring the variation in the distance between two inertial test masses by means



of a light beam. This can be achieved by measuring the variation in the travel time of the light, that is, measuring its *phase difference*. The Michelson interferometer layout (Figure 1.3) is something well known and used for such kind of measurements. A concern that might arise when thinking about the principle of measurement of the GWs is what follows: *"if light waves are stretched by gravitational waves, how can we use light as a ruler to detect gravitational waves?"* [40].

The key point here is that we are not using the light as a *ruler*, but rather as a *clock*. What we are really measuring is indeed the phase of the light, not its wavelength. During a GW passage, the distance between two test masses will change, and so also the light wavelength, but the velocity of light will remain the same. This means that the wave crests will be separated by a greater distance and it will take a greater time for the light to travel and reach the next test mass. This is why even if light itself is stretched inside the detector, it can still be used to measure the stretch of the space.

### 1.3 Gravitational wave interaction with the interferometric detector

The end test masses of gravitational-wave interferometers are not really free falling bodies, like they should be, indeed various forces act on them, like the system controls but also various Newtonian forces (the Earth indeed is not an inertial reference frame). However, these forces are static compared to the GWs we are looking for, so at high frequencies we can consider the test masses as free falling bodies (only in the direction of the laser, where they are actually free to move), and, consequently they can be used as coordinates in the TT gauge. This does not mean that at low frequencies we are not allowed to use the TT gauge, we can, but the test masses cannot any more be used as coordinates.

Assuming then to be in the frequency band where the test masses can be used as coordinates, their positions will be:  $(t, 0, L_y, 0)$  and  $(t, L_x, 0, 0)$ , while the origin is placed at the beamsplitter (see Figure 1.3). Moreover, we assume a monochromatic GW propagating along  $z$  and polarized "+":  $h_+(t) = h_0 \cos(\omega_{gw}t)$ . At this point, we can calculate the phase difference accumulated from the light during a round trip in the  $x$  arm (integrating the metric and neglecting terms  $O(h_0^2)$ ) [37]:

$$\Delta\phi_x(t) = \frac{\omega_L L_x}{c} \frac{\sin(\omega_{gw} L_x/c)}{\omega_{gw} L_x/c} h_+(t - L_x/c) \quad (1.12)$$

where  $\omega_L$  is the light frequency and  $t$  is the time at which the light returns back to the beamsplitter (BS). This relation holds only for GWs with direction

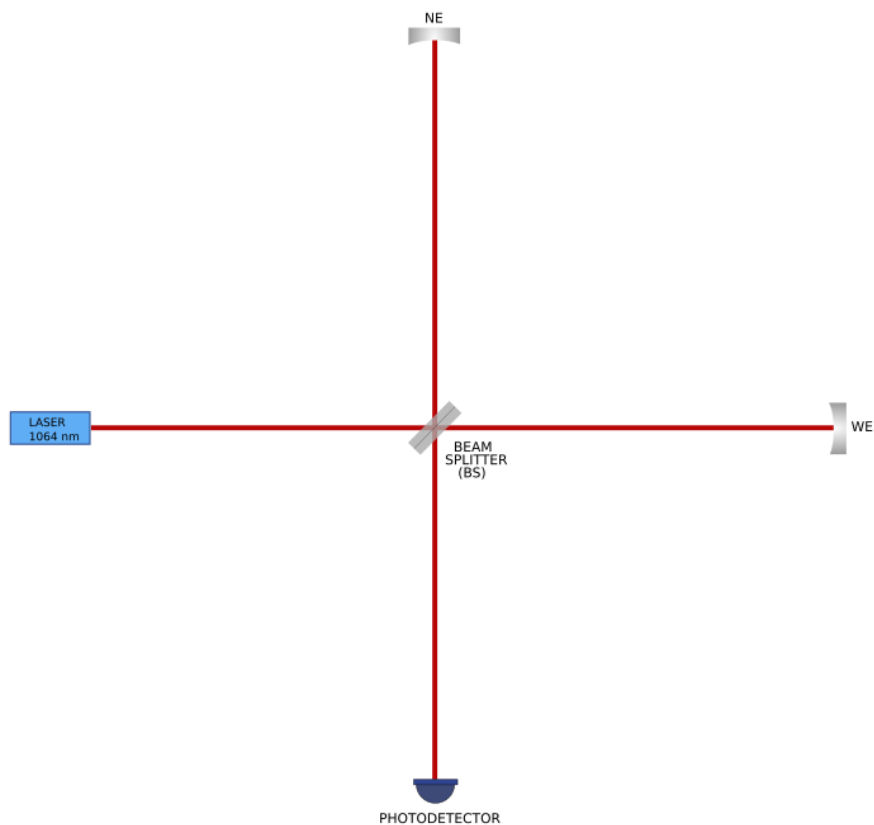


Figure 1.3: This is the most common configuration in optical interferometry and it is well known thanks to the famous experiment of Michelson–Morley, which had to prove the existence of the aether (then confuted) [39]. Gravitational-wave detector layouts are based on it: a laser beam sent towards a beamsplitter is divided into two equal beams which will travel towards two end mirrors (called test masses in gravitational-wave detectors) and will be reflected back, recombining again at the beamsplitter and then detected at the photodiode.

of propagation normal to the plane of the interferometer. For a more general interferometer response one needs to rely on a more sophisticated model with tensorial relations [41].

We can then see that for  $L_x \gg c/\omega_{gw} = \lambda_{gw}/2\pi$ , we have that  $\Delta\phi_x$  gets suppressed. This can be explained by the fact that too many wavelengths fit within the round trip, so that, in the end, the space in between will stretch and squeeze many times and the travel time of the light will remain unaffected. On the contrary, when  $\omega_{gw}L_x/c \rightarrow 0$  the GW wavelength will be longer compared to the interferometer sizes and the phase shift will just be:  $\Delta\phi_x(t) = h_+(t)\omega_L L_x/c$ . From Equation 1.12 we can see that the transfer function between  $h_+(t)$  and  $\Delta\phi_x$  depends on  $L_x$  through the factor:  $\omega_L/\omega_{gw} \sin(\omega_{gw}L_x/c)$ . We want of course maximize  $\Delta\phi_{\text{interferometer}} \equiv \Delta\phi_x - \Delta\phi_y = 2\Delta\phi_x$  (since:  $\Delta\phi_x = -\Delta\phi_y$ ), and so the optimal length for a Michelson interferometer should be:  $L = c/(4f_{gw}) = 750 \text{ km} \left( \frac{100 \text{ Hz}}{f_{gw}} \right)$ . This order of magnitude is too big to be realized on Earth, unless we fold the arms of the interferometer introducing the Fabry-Perot cavities, which will be discussed in subsection 2.2.2.

A GW passing through an interferometer will create *sidebands* that will propagate in the detector together with the carrier (which is the original electromagnetic wave coming from the laser). Actually, the sidebands formation happens everytime that a wave is phase modulated (through  $\Delta\phi_x$  in our case), but, usually, only the first two sidebands ( $\pm\omega_{gw}$ ) are considered due to the fact that the others are too small to be detected (because of the smallness of  $h_0$  - see sec. 3.1 of [42] for further details).

### 1.3.1 Proper reference frame

When describing GWs, the TT gauge is usually taken into account because it is the easiest way to represent them: within the same coordinate system we can still make arrangements exploiting the remaining degrees of freedom and expressing the wave equation in a very easy and known way (subsection 1.2.2).

In this frame of reference GWs do not change the coordinates of a freely falling test mass (but, yes, they change its proper distance from another test mass). Such a coordinate system would be easily realizable in a drag free satellite experiment like LISA [43] (see section 4.3). In an Earth bound detector, things are different because an experimentalist will measure coordinates using a rigid ruler and with respect to a fixed origin, so the test masses will be expected to change their position with respect to some fixed point. In addition to this, the experimentalist will be positioned in a rotating and accelerating system of reference. It is then clear that it is no more convenient to use the TT gauge [44].

## 1. GRAVITATIONAL WAVES AND DETECTION THEORY

---

It turns out [40, 23, 37] that if we use a coordinate system which is rotating and accelerating (the *proper detector frame*) we can describe our detector like if it was subject only to Newtonian laws. This is only valid as long as the dimensions of the detector are small compared to the incoming reduced gravitational wavelength:  $L \ll \lambda_{gw}/2\pi$ , but this is always true in Earth bound detectors.

We can then rewrite the metric using an accelerating and rotating frame: in this case GW effects will be contained in terms of order  $O(x^i x^j)$  of the metric (which lead to the  $O(x^i)$  term in Equation 1.13). Exploiting the geodesic deviation Equation 1.2, we can calculate the correspondingly geodesic equation for an element of the detector (which can be fairly considered as entirely contained in the neighbourhood of the world's line of its center of mass):

$$\frac{d^2 x^i}{d\tau^2} = -a^i - 2(\boldsymbol{\Omega} \times \mathbf{v})^i + \frac{f^i}{m} + O(x^i) \quad (1.13)$$

Where  $a^i$  is the gravity acceleration,  $\Omega$  the Coriolis acceleration and  $f^i$  an additional external force that might be applied to the detector elements (like suspension mechanisms). What about GW contributions? They have a role in the  $O(x^i)$  term. So we see that the worldlines of the detector's elements are subject to *Newtonian* forces which arise from being in a non-inertial system of reference (the laboratory bounded to the Earth) and that these forces are orders of magnitude bigger than the effect of the GWs (indeed  $x^i$  is taken to be close to the worldline of the detector's elements, thus  $O(x^i)$  are corrections to the metric). As already stated, this is not a problem if we consider GWs with high frequencies. Indeed, the Newtonian forces will appear as static since their typical frequencies are very low (below 10 Hz). If we restrict ourselves in this frequency window it is possible to demonstrate [37] that the GWs action on the detector can be accounted as a simple Newtonian force acting on it:

$$F^i = \frac{m}{2} \ddot{h}^{TT} x^i \quad (1.14)$$

Where  $m$  is the mass of the detector's element,  $x^i$  is its position with respect to the origin of the proper detector frame and  $\ddot{h}^{TT}$  is the second time derivative of the amplitude of the GW in the TT gauge (this is possible because in the calculation comes into play the curvature, which, in the linearised theory of gravity, is *invariant* instead of just covariant: so we can use  $h$  as calculated in the TT gauge).

This demonstrates that it comes natural to treat the incoming GW as a force acting on the test mass. Moreover, starting from Equation 1.14 it is possible to show [37] that the interaction of the GW with the detector gives the same result as in the TT gauge in the limit where  $\omega_{gw} L/c \ll 1$  (section 1.3).

It is important to keep in mind that, despite the proper frame description is valid for long wavelengths, at very low frequencies we cannot, any more, consider forces acting on the test masses as static: they will compete with GWs hiding them in a sea of *Newtonian noises*. For this reason, if we wish to detect GWs down to few Hz, we need to cancel them out from the data. This is equivalent to subtract from Equation 1.13 the external forces (gravitational forces, forces of controls and so on) and being left with a dominant term given by  $O(x^i)$ , which indeed contains the GWs we are seeking out.

This is precisely what we aimed to do in this Ph.D thesis work.

## 1. GRAVITATIONAL WAVES AND DETECTION THEORY

---

# 2

## ADVANCED DETECTORS

### Contents

---

2.1	Required sensitivity	24
2.2	The optical design	25
2.2.1	<i>Michelson layout</i>	25
2.2.2	<i>Fabry-Perot cavities</i>	25
2.2.3	<i>Signal and power recycling mirrors</i>	26
2.2.4	<i>Additional optics</i>	28
2.2.5	<i>Signal detection and strain reconstruction</i>	28
2.3	Suspension system	29

---

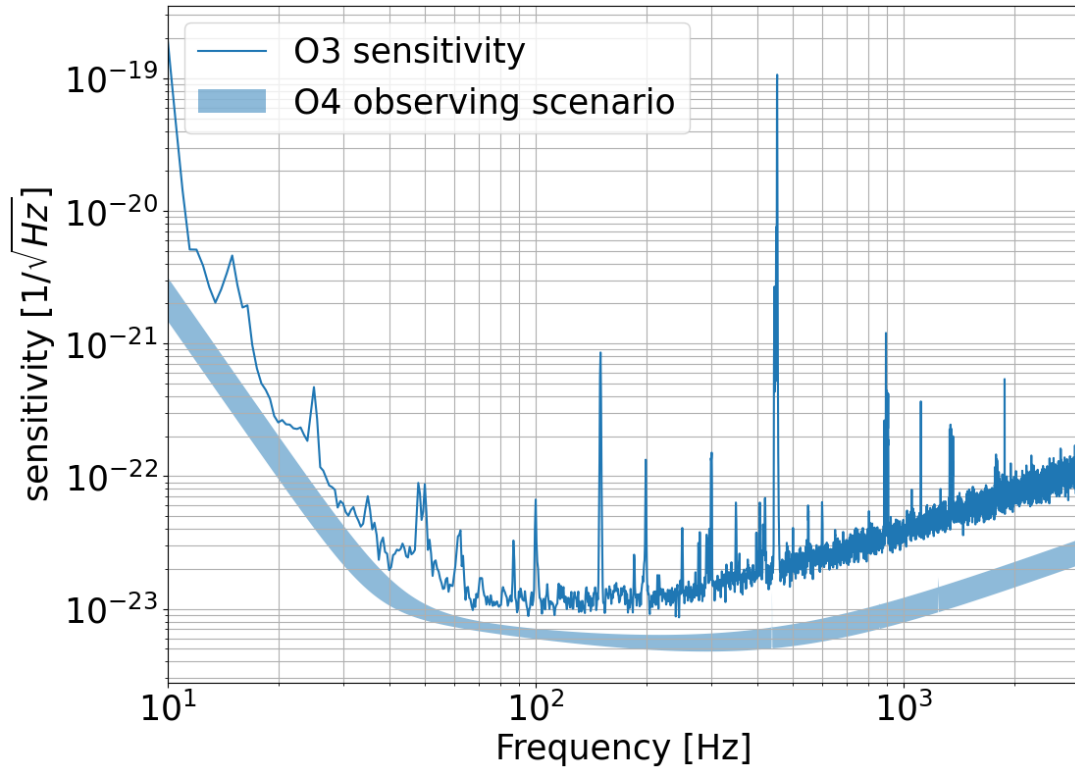


Figure 2.1: Sensitivity of AdV during O3 and the foreseen sensitivity for O4.

## 2.1 Required sensitivity

Advanced Virgo (AdV), the upgraded version of Virgo, is a second generation GW interferometric detector sited in Cascina (near Pisa), Italy. During O2 (observing run 2) its BNS sensitivity range was 25 Mpc, then improved to  $\sim 50$  Mpc during O3. Before O4 there will be a commissioning period, during which AdV will be further upgraded to Advanced Virgo Plus (AdV+). The main upgrades will include the implementation of a frequency dependent squeezing (see subsection 3.4.1), a higher input laser power, heavier test masses, the addition of a signal recycling cavity (SRC) -see subsection 2.2.3- and of the Newtonian noise (NN) cancellation system, which is indeed the subject of this Ph.D work.



## 2.2 The optical design

### 2.2.1 Michelson layout

As already anticipated in subsection 1.2.4, the Michelson interferometer (see Figure 1.3) is a well suited instrument for measuring GWs because it is meant to measure light phase differences, which are indeed the result of the passage of a GW across the interferometer.

The typical optical layout of a Michelson interferometer is depicted in Figure 1.3: a coherent light beam (from a laser) is injected into the interferometer towards the beamsplitter (BS) and divided in two (ideally) equal and perpendicular beams (one in reflection and one in transmission). These beams will travel along the two arms reaching the two end mirrors (that in gravitational wave physics are defined *test masses*) after a path long  $L = 3$  km (for Virgo). The four directions seen from the BS are often called North, West (referred to the two long arms), East and South (which are also the two outputs respectively called *bright* or *symmetric port* and *dark* or *anti-symmetric port*) [45, 46].

Energy conservation considerations allow us to easily calculate the output power of the Michelson interferometer [42]. Let us first defining the common ( $\bar{L}$ ) and the differential ( $\Delta L$ ) arm length as:

$$\bar{L} = \frac{L_N + L_W}{2} \quad (2.1)$$

$$\Delta L = L_N - L_W \quad (2.2)$$

where  $L_N$  and  $L_W$  are respectively the length of the North and the West arm. We can then write the power at the *dark port* as:

$$P = P_0 \cos^2(2\pi\Delta L/\lambda) \quad (2.3)$$

The detector is then tuned at the dark fringe by setting  $\Delta L = \lambda/4$ : in this way no output signal will be detected at the *dark port*. This means that all the laser power will be reflected back to the bright port (conservation of energy). Current interferometric detectors operate at the dark fringe or close to it, depending on which detection scheme is used, see subsection 2.2.5. Advanced Virgo Plus (AdV+) will keep using the DC scheme [47, 2].

### 2.2.2 Fabry-Perot cavities

As we have seen in section 1.3, a GW detector should be hundreds of km long in order to be able to detect a GW signal. For this reason, GW interferometers are actually modified Michelson interferometers with Fabry-Perot cavities (FPCs)

---

## 2. ADVANCED DETECTORS

---

placed in the two arms, see Figure 2.2. These cavities are meant to increase the light path inside the arms. FPCs are composed by two highly reflective mirrors: the light remains trapped in between them for many bounces before exiting and going back again to the BS.

For a specific laser frequency, there will be some particular values of the FPC length for which it will resonate ( $2k_{\text{laser}}L_{\text{FPC}} = 2\pi n$ ): then the circulating power will be maximum (and amplified). The induced phase produced by a passing GW in the enhanced interferometer will be the same as if it was produced in a simple Michelson with arm length:  $L' = (2/\pi)\mathcal{F}L$ , where  $\mathcal{F} = \pi\sqrt{r_1r_2}/(1-r_1r_2)$  is the finesse, and  $r_1$  and  $r_2$  the reflectivities of the two mirrors of the cavity. AdV+ will then be equivalent to a Michelson with  $L' \sim 860$  km (where we used  $L = 3$  km and  $\mathcal{F} = 450$ ). This is valid in the long wavelength approximation (when  $\lambda_{\text{gw}} \gg L'$ ). It is important to look also at the FPC frequency response when the long wavelength approximation is no longer valid. Indeed, when the storage time becomes comparable to the GW period, it happens that we sum over positive and negative contributions and the sensitivity degrades. The GW phase shift induced in an interferometer with FPCs can be written as:

$$|\Delta\phi_{\text{FPC}}| \simeq h_0 \frac{4\mathcal{F}}{\pi} k_{\text{laser}} L \frac{1}{\sqrt{1 + (f_{\text{gw}}/f_p)^2}} \quad (2.4)$$

Where  $h_0$  is the GW amplitude and  $f_p \simeq c/(4\mathcal{F}L)$ , which for Virgo means  $f_p \sim 55.5$  Hz: so, above this frequency the sensitivity will be degraded by the FPC [37, 46].

### 2.2.3 Signal and power recycling mirrors

As we will see in section 3.4, one of the main noises in interferometric detectors is the shot noise, which can be reduced by increasing the circulating power. A way to increase the power, besides using FPCs, is recycling the laser power that otherwise would be lost. Indeed, the symmetric port sees the interferometer as a highly reflective mirror which sends back almost all the power (we indeed work at or close to the dark fringe). This means that, if we put an additional semi-transparent mirror at the symmetric port, we can increase the circulating power inside the detector (and therefore its sensitivity) by just sending back light that otherwise would be lost. This mirror will form the power recycling cavity (PRC). Moreover, this will not impact the signal sidebands created by the GW. These sidebands, indeed, inherit the differential nature of the GW, so those coming from one arm will have a  $\pi$  phase difference with respect to those coming from the other arm. In this way, the interference at the BS will be opposite with respect to that of the main beam: the GW sidebands will be completely transmitted to the dark port and nothing will go back to the bright port, towards the

## 2. ADVANCED DETECTORS

---

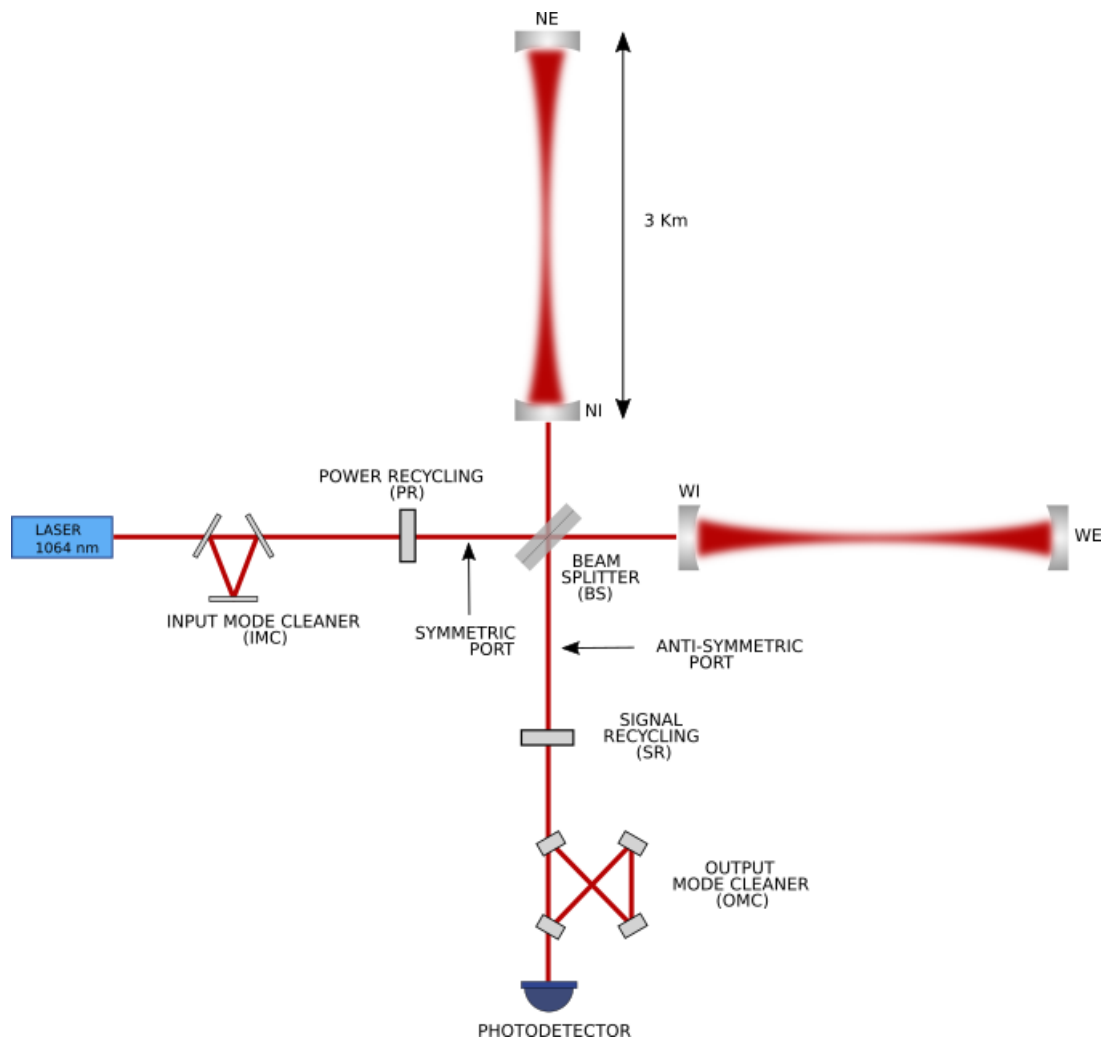


Figure 2.2: Simplified layout of Advanced Virgo+ (AdV+).

PRC.

Using the same reasoning that we used for the PRC, we can construct a signal recycling cavity (SRC). Adding a reflecting mirror at the anti-symmetric port will affect only the signal sidebands, partially sending them back to the interferometer (for symmetry reasons with respect to the BS, the laser light entering from the anti-symmetric port will not make it to the symmetric port). A Michelson interferometer enhanced with a PRC, a SRC and FPCs is called *dual-recycled Fabry-Perot-Michelson interferometer*. The SRC can also be used to change the frequency response of the interferometer. Indeed, it can be seen [46] that tuning the SRC can increase the bandwidth of sensitivity at the cost of reducing the gain, or increase the gain (and then the sensitivity) at the cost of reducing the bandwidth. This is useful in order to have a tunable GW interferometer to be set as needed, depending on the astrophysical signals we want to search for. During O3 AdV did not have the SRC that, instead, was installed during the commissioning phase in sight of O4.

#### 2.2.4 Additional optics

The laser beam inside a GW interferometer needs to meet very specific conditions, in particular it has to be a pure fundamental gaussian mode ( $TEM_{00}$ ) with very stable frequency. For meeting all the stringent laser requirements there is an injection system in between the laser and the interferometer. Inside this system, the input mode cleaner (IMC) is meant to suppress the higher order modes of the laser beam.

At the detection photodiode the only light that should arrive is the one of the GW sidebands and of the local oscillator used for the readout (see subsection 2.2.5). Any control sidebands (for which the dark port is not dark) and any higher order modes and sideband noises created inside the interferometer must be removed. For this reason the output mode cleaner (OMC) is installed just before the detection photodiode.

#### 2.2.5 Signal detection and strain reconstruction

As we have seen, the interferometer is very complicated and the best sensitivity is reached when the laser light resonates in the cavities (FPC, PRC and SRC) and the output port is set on the dark fringe.

As we will see in section 2.3, the optics are all provided with a seismic isolation which can dump mirror movements produced by seismic vibrations. At low frequencies, the residual mirror displacements become greater than the resonance width of the FPC and thus we need to control them to maintain the resonance

and to have destructive interference at the dark port: the interferometer needs to be *locked* [48]. This leads to the situation in which at high frequencies the masses behave as free-falling masses, while at low frequencies they are controlled by external forces. This is not a problem, since at such low frequencies we can use the proper reference frame to describe the detector, while the GW becomes just another force acting on the test mass together with a sea of Newtonian noises (see subsection 1.3.1) and control forces. For this reason, we cannot just use the dark port signal to measure the strain  $h(t)$ , but we need to reconstruct it by subtracting the control signals from the output: in this way the final signal will correspond to that of the freely falling mass [49].

Generally, the GW signal is very faint, many order of magnitude smaller than the carrier. So, in order to detect it, we need some local oscillator, that, through the effect of the beat between it and the GW sidebands, will allow to read the signal. The first GW interferometers were working with an heterodyne detection scheme which implies a radio frequency oscillator that should couple with the GW signal at the dark port. To allow the radio frequency bands to get out through the dark port, it was introduced a macroscopic arm length difference of several centimeters (the so called "Schnupp asymmetry"). Current detectors, like AdV+, are using a particular readout scheme called "DC-offset" which has many more advantages respect to the heterodyne detection scheme [50]. In this scheme, a small detuning with respect to the dark fringe is introduced. In this way, some of the carrier field leaks through the dark port working as a local oscillator. This new scheme requires a very stable laser, which can now be provided.

### 2.3 Suspension system

We will see in section 3.1 that the seismic noise at low frequencies is a very strong source of disturbance for GW detectors: so we need to attenuate it by at least a factor  $10^9$ . The Virgo's superattenuators (SA) are, maybe, its main peculiarity: they are seismic isolations adopted to achieve the necessary seismic suppression and are constituted by a multistage pendulum with 6 filters. Indeed, the pendulum is a natural low-pass filter above its frequency of resonance:  $f_0 = 1/(2\pi)\sqrt{g/l}$  (where  $g$  is the gravity acceleration and  $l$  is the length of the pendulum). For vibrations of the suspension point with frequencies  $f > f_0$  the oscillation of the pendulum mass will be suppressed by a factor  $\sim f_0^2/f^2$ . At the last stage of the  $N$  pendulums chain, the suppression of the vibration amplitudes is of the order of  $A/f^{2N}$ , with  $A = f_0^2 f_1^2 \cdots f_N^2$ .

Due to the Earth curvature and due to the large distance between the test masses (3 km), the suspensions are slightly misaligned between each other ( $3 \cdot 10^{-4}$  rad).

## 2. ADVANCED DETECTORS

---

So, any vertical seismic vibration will couple with the horizontal displacement of the mirrors. For this reason we also need to suppress vertical seismic vibrations. This is done by using triangular shaped cantilevers which hold the wires at which all the pendulum stages are attached. The whole  $N$  pendulums chain is attached to a three-legged inverted pendulum which serves to introduce another low frequency filtering stage. Moreover, it allows also seismic reduction through inertial sensors. At the frequencies of the normal modes, the vibrations are indeed amplified and they need to be damped using some actuators. The inverted pendulum reduces the forces needed to move the whole (1 tonne) chain allowing to apply less than 1 N to obtain 1 cm of displacement. This makes the damping with the actuators much easier.

The payload is the last part of the suspension system and it consists of an upper mass, called "marionette", which supports an optical component (either a test mass or an optical bench). Behind the test mass, attached at the marionette, there is a reference mass which acts as a reaction mass for the actuators that control the mirror position. The whole payload is under vacuum and is attached to a seventh filter designed to steer the payload.

The mirror is attached to the marionette by means of monolithic suspensions (that is a unique piece with the mirror) made of fused silica. This is done to reduce the thermal noise that otherwise would arise from the friction of the clamping points of the mirror's suspensions.

## 2. ADVANCED DETECTORS

---

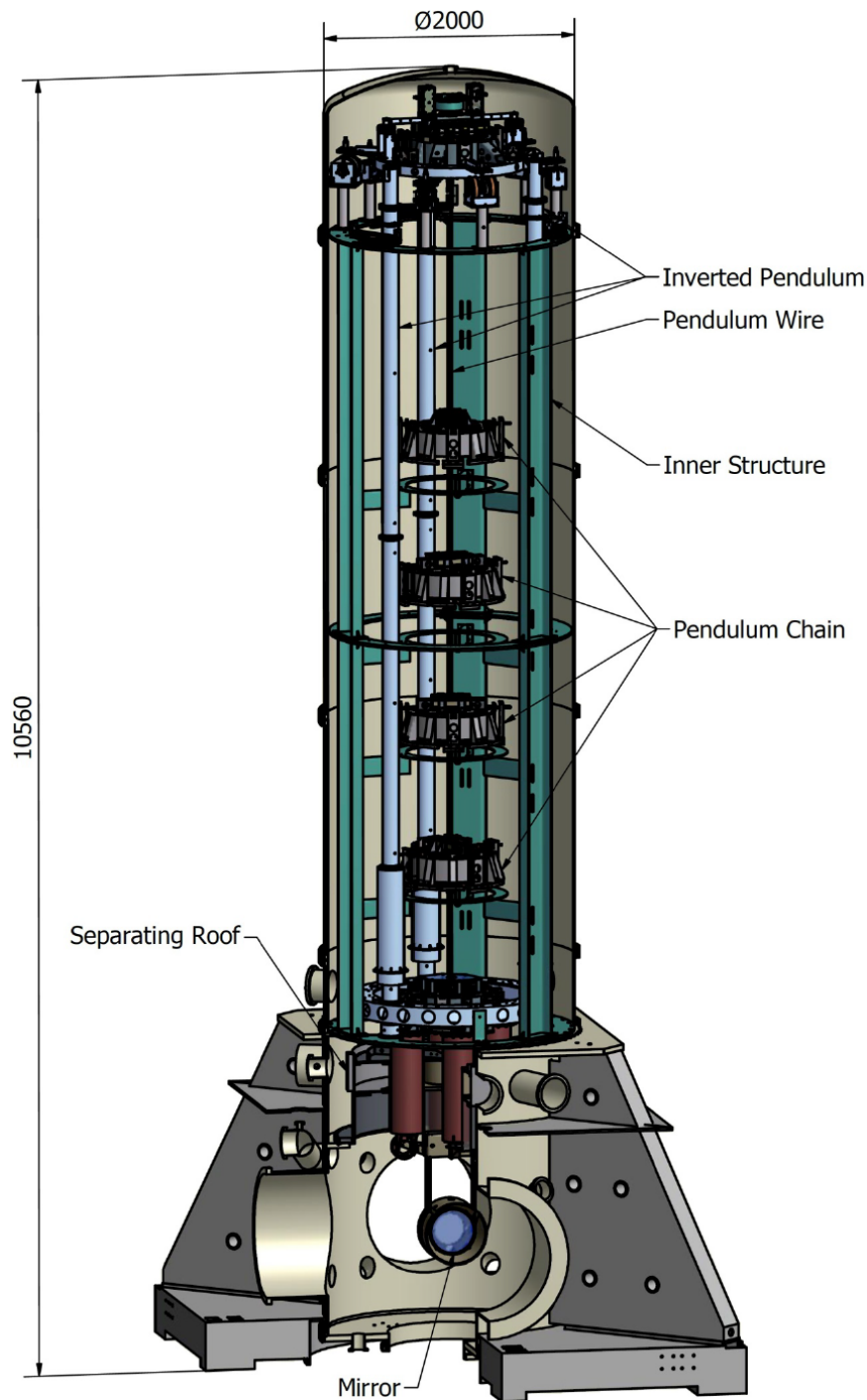


Figure 2.3: The VIRGO Superattenuator composed by the three-legged inverted pendulum, six seismic filters and the payload of the long suspension chain. Everything is inserted in a tower [45].

## 2. ADVANCED DETECTORS

---



# 3 NOISES

## Contents

---

3.1	Seismic noise	35
3.2	Newtonian noises	35
3.3	Thermal noise	37
3.4	Quantum noise	38
	3.4.1 <i>Squeezing</i>	39

---

### 3. NOISES

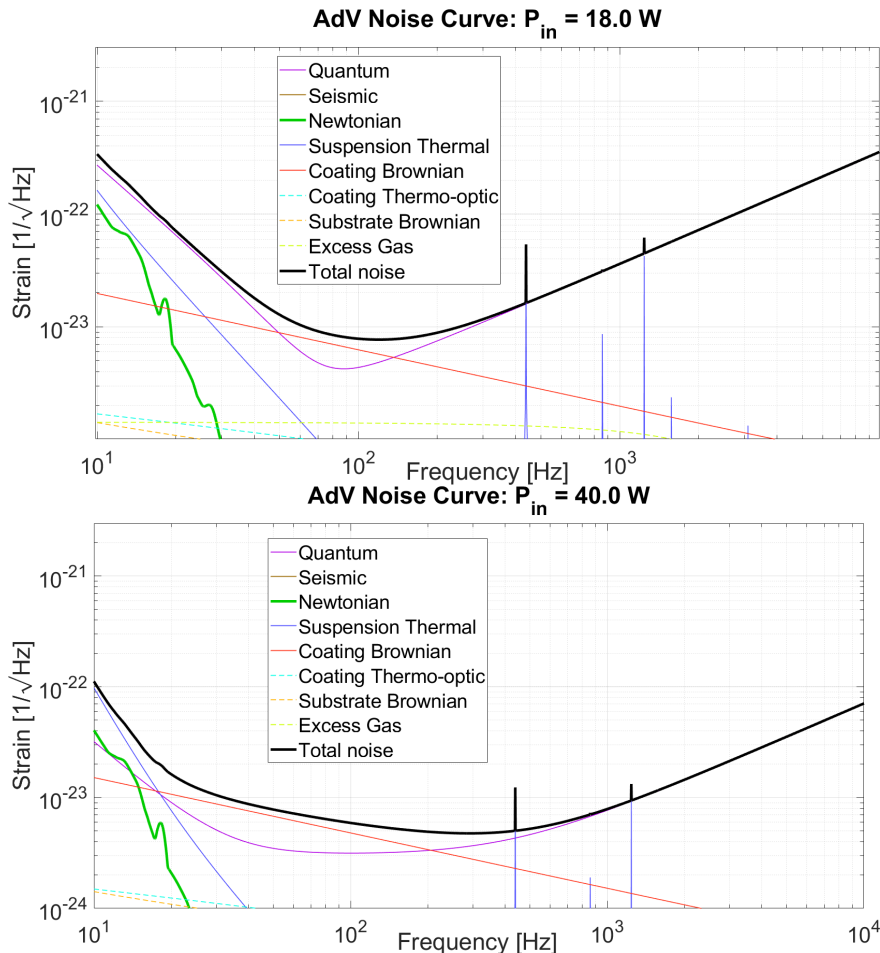


Figure 3.1: Comparison between the noises affecting AdV and its sensitivity curve during O3 and the future O4 (the latter was considered with the best achievement in noise reduction). *Upper*: sensitivity during O3. *Bottom*: predicted sensitivity curve for O4 considering high level of noises subtraction. In particular, the NN has been considered reduced of a factor 3. The predicted BNS range (1.4  $M_{\odot}$  each compact object) for this configuration is  $\sim 142$  Mpc, while the predicted BBH range (30  $M_{\odot}$  each compact object) is  $\sim 1.3$  Gpc.

An interferometric detector like AdV, needs to be very sensitive to any tiny displacement of the mirrors. We seek displacements induced by GWs which are of the order of  $\Delta L = (1/2)h_0 L = 1.5 \cdot 10^{-18}$  m (with an expected GW amplitude  $h_0 \sim 10^{-21}$ ,  $L = 3$  km and assuming that the long wavelength assumption is valid:  $\omega_{gw} L/c \ll 1$ ). This tiny displacement is smaller than the size of the nucleus of an atom. This could be seen as a limitation, since the roughness of

the mirrors will always be of the order of atom sizes, so how could we detect its position down to  $\Delta L$ ? Indeed, the laser beam has a transverse size of a few centimeters, so what it senses is the position of the surface of the mirror averaged over a macroscopic scale [37].

Anything that could induce mirror displacements greater than  $\Delta L$  is a source of noise and it needs to be suppressed. We can distinguish the noises in four main categories: fundamental noises, control noises, technical noises and environmental noises. Control and technical noises come from the electronic and the control loops implemented in the detector. Environmental noises come from the environment surrounding the detector: magnetic fields, vibrations and so on. They are kept under control by means of environmental sensors displaced all along the detector.

Fundamental noises, which will be described below, arise from limitations imposed by the underlying physics of the detector (for example the quantum or the thermal noise).

In AdV+ many noises are planned to be suppressed by some orders of magnitude, in particular the quantum noise, which otherwise would limit the sensitivity over almost all the detection band, see Figure 3.1.

### 3.1 Seismic noise

Even in the absence of earthquakes, seismic noise is a strong source of disturbance for the GW detectors. In the range of Virgo's sensitivity its typical Amplitude Spectral Density (ASD) can be written as:  $\alpha/f^2$  with  $\alpha$  of the order of  $10^{-6} \text{ m Hz}^{3/2}$  at the surface and in a relatively quiet place. At 10 Hz, this gives a strain of:  $\Delta L/L \sim 10^{-12} \text{ Hz}^{-1/2}$  [45]. So, in order to have a sensitivity of the order of  $10^{-21} \text{ Hz}^{-1/2}$  at 10 Hz, we need to suppress the seismic noise by a factor of  $10^9$ . For this reason, AdV needs a very good seismic isolation system, which is provided by the superattenuators (see section 2.3).

### 3.2 Newtonian noises

Newtonian noise (NN) has been theorised from the beginning of the GW interferometer design [28]. This kind of noise can arise when density fluctuations are present around the test mass. We know that variations in the mass density lead to fluctuations in the gravity field. There can be density fluctuations in the ground (generated by the seismic noise), and in the air (caused by variations in

### 3. NOISES

---

the atmospheric temperature or in the atmospheric pressure) [51]:

$$\delta\rho_{\text{seis}}(\mathbf{r}, t) = -\nabla \cdot (\rho(\mathbf{r})\boldsymbol{\xi}(\mathbf{r}, t)) \quad (3.1)$$

$$\delta\rho_{\text{press}}(\mathbf{r}, t) = \frac{\rho_0}{\gamma p_0} \delta p(\mathbf{r}, t) \quad (3.2)$$

$$\delta\rho_{\text{temp}}(\mathbf{r}, t) = -\frac{\rho_0}{T_0} \delta T(\mathbf{r}, t) \quad (3.3)$$

Where  $\rho(\mathbf{r}, t)$  is the density of the soil (or the air),  $\boldsymbol{\xi}(\mathbf{r}, t)$  is the seismic displacement,  $p(\mathbf{r}, t)$  and  $T(\mathbf{r}, t)$  are the air pressure and air temperature,  $\gamma \sim 1.4$  is the adiabatic index and  $\rho_0$ ,  $p_0$  and  $T_0$  the average density, pressure and temperature of the atmosphere. These density fluctuations will cause gravity perturbations that can be written as:

$$\delta\phi(\mathbf{r}_0, t) = -G \int dV \frac{\delta\rho(\mathbf{r}, t)}{|\mathbf{r} - \mathbf{r}_0|} \quad (3.4)$$

Here  $G$  is the universal gravitational constant. If we combine Equation 3.1 with Equation 3.4 we can calculate the perturbation of the gravity caused by the seismic waves [52]:

$$\delta\mathbf{a}(\mathbf{r}_0, t) = G \int dV \rho(\mathbf{r}) \frac{1}{|\mathbf{r} - \mathbf{r}_0|^3} (\boldsymbol{\xi}(\mathbf{r}, t) - 3(\mathbf{e}_{rr_0} \cdot \boldsymbol{\xi}(\mathbf{r}, t))\mathbf{e}_{rr_0}) \quad (3.5)$$

With  $\mathbf{e}_{rr_0} \equiv (\mathbf{r} - \mathbf{r}_0)/|\mathbf{r} - \mathbf{r}_0|$ .

NN can affect the detector's sensitivity at low frequencies, in particular below 10 Hz, where also the seismic noise is higher. It is not easy to physically shield the detector from this kind of noise: the interferometer is indeed aimed to detect any variation in the gravitational field caused by a GW. It would be difficult then to shield it only from the NN but not from the GW effects. One idea, would be to construct moats around the test masses to shield out the fundamental-mode Rayleigh waves [9]. These moats would need to be very deep to be effective, moreover, this method is valid as far as the assumption that Rayleigh waves come from external sources holds. Another way to reduce this kind of noise would be instead to perform an active cancellation. This is based on the use of data collected with many seismic sensors in order to reconstruct the NN acceleration on the test mass. In this way it would be possible to cancel the noise from the detector's data. In this regard, the position of the sensors need to be optimized based on the seismic field characteristics: this can make more effective the final noise cancellation. This particular aspect is the main subject of this PhD thesis and it will be addressed in Chapter 7 and Chapter 8. The same kind of cancellation could be done for what concerns the atmospheric NN. In

that case, though, the sensors need to monitor punctually the pressure and the temperature variations in a 3D space. To this end, the LIDAR technology could come to the aid [52].

### 3.3 Thermal noise

Thermal noise [53, 54] is another important source of noise for GW detectors: at temperatures  $T > 0$  atoms constituting the mirrors move randomly around their equilibrium position. The surface of the mirror will then undergo small distortions that will affect the phase of light, causing noise. We can roughly estimate these displacements through the equipartition energy theorem. The theorem states that every degree of freedom which appears only quadratically in the total energy of the system owns an average energy of:  $(1/2)k_B T$  (where  $k_B$  is the Boltzmann constant). If, for simplicity, we only consider the mean kinetic energy of the particles constituting a mirror of mass  $m = 42$  kg, we can write:  $(1/2)m\omega^2 \langle x \rangle^2(\omega) = 1/2k_B T$ , where  $\langle x \rangle(\omega)$  is the average displacement of a mirror's particle. This tells us that at 10 Hz and at room temperature we will have an average displacement of:  $\langle x \rangle(\omega) \sim 10^{-14}$  m. This is more than the expected displacement induced by a GW ( $10^{-18}$  m). The *fluctuation-dissipation theorem* can tell us which is the PSD of the thermal noise and how to reduce it: if in a system there is a dissipative process, then there must also be a reverse process related to thermal fluctuations (which are the direct cause of the dissipation). In the end the theorem tells us that the thermal noise in a system is produced by a thermal contribution ( $k_B T$ ) as well as by a dissipative one. Since more dissipation means more fluctuations (and so more noise) we can deduce that materials with low internal dissipation are better suited for GW interferometers. The fluctuation-dissipation theorem reads as:

$$S_{F_{th}}(\omega) = 4k_B T \Re(Z(\omega)) \quad (3.6)$$

Here  $S_{F_{th}}$  is the PSD of the thermal force that induces *random* movements in the system (the fluctuations), while  $Z(\omega)$  is the impedance and it is defined as:  $F(\omega) = Z(\omega)v(\omega)$ . The real part of the impedance is a measurement of the dissipation (damping) in the system. Alternatively, we can rewrite the theorem as:

$$S_x(\omega) = \frac{k_B T \Re(Z^{-1}(\omega))}{\pi^2 f^2} \quad (3.7)$$

If we consider a damped harmonic oscillator, then  $Z^{-1}(\omega) = \omega/(\omega_0^2 \phi(\omega) + i(\omega^2 - \omega_0^2))$ , where  $\phi(\omega)$  is related to the internal damping and is the inverse of the Q-factor:  $\phi = 1/Q$ . This tells us how the system is damped at resonance: the

bigger the  $Q$ , the lower the damping. Moreover, we can see that in the limit  $\omega \ll \omega_0$  then  $S_x(\omega) \propto \phi(\omega)/\omega$ , in the limit  $\omega \gg \omega_0$  then  $S_x(\omega) \propto \phi(\omega)/\omega^5$ , while at resonance:  $S(\omega)_x \propto 1/\phi(\omega)$ . This means that if we manage to have a material with low  $\phi(\omega)$  the noise will be concentrated in the narrow peak of the resonance and it will be lower far from the peak.

In the end, the thermal noise is generated inside the mirrors, but also inside the suspensions and in the clamps of the mirror's suspensions. For these reasons, monolithic suspensions and fused silica fibers [55] are employed for suspending the mirrors and special care is devoted to their coating.

### 3.4 Quantum noise

Quantum noise has traditionally been described as two separate effects: shot noise (affecting the high frequency band) and radiation pressure noise (affecting the low frequency band), but, in the end, both share the same origin: vacuum fluctuation coupling into the dark port [56].

Differently from what happens with other fundamental noises, this one arises directly from the measurement process.

We can describe quantum noise ASD by means of simple classical considerations, but we need to keep in mind that a better and mathematically rigorous description is needed (see [57]). The light photons hitting the photodetector can be described with a Poissonian process, this means that the photocurrent will fluctuate: these fluctuations are called *shot noise* and their ASD in a Michelson interferometer (without cavities) is:

$$h_{\text{shot}}(f) = \frac{1}{L} \sqrt{\frac{hc\lambda}{4\pi^2 P}} \quad (3.8)$$

So, we can reduce this kind of noise by simply increasing the circulating power by using Fabry-Perot cavities or just increasing the laser power. The shot noise in a simple Michelson interferometer (i.e. without FPCs) of length 3 km with laser wave length  $\lambda = 1064 \text{ nm}$  and circulating power  $P = 20 \text{ W}$  is:  $h_{\text{shot}}(f) \sim 10^{-19} \text{ Hz}^{-1/2}$ . We can then see that, if we wish to measure GWs, we need also to reduce the shot noise.

There is another factor that induces noise and it is linked to the light: the radiation pressure. Each photon impinging on the mirror will transfer momentum, but this will not be constant in time: it will instead fluctuate according to the Poisson distribution. This results in a fluctuating force on the mirror. The ASD of this noise can be calculated as follows:

$$h_{\text{rad}}(f) = \frac{1}{mf^2 L} \sqrt{\frac{hP}{4\pi^4 c\lambda}} \quad (3.9)$$

### 3. NOISES

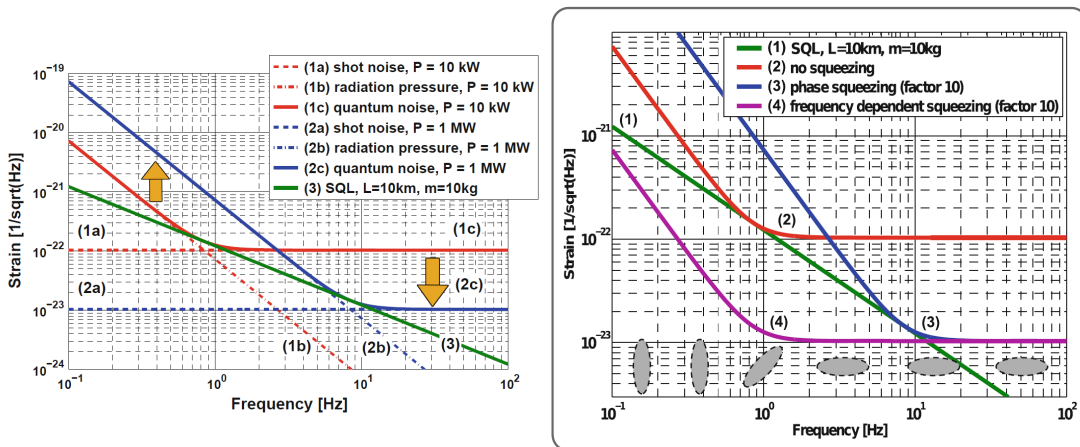


Figure 3.2: *Left*: the SQL (trace 3) and the quantum noise contribution for a simple Michelson interferometer with  $L = 10$  km and test masses with  $m = 10$  kg. Low (traces 1a–1c) and high (traces 2a–2c) circulating power has been considered. *Right*: quantum noise without squeezing and with phase and frequency dependent squeezing. The ellipses at the bottom show how the squeezing angle varies with the frequency in the quadrature picture for the frequency dependent squeezing. Figure taken from [60].

In this case the noise is frequency dependent and, hence, it will dominate the lower frequency band. We can of course reduce it by increasing the mass of the mirrors or lowering the circulating power. However, any attempt to reduce the radiation pressure noise by lowering the circulating power will end in an increase of the shot noise and vice versa. This leads to the concept of the Standard Quantum Limit (SQL) [58, 59] which is constituted by all the points where shot and radiation pressure noises are equal at each frequency (it is the green curve formed by all the knees in the noise curves of Figure 3.2). At the beginning, it was believed that this would have been the last insurmountable limit for interferometric GW detectors. It turned out it was not.

#### 3.4.1 Squeezing

To understand the squeezing [56] and how we can use it to improve sensitivity and to overcome the SQL, we can introduce the concept of amplitude  $A(\mathbf{r})$  and phase  $P(\mathbf{r})$  quadrature [60, 57]:

$$A(\mathbf{r}) = a^*(\mathbf{r}) + a(\mathbf{r}) \quad (3.10)$$

$$P(\mathbf{r}) = ia^*(\mathbf{r}) - ia(\mathbf{r}) \quad (3.11)$$

### 3. NOISES

---

Where  $a(\mathbf{r})$  is the complex amplitude of an electro-magnetic field with frequency  $\omega$  and polarization vector  $\mathbf{p}(\mathbf{r}, \mathbf{t})$ :  $\mathbf{E}(\mathbf{r}, \mathbf{t}) = E_0 [a(\mathbf{r})e^{-i\omega t} - a^*(\mathbf{r})e^{i\omega t}] \mathbf{p}(\mathbf{r}, \mathbf{t})$ . With these definitions we can rewrite the electromagnetic field in terms of its quadratures:

$$\mathbf{E}(\mathbf{r}, t) = E_0 [A(\mathbf{r}) \cos(\omega t) - P(\mathbf{r}) \sin(\omega t)] \mathbf{p}(\mathbf{r}, \mathbf{t}) \quad (3.12)$$

Each quadrature has its own noise: in a coherent state the two quadrature noises are uncorrelated, but, as a consequence of the Heisenberg uncertainty principle, if we reduce the noise in one quadrature, it will increase in the other one. In particular, amplitude quadrature couples via radiation pressure to the position of the mirror. Then, the displacement is translated in an additional component of the phase quadrature: this means that the noise of the two quadratures are now correlated. This correlation will help to beat the SQL. Indeed, we can think of injecting phase squeezed light into the interferometer (i.e. low noise in the quadrature phase). This will result in a shot noise decrease, but, due to the increased amplitude quadrature, which in turn induces radiation pressure, it will have the side effect of increasing the noise at low frequencies. So, in the end, injecting phase squeezed light will have the same effect of just increasing power. However, we can exploit the coupling of the radiation pressure with the phase quadrature by exploiting a homodyne detection scheme where it is possible to change the phase of the local oscillator. Indeed, the readout axis is the axis of the quadrature space along which we read the signal: a modification in the phase of the local oscillator is equivalent to steer the read out angle (look at [60]). This allows us to use a readout angle for which the radiation pressure coupled with the phase quadrature is cancelled out by the amplitude quadrature (radiation pressure and amplitude quadrature are correlated). In this way, we are left with only the phase quadrature noise and we can drop our sensitivity below the SQL, to the same level induced by the shot noise (which is frequency independent). We can thus be limited only by the shot noise contribution and no longer by the radiation pressure one. Unfortunately, the read out angle is different for each frequency: indeed the radiation pressure coupled with the phase quadrature is frequency dependent. So, in order to improve our sensitivity, we would need to change it according with the frequency. This method is called *variational readout* [61]. In AdV+ it will be instead implemented another technique: the *frequency dependent squeezing* [62]. Considering the squeezing angle as the direction along which the noise is reduced, we can change it according with the frequency, while leaving the readout angle always along the phase quadrature. In this way we could phase squeezing at high frequencies and amplitude squeezing at low frequencies, thus achieving sensitivities below the SQL - see Figure 3.2. This will also be one of the key technologies for the Einstein Telescope [63].



# 4

## CONCEPTS FOR FUTURE GW-DETECTORS

### Contents

---

4.1	Introduction	42
4.2	ET - Einstein Telescope	42
4.3	LISA - Laser Interferometer Space Antenna	45
4.4	Low frequency Terrestrial GW detectors	45
4.4.1	<i>ELGAR - European Laboratory for Gravitational wave and Atom-interferometry Research</i>	45
4.4.2	<i>TOBA: Torsion Bar Antenna</i>	46
4.4.3	<i>SOGRO: Superconducting Omni-directional Gravitational Radiation Observatory</i>	47
4.5	LGWA: Lunar Gravitational Wave Antenna	48

---

## 4.1 Introduction

Second generation detectors, like AdV and LIGO, have already led to a remarkable boost in astrophysics and fundamental physics.

Future GW detectors will be able to access better sensitivities and lower frequency bands. It is important to be able to detect signals in the low frequency band, indeed, most of a GW signal is emitted here, when the compact binary system is still in the inspiralling stage and the masses are far apart. Being able to detect part of the inspiralling phase would allow us to increase the SNR [64]. At low frequencies we can also detect white dwarf mergers (at the mHz scale) and massive black holes. Moreover, detecting GWs at other frequencies than those now accessible could bring to the discovery of some completely new phenomena. For these reasons, in the next future, new detector concepts will arise in order to cover as much frequency band as possible. It is also of fundamental importance to develop new detectors capable to better detect polarization and localization of the GW signal. The polarization could help to test alternative GR theories [65].

There are many projects for future GW detectors, among them there are the Einstein Telescope (ET, see section 4.2), the Cosmic Explorer [66], and LISA (Laser Interferometer Space Antenna, see section 4.3) that will be all constructed and run in the next few years. A frequency gap in between LISA and ET sensitivity curves will remain uncovered: it could be filled by some ground based low frequency GW detector (see section 4.4). However, the low frequency band is very challenging, indeed ground-based GW detectors are strongly affected by the seismic and the Newtonian noise. This is an important limitation, which can be mitigated, but that will forbid any detection below 0.1 Hz (maybe a bit lower if enhanced seismic sensors will be available). Anyway, a suppression of the NN by 4 or 5 orders of magnitude is required at 0.1 Hz for ground-based low frequency GW detectors [67]. For even lower frequencies we will have no other choices but to construct space-based GW detectors.

## 4.2 ET - Einstein Telescope

Current GW detectors (LIGO, Virgo, KAGRA and GEO600) have ageing infrastructure or infrastructure imposing constraints on potential future sensitivity improvements. For this reason, it is important to look at the (by now near) future in order to construct a third generation detector able to do a more precise and enhanced GW astronomy [68]. The Einstein Telescope (ET) is a proposed European third generation GW interferometric ground-based detector [69]: it would access low frequencies above  $\sim 3$  Hz and it targets a factor 10 enhanced

#### 4. CONCEPTS FOR FUTURE GW-DETECTORS

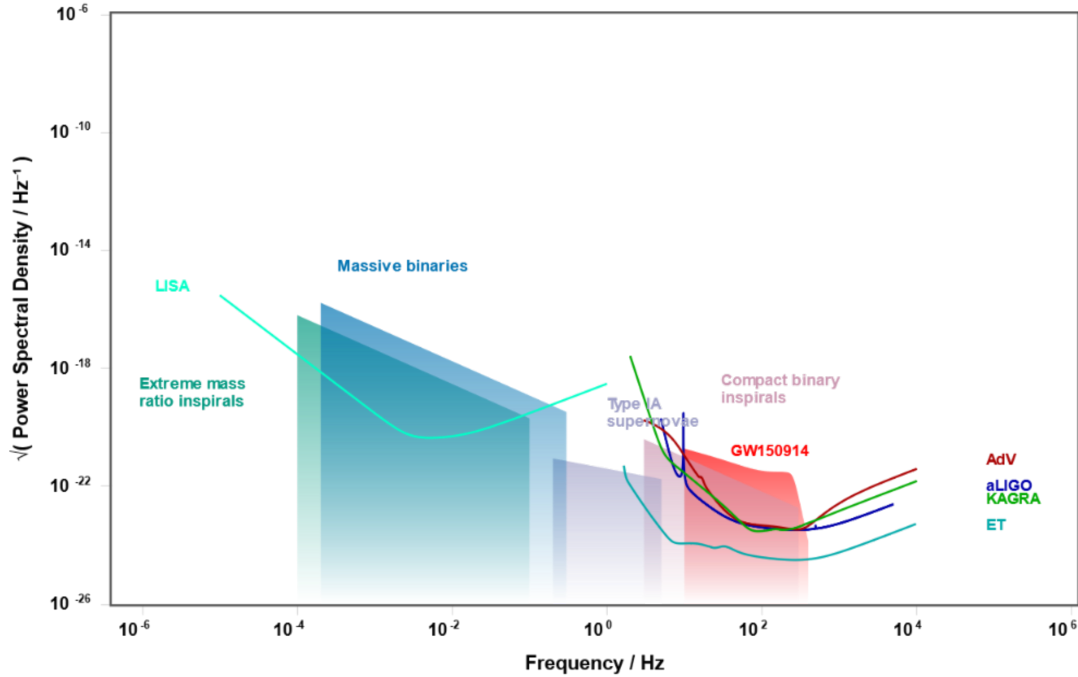


Figure 4.1: Sensitivities of current and future GW detectors. Figure produced with <http://gwplotter.com>.

sensitivity with respect to the 2<sup>nd</sup> generation GW detectors, like AdV [16, 63, 70]. In order to achieve the required sensitivity for ET, it will be necessary to push the current technologies up to their physical limits [71]. The most important improvement will be related to the construction of longer arms, which now are 3 km for Virgo and 4 km for LIGO. ET aims to have arms 10 km long, moreover it will be constructed underground in order to limit seismic and Newtonian noises. ET will consist of three nested detectors (see Figure 4.2) arranged in a triangular shape, and each detector will comprise two *dual-recycled Michelson interferometers*. The simultaneous presence of at least two detectors will allow to better constrain the polarization of the GW signals, which, in turn, will let to do a better parameter estimation and to have a better overall response (that is: less blind spots). Moreover, adding a third detector in a triangular shape will permit to construct a *null-data stream*, which is a linear combination of the individual detector streams, such that the GW signal cancels out: any signal detected both in the null stream and in the single detector-streams shall be considered noise. The fact that each detector will be composed of two interferometers implies that we can optimize one interferometer for low frequencies and one for high frequencies. The low frequency interferometer will be sensitive mostly in the 1.5 Hz -

#### 4. CONCEPTS FOR FUTURE GW-DETECTORS

30 Hz band and it will operate at cryogenic temperatures (10-20 K). This will be done in order to suppress as much as possible the thermal noise which spoils the sensitivity curve in this frequency band. To reduce the radiation pressure noise, the low frequency interferometer will work at lower power (18 kW) in the arm cavities. Mirrors of the low frequency interferometer will be made of silicon or sapphire, which at cryogenic temperatures have a better behaviour than the fused silica. The high frequency interferometer will instead work at room temperature, at a higher circulating power (3 MW) and with fused silica optics: its best sensitivity will lay in between 30 Hz and 10 kHz. Both the low and the high interferometer will have mirror masses around 200 Kg.

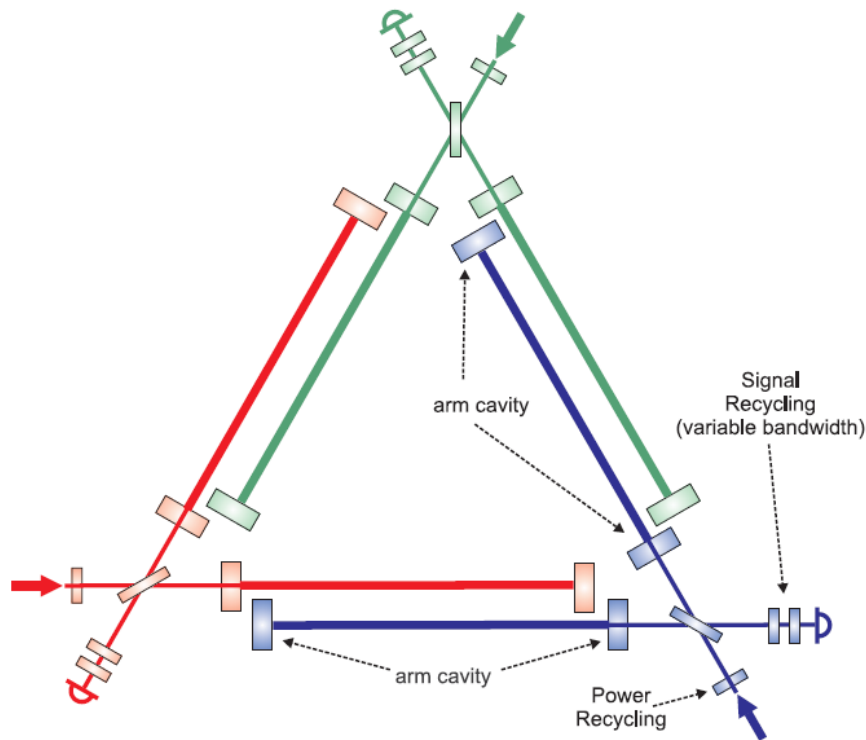


Figure 4.2: Example of the triangular layout that will be adopted for ET. The detector will be formed by three coplanar interferometers forming an equilateral triangle. As for Virgo, the interferometers will be based on the Michelson topology, but with the inclusion of additional optical technologies. Figure from [72].

### 4.3 LISA - Laser Interferometer Space Antenna

LISA [73] will be the first space-based large-scale GW detector designed to be sensitive in the 0.1 mHz - 1 Hz frequency band. It will be composed by three free-drag spacecrafts in a triangular formation and separated by 2.5 million km. Each spacecraft will host two free falling test masses and a telescope aimed to transmit and receive a laser beam to and from the other spacecrafts. LISA configuration allows to have two Michelson interferometers plus a third null-stream (said “Sagnac” configuration) which can help in the detection.

LISA will be able to study GW signals otherwise inaccessible from Earth and for this reason it will be a very important new instrument for GW astronomy [74].

### 4.4 Low frequency Terrestrial GW detectors

Low frequency detectors are aimed to cover the frequency gap in between LISA and ET but they will also offer the possibility of an easier maintenance respect to a space-based detector.

#### 4.4.1 ELGAR - European Laboratory for Gravitational wave and Atom-interferometry Research

ELGAR’s main aim is to fill the frequency gap in between LISA and ET with a sensitivity laying in the frequency band 0.1 Hz-1 Hz. ELGAR’s data production would also provide many other applications in other fields like fundamental physics, quantum gravity, general relativity and also geophysics [75].

In an optic interferometer like AdV and LIGO, the test masses are the mirrors at the end of the arms of the interferometer. ELGAR proposes a matter-wave interferometer where the test masses are cooled atoms dropped into a laser beam. Its geometry would still be L-shaped (Figure 4.3). An array of atom gradiometers will be placed along the arms: they will provide the way to measure the light phase. Each gradiometer is essentially composed by two atom interferometers separated by a distance  $L$ . An atom interferometer utilizes matter-wave BSs and mirrors to create a quantum mechanical version of the optical one. The BSs and the mirrors are made through light pulses of different time length which induce coherent state transitions between the atoms called Raabi oscillations. The scheme adopted by ELGAR will consist of four pulses: a cloud with some initial momentum will be interrogated and a superposition of two states of equal probability will be created by a lower BS-like pulse. The atoms will reach an upper beam (where the apogee is) which operates as a reflecting mirror (flipping

the atom states), and then they will be reflected twice (one before and one after the apogee, see Figure 4.3). At the end of the atom's gravity fall they will be recombined with another BS-like pulse in the lower interrogation beam. After, the population imbalance will provide a direct measurement of the atomic phase. In the end, the measured GW signal will be calculated as the difference between the two averaged signals of the two perpendicular arms. This will let us to reject all the common signals, while mitigating gravity gradient noises thanks to the average process [76].

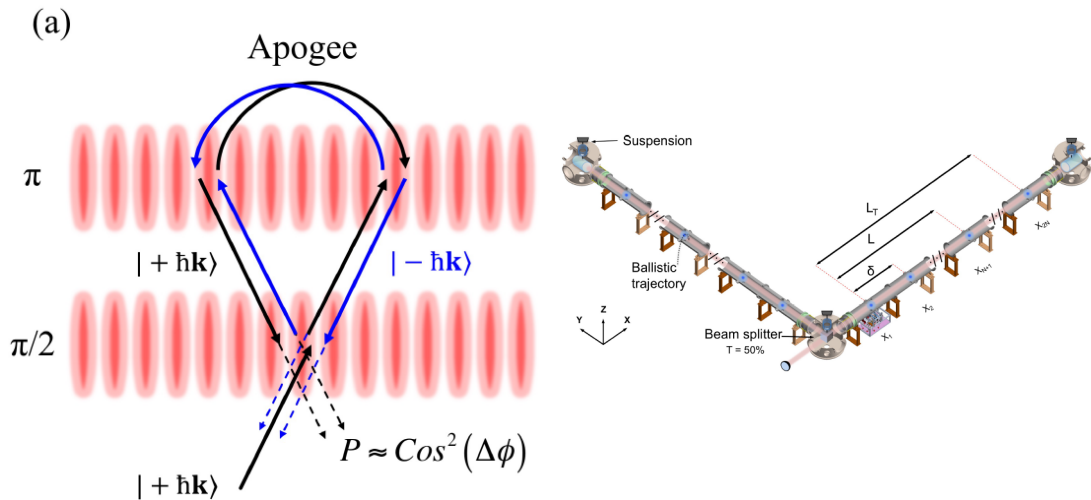


Figure 4.3: *Left*: Schematic example of the four-pulse atom interferometer that serves to read the phase acquired by the light in its travel. *Right*: ELGAR layout: each arm will be  $L_T = 32.1$  km long. A number of  $N = 80$  atom gradiometers of length  $L = 16.3$  km each and placed with their starting point at a distance of  $\delta = 200$  m one from the other will be placed along ELGAR's arms:  $(N - 1)\delta + L = L_T$ . Figures from [75]

#### 4.4.2 TOBA: Torsion Bar Antenna

A TOBA [77] is another project proposed for low frequency GW detection. It would be suitable both as ground-based and space-borne GW detector (it could be indeed placed on a spacecraft). It comprises two bars (the test masses) orthogonal to each other and parallel to the ground. Each bar would be suspended by its center of mass and free to rotate around the vertical axis. In this way an incoming GW (assumed with wavelength much bigger than the TOBA dimensions) would impress on it tidal forces ending in a rotation [79]. The GW signal would then be read using a laser beam impinging on the two bar's ends.

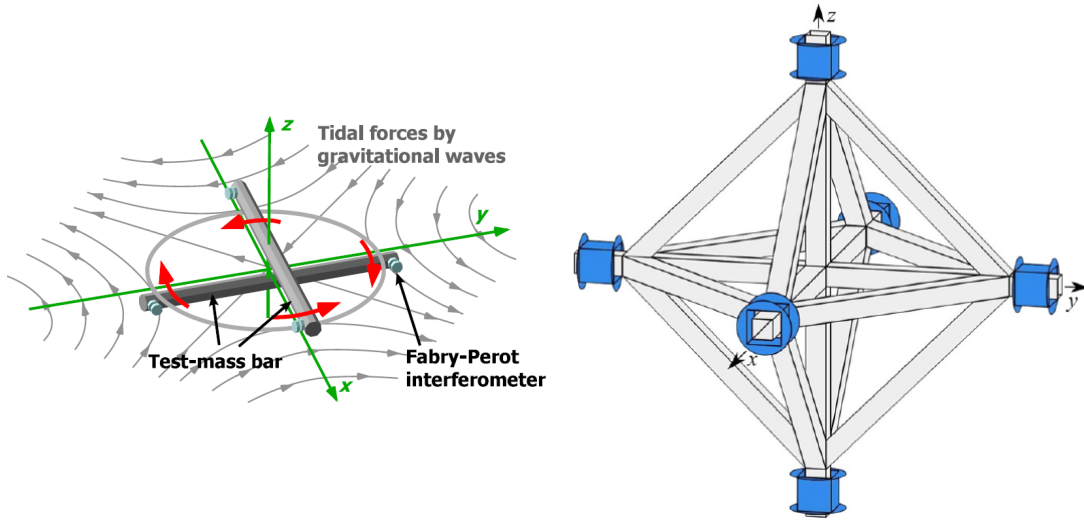


Figure 4.4: *Left*: Principle of a torsion-bar antenna. Two orthogonal bars feel differential torques due to the passing GW. *Right*: SOGRO's test mass configuration: six magnetically levitated superconducting test masses (in blue) are used to measure the six components of the curvature tensor. Figures from [77] and [78]

The resonance of such a torsion pendulum would be lower than that of AdV's pendulums, with a fundamental torsion frequency of  $\sim 30\mu\text{Hz}$ : this is important in order to be sensitive in the lower frequency band.

#### 4.4.3 SOGRO: Superconducting Omni-directional Gravitational Radiation Observatory

SOGRO [80] is thought to be a *tensor detector*, which means that a single antenna would be capable of resolving the source direction and polarization of an incoming GW. In this regard, all the *six* independent components of the metric tensor need to be measured. SOGRO would be composed of six superconducting test masses (with three degrees of freedom each) levitated over three orthogonal mounting bars. Movements of the test masses would be measured with respect to sensing circuit elements mounted on the bars (which should be rigid and with resonance frequencies above the sensitivity frequency band). SOGRO has been proposed to be constructed underground at a depth of 500 m or more and at cryogenic temperatures. The entire platform should then be suspended like a pendulum in order to suppress the seismic noise, which dominates at lower frequencies. NN would be an important source of noise [78].

## 4.5 LGWA: Lunar Gravitational Wave Antenna

Another interesting project that aims to be sensitive in the frequency band of 1 mHz - 1 Hz is the LGWA [81]. It is supposed to monitor Moon's normal modes excited by GWs by means of an array of high-end inertial sensors. The Moon is a very large body with very low seismic activity [82]. For this reason, it is an ideal candidate for such a detector [83, 84]. The seismometer technology is already under development as part of ET R&D, [85, 86, 87] but it would need additional improvements beyond ET requirements to make GW detection possible. In this case the test mass would be the Moon itself. This is feasible because the seismic noise would be very low due to the absence of an atmosphere and oceans. The choice of the readout system will be important as well, in particular, if cryogenic technologies will be employed (like levitating test masses) [88], the sensitivity of LGWA above 0.1 Hz would beat those of LISA (of course, cryogenic technologies are not of easy implementation on the Moon, but there we can find regions with continuously very cold temperatures which could help).



## Part II



# 5 ALGORITHMIC TOOLS

## Contents

---

5.1	Global optimization algorithms	52
5.1.1	<i>Basin hopping optimization</i>	52
5.1.2	<i>Evolutionary algorithms for optimization</i>	53
5.1.3	<i>Particle swarm optimization</i>	54
5.2	Gaussian Process Regression	55
5.3	Wiener filter for NN cancellation	57
5.3.1	<i>Could the Wiener filter also cancel part of the GW signal?</i>	63
5.3.2	<i>Stationarity of the seismic data</i>	64
5.3.3	<i>SNR limiting curve</i>	64

---

In this short chapter some algorithms that have been used in this PhD thesis will be introduced. In particular, optimization algorithms and Gaussian process regression (GPR) will be discussed in section 5.1 and in section 5.2, respectively. Finally, section 5.3 will present the theory of Wiener filter (WF) which is the core of the NN cancellation.

## 5.1 Global optimization algorithms

In Chapter 7 and Chapter 8 we will show that, in order to maximize the capability of cancelling the NN by means of a WF, we need first to find the *optimized array* of witness sensors. Indeed, as we have seen, WF performances are well described by the residual,  $R(\omega)$ , which represents the NN left in the data after the cancellation -see Equation 5.20. The lower the residual the better the cancellation performances: this leads us to the concept of *global optimization*: we need to find the global minimum of  $R(\omega)$ .  $R(\omega)$  depends of the positions of the N witness sensors ( $R(\omega) : \mathbb{R}^{dN} \rightarrow \mathbb{R}$ , with  $d = 2, 3$  representing the dimensions of the physical space where we put the seismometers). Finding the minimum of  $R(\omega)$  means finding the optimal locations of the sensors that will maximize the cancellation performances (giving the smallest possible  $R(\omega)$ ).

Normally, local optimization algorithms are able to find a local minimum in the neighbourhood of a given point of a N-dimensional function. This is not enough if we wish to find the optimal array for the noise cancellation: the residual function  $R(\omega)$  might be a *non-convex function* and have many local minima higher than the global minimum. Each one of these local minima would give us a *sub-optimal* array. So we need to search for the *global* minimum scanning a broad compact subset of the  $R(\omega)$  domain:  $\Omega \subset \mathbb{R}^{dN}$ . In the global optimization field,  $R(\omega)$  is called *cost function*.

### 5.1.1 Basin hopping optimization

In chemical physics there is much interest in efficient global optimization methods for finding the lowest energy configuration of macromolecular systems. In this framework, the basin-hopping global optimization algorithm was developed, it attempts to stochastically find the global minimum and it is part of the annealing algorithms. The basin-hopping algorithm [89, 90, 91, 92] transforms the potential energy surface into a collection of interpenetrating staircases (see Figure 5.1): this transformation associates every point of the configuration space with the local minimum obtained by a geometry optimization started from that point. In this way, transition state regions are removed from the problem.

Basin-hopping is an iterative algorithm, and in each cycle three steps are performed:

- A stochastic perturbation of the coordinates
- A local minimization
- An application of an acceptance/rejection criterion of new coordinates based on the minimized function value

The acceptance test is usually the Metropolis criterion of the standard Monte Carlo algorithms [93].

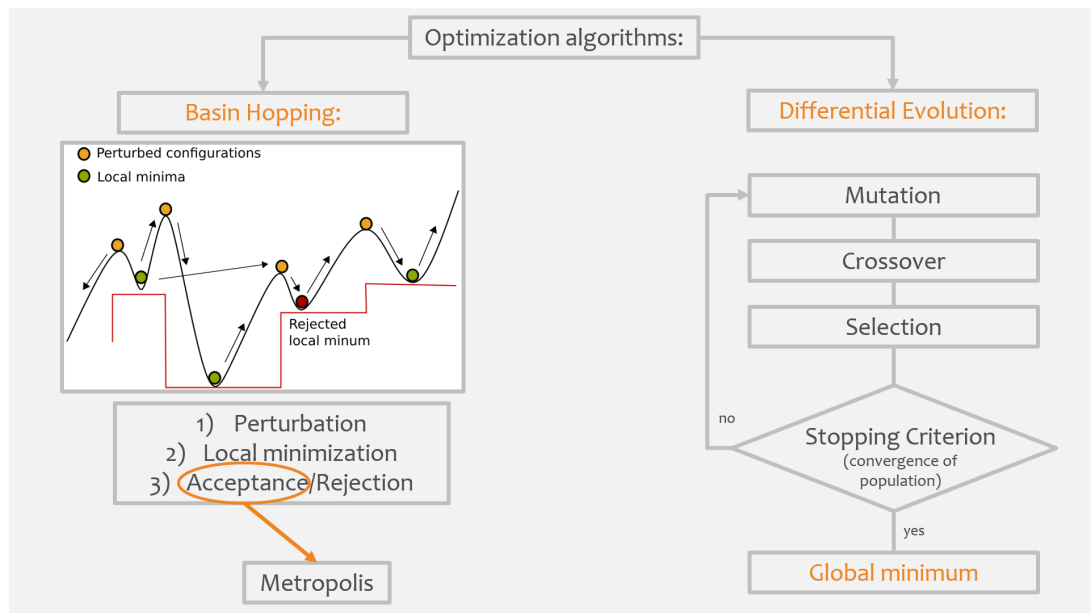


Figure 5.1: Scheme of the two optimization algorithms Basin hopping and Differential evolution.

### 5.1.2 Evolutionary algorithms for optimization

Evolutionary algorithms [94, 95] use simulated evolution to explore the solutions of complex real world problems. They are a subclass of the Evolutionary computation and are stochastic search algorithms. An evolutionary algorithm is inspired by the mechanisms of biological evolution: such as reproduction, mutation, recombination, and selection. In particular, we will briefly describe the differential evolution algorithm (DE) [96, 97]. DE can be run in parallel, so, depending on the computing infrastructure, it can be made faster.

The algorithm starts by choosing a random population that should cover the entire space of solutions. For the optimization of an array of sensors the *starting population* (or first generation) should cover many possible configurations of the array. If prior knowledge of the problem is available, it can be included in the search by choosing the initial population accordingly. Then, the algorithm performs a *mutation*: for each individual belonging to the starting population it is generated a mutated individual by combining the former one with the difference of other two randomly chosen individuals of the starting population. Every individual is a vector containing the coordinates of the array configuration: in order to amplify population diversity, it is created another group of individuals mixing some vector elements from the first generation with the mutated vector elements. This passage is called *crossover*. The last step is the *selection*: the individuals of the next generation will be selected choosing between the individuals of the first generation and the individuals obtained from the crossover. Those that will lead to a smaller cost function (residual for us) will be part of the next generation, the others will be discarded. These steps will be repeated until some convergence criterion will be met (for example until  $R(\omega) > \epsilon$ ), see Figure 5.1.

### 5.1.3 Particle swarm optimization

Particle swarm optimization arose in the context of simulating the ability of human society to improve its knowledge [98], but it can be used as well to describe bird flocks behaviour [99]. The psychological assumption of particle swarm relies on the fact that individuals usually tend to follow their beliefs that proved to be the best ones in its experience. But the single individual will also consider beliefs of others if these are proved to be better than its own beliefs.

This can be translated in an algorithm where the individuals (for example the configurations of the array) update their position in the hyperspace of the all possible solutions based on their prior best solution (*individual behaviour*) and on the swarm global best solution (*social behaviour*). Some randomness needs also to be inserted in order to help the swarm to escape from possible local minima.

This kind of algorithm has been found to be effective with several kind of problems. Moreover, it is in some sense related to evolutionary algorithms even though, differently from them, the particle swarm algorithm relies on the previous memory of the best position. As for DE, particle swarm can run in parallel.

## 5.2 Gaussian Process Regression

In the *statistic* field, people are usually interested in *inferring models* from data and then interpreting them. *Machine learning* is instead oriented to *learn* from data algorithms that are capable of *predicting* new data very accurately, but with no possibility of interpreting the results (for examples neural networks are mostly black boxes applied to data).

*Gaussian processes* merge these two aspects: they are mathematically equivalent to known models but can learn from data to accurately predict new values [100] (under certain conditions Gaussian processes are also very similar to large neural networks). The problem of learning in Gaussian processes is related to find the best values of the hyperparameters of the covariance function (see below), this allows us to have a model for the data which we can interpret. Gaussian processes are a very powerful tool in machine learning, and they can be used for regression problems as well as for classification ones [101]. Gaussian processes regression (GPR) are also known in the geophysical field as "kriging" [102, 103]

We will focus on the Gaussian processes for regression problems.

A Gaussian process is a collection of random variables, any number number of which has a joint Gaussian distribution. We can then think at a Gaussian process over functions: this means that we can consider the values taken by a function in a point  $x_i$ ,  $f(x_i) = f_i$ , as the random variables of the process. If we take any N number of points  $x_1, \dots, x_N$  we will have N random variables  $f_1, \dots, f_N$  whose joint distribution will be a Gaussian described by a *mean function* and a *covariance function*:

$$m(x) = E[f(x)] \quad (5.1)$$

$$k(x, x') = E[(f(x) - m(x))(f(x') - m(x')))] \quad (5.2)$$

so, we can extract values taken by functions by drawing them from a multivariate Gaussian:

$$f(x) \sim \mathcal{GP}(m(x), k(x, x')) \quad (5.3)$$

GPR takes the form of a Bayesian inference over a "latent function",  $f(x)$ , [104]:

$$y = f(x) + \epsilon \quad (5.4)$$

Where  $y$  represents the noisy observation of  $f(x)$ :  $\epsilon$  is the noise affecting  $f(x)$  and we assume it to be Gaussian distributed.

Following a Bayesian approach we can think of Equation 5.3 as a *prior* for the distribution of the values of  $f(x)$ . We can also set  $m(x) = 0$  because assuming

## 5. ALGORITHMIC TOOLS

---

some function for  $m(x)$  usually does not change too much the GPR performances, so:

$$f(x) \sim \mathcal{N}(0, k(x, x')) \quad (5.5)$$

We can choose the model for the covariance function (or kernel)  $k(x, x')$  and this will represent our prior knowledge about  $f(x)$ . In the majority of cases a squared exponential is a good choice:

$$k(x_i, x_j) = \sigma_f^2 e^{-\frac{(x_i - x_j)^2}{2\ell}} - \sigma_\epsilon \delta_{ij} \quad (5.6)$$

Where  $\sigma_f$ ,  $\ell$  and  $\sigma_\epsilon$  are the signal variance, the length scale and the noise variance, respectively; they are the *hyperparameters* of the GPR. This are free parameters that can be inferred by the data. We can draw many functions from the prior of Equation 5.5 and with fixed hyperparameters and covariance function defined by Equation 5.6. For example, Figure 5.2 shows 150 sampled functions from the prior described by Equation 5.5 and with fixed hyperparameter values. If we

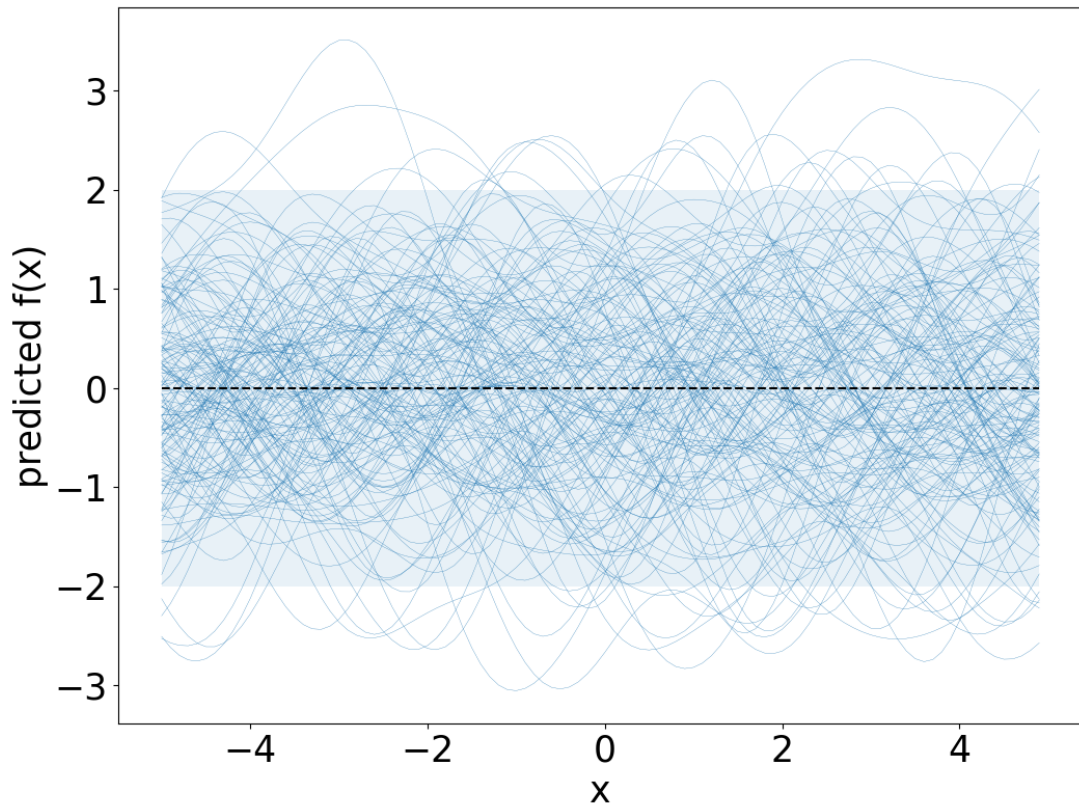


Figure 5.2: Functions  $f(x)$  sampled by a prior with fixed hyperparameters:  $\sigma_f = 1$ ,  $\ell = 0$  and  $\sigma_\epsilon = 0$  and zero mean.



wish to infer the Gaussian process model from some data points what we need to do is to *condition* (Bayes's theorem) the prior joint distribution, Equation 5.5, on the  $N$  observed data (that will be expressed like vectors:  $\mathbf{x}_o$  and  $\mathbf{y}_o$ ). Exploiting some properties of the multivariate Gaussian distributions we can express the posterior of  $f_*$  evaluated at the point  $x_*$  as:

$$f_*|x_*, \mathbf{x}_o, \mathbf{y}_o \sim \mathcal{N}(\mu_*, \sigma_*) \quad (5.7)$$

Where the asterisk indicates the predicted value that we wish to obtain from the posterior distribution, and:

$$\mu_* = k(x_*, \mathbf{x}_o)^T (k(\mathbf{x}_o, \mathbf{x}_o) + \sigma_\epsilon^2 \mathbf{I})^{-1} \mathbf{y}_o \quad (5.8)$$

$$\sigma_* = k(x_*, x_*) - k(x_*, \mathbf{x}_o)^T (k(\mathbf{x}_o, \mathbf{x}_o) + \sigma_\epsilon^2 \mathbf{I})^{-1} k(x_*, \mathbf{x}_o) \quad (5.9)$$

Here,  $k$  can be a scalar ( $k(x_*, x_*)$ ) a vector ( $k(x_*, \mathbf{x}_o)$ ) or a matrix ( $k(\mathbf{x}_o, \mathbf{x}_o)$ ). In Figure 5.3 we plotted  $\mu_*(x_*)$  and a  $\pm 2\sigma_*(x_*)$  shaded area for a noise-free model ( $\sigma_\epsilon = 0$ ) and for a noisy model. We should note in Figure 5.3 that for noise-free data the variance of the posterior is zero at the observed data points, while it is smaller than the other points, but not zero, for a noisy model.

Of course, for a proper regression, we should *infer* the values of the hyperparameters from the data. This can be done in two ways, but always relying on the Bayesian framework. The first way is a fully Bayesian approach which consists in marginalizing over the hyperparameters to get the predictions. This would necessitate to define a prior for the hyperparameters: the problem here, is that we cannot rely any more on the straightforward math which is typical of the Gaussian probability distributions. This is due to the fact that the marginalization over the hyperparameters leads to a non-Gaussian likelihood so that we can marginalize only through computationally expensive methods like Markov-Chains Monte Carlo. The second way of learning the hyperparameters is easier and it consists in maximizing the likelihood. This is the most common approach and it is what I used Chapter 8.

### 5.3 Wiener filter for NN cancellation

Norbert Wiener formulated the underlying theory for continuous time least mean square error filters in his 1949 work [105]: the extrapolation to discrete time signals is then straightforward. A WF is typically used to estimate signals immersed in the noise. It can also be used in the opposite way: to estimate a noise that needs to be removed from some signal (that is exactly what will be done for the

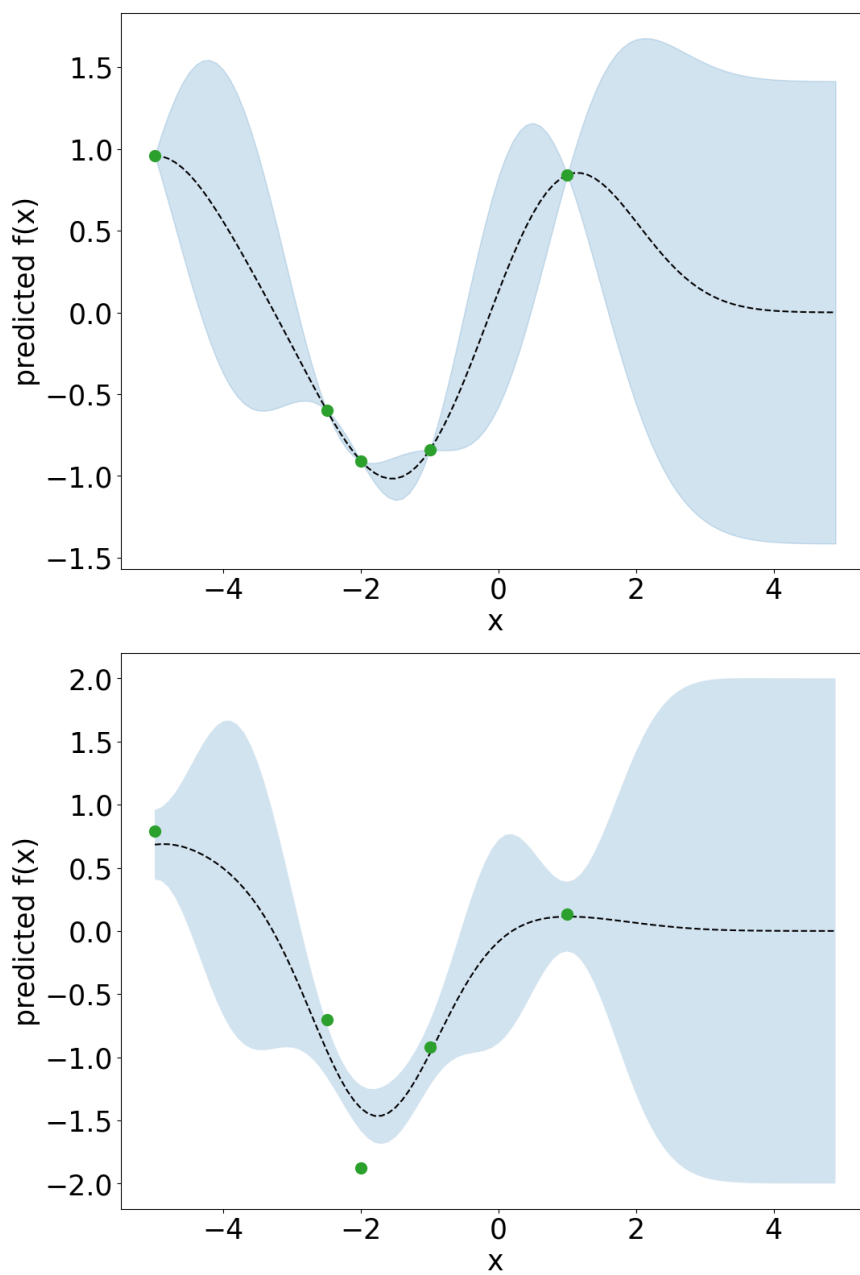


Figure 5.3: Posterior obtained from the conditioning of the prior over the green data point. The black curve represents  $\mu_*(x_*)$  and the shaded area  $\pm 2\sigma_*(x_*)$ . The hyperparameters were fixed:  $\sigma_f = 1$ ,  $\ell = 0$ ,  $\sigma_\epsilon = 0$  for the free noise signal (*Top*) and  $\sigma_\epsilon = 0.4$  for the noisy signal (*Bottom*).

---

## 5. ALGORITHMIC TOOLS

---

NN). It also finds application in removing the effects of some *linear* distortions in images or in the telecommunication field. An historical application of the WF is its use to predict the trajectory of a projectile during the World War II. Moreover, the prediction of signal fluctuations based on past values finds application in audio and video coding. The Wiener filter theory is the basis of least square applications, such as linear predictions (used in economy) and adaptive filters.

The least square error theory assumes that the signal is a random stationary process<sup>1</sup>. In reality, signals are unlikely stationary, but they can usually be considered almost stationary over a small number of samples: in this case it is possible to recalculate the filter coefficients over every block (the filter is said to be block adaptive).

In the following we will consider a Finite Impulse Response filter (FIR)<sup>2</sup>. The signal that has to be reconstructed is denoted as *target*: in the NN cancellation this is the strain response of the test masses, while the *witness* sensors provide the input signals to the linear filter. Being that we reconstruct the target signal,  $x(t)$ , with a linear combination of the input signals,  $y(t)$ , it is necessary that they are linearly related one to the other. This is indeed true in the case of the NN acceleration induced by a seismic wave (see Equation 3.5). Signals are actually discrete and sampled at a rate of  $1/\Delta t$ , so, let  $y[m]$  represent the discrete signal  $y(t)$  at the time  $t_m = t_0 + m\Delta t$ . With  $N$  witness sensors the estimated target time series,  $\hat{x}[m]$ , will read:

$$\begin{aligned}
 \hat{x}[m] &= \sum_{k=0}^{P-1} w_{k_0} y_0[m-k] + \dots + \sum_{k=0}^{P-1} w_{k_N} y_N[m-k] = \\
 &= \sum_{k=0}^{P-1} \sum_{n=0}^{N-1} w_{k_n} y_n[m-k] = \\
 &= \sum_{k=0}^{P-1} \mathbf{w}_k^T \mathbf{y}[m-k]
 \end{aligned} \tag{5.10}$$

---

<sup>1</sup>A stochastic process,  $\{X_t\}$ , is said to be strictly stationary if the cumulative distribution of the unconditioned joint distribution of  $\{X_t\}$ ,  $F_X(x_{t_1+\tau}, \dots, x_{t_n+\tau})$ , at times  $t_1 + \tau, \dots, t_n + \tau$ , satisfies:  $F_X(x_{t_1+\tau}, \dots, x_{t_n+\tau}) = F_X(x_{t_1}, \dots, x_{t_n})$ , for all  $\tau, t_1, \dots, t_n \in \mathbb{R}$  and for all  $n \in \mathbb{N}$ . This means that  $F_X$  is not a function of time: the properties of the stationary process do not change with it. A less strict definition is that of a wide-sense stationary process, where the expectation value  $E[X(t)] = \mu$  is constant in time and the variance is  $E[(X(t_1) - \mu)(X(t_2) - \mu)] = \sigma(\tau)$ , where  $\tau = t_2 - t_1$  ( $\sigma$  does not depend on the specific time, but only on time differences).

<sup>2</sup>It is a filter whose impulse response is of finite duration. An  $N^{\text{th}}$ -order discrete-time FIR filter has an impulse response (i.e. the output in response to a Kronecker delta input) that is long precisely  $N+1$  samples.

---

## 5. ALGORITHMIC TOOLS

---

This is a Multiple Input Single Output (MISO) linear filter of order  $P$ , which means that we use  $P$  Wiener coefficients and  $P$  past values of each witness signal,  $y_n[m]$ .  $\mathbf{w}_k$  represents the  $k^{th}$  vector of filter coefficients:

$$\mathbf{w}_k = \begin{pmatrix} w_{k_0} \\ \dots \\ w_{k_N} \end{pmatrix} \quad (5.11)$$

While  $\mathbf{y}[m]$  is the vector containing the signals from all the  $N$  witness channels at the time  $t_0 + \Delta m$ :

$$\mathbf{y}[m] = \begin{pmatrix} y_0 \\ \dots \\ y_N \end{pmatrix} \quad (5.12)$$

The WF is then defined by the coefficients that minimize the ensemble average of the square error function,  $E[e^*[m]e[m]]$ , with  $e[m] = x[m] - \hat{x}[m]$ .

The work presented in this thesis deals with the problem of optimizing the positions of the witness sensors in order to improve the WF capabilities to reduce the NN of seismic origin. This is done in the frequency domain, so for this particular goal we do not need a time domain discussion of the WF; even though, when the time of setting up the pipeline for the NN cancellation will come, the WF will need to be considered in the time domain. The distinction between the time domain WF and the frequency domain WF lays principally in the fact that in the frequency domain the information regarding the order of the filter disappears. Indeed Equation 5.10 is a discrete convolution of functions with finite support, so we can apply the convolution theorem. This means that we can apply the Fourier transform to a block of  $M$  samples and rewrite Equation 5.10 as:

$$\hat{X}(\omega) = \mathbf{W}^T(\omega)\mathbf{Y}(\omega) = \mathbf{Y}^T(\omega)\mathbf{W}(\omega) \quad (5.13)$$

Where both  $\mathbf{W}(\omega)$  and  $\mathbf{Y}(\omega)$  are  $N$ -dimensional vectors containing the Fourier transforms of the WF coefficients and the  $N$  witness signals respectively. We will directly perform the minimization to obtain the least square error in the frequency domain. To lighten the calculations in the following steps we will omit

the dependence on  $\omega$ .

$$\begin{aligned}
 E[e^*e] &= E[(X - \mathbf{Y}^T \mathbf{W})^* (X - \mathbf{Y}^T \mathbf{W})] \\
 &= E[XX^* - X(\mathbf{Y}^T \mathbf{W})^* - X^* \mathbf{Y}^T \mathbf{W} + (\mathbf{Y}^T \mathbf{W})(\mathbf{Y}^T \mathbf{W})^*] = \\
 &= E\left[XX^* - X \sum_i Y_i^* W_i^* - X^* \sum_i Y_i W_i + \left(\sum_i Y_i W_i\right) \left(\sum_j Y_j^* W_j^*\right)\right] = \\
 &= P_{XX} - \sum_i W_i P_{XY_i}^* - \sum_i W_i^* P_{XY_i} + \sum_{i,j} W_i W_j^* P_{Y_i Y_j}
 \end{aligned} \tag{5.14}$$

Where  $P_{XX}(\omega) = E[X^*(\omega)X(\omega)]$  is the PSD of the target signal,  $P_{Y_i Y_j}(\omega) = E[Y_i^*(\omega)Y_j(\omega)]$  is the element  $ij$  of the  $N \times N$  matrix of the CPSD<sub>s</sub> between the  $i^{\text{th}}$  and  $j^{\text{th}}$  witness signals and it will be denoted as  $\bar{\mathbf{P}}_{YY}$ .  $P_{XY_i}(\omega) = E[Y_i^*(\omega)X(\omega)]$  is the  $i^{\text{th}}$  element of the the  $N$ -vector of the CPSD between the target signal and the  $i^{\text{th}}$  witness sensor signal and it will be denoted as  $\mathbf{P}_{XY}$ . To get the WF coefficients we have to minimize Equation 5.14 with respect to  $W$ . In the time domain this is easy, since everything can be considered real. In the frequency domain we have to deal with complex quantities and we must be careful. Indeed, if  $z \in \mathbb{C}$  we have that  $f(z) = z^*$  is not analytical, which means that the derivative of  $f(z)$  respect to  $z$  does not exist and, consequently, every  $f(z)$  containing  $z^*$  is not analytical. Since we just have to find the minima of Equation 5.14, we can find a way around and use the *Wirtinger derivative* [106], which allows us to perform the derivative with respect to  $z^*$ . The Wirtinger derivatives are so defined:

$$\frac{\partial}{\partial z} = \frac{1}{2} \left( \frac{\partial}{\partial x} - i \frac{\partial}{\partial y} \right) \tag{5.15}$$

$$\frac{\partial}{\partial z^*} = \frac{1}{2} \left( \frac{\partial}{\partial x} + i \frac{\partial}{\partial y} \right) \tag{5.16}$$

$$\tag{5.17}$$

with  $z = x + iy$ , in this way we have that:  $\partial_z z^* = 0$ ,  $\partial_{z^*} z^* = 1$  and all the normal rules of the derivatives will apply. So we minimize with respect to  $\mathbf{W}^*$ :

$$\frac{\partial}{\partial \mathbf{W}^*} E[e^*e] = (\partial_{W_1^*}, \dots, \partial_{W_N^*}) E[e^*e] = 0 \tag{5.18}$$

And we finally obtain:

$$\mathbf{P}_{XY} = \bar{\mathbf{P}}_{YY} \mathbf{W} \rightarrow \mathbf{W} = (\bar{\mathbf{P}}_{YY})^{-1} \mathbf{P}_{XY} \tag{5.19}$$

---

## 5. ALGORITHMIC TOOLS

---

Some considerations about  $P_{XX}$ ,  $\mathbf{P}_{XY}$  and  $\bar{\mathbf{P}}_{YY}$ .  $P_{XX}$  is a scalar and it is real ( $P_{XX} = P_{XX}^*$ ), while  $\mathbf{P}_{XY}$  and  $\bar{\mathbf{P}}_{YY}$  are a complex vector and a complex matrix, respectively. Indeed, the CPSD of two signals contains information about their phase difference, which is stored in a complex exponential. Moreover,  $\bar{\mathbf{P}}_{YY}$  is hermitian.

So far we have found the values of the WF coefficients that minimize the square root error. With this result we can rewrite  $E[e^*e]$  in a way that will be useful in the following chapters:

$$\begin{aligned} E[e^*e] &= P_{XX} - 2 \sum_{i,j} (P_{YY}^{-1})_{ij} P_{XY_j} P_{XY_i}^* + \sum_{i,j} \sum_{m,l} (P_{YY}^{-1})_{im} P_{XY_m} (P_{YY}^{-1})_{jl}^* P_{XY_l} (P_{YY})_{ij} = \\ &= P_{XX} - \sum_{i,j} (P_{YY}^{-1})_{ij} P_{XY_j} P_{XY_i}^* = \\ &= P_{XX} - \mathbf{P}_{XY}^\dagger \bar{\mathbf{P}}_{YY}^{-1} \mathbf{P}_{XY} \end{aligned}$$

Where we exploited the fact that  $\bar{\mathbf{P}}_{YY}$  is hermitian and that  $\bar{\mathbf{P}}_{YY} \bar{\mathbf{P}}_{YY}^{-1} = \bar{\mathbf{I}}$ , with  $\bar{\mathbf{I}}$  the identity matrix. We can finally define the residual as the ensemble average of the least square error normalized by the target signal PSD:

$$R(\omega) = 1 - \frac{\mathbf{P}_{XY}^\dagger \bar{\mathbf{P}}_{YY}^{-1} \mathbf{P}_{XY}}{P_{XX}} \quad (5.20)$$

Since both  $E[e(\omega)^*e(\omega)]$  and  $P_{XX}(\omega)$  are real and positive scalars,  $R(\omega)$  will also be positive and real.

The square root of  $E[e(\omega)^*e(\omega)]$  is the amplitude of the noise left after the cancellation. This means that  $\sqrt{R(\omega)}$  represents the reduction factor that we can achieve applying the WF to the NN: it is therefore a well representation of the capability of the WF of cancelling the noise. For this reason it will be used as cost function in the optimization of the witness sensor array (see Chapter 7 and Chapter 8).

The information regarding the order of the filter did not enter in our calculations, however, the interferometer data is a time series and for the noise cancellation the WF will have to be implemented in the time domain. It is then important to understand the impact of the WF order on the cancellation. In [107] the WF order has been examined and it was shown that it plays an important role in the effectiveness on the NN cancellation, moreover it was found that increasing the order not always results in a better residual: in [108] it was demonstrated that a high number of WF coefficients leads to higher statistical errors in the correlation measurements and then worse WF performances. Moreover, we have to keep in mind that a higher WF order implies more computational complexity:

large filter orders may lead to numerical instabilities with ill-conditioned matrix of correlation (in the WF time domain exposition the matrix dimensions depend also on the order of the filter).

The WF is considered the optimal filter because it minimizes the square error function. In reality, using a WF in the time domain (which is necessary if we want to remove the noise in real time and without introducing any artefacts) implies the inversion of a huge matrix. This introduces statistical errors, which make the WF, not really optimal. Even taking a very long correlation time would not be very useful: the seismic field is indeed non-stationary and the filter would need to be updated regularly to adapt it to the drifts in the seismic field.

As suggested by J. Harms [109], one solution could be using a gradient descent to find the optimal values of the linear FIR coefficients such that they can optimally reduce the noise (it would mean applying the gradient descent to the square error).

In Chapter 7 and Chapter 8 we will refer at  $\bar{\mathbf{P}}_{YY}$ ,  $\mathbf{P}_{YX}$  and  $P_{XX}$  as  $\bar{\mathbf{C}}_{SS}$ ,  $\mathbf{C}_{SN}$  and  $C_{NN}$  respectively.

### 5.3.1 Could the Wiener filter also cancel part of the GW signal?

A concern might arise regarding the use of a WF to reduce the NN: could it also cancel part of the GW signal that we want to measure?

This is possible only if the GW has some effect on the seismometers. For example, the GW might excite normal modes of the Earth that could then be recorded by the seismometers. This possibility would be a very small effect. Indeed, already at 1 Hz, the seismic noise would be larger than the effect induced by a GW by 5 orders of magnitude [110]. The seismic noise background is the main reason for which the LGWA project is aimed to be located on the Moon (see section 4.5). On the Earth, instead, the coupling between the GWs and our seismometers would be very small and negligible, especially in the frequency band of interest of the interferometric detectors.

We can also have other effects that could induce coupling between the GW and the seismic sensors. The actuators of the test masses could couple in various ways to the seismometers, for example by means of magnetic fields or through the recoil of the actuators transmitted to the ground and then to the seismic sensors. Since the actuators contain also part of the GW signal (this happens especially at low frequencies, where the cavities must be kept locked, see subsection 2.2.5) this could lead to some cancellation of the GW signal. Also in this case, however, the coupling effect can be neglected because it is very small [111].

Another possibility [111] that could lead to a partial cancellation of the GW signal would be training the WF on a too short data set. This would lead to random correlations between the GW signal and some seismic transients, but this can be avoided using data much longer than the expected GW signal, thus averaging out the seismic transients.

### 5.3.2 Stationarity of the seismic data

The WF theory assumes to deal with wide-sense stationary signals, otherwise the WF trained on a piece of non-stationary data might not perform optimally. It is clear that seismic noise cannot be stationary: there will be transients, small earthquakes, glitches induced by some source (i.e. moving objects like cars). Virgo is located near a lot of possible sources of this type, in particular there are some bridges in its vicinity [112] which can provoke glitches in the seismic data due to passing cars. Apart from these transients, the underlying seismic noise is produced by sources, such as wind, ocean waves and natural phenomena that are mostly stationary over the course of the day (except for stormy days).

Tringali et al. in [19] found that the seismic field in Virgo is inhomogeneous and anisotropic, which is likely due to the presence of local sources as well as to the scattering of seismic waves from the building structures laying under the ground. This is particular evident above 10 Hz. The paper also showed that the noise cancellation performances of a WF applied to seismic data collected in the vicinity of the test mass varied significantly over the day. These results suggest that the WF should be updated at least every hour in order to follow diurnal evolutions of anthropogenic noise.

### 5.3.3 SNR limiting curve

The SNR of the witness sensors is very important for the performance of the cancellation: in the end the WF will be limited by it.

The best possible case for a WF with N witness sensors is when each sensor records the target signal plus some noise:

$$Y_i(\omega) = X(\omega) + n_i(\omega) \quad (5.21)$$

We assume that the noise of the  $i^{th}$  sensor,  $n_i$ , is uncorrelated both with the target signal,  $X(\omega)$ , and with the noise of the  $j^{th}$  sensor:

$$\bar{\mathbf{P}}_{YY} = E[\mathbf{Y}(\omega)^* \mathbf{Y}(\omega)] = P_{XX}(\omega) \bar{\mathbf{A}} + P_{nn}(\omega) \bar{\mathbf{I}} \quad (5.22)$$

$$P_{XY_i} = E[X(\omega)^* Y_i(\omega)] = P_{XX}(\omega) \quad (5.23)$$

$$(5.24)$$



---

## 5. ALGORITHMIC TOOLS

---

Where  $\bar{\mathbf{A}}$  is a matrix of ones with dimensions  $N \times N$ :

$$\bar{\mathbf{A}} \equiv \begin{pmatrix} 1 & 1 & \cdots & 1 & 1 \\ 1 & 1 & \cdots & 1 & 1 \\ \vdots & \vdots & \ddots & \vdots & \vdots \\ 1 & 1 & \cdots & 1 & 1 \\ 1 & 1 & \cdots & 1 & 1 \end{pmatrix} \quad (5.25)$$

In order to calculate the residual in Equation 5.20 we need to find the inverse of  $\bar{\mathbf{P}}_{YY}$ :

$$(P_{XX}\bar{\mathbf{A}} + P_{nn}\bar{\mathbf{I}})(k\bar{\mathbf{A}} + P_{nn}^{-1}\bar{\mathbf{I}}) = \bar{\mathbf{I}} \quad (5.26)$$

Which means solving for  $k$ , where:

$$\bar{\mathbf{P}}_{YY}^{-1} = (P_{XX}\bar{\mathbf{A}} + P_{nn}\bar{\mathbf{I}})^{-1} \equiv k\bar{\mathbf{A}} + P_{nn}^{-1}\bar{\mathbf{I}} \quad (5.27)$$

To solve Equation 5.26 we notice that:

$$\bar{\mathbf{A}}^2 = N\bar{\mathbf{A}} \quad (5.28)$$

And finally:

$$k = \frac{-P_{XX}}{P_{nn}(P_{nn} + NP_{XX})} \quad (5.29)$$

Inserting  $\bar{\mathbf{P}}_{YY}^{-1}$  in Equation 5.20 we find:

$$R(\omega) = 1 - \frac{1}{1 + \frac{1}{N \text{SNR}^2}} \quad (5.30)$$

Where we defined  $\text{SNR}^2 = P_{XX}/P_{nn}$ . Equation 5.30 tells us that the WF averages the noise of the  $N$  sensors: the more the sensors that we use, the better the overall SNR and therefore the estimation of the target signal  $X(\omega)$ .

## 5. ALGORITHMIC TOOLS

---

# 6 SEISMIC NEWTONIAN NOISE CANCELLATION

## Contents

---

6.1	Introduction	68
6.2	Seismic fields generating NN	69
6.3	Required Newtonian noise suppression in GW interferometers	72
6.4	NN in ELGAR	74
6.5	NN from body waves	76
6.6	NN from surface waves	81
6.7	Active NN cancellation	84
6.8	Two point spatial correlation for the NN cancellation	84
6.8.1	<i>Isotropic and homogeneous seismic field</i>	86
6.8.2	<i>Two point spatial correlation for isotropic and homogeneous body waves field</i>	87
6.8.3	<i>Two point spatial correlation for isotropic and homogeneous Rayleigh waves field</i>	89
6.8.4	<i>Two point spatial correlation for a generic seismic field</i>	92

---

## 6.1 Introduction

At low frequencies, a GW detector can be described using a proper reference frame - see subsection 1.3.1. This allows us to describe the movements of the test masses as if they were caused by external forces, in particular, it can be shown that the GW signals are immersed in a sea of Newtonian noises. One of these noises is caused by fluctuations in the gravity field, which are produced by variations in the density of the materials surrounding the test masses (see section 3.2).

Weiss, in his famous paper (1972) [28] about the design of an interferometric GW detector, already recognized that gravity fluctuations could be a possible source of noise for this kind of instruments. More than 10 years later (1984) Peter Saulson [113] provided a more accurate model, which later was further developed in two distinct works: [15] and [9]. In these two last works the wave nature of the seismic field is taken into consideration and, moreover, it is argued that the dominant contribution to NN comes from seismic surface waves, in particular from Rayleigh waves (see section 6.2). In these works it was considered that the Rayleigh field produces density perturbations beneath the surface, and correlated displacements at the surface. Taking this into account, the coherent summation of these effects was directly obtained. Models of NN from Rayleigh waves have not improved much since these works.

Newtonian noises impact particularly on the lower frequency band of a GW interferometer: below 10-20 Hz. Thermal and quantum noise are planned to be reduced in AdV+ (in sight of O4) to a level such that the NN will become the dominant noise at low frequencies - see Figure 3.1. It is then important to find a way to also reduce the NN. While it is possible to physically shield the detector from seismic vibrations, it is more difficult to do the same for Newtonian noise: it would indeed require major modifications in the infrastructure of the detector, like constructing narrow moats close to test masses [9] or digging recess structures around them [10]. Another way is to actively mitigate the NN, which can also be done offline. Techniques of this kind have already been implemented in GW detectors to reduce other noises [11, 12, 13, 14].

The active noise cancellation is based on the idea that the NN acting on a test mass can be reconstructed by simply monitoring nearby seismic displacements by means of many auxiliary sensors. As we can see in Equation 3.5, the gravity field perturbation is linear with respect to the seismic displacement. This allows us to use a linear filter to estimate the NN: the Wiener filter (WF), see section 5.3. The capability of the WF to estimate the NN depends a lot on the quality of the information gathered with the array of sensors and on the stationarity of the noise (section 5.3 and subsection 5.3.2), it is then of fundamental importance to

optimally deploy high quality sensors (with very high SNR - see subsection 5.3.3). The performances of the WF can indeed change depending on the array geometry: the best one will allow to collect the most complete information about the seismic field. For this reason, one of the most important tasks for the NN cancellation is to find the *optimal geometry* for the sensor array. This will be addressed in Chapter 7 for what concerns underground detectors (which implies the possibility of deploying a 3D array) and in Chapter 8 for what concerns the specific case of Virgo.

## 6.2 Seismic fields generating NN

Seismic waves can be divided into longitudinal and transverse waves [114], the former are addressed as primary waves (also as *P waves* or compressional waves) because they are faster and are the first to arrive during an earthquake. They cause a compression/decompression displacement along their propagation direction (see Figure 6.1). This kind of wave causes a modification in the local density of the material that they cross and, for this reason, they can give rise to gravity fluctuations. Transverse waves are also denoted as secondary waves (also *S waves* or shear waves) because they are slower and during an earth quake they arrive after the P waves. They produce a shear displacement perpendicular to their propagation direction (see Figure 6.1). S waves can be distinguished in SV and SH, depending on the direction of the shear respect to the surface (vertical or horizontal). Since the shear stress does not modify the local density of the materials, S waves are usually not responsible for producing gravity fluctuations. However, if there is some discontinuity in the medium, then S waves will also produce gravity fluctuations (for example at the surface of a cavern, see Chapter 7).

Seismic waves on Earth can be distinguished into *body* and *surface* waves, depending on where they propagate. Body waves are constituted by P and S waves which propagate inside the medium. Surface waves could be instead called *guided waves* [115] because they arise from P and S waves when the medium is bounded: the waves are then guided along the surface (or along the boundary layer). Two kinds of surface waves can then be formed: *Love* and *Rayleigh waves*. Rayleigh waves arise at a discontinuity in the medium when P waves couple with vertical S waves (SV). They are elliptically polarised: the motion of a particle laying on a surface crossed by Rayleigh waves will be a retrograde vertical ellipse in the plane normal to the surface and to the wave propagation direction (see Figure 6.1). Also, Rayleigh waves are responsible for Newtonian noise: they are indeed able to provoke density changes in the crossed medium. We can divide

Rayleigh waves in two groups: fundamental Rayleigh modes (RF) and Rayleigh overtones, which are composed by all the higher modes. The overtones exist only if the medium is stratified.

Love waves are generated by horizontal S waves (SH) resonating near the surface (or near a discontinuity between two different layers). They do not cause density variations (see Figure 6.1) and therefore neither gravity fluctuations (unless the ground is not flat and presents complicated shapes).

The velocities of P and S waves depend on the material's density ( $\rho$ ), the shear module ( $\mu$ ) and the bulk module ( $K$ ) in the following way [9]:

$$c_P = \sqrt{\frac{K + \frac{4}{3}\mu}{\rho}} \quad (6.1)$$

$$c_S = \sqrt{\frac{\mu}{\rho}} \quad (6.2)$$

In the bedrock, located deep below the surface,  $c_P \sim 5000-6000$  m/s and  $c_S \sim 3200$  m/s. Near the surface, velocities are instead lower:  $c_P \sim 500-2000$  m/s and  $c_S \sim 250-700$  m/s. For what concerns surface waves it is a different matter: in a homogeneous and isotropic half space Rayleigh waves have velocity values:  $c_R \sim 0.9 c_S$  and they show a non dispersive behaviour (i.e  $c_R$  is independent from the frequency). If on the top of the half space there is also a homogeneous and isotropic layer, then Love waves propagate too and both them and the Rayleigh waves will show a dispersive behaviour.

Seismic noise is always present on the Earth's surface: in his 1993 paper [116] Peterson collected data from 75 seismic stations distributed all over the globe. He then parametrized the data and provided a New Low Noise Model (NLNM) and a New High Noise Model (NHNM), which are usually taken as a reference in seismic studies (NLNM is also plotted in Figure 6.2). Below 10 Hz, every seismic spectrum recorded on the globe follows the shape of Peterson's models: this shape is generated by different mechanisms. The part of the spectrum below 2 mHz is generated by atmospheric effects [117]: in particular by gravity fluctuations consequent to variations in the atmospheric density. Between 2 and 7 mHz there are many small peaks (called normal-mode resonances), denoted as *hum*, that show seasonal variations. This leads to think that the mechanism of generation could be due to infragravity waves (waves with frequency lower than that of their forcing process), but the hypothesis are still many and the mechanism still needs to be fully understood. The part of the the spectrum between 0.02 Hz and 1 Hz is called *microseism* and shows two distinct peaks: the *primary microseism* peak, at 0.05-0.07 Hz, which is mainly constituted by Love waves and the *secondary microseism* which lies around 0.1-0.4 Hz and it is

## 6. SEISMIC NEWTONIAN NOISE CANCELLATION

---

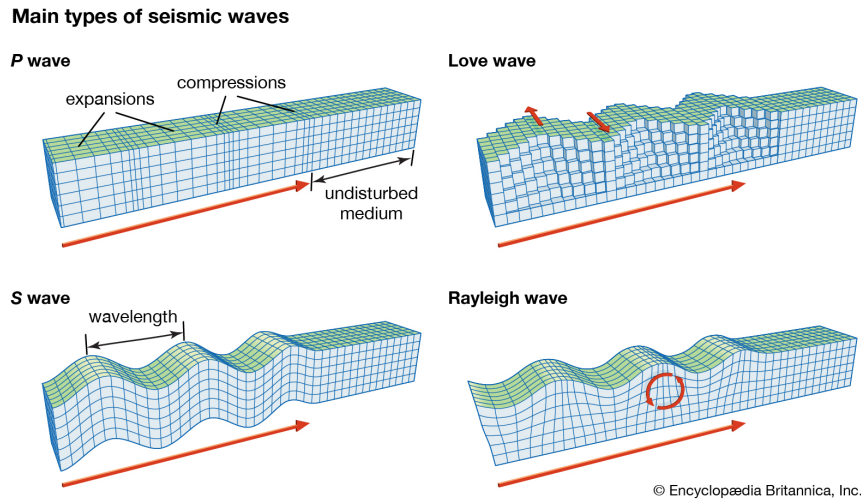


Figure 6.1: Representation of the displacement caused by the body waves (P and S) and by the surface waves (Rayleigh and Love). Image from Encyclopædia Britannica ([www.britannica.com](http://www.britannica.com)).

mainly composed by Rayleigh waves. The primary microseism has the same frequency of the ocean swells, while the secondary microseism has a frequency that is about the double of the first one, but with larger amplitudes. Longuet-Higgins

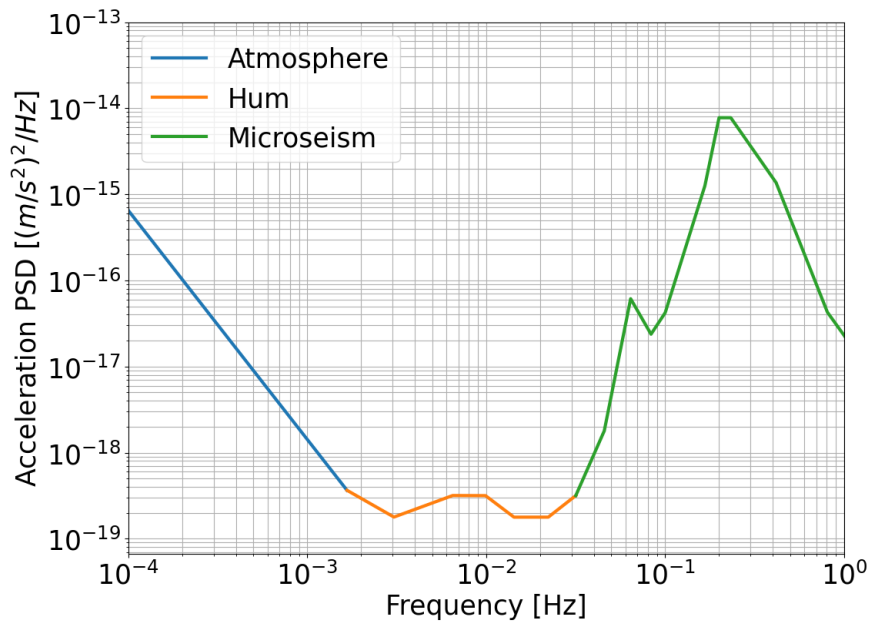


Figure 6.2: PSD of the NLNM in unit of acceleration [117].

[118] showed that the secondary microseism peak might be generated by the interaction of counterpropagating ocean waves. The characteristics of the primary microseism (same frequency as the ocean waves and large content of Love waves) suggest instead that the excitation mechanism is likely due to the interaction of the ocean waves with the bottom of the sea [119]. At frequencies  $> 0.5$  Hz the seismic noise depends primarily on winds, cultural noise (human activity) and also movement of water [120], while the displacement spectrum follows a power law of  $1/f^2$  [121], which is the main cause of seismic noise in interferometric GW detectors (see section 3.1).

### 6.3 Required Newtonian noise suppression in GW interferometers

Until now, Newtonian Noise has not been a concern for GW detectors, but with the new upgrades it will become a limiting factor. The latest models on NN can be found in [15] and [9]. The work of Beccaria et. al ([15]) shows that, given the spectral amplitude of the seismic noise ( $\sim 10^{-6}/f^2$  m/ $\sqrt{\text{Hz}}$ ), the spectral amplitude of the NN will be:

$$S_{h_{NN}}(f) \sim 3 \cdot 10^{-17} \times \frac{1}{f^4} \quad (6.3)$$

Since the beginning, it was known that after all the final improvements the NN would have been a final limitation for Virgo below 10 Hz. In particular, we can see (Figure 3.1) that for the sensitivity curve aimed for O4, Virgo will have to suppress the NN by at least a factor 3. In Chapter 8, the problem of finding the optimal array for performing the NN cancellation in AdV+ will be addressed. It will also be shown that, at a given frequency, it is (in principle) possible to reach the required reduction factor with already 15 seismometers.

Despite the fact that ET will be located underground, we will still have to take care of the NN cancellation. The main motivation of constructing ET underground is to strongly suppress NN from atmospheric [51] and seismic fields [122]. However, NN will still play an important role. As shown in Figure 6.3, NN from surface waves will be insignificant if the detector will be constructed a few 100 m underground (as long as frequencies are considered above  $\sim 1$  Hz). However, the NN from seismic body waves cannot be avoided at any depth, and it becomes a sensitivity-limiting noise contribution below 10 Hz. Depending on the quality of the underground site, one still needs to mitigate body-wave NN up to a factor



10.

The range of body-wave NN shown in the two plots of Figure 6.3 assumes that underground seismic spectra are a factor 3 to 12 above the NLNM [116], and that an isotropic field is composed entirely of P waves (conservative assumption since if it were composed entirely of S waves, then the NN would have been a factor 2 smaller). The prediction of Rayleigh NN (denoted *Surface* in the two plots) in underground detectors requires an assumption about the seismic surface spectrum, which is a factor 50 to 1000 above the NLNM in the two plots, but also an assumption about the dispersion curve. The assumed dispersion curve of Rayleigh waves has been taken as [123]:

$$c(f) = 2000 \text{ m/s} e^{-f/4\text{Hz}} + 300 \text{ m/s} \quad (6.4)$$

The slower (and therefore the shorter) the Rayleigh waves, the stronger the suppression of the associated NN with depth [52]. The dispersion model used

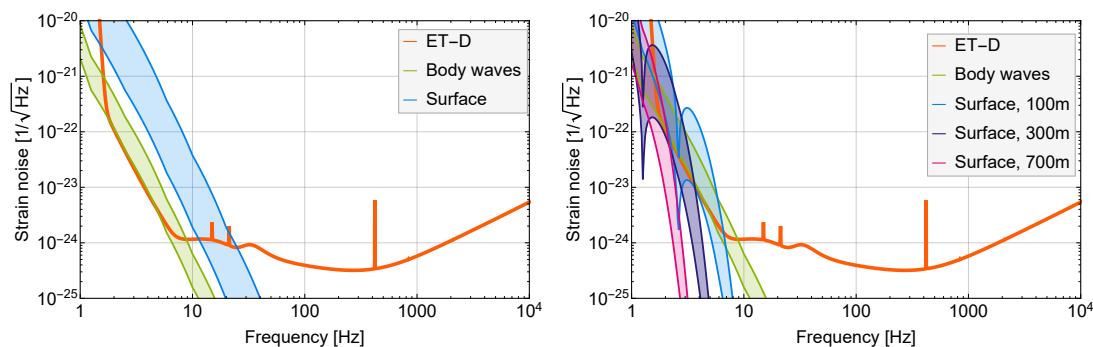


Figure 6.3: Seismic NN predictions for the Einstein Telescope.

(Rayleigh wavelength plays a negligible role for NN in surface detectors) yields a Rayleigh-wave speed of 1.8 km/s at 1 Hz falling to  $\sim 500$  m/s at 10 Hz. There can be significant regional variations, but these values are typical.

Rayleigh waves produce NN through rock compression, cavern-wall displacement, and surface displacement: all these three contributions must be taken into account in the model for the surface NN budget in underground detectors. These three contributions interfere suppressing the surface NN estimation of Figure 6.3 at specific frequencies.

The model for the NN from body waves, instead, has to take into account the different contributions coming from the bulk (only P waves) and from the cave walls (P and S contribution). The reflection of body waves from the surface topography is not taken into account, but this might need further investigations [52]. Both for body-wave and Rayleigh-wave fields, anisotropies can increase or decrease the NN relative to the isotropic level shown in Figure 6.3, but since

the final location (and so any potential anisotropy) for ET is not known yet, introducing any anisotropy in the NN estimations would not make sense.

We can conclude that planning for ET must include also NN cancellation, and it will be essential to have a detailed understanding of the seismic field in terms of spectra, speeds, or more accurately, two-point spatial correlations. This will make possible the precise prediction of NN in the underground detector, also considering the possible presence of anisotropies. Only then we will be able to determine the required NN cancellation, and to calculate the optimal sensor locations as it has been done for Virgo [124]. At the present time, due to the lacking of a detailed understanding of the seismic field in the ET location, NN suppression of up to a factor 10 is *potentially* required, if the underground site will be among the quieter ones, a factor 3 will be very likely sufficient (see Figure 6.3).

## 6.4 NN in ELGAR

If NN has not been a concern in interferometric GW detectors up to now, it will be instead a very important noise for low-frequency GW detectors located on Earth. In subsection 4.4.1 the ELGAR detector was introduced. Its operating window, 0.1 - 10 Hz, lays in the frequency band of the seismic microseism, for this reason it is important to understand how the NN will impact this instrument.

As for ET, the main source of NN will come from atmospheric NN (which will be anyway damped by going underground) and from seismic NN generated by body and Rayleigh waves that, in the microseism band, are typically dominant [125]. Of course, also for ELGAR, selecting a very quiet underground site will be of great help in reducing this kind of noise.

Both GW-interferometers, like AdV+, and ELGAR exploit the phase difference induced in a laser beam by a passing GW: however, the main difference between them is that ELGAR will measure this phase difference by means of  $N$  gradiometers regularly spaced along the arms (see Figure 6.4). Having many gradiometers will help to average the NN affecting ELGAR. Indeed, in the frequency band covered by the instrument, GWs can be considered constant along the whole arm length. Instead, the NN coherence length will be of the same order of the one of the seismic waves from which it is generated. This means that ELGAR will repeat the same GW measurement affected by different NN content and then it will average out the NN without influencing the GW signal. Following [76] we can write the strain relative to the NN in ELGAR like:

$$\sqrt{S_{NN\text{average}}(\omega)} = \frac{K(\omega)}{\sqrt{N}} \sqrt{S_{NN_1}(\omega)} \quad (6.5)$$

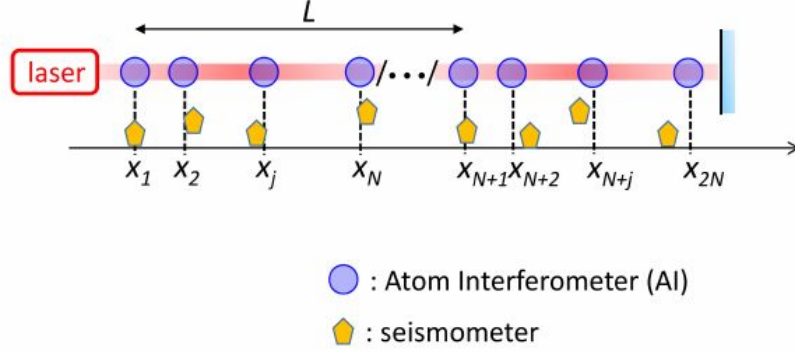


Figure 6.4: Geometry of one arm of ELGAR. Each arm is composed by  $N$  gradiometers (two atom interferometers (also said atom fountains) placed at  $x_i$  and  $x_{N+i}$ ) regularly spaced all over the arm.

Where  $\sqrt{S_{NN_{\text{average}}}(\omega)}$  is the NN strain obtained averaging over the  $N$  gradiometers and  $\sqrt{S_{NN_1}(\omega)}$  is the NN strain of the single one.  $K(\omega)$  is a factor that guides the reduction gain of the ELGAR NN with respect to that of the single gradiometer.  $K(\omega)$  ranges from 0 to  $\sqrt{N}$  and so we can have three different configurations. When successive atom fountains are *uncorrelated*, then  $K(\omega) = 1$  and ELGAR simply averages the noises of the single gradiometers. If the successive atom fountains are *correlated*, then  $K(\omega) > 1$  and the gain diminishes until the maximum value of  $K(\omega) = \sqrt{N}$ , that means that the atom fountains are completely correlated over the whole arm length: this makes the averaging process ineffective since every gradiometer will measure exactly the same NN. The best configuration is the one with  $K(\omega) < 1$ : when the atom fountains are *anti-correlated*. Having anti-correlated gradiometers means that when a gradiometer contributes positively to the NN, another one will contribute negatively and the average process will just cancel everything out.

If the seismic field is homogeneous and isotropic, then the spatial CPSD,  $C(r, \omega)$ , will satisfy [126]:  $C(r < \lambda/2, \omega) > 1$ ,  $C(\lambda/2 < r < \lambda, \omega) < 1$  and  $C(r > \lambda, \omega) \simeq 0$ , where  $r$  represents the distance between two points. One can then optimize the gradiometers disposition accordingly to the frequency band of interest following the procedure that will be explained in Chapter 7 but in a 2D space. Actually, the field will not be really homogeneous nor isotropic, so it will be necessary to make a survey to evaluate the spatial correlations and only then proceeding with the optimization (see Chapter 8). In both cases, (homogeneous-isotropic and inhomogeneous - anisotropic field) the optimization procedure will be lighted by the fact that the space of the possible positions will be constrained along the ELGAR baseline. In the end, the mitigation of the NN for ELGAR could benefit

from the averaging of the different gradiometers and also from the use of a linear filter to further reduce the noise. With both these contributions Equation 6.5 becomes:

$$\sqrt{S_{NN_{\text{average}}}(\omega)} = \frac{K(\omega)R(\omega)}{\sqrt{N}} \sqrt{S_{NN_1}(\omega)} \quad (6.6)$$

Where  $R(\omega)$  can be calculated from Equation 5.20.

Following [17] we can see that an optimized 3D seismic array around a test mass (which in ELGAR would be represented by a single atom fountain) needs to be placed at  $\simeq 0.2\lambda$ . So at  $\simeq 1$  Hz and with body waves velocities  $c_{\text{body}} \simeq 6$  km/s this would imply to have distances of the order of kilometers. In [17] the array was calculated assuming NN contribution only from body waves and in a 3D space. For ELGAR, we need to keep in mind that the experiment will operate at a frequency band where Rayleigh waves will dominate [125], so the optimized array might be different than that obtained in [17]. Usually, performing a seismic survey in underground sites would require to dig boreholes where to place the seismic sensors. Assuming that at those frequencies Rayleigh waves dominate, we could, in a first place, exploit the already deployed surface seismic stations and understand if there are anisotropies and where. After that, one might want to explore the seismic field more deeply by means of boreholes.

## 6.5 NN from body waves

It is important to understand the impact of the presence of a cavity on the NN estimate in underground detectors. Indeed, the presence of a cavity is mathematically equivalent to the introduction of some discontinuity inside the medium: this will lead to boundary effects that need to be taken into account. In particular, if we consider only body waves, we know that S waves will contribute to gravity perturbations only when some discontinuity is present. Hereinafter, I will follow the derivation in Harm's LRR [52], section 3.3. Before going into details about the NN generated by body waves in the presence of a cavity, we will show that we can split Equation 3.4 into two contributions: one due to the presence of a surface (i.e a discontinuity) and the other one due to the bulk contribution. To do that we first need to insert Equation 3.1 in Equation 3.4:

$$\nabla \cdot (\rho(\mathbf{r})\boldsymbol{\xi}(\mathbf{r}, t)) = \nabla\rho(\mathbf{r}) \cdot \boldsymbol{\xi}(\mathbf{r}, t) + \rho(\mathbf{r})\nabla \cdot \boldsymbol{\xi}(\mathbf{r}, t) \quad (6.7)$$

This makes clear that it is possible to split Equation 3.4 in a surface and in a body contribution: in particular we can see that  $\nabla\rho(\mathbf{r}) \cdot \boldsymbol{\xi}(\mathbf{r}, t)$  allows us to switch to a surface integral. Indeed, the gradient of a field gives the direction and the rate where the field increases faster, so in the case of a homogeneous and

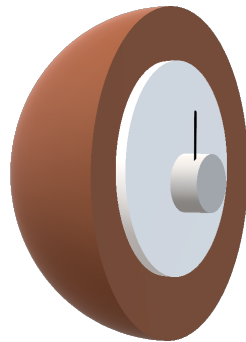


Figure 6.5: In underground detectors the test masses will be hosted in cavities, and their presence must be taken into account when modelling the NN contribution. In the text, it has been considered a spherical cavity with radius  $a$  and a test mass placed in the origin (even though it is only an approximation).

isotropic medium, separated from the empty space by a general surface  $\Sigma(\mathbf{r})$ :

$$\nabla\rho(\mathbf{r}) = -\mathbf{n}(\mathbf{r})\delta(\mathbf{r} - \Sigma(\mathbf{r})) \quad (6.8)$$

where  $\Sigma(\mathbf{r})$  describes the surface of the medium and  $\mathbf{n}(\mathbf{r})$  is the vector normal to it and pointing from the medium to the empty space (in the opposite direction of the increase). Considering also that inside the bulk  $\rho(\mathbf{r}) = \rho_0$  (where  $\rho_0$  is the density of the medium) and  $\rho(\mathbf{r}) = 0$  outside it, we can see that the volume integral reduces to a surface one:

$$\delta\phi_{\text{surf}}(\mathbf{r}_0, t) = -G\rho_0 \int_{\Sigma} d\Sigma \frac{\mathbf{n}(\mathbf{r}) \cdot \boldsymbol{\xi}(\mathbf{r}, t)}{|\mathbf{r} - \mathbf{r}_0|} \quad (6.9)$$

The bulk integral comes instead from the other term in Equation 6.7:

$$\delta\phi_{\text{bulk}}(\mathbf{r}_0, t) = G\rho_0 \int dV \frac{\nabla \cdot \boldsymbol{\xi}(\mathbf{r}, t)}{|\mathbf{r} - \mathbf{r}_0|} \quad (6.10)$$

At this point we have everything we need to calculate the NN from body waves propagating in an infinite homogeneous and isotropic medium with a spherical cavity. We start with Equation 3.5 by simply solving the integral with the displacement  $\boldsymbol{\xi}(t, \mathbf{r})$  of a plane wave and leaving a sphere of radius  $a$  and centred in the origin out from the integration volume. In the bulk, we have two types of waves: compressional (P) and shear waves (S) (section 6.2): so we need to solve Equation 3.5 for both of them:

$$\boldsymbol{\xi}^P(\mathbf{r}, t) = \mathbf{e}_P \xi_0^P(\mathbf{k}^P, \omega) e^{i(\mathbf{k}^P \cdot \mathbf{r} - \omega t)} \quad (6.11)$$

$$\boldsymbol{\xi}^S(\mathbf{r}, t) = \mathbf{e}_S \xi_0^S(\mathbf{k}^S, \omega) e^{i(\mathbf{k}^S \cdot \mathbf{r} - \omega t)} \quad (6.12)$$

With  $\mathbf{e}_P \equiv \mathbf{k}^P/|\mathbf{k}^P|$  (longitudinal/compressional wave) and  $\mathbf{e}_S \cdot \mathbf{k}^S = 0$  (transverse wave). From Equation 6.11 and Equation 3.5 we get the *gravity acceleration* induced by a P wave at the center of the spherical cavity: this is of course only an approximation, since the cavity will not be spherical, nor the test mass will be placed in the cavity center.

$$\delta\mathbf{a}^P(\mathbf{0}, t) = 8\pi G\rho_0 \boldsymbol{\xi}^P(\mathbf{0}, t) \frac{j_1(k^P a)}{k^P a} \quad (6.13)$$

This is the NN acceleration caused by P waves at the center of a spherical cavity of radius  $a$ , here  $j_1(k^P a)$  is the spherical Bessel function of order one. Until now, the contribution to the gravity acceleration from S waves has not been considered. To take that into account we need again to solve Equation 3.5 for a homogeneous and isotropic space with a spherical cavity centred in  $\mathbf{r} = \mathbf{0}$ .

---

## 6. SEISMIC NEWTONIAN NOISE CANCELLATION

---

Since we already know that S waves can only cause gravity fluctuations at the surface of the cavity, it is more straightforward to directly calculate their surface contribution with Equation 6.9, this leads to:

$$\delta \mathbf{a}^S(\mathbf{0}, t) = -4\pi G \rho_0 \boldsymbol{\xi}^S(\mathbf{0}, t) \frac{j_1(k^S a)}{k^S a} \quad (6.14)$$

Finally, the total induced gravity acceleration on the test mass will be:

$$\delta \mathbf{a}^{\text{body-waves}}(\mathbf{0}, t) = 4\pi G \rho_0 \left( 2\boldsymbol{\xi}^P(\mathbf{0}, t) \frac{j_1(k^P a)}{k^P a} - \boldsymbol{\xi}^S(\mathbf{0}, t) \frac{j_1(k^S a)}{k^S a} \right) \quad (6.15)$$

We can see that the acceleration depends on the displacement caused by P and S waves at the cavity center and on a weight term,  $j_1(k^{P,S} a)/(k^{P,S} a)$ , that we will call *gravity contribution*. Of course, measuring the displacement of a seismic wave at the center of an empty space is not possible. In reality, we will measure the displacement at the cavity walls: this will introduce only a small error  $\propto (k^{P,S} a)^2$  in the real part of the displacement amplitude,  $\boldsymbol{\xi}^{P,S}(\mathbf{0}, t)$ . We should note that P waves contribute to  $\delta \mathbf{a}$  with a factor 2 respect to S waves: this is easily explained by the fact that P waves contribute to the NN through two mechanisms: cavity walls displacement and bulk compression/decompression, while S waves enter into play only through the cavity walls displacement. Equation 6.15 tells us in which cases the cavity has a real impact on the NN: in Figure 6.6 the gravity contributions of P and S waves are plotted. The plot is in units of P wavelengths and the velocity of S waves was taken to be:  $v_S \sim v_P/2$ , relation that can be retrieved by rewriting Equation 6.1 and Equation 6.2 in terms of the Poisson ratio [9]. In Figure 6.6 we can see that when the cavity radius is  $\sim 0.4 \lambda_P$  then the gravity contribution is already reduced by a factor  $\sim 2$ . If we consider a cavern located in a bedrock medium, then  $v_P \sim 4$  km/s, so, in order to halve the gravity contribution at 10 Hz, we need a cavity radius of  $a \sim 160$  m. Constructing such a big cavern is probably unrealistic, so, even if the use of big caves would help in reducing the NN, this is not a doable solution. If instead we consider a cavity radius of the order of  $a = 30$  m, we can see that already at 10 Hz and with  $v_P \sim 4$  km/s we have  $k^P a \sim 15 \cdot 10^{-3}$ , which is small. So, for real applications we can make the following approximation:  $k^{P,S} \ll 1$  and rewriting Equation 6.15:

$$\delta \mathbf{a}^{\text{body-waves}}(\mathbf{0}, t) \sim 4\pi G \rho_0 \left( \frac{2}{3} \boldsymbol{\xi}^P(\mathbf{0}, t) - \frac{1}{3} \boldsymbol{\xi}^S(\mathbf{0}, t) \right) \quad (6.16)$$

Where we used that:  $\lim_{x \rightarrow 0} j_1(x)/x \sim 1/3$ . The possible wave scattering from the cavern walls has not been considered yet. Since at low frequencies  $k^{P,S} a$  is very small and so also the scattering cross-section of the seismic waves from the obstacle [127], we might think that the scattering over the cavern walls is

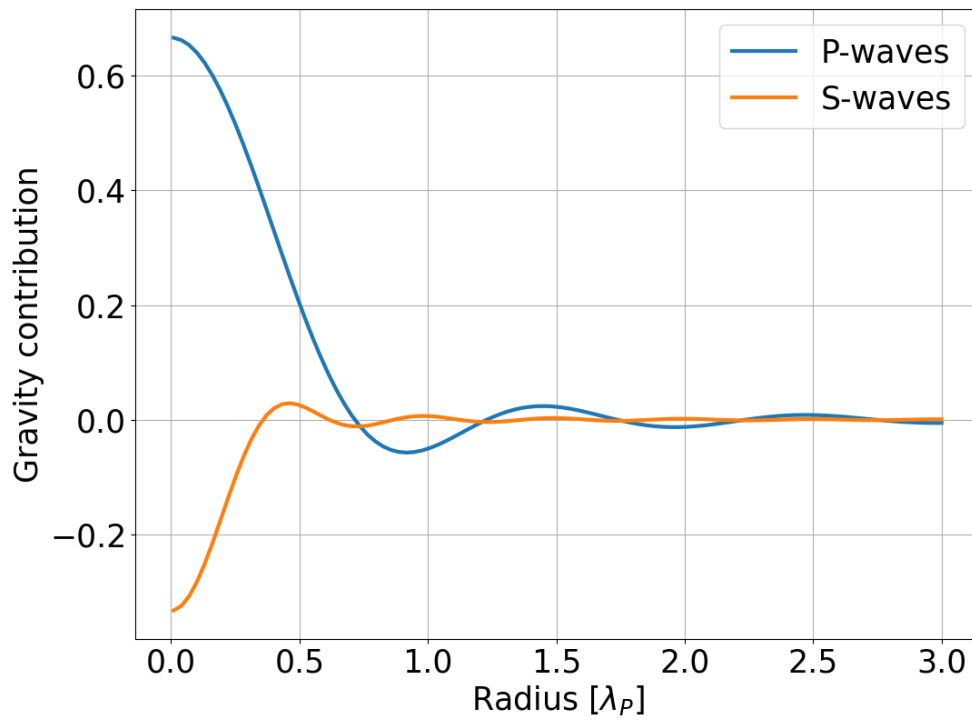


Figure 6.6: Gravity contribution  $(j_1(k^{P,S}a)/(k^{P,S}a))$  for S and P waves. It is represented in P wavelength units and it was considered that usually:  $v_P \sim 2v_S$ .



negligible. However, due to the scattering, P and S waves can be converted one into another. This might lead to different numerical factors in Equation 6.15, so neglecting the scattering might have the side effect of overestimating or underestimating the NN on the test mass. However, in [52] it is shown that in the limit where  $k^{P,S}a \rightarrow 0$  holds, we can actually neglect the scattering on the cavern walls. So, in Chapter 7, we will consider this assumption valid.

## 6.6 NN from surface waves

Surface detectors, like AdV+ and LIGO, will suffer from seismic NN mainly generated by surface waves. In most cases, surface wave amplitudes are indeed larger than body waves amplitudes [125], this is for sure true in AdV+, where a lot of nearby (cultural) seismic sources are present [128, 112]. Being that Love waves do not impact on the vertical spectrum, which is the most important one for what concerns NN, we will assume that NN in surface detectors is only due to Rayleigh waves contribution.

We can write Rayleigh waves following [129]:

$$\begin{aligned}\boldsymbol{\xi}(\mathbf{r}, t) &= \xi_k(\mathbf{r}, t)\mathbf{e}_k + \xi_z(\mathbf{r}, t)\mathbf{e}_z \\ \xi_k(\mathbf{r}, t) &= i(H_1e^{h_1z} + H_2e^{h_2z})e^{i(\mathbf{k}\cdot\boldsymbol{\rho}-\omega t)} \\ \xi_z(\mathbf{r}, t) &= (V_1e^{v_1z} + V_2e^{v_2z})e^{i(\mathbf{k}\cdot\boldsymbol{\rho}-\omega t)}\end{aligned}\tag{6.17}$$

Here  $H_i, h_i, V_i, v_i$  are real parameters that describe the Rayleigh wave. The  $90^\circ$  phase difference between the vertical and the horizontal component is related to the characteristic elliptical motion of Rayleigh waves.

To have an analytical model of the NN generated in a test mass, we need to solve Equation 6.9 and Equation 6.10 for a Rayleigh wave displacement (Equation 6.17) in a homogeneous and isotropic half space. For what concerns the surface part, we can notice that only the  $z$ -component of Equation 6.17 will contribute to the NN; moreover, the problem is symmetric for test masses placed above or below the surface, so the final result is valid for both the cases.

The part of the NN produced by the Rayleigh waves propagating inside the half space needs instead to be solved using Equation 6.10 and distinguishing between the two cases of a test masses located above and below the surface. When solved for a test mass below the surface, a new term that will slightly increase the  $z$ -component of the NN acceleration will arise. The result that we obtain following this procedure represents the contribution of the Rayleigh waves from the surface displacement and from the rock compression inside the bulk. For an underground test mass we still need to take into account the presence of a cavity. This can be done noting that Equation 6.17 contains a shear and a compressional part: this

---

## 6. SEISMIC NEWTONIAN NOISE CANCELLATION

---

allows us to exploit the result of Equation 6.10 and get the cavity contribution. From now on, however, we will consider only the case of a test mass located above the surface, like in AdV and LIGO; in this case the NN acceleration from a single Rayleigh wave can be written as (see also [52]):

$$\delta a^{\text{Rayleigh}}(\mathbf{r}_0, t) = 2\pi G\rho_0\gamma(\nu)e^{-hk_\rho\xi_z}(\mathbf{0}, 0)e^{i(\mathbf{k}_\rho\cdot\mathbf{r}_0-\omega t)} \begin{pmatrix} i\cos(\phi) \\ i\sin(\phi) \\ -1 \end{pmatrix} \quad (6.18)$$

Here  $\gamma(\nu)$  is a factor determined by the Poisson ratio (i.e. by the elastic properties of the medium) and its value ranges from 0.5 to 1,  $\phi$  is the angle that  $\mathbf{k}$  forms with the  $x$ -axis and  $\mathbf{k}_\rho$  is the surface component of  $\mathbf{k}$ . We obtain Equation 6.18 by calculating the gravity potential induced by a Rayleigh wave and then taking its gradient with respect to  $\mathbf{r}_0$ . The gravity potential can be calculated by inserting Equation 6.17 in Equation 6.9 and in Equation 6.10 and then solving for a test mass located *above* the surface.

We should notice that Equation 6.18 represents the NN acceleration on a single test mass. If the correlation length of the seismic wave is much shorter than the interferometer arm length, then the NN acceleration in the input test mass will be uncorrelated with respect to that in the end test mass. So, in the differential output of the interferometer, the NN will be present as an incoherent sum of the noises at the two test masses. Since the noise strain amplitude is inversely proportional to the arm length,  $h \propto 1/L$ , the longer will be  $L$ , the lower will be the NN strain in the interferometer (see Figure 6.7). For surface interferometers like AdV, we can assume uncorrelated NN. It is then enough to estimate the NN by using the single test mass equation (Equation 6.18).

If instead the arm length is much shorter than the seismic wavelength, the correlation between the end and the input test mass will be very good and the common-mode noise will be suppressed: only the NN coming from the uncorrelated contributions to the NN will survive. The spectra of the differential NN strain (in units of 1/Hz) along the direction of freedom of the input and the end test masses, for a fixed seismic wavelength can be written as [52]:

$$C((\delta x_0 - \delta x_L)/L; \omega) = \frac{(2\pi G\rho_0 e^{-hk_R}\gamma(\nu))^2}{c_R^2\omega^2} C(\xi_z; \omega) \mathfrak{F}(k_R L) \quad (6.19)$$

Where we defined:

$$\mathfrak{F}(k_R L) = (1/(k_R L)^2)(1 - 2J_0(k_R L) + 2J_1(k_R L)/(k_R L)) \quad (6.20)$$

In Figure 6.7 we plotted the dimensionless quantity  $\sqrt{\mathfrak{F}}$  in units of  $\lambda_R = 2\pi/k_R$ , where  $c_R = \omega/k_R$ ;  $\sqrt{\mathfrak{F}}$  tells us how the strain noise changes varying  $L$  for a fixed wavelength.

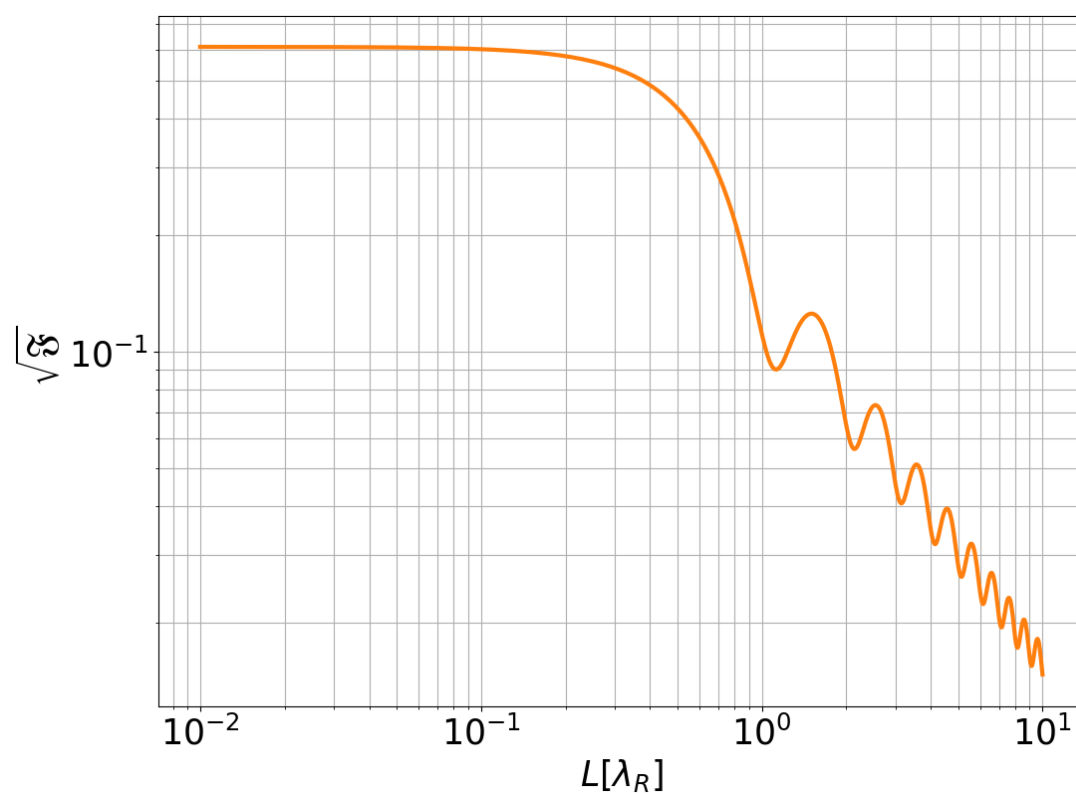


Figure 6.7: Evolution of the differential NN strain in a detector arm with respect to the arm length at a fixed Rayleigh wavelength  $\lambda_R$ .

## 6.7 Active NN cancellation

Active noise cancellation has already been employed in GW interferometers to further suppress noises in the instrument [13, 11, 12]: in LIGO, for example, this method is used to actively suppress seismic noise [14].

The basic idea underlying the active noise cancellation is to monitor a noise source with some witness sensors and with them feeding a linear filter and reconstructing the noise produced in the data stream of the GW detector (the target). The least square error estimation leads to the formulation of the Wiener filters (WF) and it has been discussed in Chapter 5. For the cancellation of the seismic NN we have to deploy seismic sensor arrays around the test masses of the interferometer and then use a Wiener filter to proceed with the NN cancellation, operation that can also be done off-line. The main problem here relies in finding the optimized array which can lead to the best cancellation performances. These are well represented by the residual function introduced in section 5.3 (Equation 5.20). With the goal of pinpointing the optimal array, we aim to find the minimum value of the residual function. This can be done with a global optimization algorithm (see section 5.1). In the following sections we will derive the equations that are needed to calculate the residual of Equation 5.20. We will calculate them for three cases that were addressed during this PhD work: an isotropic and homogeneous seismic field composed by a mixture of P and S waves, an isotropic and homogeneous Rayleigh wave field and a general Rayleigh wave field, with no other assumptions.

## 6.8 Two point spatial correlation for the NN cancellation

In principle, to estimate the NN, one could construct an analytical model of the seismic field and then use it together with a finite element model of the medium, letting every element moving according to the seismic field model. This is a kinematic simulation and it is very powerful if the *seismic field* and the *ground models* are very well known. One could instead use a dynamical simulation, for which we only need the analytical model of the *seismic sources* and of the *medium*, but, again, the models should be well known.

Virgo has a complex structure (see Chapter 8) and neither the seismic sources, nor the the seismic field can be modelled. This leads us to the development of some method that allows us to estimate the NN using easily measurable quantities [18]. As explained in section 5.3, in order to perform the NN cancellation, we need the cross correlations of the seismic field at different locations and the cross

correlations between the seismic field and the test mass strain signal. The key point here is that we do not have to rely on complicated models of the seismic field or its sources and on the medium model. We just need to know the values of *two-point spatial seismic correlations*.

We will now derive a general form of the two-point cross power spectral density (CPSD) between the NN acceleration at different locations. From this general equation we will be able to give the expression of the quantities needed for the WF in various different cases (it will be enough to substitute the acceleration with the seismic displacement when required).

We start defining the two-point CPSD of a quantity  $\zeta$  as:

$$C(\zeta; \mathbf{r}', \mathbf{r}'', \omega) \equiv \langle \zeta^*(\mathbf{r}', \omega) \zeta(\mathbf{r}'', \omega) \rangle \quad (6.21)$$

Where  $\langle \dots \rangle$  is the ensemble average<sup>1</sup>. What we now want to find is the expression of:

$$C(\delta a_x; \mathbf{r}_1, \mathbf{r}_2, \omega) = \langle \delta \tilde{a}_x^*(\mathbf{r}_1, \omega) \delta \tilde{a}_x(\mathbf{r}_2, \omega) \rangle \quad (6.22)$$

Where  $\delta \tilde{a}_x(\mathbf{r}, \omega)$  is the Fourier transform of  $\delta a_x(\mathbf{r}, t)$ . Considering the Fourier transform in the space domain:

$$\delta \tilde{a}_x(\mathbf{r}, \omega) = \mathfrak{F}^{-1} \{ \delta \bar{a}_x(\mathbf{k}, \omega) \} = \int \frac{d^3 \mathbf{k}}{(2\pi)^3} \delta \bar{a}_x(\mathbf{k}, \omega) e^{i\mathbf{k} \cdot \mathbf{r}} \quad (6.23)$$

and inserting Equation 6.23 in Equation 6.22 we get:

$$\begin{aligned} C(\delta a_x; \mathbf{r}_1, \mathbf{r}_2, \omega) &= \langle \delta \tilde{a}_x^*(\mathbf{r}_1, \omega) \delta \tilde{a}_x(\mathbf{r}_2, \omega) \rangle = \\ &= \left\langle \left( \int \frac{d^3 \mathbf{k}'}{(2\pi)^3} \delta \bar{a}_x^*(\mathbf{k}', \omega) e^{-i\mathbf{k}' \cdot \mathbf{r}_1} \right) \left( \int \frac{d^3 \mathbf{k}}{(2\pi)^3} \delta \bar{a}_x(\mathbf{k}, \omega) e^{+i\mathbf{k} \cdot \mathbf{r}_2} \right) \right\rangle = \\ &= \int \frac{d^3 \mathbf{k}}{(2\pi)^3} \int \frac{d^3 \mathbf{k}'}{(2\pi)^3} \langle \delta \bar{a}_x^*(\mathbf{k}', \omega) \delta \bar{a}_x(\mathbf{k}, \omega) \rangle e^{+i(\mathbf{k} \cdot \mathbf{r}_2 - \mathbf{k}' \cdot \mathbf{r}_1)} = \\ &= \int \frac{d^3 \mathbf{k}}{(2\pi)^3} \int \frac{d^3 \mathbf{k}'}{(2\pi)^3} C(\delta a_x; \mathbf{k}, \mathbf{k}', \omega) e^{+i(\mathbf{k} \cdot \mathbf{r}_2 - \mathbf{k}' \cdot \mathbf{r}_1)} \end{aligned} \quad (6.24)$$

Considering that the NN acceleration,  $\delta a_x$ , is linear with respect to the seismic displacement,  $\xi$ , we can write  $\delta a_x$  in the general form:

$$\delta a_x(\mathbf{k}, \omega) = \xi(\mathbf{k}, \omega) g(\mathbf{k}) \quad (6.25)$$

---

<sup>1</sup>It is assumed that the seismic noise is a stochastic process, and therefore also the NN on the test mass. The ensemble average is intended as the average of all the possible outcomes of  $\zeta$  in the frequency domain.

This allows us to rewrite Equation 6.24 as:

$$C(\delta a_x; \mathbf{r}_1, \mathbf{r}_2, \omega) = \int \frac{d^3\mathbf{k}}{(2\pi)^3} \int \frac{d^3\mathbf{k}'}{(2\pi)^3} C(\xi; \mathbf{k}, \mathbf{k}', \omega) g(\mathbf{k}) g^*(\mathbf{k}') e^{+i(\mathbf{k}\cdot\mathbf{r}_2 - \mathbf{k}'\cdot\mathbf{r}_1)} \quad (6.26)$$

This is a good starting point, since it allows us to express  $C(\delta a_x; \mathbf{r}_1, \mathbf{r}_2, \omega)$  as a function of the CPSD of the displacement:  $C(\xi, \mathbf{r}', \mathbf{r}'', \omega)$ . Indeed, using the same reasoning as done for Equation 6.24, we can write  $C(\xi; \mathbf{k}, \mathbf{k}', \omega)$  as a function of the two-point CPSD of  $\xi$ :

$$C(\xi; \mathbf{k}, \mathbf{k}', \omega) = \int \int d^3\mathbf{r}' d^3\mathbf{r}'' C(\xi; \mathbf{r}', \mathbf{r}'', \omega) e^{-i(\mathbf{k}\cdot\mathbf{r}' - \mathbf{k}'\cdot\mathbf{r}'')} \quad (6.27)$$

So that we can obtain the general form of  $C(\delta a_x; \mathbf{r}_1, \mathbf{r}_2, \omega)$ :

$$\boxed{C(\delta a_x; \mathbf{r}_1, \mathbf{r}_2, \omega) = \int d^3\mathbf{r}' \int d^3\mathbf{r}'' \int \frac{d^3\mathbf{k}}{(2\pi)^3} \int \frac{d^3\mathbf{k}'}{(2\pi)^3} \mathcal{H}(\xi; \mathbf{k}, \mathbf{k}', \mathbf{r}', \mathbf{r}'', \omega) e^{+i(\mathbf{k}\cdot\mathbf{r}_2 - \mathbf{k}'\cdot\mathbf{r}_1)} e^{-i(\mathbf{k}\cdot\mathbf{r}' - \mathbf{k}'\cdot\mathbf{r}'')} \quad (6.28)}$$

Where  $\mathcal{H}(\xi; \mathbf{k}, \mathbf{k}', \mathbf{r}', \mathbf{r}'', \omega) = C(\xi; \mathbf{r}', \mathbf{r}'', \omega) g(\mathbf{k}) g^*(\mathbf{k}')$ . This last equation might seem complicated, but once the model for  $\delta a_x$  is known, we can get some interesting equations that allow us to evaluate Equation 5.20 and to perform the optimization of the sensor locations.

### 6.8.1 Isotropic and homogeneous seismic field

We can solve Equation 6.28 for a *isotropic* and *homogeneous* seismic field by inserting Equation 6.18 in Equation 6.28 and considering the NN acceleration component which is parallel to the direction where the test mass is free to move ( $\delta a_x$ ). The isotropic assumption is valid as far as we can assume to have far-field sources located in all directions, while the homogeneous assumption assures that every point in the space is equivalent. Homogeneity means invariance under translations and isotropy means invariance under rotations. So, the seismic field will look the same in every point (no locations are more special than others) and in every direction. For example: a homogeneous seismic field could be composed by plane waves propagating in a single direction, this implies that an observer will see the waves coming always from the same direction, independently by his/her position in the space. If the field is also isotropic the observer will see the waves coming from all directions (isotropy) and in every point he/she will see the same thing (homogeneity).

$$\begin{aligned} \text{homogeneous field:} \quad & f(\mathbf{r}_1, \mathbf{r}_1 + \Delta\mathbf{r}) = f(0, \Delta\mathbf{r}) \\ \text{isotropic field:} \quad & f(\bar{\mathbf{R}}\mathbf{r}) = f(\mathbf{r}) \end{aligned} \quad (6.29)$$

Where  $\Delta = \mathbf{r}_2 - \mathbf{r}_1$  and  $\bar{\mathbf{R}}$  is a rotational matrix. First of all, we note that homogeneity means that:  $\mathcal{H}(\xi; \mathbf{k}, \mathbf{k}', \mathbf{r}', \mathbf{r}'', \omega) = \mathcal{H}(\xi; \mathbf{k}, \mathbf{k}', \mathbf{r}', \mathbf{r}' + \Delta \mathbf{r}, \omega) = \mathcal{H}(\xi; \mathbf{k}, \mathbf{k}', \Delta \mathbf{r}, \omega)$ ;  $C(\delta a_x; \mathbf{r}_1, \mathbf{r}_2, \omega)$  then becomes:

$$\begin{aligned}
 C(\delta a_x; \mathbf{r}_1, \mathbf{r}_2, \omega) = & \\
 & \int d^3 \mathbf{r}' \int d^3 \Delta \mathbf{r} \int \frac{d^3 \mathbf{k}}{(2\pi)^3} \int \frac{d^3 \mathbf{k}'}{(2\pi)^3} \\
 & \mathcal{H}(\xi; \mathbf{k}, \mathbf{k}', \Delta \mathbf{r}, \omega) e^{+i(\mathbf{k} \cdot \mathbf{r}_2 - \mathbf{k}' \cdot \mathbf{r}_1)} e^{-i(\mathbf{k} - \mathbf{k}') \cdot \mathbf{r}'} e^{+i\mathbf{k}' \cdot \Delta \mathbf{r}} = \quad (6.30) \\
 & \int d^3 \Delta \mathbf{r} \int \frac{d^3 \mathbf{k}}{(2\pi)^3} \int \frac{d^3 \mathbf{k}'}{(2\pi)^3} \\
 & \mathcal{H}(\xi; \mathbf{k}, \mathbf{k}', \Delta \mathbf{r}, \omega) \delta(\mathbf{k} - \mathbf{k}') e^{+i(\mathbf{k} \cdot \mathbf{r}_2 - \mathbf{k}' \cdot \mathbf{r}_1)} e^{+i\mathbf{k}' \cdot \Delta \mathbf{r}} =
 \end{aligned}$$

We then obtain the general expression of  $C(\delta a_x; \mathbf{r}_1, \mathbf{r}_2, \omega)$  for a homogeneous field:

$$\boxed{C(\delta a_x; \mathbf{r}, \omega) = \int d^3 \Delta \mathbf{r} \int \frac{d^3 \mathbf{k}}{(2\pi)^3} \mathcal{H}(\xi; \mathbf{k}, \Delta \mathbf{r}, \omega) e^{+i\mathbf{k}\mathbf{r}} e^{+i\mathbf{k} \cdot \Delta \mathbf{r}}} \quad (6.31)$$

Where the homogeneity applied to  $\mathcal{H}$  automatically reflects on  $C(\delta a_x; \mathbf{r}_1, \mathbf{r}_2, \omega) = C(\delta a_x; \mathbf{r}, \omega)$ , with  $\mathbf{r} = \mathbf{r}_2 - \mathbf{r}_1$ . We also notice that if we calculate the PSD (i.e.  $\mathbf{r}_2 = \mathbf{r}_1$ ), the dependence from  $\mathbf{r}$  disappears: since the field is homogeneous it does not matter *where* we calculate the PSD.

To take into consideration the isotropy assumption it is better to express  $\mathcal{H}(\xi; \mathbf{k}, \Delta \mathbf{r}, \omega)$  explicitly: see subsection 6.8.2 and subsection 6.8.3.

## 6.8.2 Two point spatial correlation for isotropic and homogeneous body waves field

In Chapter 7 we will deal with the optimization of underground seismic arrays in presence of cavities with negligible radius with respect to the seismic field wavelength ( $ak \ll 1$ ). Now, we will calculate some quantities that will be useful in Chapter 7.

Firstly, we will calculate the CPSDs -Equation 6.21- relative to a homogeneous and isotropic seismic field composed only by body waves. We intentionally neglect the presence of Rayleigh waves, since we consider the case in which the detector is located underground and works at frequencies  $\gtrsim 1$  Hz, where the Rayleigh waves are still not dominant. At those frequencies, with body wave velocities  $\sim 4 - 6$  km/s and cavity radius  $a \lesssim 30$  m, we can rely on the assumption that  $ak \ll 1$  without introducing too many errors.

We write the seismic field as:

$$\boldsymbol{\xi}^{\text{tot}}(\mathbf{r}, \omega) = \boldsymbol{\xi}^P(\mathbf{r}, \omega) + \boldsymbol{\xi}^S(\mathbf{r}, \omega) \quad (6.32)$$

---

## 6. SEISMIC NEWTONIAN NOISE CANCELLATION

---

Where  $\boldsymbol{\xi}^P(\mathbf{r}, \omega)$  and  $\boldsymbol{\xi}^S(\mathbf{r}, \omega)$  are the Fourier amplitudes of the displacement caused by P and S waves, respectively. When we deal with NN from Rayleigh waves we limit ourselves to the measurement of the vertical displacement,  $\xi_z$ , since it is indeed the only one responsible for the gravity fluctuations. For what concerns body waves NN, instead, we need to consider the displacement along all the three spatial directions. The seismic measurement along a direction will be indicated as:  $\mathbf{e}_i \cdot \boldsymbol{\xi}(\mathbf{r}, \omega)$ , where we will refer at  $\mathbf{e}_i$  and  $\mathbf{e}_j$  as at the direction of measurement of the first and the second seismometer (note that the direction can be the same or not). Therefore the two-point CPSD will depends on the directions of the two measurements. Using Equation 6.16 and the definition in Equation 6.21 we find:

$$C_{SS_{ij}}(r, \omega) = C(\mathbf{e}_i \cdot \boldsymbol{\xi}_i^P; \mathbf{e}_j \cdot \boldsymbol{\xi}_j^P; r, \omega) + C(\mathbf{e}_i \cdot \boldsymbol{\xi}_i^S; \mathbf{e}_j \cdot \boldsymbol{\xi}_j^S; r, \omega) \quad (6.33)$$

$$C_{SN_i}(r, \omega) = \mathfrak{C} \left[ \frac{2}{3} C(\mathbf{e}_i \cdot \boldsymbol{\xi}_i^P; \mathbf{e}_j \cdot \boldsymbol{\xi}_0^P; r, \omega) - \frac{1}{3} C(\mathbf{e}_i \cdot \boldsymbol{\xi}_i^S; \mathbf{e}_j \cdot \boldsymbol{\xi}_0^S; r, \omega) \right] \quad (6.34)$$

$$C_{NN}(0, \omega) = \mathfrak{C}^2 \left[ \frac{4}{9} C(\mathbf{e}_i \cdot \boldsymbol{\xi}_0^P; \mathbf{e}_j \cdot \boldsymbol{\xi}_0^P; 0, \omega) + \frac{1}{9} C(\mathbf{e}_i \cdot \boldsymbol{\xi}_0^S; \mathbf{e}_j \cdot \boldsymbol{\xi}_0^S; 0, \omega) \right] \quad (6.35)$$

With  $\mathfrak{C} = (4\pi G\rho_0)$ . In the following,  $\bar{\mathbf{C}}_{SS}$  will denote the matrix of the CPSDs of the N signals recorded by the N witness sensors,  $\mathbf{C}_{SN}$  will denote the vector containing the CPSD between the NN acceleration on test mass and the signals from the witness sensors, while  $C_{NN}$  will denote the PSD of the NN acceleration on the test mass (placed in the origin).  $\boldsymbol{\xi}_i^{P,S}$  represents the P or the S seismic displacement calculated in  $\mathbf{r}_i$  and  $r \equiv |\mathbf{r}_j - \mathbf{r}_i|$ . The symbol  $\boldsymbol{\xi}_0^{P,S}$  indicates instead the P or the S displacement measured at the test mass location. With negligible scattering we can consider uncorrelated P and S contributions, then:  $C(\boldsymbol{\xi}^S, \boldsymbol{\xi}^P; r, \omega) \simeq 0$ . Moreover, we already considered the seismic field to be homogeneous and isotropic, so the CPSD will depend on  $r$ . We now introduce the polarization mixing parameter,  $p$ :

$$p = \frac{E[\boldsymbol{\xi}^{P*} \boldsymbol{\xi}^P]}{E[\boldsymbol{\xi}^{\text{tot}*} \boldsymbol{\xi}^{\text{tot}}]} \equiv \frac{C(\boldsymbol{\xi}^P; \omega)}{C(\boldsymbol{\xi}^{\text{tot}}; \omega)} \quad (6.36)$$

Here,  $C(\boldsymbol{\xi}^P; \omega)$  represents the energy carried by the P waves while  $C(\boldsymbol{\xi}^{\text{tot}}; \omega)$  is the total energy of the field (P + S). Since we are neglecting mixed correlations between S and P, then  $C(\boldsymbol{\xi}^{\text{tot}}; \omega) = C(\boldsymbol{\xi}^P; \omega) + C(\boldsymbol{\xi}^S; \omega)$ , and so:

$$1 - p = \frac{C(\boldsymbol{\xi}^S; \omega)}{C(\boldsymbol{\xi}^{\text{tot}}; \omega)} \quad (6.37)$$



With  $C(\boldsymbol{\xi}^S = E[\boldsymbol{\xi}^{S*} \boldsymbol{\xi}^S])$ . At this point, we can evaluate equations from 6.33 to 6.35. Following [52], we express  $C(\mathbf{e}_i \cdot \boldsymbol{\xi}^P; \mathbf{e}_j \cdot \boldsymbol{\xi}^P; \omega)$  and  $C(\mathbf{e}_i \cdot \boldsymbol{\xi}^S; \mathbf{e}_j \cdot \boldsymbol{\xi}^S; \omega)$  as:

$$C(\mathbf{e}_i \cdot \boldsymbol{\xi}^P; \mathbf{e}_j \cdot \boldsymbol{\xi}^P; \omega) = C(\boldsymbol{\xi}^P; \omega) f_{P_{ij}}(k^P, r) \quad (6.38)$$

$$C(\mathbf{e}_i \cdot \boldsymbol{\xi}^S; \mathbf{e}_j \cdot \boldsymbol{\xi}^S; \omega) = C(\boldsymbol{\xi}^S; \omega) f_{S_{ij}}(k^S, r) \quad (6.39)$$

$$(6.40)$$

$f_{P,S}$  have been defined as:

$$f_{P_{ij}}(k^P, r) = (j_0(\Phi_{ij}^P) + j_2(\Phi_{ij}^P))(\mathbf{e}_i \cdot \mathbf{e}_j) - 3j_2(\Phi_{ij}^P)(\mathbf{e}_i \cdot \mathbf{e}_{ij})(\mathbf{e}_j \cdot \mathbf{e}_{ij}) \quad (6.41)$$

$$f_{S_{ij}}(k^S, r) = (j_0(\Phi_{ij}^S) - \frac{1}{2}j_2(\Phi_{ij}^S))(\mathbf{e}_i \cdot \mathbf{e}_j) + \frac{3}{2}j_2(\Phi_{ij}^S)(\mathbf{e}_i \cdot \mathbf{e}_{ij})(\mathbf{e}_j \cdot \mathbf{e}_{ij}) \quad (6.42)$$

where:  $\Phi_{ij}^{P,S} = k^{P,S} |\mathbf{r}_j - \mathbf{r}_i|$  and  $\mathbf{e}_{ij} \equiv (\mathbf{r}_j - \mathbf{r}_i) / |\mathbf{r}_j - \mathbf{r}_i|$ .

Finally we can rewrite equations from 6.33 to 6.35 as:

$$C_{SS_{ij}}(r, \omega) = C(\boldsymbol{\xi}^{tot}; \omega) (p f_{P_{ij}} + (1-p) f_{S_{ij}}) \quad (6.43)$$

$$C_{SN_i}(r, \omega) = (4\pi G \rho_0) C(\boldsymbol{\xi}^{tot}; \omega) (\frac{2}{3} p f_{P_{i0}} - \frac{1}{3} (1-p) f_{S_{i0}}) \quad (6.44)$$

$$C_{NN}(0, \omega) = (4\pi G \rho_0)^2 C(\boldsymbol{\xi}^{tot}; \omega) (\frac{4}{9} p + \frac{1}{9} (1-p)) \quad (6.45)$$

These equations are the expressions needed for calculating the residual: they are the equivalent of  $\bar{\mathbf{P}}_{YY}$ ,  $\mathbf{P}_{XY}$  and  $P_{XX}$  in Equation 5.20.

### 6.8.3 Two point spatial correlation for isotropic and homogeneous Rayleigh waves field

To calculate the NN spectrum for an isotropic and homogeneous Rayleigh field we have to insert Equation 6.18 in Equation 6.31 with  $\mathbf{r} = \mathbf{0}$  (we are calculating the PSD, not the two-point CPSD) and then solve assuming isotropy of the field in 2D. The procedure to get Equation 6.31 does not change if we are in a 2D space instead of a 3D one. Moreover, to simplify the notation we will indicate  $\Delta \mathbf{r}$  simply with  $\mathbf{r}$ :

$$C(\delta a_x; \omega) = (2\pi G \rho_0 \gamma(\nu))^2 \int r dr d\theta \int \frac{k dk d\phi}{(2\pi)^2} C(\boldsymbol{\xi}_z; \mathbf{r}, \omega) e^{-2hk} \cos^2(\phi) e^{ikr \cos(\theta)} \quad (6.46)$$

Where  $\phi$  is the angle that the wave vector  $\mathbf{k}$  forms with the  $x$ -axis, which is also the direction where the test mass is free to move, while  $\theta$  is the angle formed by

$\mathbf{r}$  respect to  $\mathbf{k}$ . Since we assume isotropy,  $C(\xi_z; r, \omega)$  depends only on  $|\mathbf{r}| = r$ . Performing the integral over  $\phi$  and  $\theta$  we obtain:

$$\begin{aligned} C(\delta a_x; \omega) &= \frac{1}{2}(2\pi G\rho_0\gamma(\nu))^2 \int_0^\infty dr r C(\xi_z; r, \omega) \int_0^\infty dk k e^{-2hk} J_0(kr) \\ &= \frac{1}{2}(2\pi G\rho_0\gamma(\nu))^2 \int_0^\infty dr C(\xi_z; r, \omega) \frac{2hr}{(r^2 + (2h)^2)^{3/2}} \\ &= \frac{1}{2}(2\pi G\rho_0\gamma(\nu))^2 \int_0^\infty dr C(\xi_z; r, \omega) \mathcal{K}(r, h) \end{aligned} \quad (6.47)$$

Where  $2\pi J_0(kr) \equiv \int_0^{2\pi} e^{ikr \cos(\theta)} d\theta$  and in the last passage we used the Hankel transform of order zero:

$$\mathcal{H}\{f(k)\}(r) \equiv \int_0^\infty f(k) J_0(kr) k dk \quad (6.48)$$

and:

$$\mathcal{H}\{e^{-\alpha k}\}(r) = \frac{\alpha}{(r^2 + \alpha^2)^{3/2}} \quad (6.49)$$

For an isotropic and homogeneous Rayleigh field we can also write the expression of  $C(\xi_z; r, \omega)$ . Indeed, for a wave field composed by plane waves propagating in all the directions with same velocity, we can directly evaluate the correlation function between two points at a distance  $r$  [130]:

$$C(\xi_z; r, \omega) = C(\xi_z; \omega) J_0(kr) \quad (6.50)$$

Here  $C(\xi_z; \omega)$  is the PSD of the displacement  $\xi_z$  in the origin. Inserting this equation in Equation 6.47 leads to a Hankel transform with result:

$$C(\delta a_x; \omega) = \frac{1}{2}(2\pi G\rho_0\gamma(\nu)e^{-hk})^2 C(\xi_z; \omega) \quad (6.51)$$

Equation 6.50 is only valid for a seismic field composed by planar waves, this implies that the sources are far from the test mass.

It is worth studying the kernel  $\mathcal{K}(r, h)$  of Equation 6.47 for a more general  $C(r, \omega)$  (always homogeneous and isotropic but not necessarily composed by planar waves). In Figure 6.9,  $2h\mathcal{K}$  has been plotted with respect to  $r$  expressed in units of  $2h$ : the fact that  $\mathcal{K}(r, h)$  has its maximum in  $r = \sqrt{2}h$  means that in a homogeneous and isotropic Rayleigh field the points that contribute most to the NN are those at a distance  $\sim \sqrt{2}h$ . Already at  $r \sim 4h$  the contribute is halved. This means that there will be no need of putting the witness sensors for the active cancellation too far. In Virgo, for example, the test mass is 1.5 m above the ground (but 5 m above the floor of the recess - see Chapter 8), this

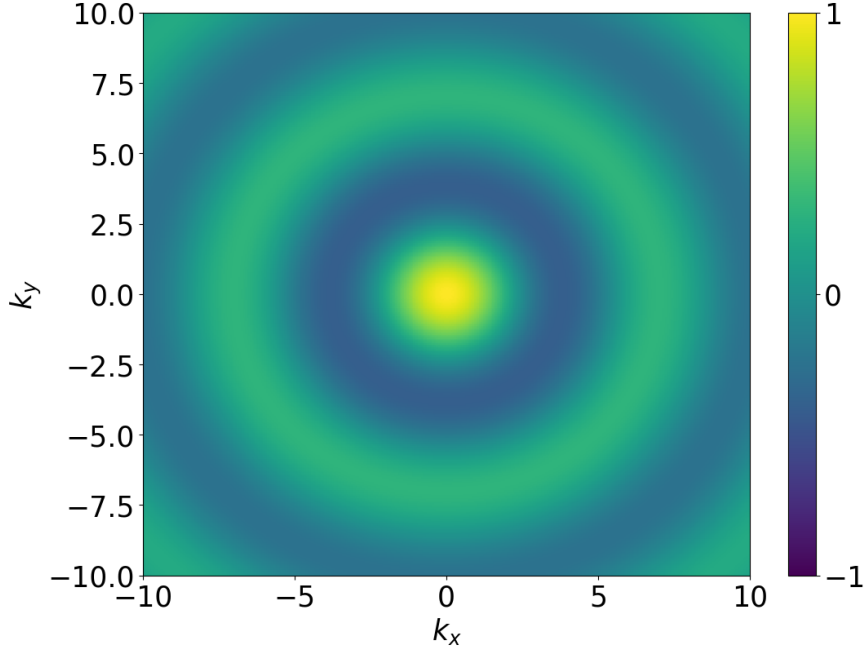


Figure 6.8: Two-point correlation of  $(0,0)$  with the field in all the other points of the plane. The Rayleigh seismic field is considered isotropic and homogeneous and the plot has been normalized with respect to  $C(\xi_z; \omega)$ .

means that sensors at a distance  $> 6$  m from the test mass will not gather important information for the reconstruction of the NN. We still need to keep in mind that this result is valid for an isotropic and homogeneous field, which in many cases does not hold (especially for Virgo). With Equation 6.31, Equation 6.50 and Equation 6.51 we we have everything we need to calculate the residual of Equation 5.20:

$$C_{SS_{ij}}(r, \omega) = C(\xi_z; \omega)(J_0(kr_{ij}) + \delta_{ij}SNR^{-2}) \quad (6.52)$$

$$C_{SN_i}(r, \omega) = 2\pi G\rho_0\gamma(\nu)e^{-hk}C(\xi_z; \omega)J_1(kr_{0i})\cos(\phi_i) \quad (6.53)$$

$$C_{NN}(\omega) = \frac{1}{2}(2\pi G\rho_0\gamma(\nu)e^{-hk})^2C(\xi_z; \omega) \quad (6.54)$$

Where  $r_{ij}$  is the distance between the  $i^{\text{th}}$  and the  $j^{\text{th}}$  sensor and  $r_{0i}$  is the distance of the  $i^{\text{th}}$  sensor from the test mass located in the origin. Here  $\phi_i$  is the angle formed by  $\mathbf{r}_{0i}$  with the  $x$ -axis (where the test mass is free to move). Equation 6.53 can be calculated using Equation 6.31: a detailed calculation of it can be found in section A.2. In the expression for  $\tilde{\mathbf{C}}_{SS}$  the self noise contribution of the sensors has also been added.

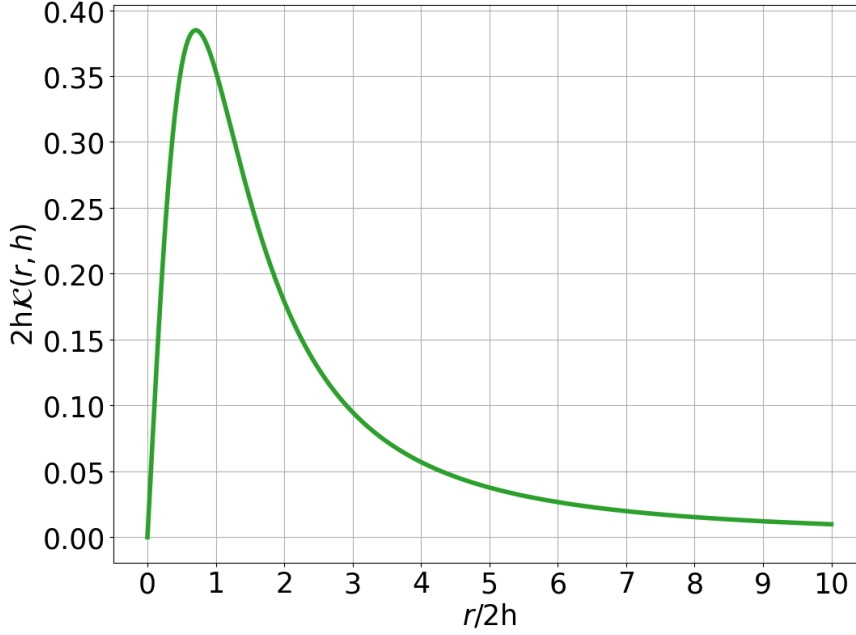


Figure 6.9: Plot of  $2h\mathcal{K}(r, h)$  with  $r$  in units of  $2h$ . The maximum value is obtained at  $r = \sqrt{2}h$ .

#### 6.8.4 Two point spatial correlation for a generic seismic field

As we will see in Chapter 8, the seismic field in reality is not homogeneous nor isotropic. This makes it impossible to use equations of subsection 6.8.3 to calculate the residual and optimize the seismic array for Virgo.

In a situation in which the properties of the seismic field are unknown, we need to rely only on seismic data:  $C_{SSij}$  can be completely known experimentally (see Chapter 8 to know how to address the problem of a continuous  $\bar{C}_{SS}$ ). From Equation 6.28, we get the expressions for both  $C_{SN}$  and  $C_{NN}$  as a function of the solely known quantity:  $C(\xi_z; \mathbf{r}_1, \mathbf{r}_2, \omega)$ .

These equations can also be found in [18] while a derivation of them is shown in section A.3:

$$C_{SS}(\mathbf{r}_i, \mathbf{r}_j, \omega) = C(\xi_z; \mathbf{r}_i, \mathbf{r}_j, \omega) \quad (6.55)$$

$$C_{SN}(\mathbf{r}_0, \mathbf{r}_i, \omega) = G\rho_0\gamma(\nu) \int d^2\mathbf{r}' C(\xi_z; \mathbf{r}_i, \mathbf{r}', \omega) \mathcal{K}(\mathbf{r}', \mathbf{r}_0) \quad (6.56)$$

$$C_{NN}(\mathbf{r}_0, \omega) = (G\rho_0\gamma(\nu))^2 \int d^2\mathbf{r} \int d^2\mathbf{r}' C(\xi_z; \mathbf{r}, \mathbf{r}', \omega) \mathcal{K}(\mathbf{r}, \mathbf{r}_0) \mathcal{K}(\mathbf{r}', \mathbf{r}_0) \quad (6.57)$$

## 6. SEISMIC NEWTONIAN NOISE CANCELLATION

---

Where:  $\mathbf{r}_{ij} = \mathbf{r}_i - \mathbf{r}_j$  is the vector distance between the  $i^{\text{th}}$  and the  $j^{\text{th}}$  sensor placed in  $\mathbf{r}_i$  and  $\mathbf{r}_j$ , while the test mass is located in  $\mathbf{r}_0$ . The kernel is defined as:

$$\mathcal{K}(\mathbf{r}_1, \mathbf{r}_2) \equiv \frac{x_1 - x_2}{(h^2 + |\mathbf{r}_1 - \mathbf{r}_2|^2)^{3/2}} \quad (6.58)$$





# OPTIMIZED ARRAYS FOR UNDERGROUND NN CANCELLATION

## Contents

---

7.1	Introduction	96
7.2	Wiener filters for underground NN cancellation	97
7.3	Optimization of seismic arrays for NN cancellation	100
7.3.1	<i>Validation of algorithms using the case of surface isotropic and homogeneous Rayleigh waves</i>	100
7.3.2	<i>Cancellation of NN from body waves</i>	101
7.4	Conclusion	110

---

The work presented in this chapter was published in 2019 [17].

## 7.1 Introduction

Analyses at the LIGO Hanford detector showed that surface displacement is dominated by Rayleigh waves [131] (similar unpublished results were obtained for the Virgo detector). This result was anticipated since the dominant ground vibrations are produced by local seismic sources located at the surface such as ventilation fans and pumps. Consequently, the development of NN cancellation systems for LIGO and Virgo focuses on NN from Rayleigh waves [18]. Contributions from body waves are being neglected. The situation changes once a detector upgrade relies on high suppression of NN by a factor 10 or more. In this case, relatively weak body-wave NN might become significant. More importantly even, body-wave NN might be the dominant contribution to NN in underground GW detectors such as KAGRA [3] or the planned Einstein Telescope [132], where the main incentive to build a GW detector underground is to strongly suppress NN from atmospheric and seismic surface fields [122, 51]. Since first NN estimates for the Einstein Telescope neglected contributions from body waves, it was not immediately realized that NN cancellation will still be required to reach the low-frequency sensitivity target as shown for example in [63]. Educated guessing of underground array configurations to achieve body-wave NN cancellation did not lead to satisfactory results [52]. It is therefore necessary to search for optimal array configurations and understand how these depend on properties of the seismic field.

In this work, the performance of optimized seismometer arrays for the cancellation of NN from body waves were investigated. We consider a test mass sufficiently far underground so that the seismometers can be placed anywhere around the test mass up to distances of a few 100 m. Body waves can be shear or compressional waves. Both produce NN through displacement of cavity walls, where the test mass of the GW detector is hosted. Compressional waves produce additional NN through compression and dilation of rock (see section 6.2). In section 7.2, we present the correlation functions of an isotropic seismic field required to calculate the Wiener filter. In the following, the two-point CPSDs will be simply named as *correlations*. In section 7.3, we present our solutions of optimized arrays. Cancellation performance is investigated as a function of the number of seismometers, and on the compressional-wave to shear-wave content ratio. Furthermore, it is studied how sensitive the performance is to the



exact placement of seismometers, while implications for the Einstein Telescope has been already discussed in section 4.2. We then conclude in section 8.5.

## 7.2 Wiener filters for underground NN cancellation

In underground detectors, test masses will be located in cavities fully surrounded by hard rock. Seismic waves propagating through the rock will cause NN. A possible mitigation strategy is to cancel part of the NN using an optimal linear filter (the Wiener filter) [133, 107], which provides a coherent estimate of NN from seismic observations (see section 5.3). For long, perpendicular detector arms and isotropic seismic fields, NN picked up by different test masses is uncorrelated (see section 6.6). In this case, one can cancel the NN from each test mass individually. It should be noted though that the seismic measurements for NN cancellation at the two input test masses will in any case be correlated, since they are close to each other, which means that even if seismic arrays deployed at all four test masses have identical configuration, the Wiener filter will be different at the vertex station due to correlations between the two seismic arrays. Following Newton's law, we can write the perturbation of gravity acceleration inserting Equation 3.1 in Equation 3.4:

$$\delta \mathbf{a}(\mathbf{r}_0, t) = -G \int dV \rho(\mathbf{r}) (\boldsymbol{\xi}(\mathbf{r}, t) \cdot \nabla_0) \frac{\mathbf{r} - \mathbf{r}_0}{|\mathbf{r} - \mathbf{r}_0|^3} \quad (7.1)$$

where  $\boldsymbol{\xi}(\mathbf{r}, t)$  is the seismic displacement field,  $\rho(\mathbf{r})$  the density of the ground medium,  $\mathbf{r}_0$  the position vector of the test mass, and  $r$  points to locations inside the ground medium. The linear dependence of the gravity perturbation on the displacement field makes it explicit that correlations between seismic displacement and NN must exist. These correlations determine the Wiener filter. Wiener filters can be formulated in time or frequency domain (see section 5.3). For Gaussian, stationary noise as considered throughout this work, frequency-domain correlations are expressed as cross-spectral densities (CPSDs) (see subsection 6.8.2). The performance of a Wiener filter can be quantified by the relative residual of the NN spectral density,  $R(\omega)$ , left in the GW data [134] after the cancellation.  $R(\omega)$  that can be expressed by Equation 5.20 which we conveniently rewrite here using a different notation:

$$R(\omega) = 1 - \frac{\mathbf{C}_{\text{SN}}^\dagger(\omega) \cdot (\bar{\mathbf{C}}_{\text{SS}}(\omega))^{-1} \cdot \mathbf{C}_{\text{SN}}(\omega)}{C_{\text{NN}}(\omega)} \quad (7.2)$$

Here,  $\mathbf{C}_{\text{SN}}$  represents the vector of CPSDs between the displacement recorded by the  $N$  seismometers and the NN at the test mass,  $\bar{\mathbf{C}}_{\text{SS}}$  is the matrix of CPSDs

## 7. OPTIMIZED ARRAYS FOR UNDERGROUND NN CANCELLATION

---

between all seismometers, and  $C_{\text{NN}}$  is NN spectral density. *In the following, we will use  $\sqrt{R}$  to quantify the noise reduction.* The best possible cancellation using  $N$  equal seismometers characterized by a certain signal-to-noise ratio (SNR) is achieved if the seismometers' data are all exact copies (up to some irrelevant transfer function) of the NN so that the CPSD between NN and seismometers assumes its theoretical maximum. In this case, the noise residual is given by Equation 5.30 which for a big number  $N$  of seismometers can be approximated as:

$$R_{\min}(\omega) \approx \frac{1}{N \cdot \text{SNR}(\omega)^2}. \quad (7.3)$$

For sufficiently high  $N$  the residual  $R$  will be limited by the SNR of the sensors and it will fall at least with  $1/N$ , indeed, one can always add a new seismometer next to an existing one to effectively average over the seismometer instrument noise.

In the following we will only consider the cancellation of NN from a single test mass. The residual  $R$  can be understood as a function of the seismometer positions with a fixed number of seismometers. One can then search for the seismometer positions that minimize the residual. We choose here to optimize the array for a fixed frequency, which translates into a fixed length of the seismic waves.

Sufficiently far underground, we have two kinds of body waves: compressional waves (also called primary waves or P waves) and shear waves (also called secondary waves or S waves), see section 6.2.

Having two kinds of body waves reduces the efficiency of the Wiener filter. Because of their different propagation velocity in the ground, P and S waves produce two-point correlations that are out of phase affecting the configuration of the optimal array (see also B).

The isotropic CPSDs are shown as a function of seismometer separation in Figure 7.1): when the mixing parameter (Equation 6.36) is less than 1 we have a visible degradation of the correlation. We can assume that polarizations are equally distributed in energy, so S waves will contribute with the two transverse polarizations and P waves only with the longitudinal polarization (for 1/3 of the total energy as in Figure 7.1).

We now consider the example of an isotropic, homogeneous seismic field. Correlation functions (CPSDs) between seismometers and with the associated gravity fluctuations have been calculated analytically in subsection 6.8.2 - Equation 6.43, Equation 6.44 and Equation 6.45 (see also chapter 7 of [52]). We remind that for those equations the CPSD between the displacement caused by P waves and the one caused by S waves has been considered negligible.

The diagonal of the CPSD matrix  $\bar{C}_{\text{SS}}$  contains the spectral densities of all seis-

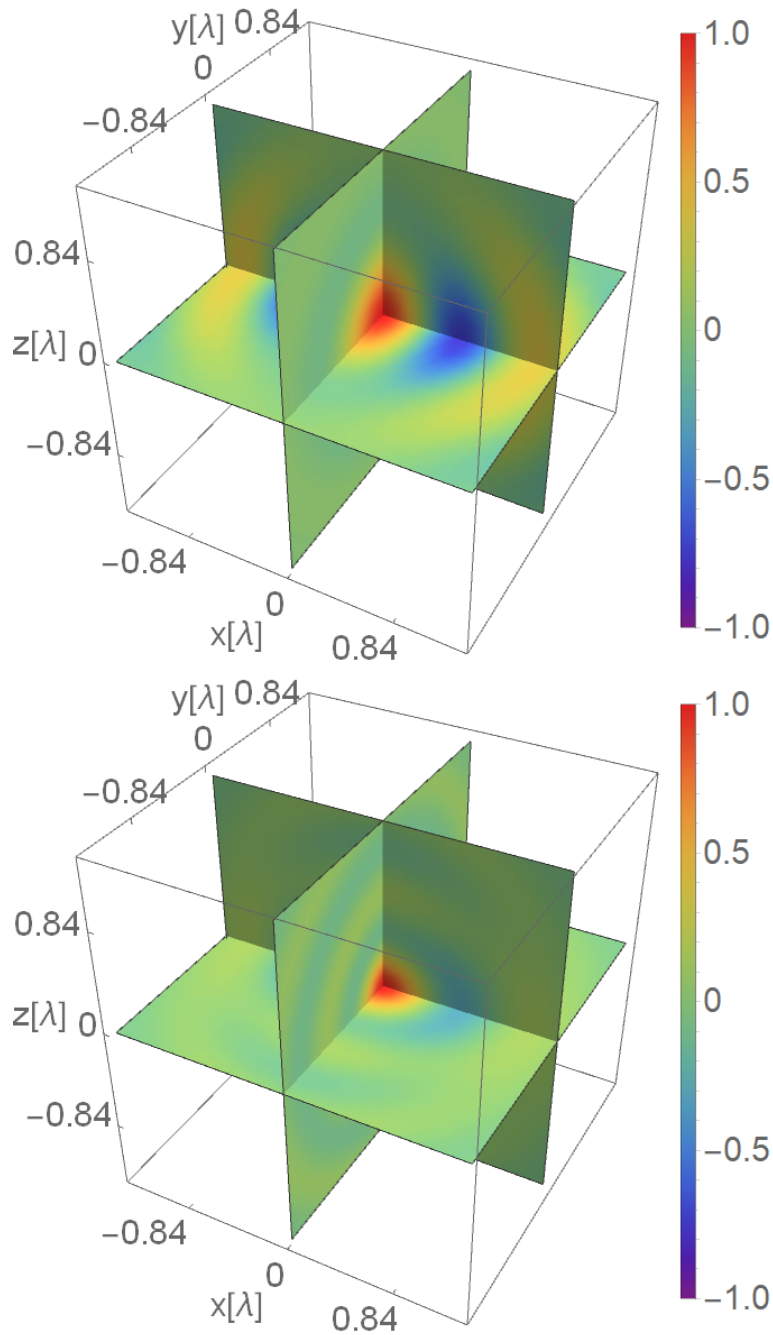


Figure 7.1: Normalized CPSDs between two sensors measuring the displacement along the x-axis in an isotropic and homogeneous body-wave field. The CPSD is real-valued. Here,  $p$  is the polarization mixing parameter ( $p = 1$  means only P waves). *Top:*  $p = 1$ . *Bottom:*  $p = 1/3$

mometers. If we want to simulate a more realistic case, we need to add a contribution coming from the seismometers' instrument noise (which we consider uncorrelated with the signal and between one sensor and another, for this reason it is present only in the diagonal elements). This can be achieved by multiplying the seismic spectral density on the diagonal by  $(1 + 1/\text{SNR}^2)$ . Since the seismic field is homogeneous, all seismometers will observe the same seismic spectral density, and if all seismometers have the same sensitivity, then the values on the diagonal of  $\bar{\mathbf{C}}_{\text{SS}}$  will be all the same and equal to  $C(\xi, \omega)(1 + 1/\text{SNR}^2)$ .

In order to calculate the CPSD between the test-mass acceleration  $\delta\mathbf{a}$  due to gravity fluctuations (NN) and the seismometers, we first need a *gravitational coupling model*. As mentioned earlier, the test mass is assumed to be located in a underground cavity. For simplicity, the cavity has a spherical shape and the test mass is at its center. Also, it is assumed that the cavity has a small radius  $a$  so that  $k^{\text{P}}a \ll 1$  and  $k^{\text{S}}a \ll 1$ . The last conditions will clearly be fulfilled in underground detectors with typical body-wave speeds of a few km/s. This greatly simplifies the equations describing the gravitational coupling between seismic field and test mass, and also makes sure that we do not need to consider seismic waves scattered from the cavity [52] (see also section 6.5). If the test mass is not located at the center of the cavity, then the coupling will obtain an additional negligible phase term. The impact of the shape of the cavity volume on the gravitational coupling between seismic field and test mass has not been investigated yet. Under these conditions, the seismic gravity perturbation is that of Equation 6.16, which has been used to calculate the analytical expression of  $\mathbf{C}_{\text{SN}}$ . All terms inside Equation 7.2 are then available as analytic expressions for the isotropic seismic field (boxed equations of subsection 6.8.2). This allows us to study cancellation performance of Wiener filters using seismometer arrays and to search for optimal array configurations under the assumptions of an isotropic and homogeneous field.

## 7.3 Optimization of seismic arrays for NN cancellation

### 7.3.1 Validation of algorithms using the case of surface isotropic and homogeneous Rayleigh waves

The optimization of seismometer arrays for isotropic Rayleigh-wave fields was addressed in previous publications [111, 18]. We have used this case to validate our optimization algorithms, which however requires a different tuning of certain parameter settings in the optimization algorithms. Consistency with previous

results was achieved and a new analysis regarding the robustness of the cancellation performance with respect to small deviations of the seismometer locations from their optimum was carried out.

The equations for a isotropic homogeneous plane wave model used for the validation can be found in subsection 6.8.3. The case presented here is that of  $N = 6$  seismometers measuring vertical surface displacement with a  $\text{SNR} = 100$  and located on a flat surface monitoring an isotropic, homogeneous Rayleigh-wave field. In the optimal configuration that we found, the approximate distance between seismometers and test mass is about  $0.3\lambda$ , where  $\lambda$  is the length of the Rayleigh waves at the optimization frequency. This distance depends on the seismometer SNR (see Figure 7.2). In Figure 7.2 we show the optimal arrays for  $N = 6$  for varying SNR values. The outer four seismometers in this plot describe S-shaped trajectories moving towards smaller  $\text{abs}(x)$ -values, and larger  $\text{abs}(y)$ -values with increasing SNR. The two seismometers located at  $y = 0$  move outwards with increasing SNR. We compare this result with the one obtained in [18] shown in Figure 7.2 (bottom plot). The optimal sensor coordinates found in previous works can be found in section 7.1.6 of [52] and they are completely comparable with our result. So we confirmed what already found for isotropic and homogeneous Rayleigh fields.

We moved a step forward and tried to understand how much the performances of the cancellation change if we commit some errors in the placement of the sensors with respect to the optimal positions. This is made by modifying the array coordinates adding Gaussian errors to the location coordinates of each sensor. We used two different zero-mean Gaussian distributions with standard deviations:  $\sigma = 0.01\lambda$  and  $\sigma = 0.1\lambda$ . For each of the resulting array configurations that we obtained the NN residual was calculated. The values  $\sqrt{R}$  are collected in the histogram shown in Figure 7.3. Coordinate mismatches of a bit less than  $0.1\lambda$  could be tolerated to achieve a NN reduction by a factor 10 with  $\text{SNR} = 100$  seismometers. At the LIGO and Virgo sites, Rayleigh-wave speeds at 10 Hz are about 300 m/s, which means that we can misplace the sensor by  $0.1\lambda \approx 3$  m and still obtaining a factor 10 of NN reduction.

### 7.3.2 Cancellation of NN from body waves

Finding the optimal array for NN cancellation means to find the configuration that minimizes the residual in Equation 7.2. This kind of calculation becomes very demanding as the number of seismometers increases. We deal with functions in  $3N$ -dimensional spaces, where  $N$  is the number of seismometers. From now on, we will be focused on the optimization of an array of seismometers in underground

## 7. OPTIMIZED ARRAYS FOR UNDERGROUND NN CANCELLATION

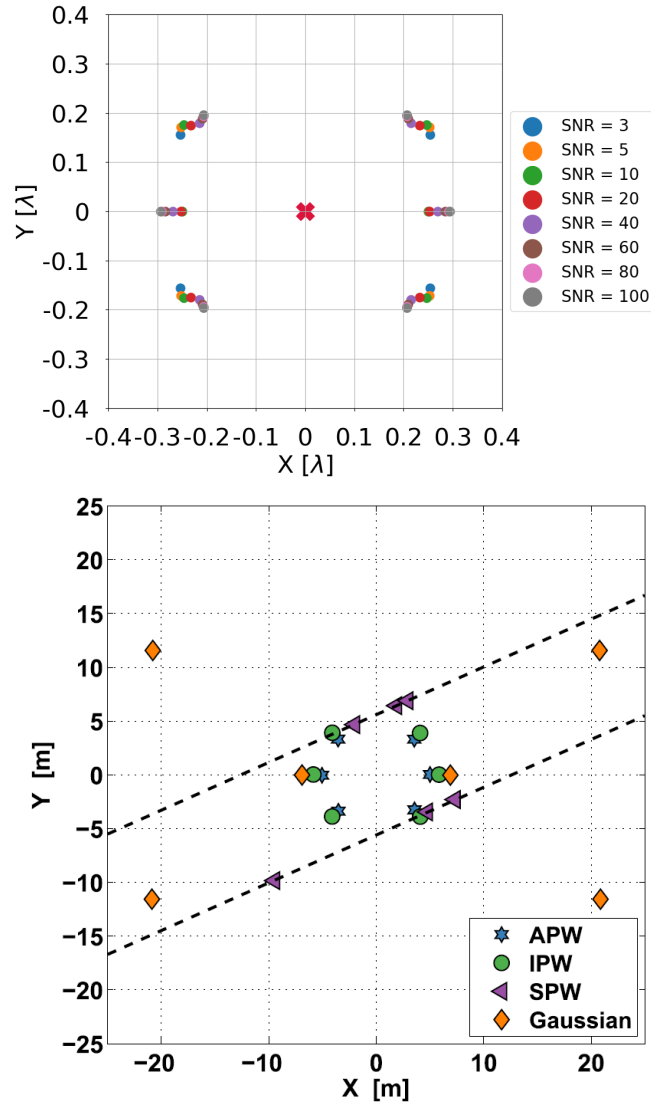


Figure 7.2: Comparison between the results obtained with our optimization and the results of [18]. *Top*: Optimal array configurations that I found for  $N = 6$  seismometers and with varying SNR. A homogeneous and isotropic Rayleigh field (and plane wave assumptions) has been considered. The red cross represents the test mass. *Bottom* The results obtained from Coughlin et al. in [18]. The optimal arrays for  $N = 6$  sensors are shown for an isotropic plane wave model (IPW), an isotropic Gaussian model, an anisotropic plane wave (APW) and a single plane wave model (SPW). The resulting geometries and positions are comparable with our results except for the isotropic Gaussian model optimal array.

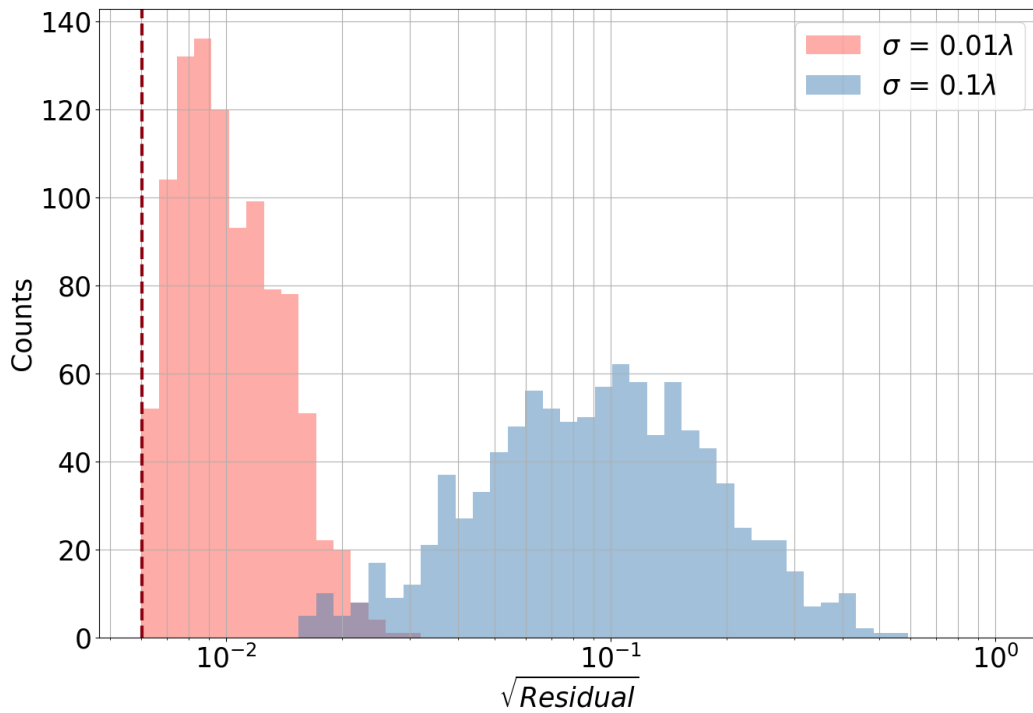


Figure 7.3: Robustness of cancellation performance for NN from Rayleigh waves determined by random Gaussian shifts of seismometer coordinates from their optimal values. The array contains  $N = 6$  sensors with  $\text{SNR} = 100$ . The dashed red line represents the residual of the optimized array.

## 7. OPTIMIZED ARRAYS FOR UNDERGROUND NN CANCELLATION

---

environments. Thus, we will use the assumptions made in [section 7.2](#). The optimization algorithms do not guarantee to find the global minimum (within a finite time). The optimization of seismometer arrays for body-wave NN cancellation is more demanding than in the case of seismic surface waves for two main reasons: the array needs to disentangle NN contributions from compressional and shear waves, which gives the residual function a richer structure in terms of local minima, and, as we will see, there is no unique optimum due to symmetries of the seismic field.

We used two different global optimizers (see [Chapter 5](#)): Basin Hopping (BH) and Differential Evolution (DE). Basin Hopping is a combination of a local minimizer with a global Monte Carlo search of the minimum [[90](#), [89](#)] based on the Metropolis criterion [[93](#)], while DE is part of the family of evolutionary algorithms [[95](#), [135](#)]. Both algorithms require parameter tuning to efficiently find the global minimum instead of some local minimum with higher noise residuals. For DE, we had to specify the coordinate boundaries to look for the minimum. For BH, we had to specify the step size (which tunes how the space is explored to find the minimum) and another parameter, called "temperature" (high temperature means that longer jumps in parameter space are accepted).

We adopted three different methods to validate our solutions. First, as mentioned already, we checked to achieve a match of the Rayleigh-wave results with the published solutions. Second, we have analytic solutions ([Equation 7.4](#)) of the optimal arrays and their residuals for  $N = 1$  (and arbitrary values of  $p$ ), and for  $p = 0$  and  $p = 1$  (for arbitrary number  $N$ ) that can be compared with the numerical solutions. For  $p = 0$  and  $p = 1$ , the residual is given by [Equation 7.3](#). Third, as explained by [Equation 7.3](#) and in [subsection 5.3.3](#), for sufficiently high  $N$ , the noise residual  $R$  needs to fall at least with  $1/N$  when increasing  $N$ . We found that the results passed all the three tests.

$$R(\omega) = 1 - \frac{(2pf_P - (1-p)f_S)^2}{(3p+1)(1 + \frac{1}{\text{SNR}^2})} \quad (7.4)$$

Nevertheless, different solutions were found by running the global optimizers many times: many of them corresponded to local minima, others were degenerate optimal solutions (the degeneracy due to the symmetry). [Figure 7.4](#) shows the seismometer locations of the 100 overlapped solutions obtained from the 100 optimization runs made for  $N = 6$  sensors. The x-axis corresponds to the direction of the detector arm, which means that it corresponds to the relevant direction of test-mass displacement (where it is free to move). We considered two kinds of seismometers: a single-axis seismometer monitoring displacements along the x-axis, and a three-axis seismometer monitoring displacements along the three directions (x,y,z). We used  $\text{SNR} = 15$  for all the seismometers (which



## 7. OPTIMIZED ARRAYS FOR UNDERGROUND NN CANCELLATION

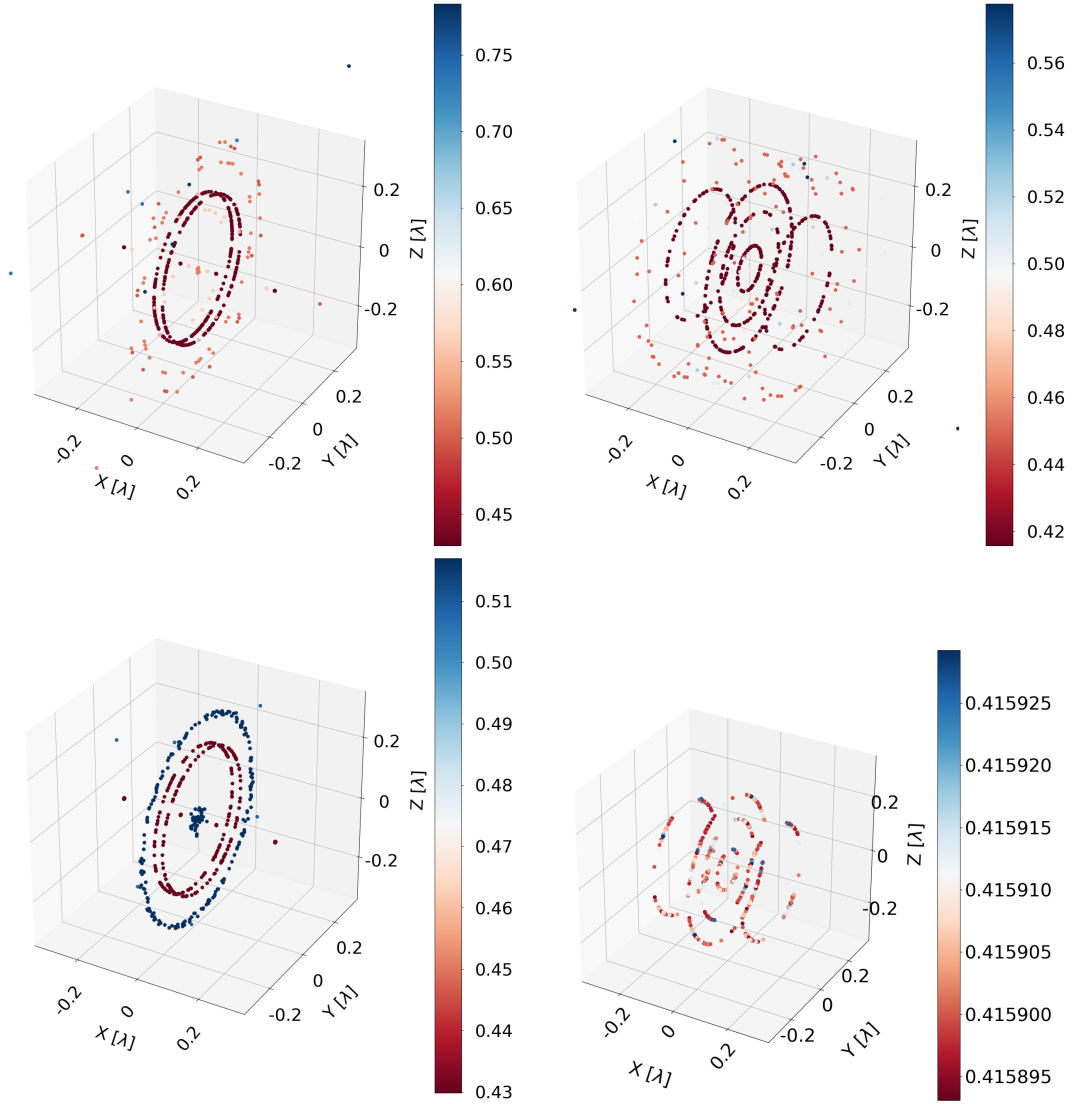


Figure 7.4: Comparison of DE with BH algorithm, for single-axis sensors and for three-axis sensors. The number of seismometers is  $N = 6$  with  $\text{SNR} = 15$ . The seismic field has a mixing ratio  $p = 1/3$ . In each case, the optimization was run 100 times and the solutions were collected in a single plot. The colors on the bar measure the different values of residual obtained with the minimization. See Figure 7.8 for a better understanding of the optimal array configurations.

## 7. OPTIMIZED ARRAYS FOR UNDERGROUND NN CANCELLATION

---

is a reasonable assumption since we are in a low-noise environment [18]), and the residual was minimized at the single frequency of 10 Hz, so that the compressional wavelength  $\lambda$  used as length unit in the plots was fixed. The corresponding length of shear waves is then  $\lambda_s = 0.67\lambda$ . The markers are coloured according to the residual achieved by the array: blue dots represent local minima and then lead to higher values of the residual function (and worst cancellation performances).

The DE algorithm performs better on average, but best solutions found with BH and DE over 100 runs perform equally well. Interestingly, the three-axis arrays do not perform significantly better than the single-axis arrays even though the number of channels is  $3N$  vs  $N$ . It means that there is very little extra information that can be extracted from the y,z-axes (the x-axis being the relevant direction of test-mass displacement).

In Table 7.1, we present values of optimal sensor locations for  $N = 6$  and  $\text{SNR} = 15$  as a benchmark. These results were obtained with DE using decreased tolerances on the sensor positions to give precise values up to 5 decimal places (this was useful to obtain a better optimization result), while larger tolerances are acceptable (and used throughout the rest of the paper) to get arrays with very similar configuration and performing equally well for all practical purposes.

Configuration	Sensor coordinates [ $\lambda$ ]	Noise residuals $\sqrt{R}$
Single-axis	$(-0.014, 0, -0.224),$ $(-0.014, 0, 0.224),$ $(-0.014, -0.224, 0),$ $(-0.014, 0.224, 0),$ $(0.059, 0, 0), (0.250, 0, 0)$	0.430
Three-axis	$(0.152, 0, 0.183),$ $(-0.152, 0, 0.183),$ $(0, -0.230, 0.040),$ $(0, 0.230, 0.040),$ $(0, 0, 0.064), (0, 0, -0.158)$	0.416

Table 7.1: Benchmark solution for  $N = 6$ ,  $\text{SNR} = 15$ , and  $p = 1/3$ . Coordinates are given in units of compressional-wave length  $\lambda$ . It is one possible solution among many.

The solutions for the single-axis and three-axis solutions are not unique. Any rotation of the array around the x-axis yields another solution with the same noise residual. Therefore, these benchmark values are obtained by taking the result

## 7. OPTIMIZED ARRAYS FOR UNDERGROUND NN CANCELLATION

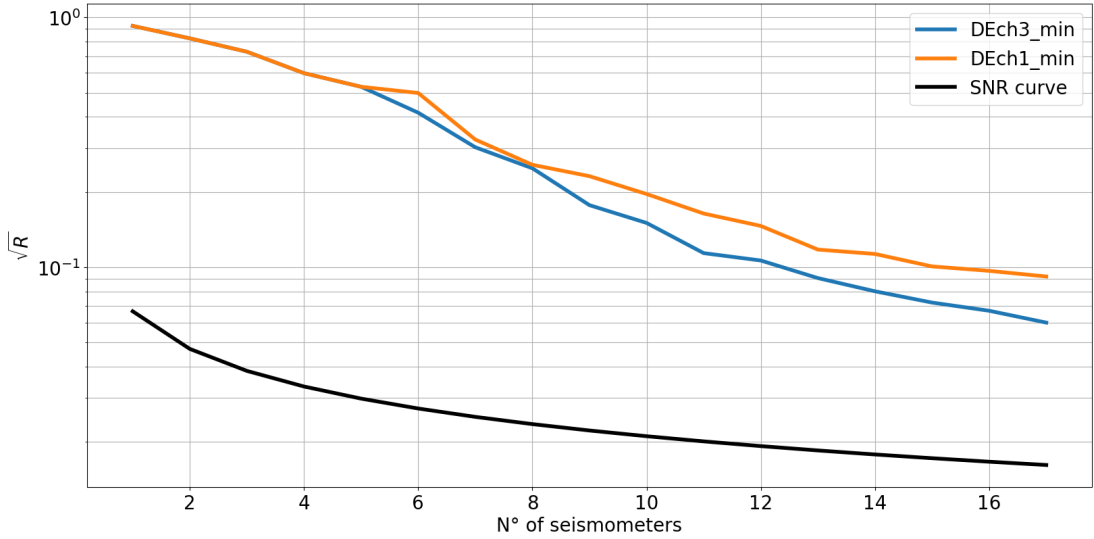


Figure 7.5: Results obtained with DE with three-axes or single-axis sensors and with  $p = 1/3$ . The theoretical sensor-noise limit is shown as a black curve (SNR curve). The residuals correspond to the minimum over 100 optimization runs for each number of seismometers.

of the optimization and rotating it such that symmetry axes are aligned with coordinate axes. In Figure 7.5, the residuals are shown for single and three-axis sensors as a function of  $N$ . A residual of  $\sqrt{R} < 0.1$  is achieved for  $N > 14$ . For comparison, the plot also shows the theoretical sensor-noise limit from Equation 7.3). At high  $N$ , the curves start to fall with similar slope, which means that any new sensor just serves to effectively improve the sensitivity of the array without significantly affecting the Wiener filter’s ability to disentangle different modes and polarizations of the field.

We investigate the robustness of cancellation performance with respect to shifts in sensor locations from their optimum as it was done for the Rayleigh wave case in subsection 7.3.1. Random errors for the location coordinates are drawn from two zero-mean Gaussian distributions with standard deviations:  $\sigma = 0.01\lambda$  and  $\sigma = 0.07\lambda$ . As shown in Figure 7.6, sensor coordinates for an array of three-axis seismometers can deviate by (in average)  $0.07\lambda$  from their optimal values to achieve a factor 3 of reduction for body-wave NN. In section 6.3, we argued that a factor 3 of NN suppression is likely sufficient to achieve sensitivity targets of the future GW detector Einstein Telescope. One additional aspect of noise cancellation is the width of the frequency band over which it is effective. According to the noise plots in Figure 6.3, cancellation for ET might be required over a larger band of frequencies between about 2 Hz and 10 Hz. Figure 7.7 shows the results

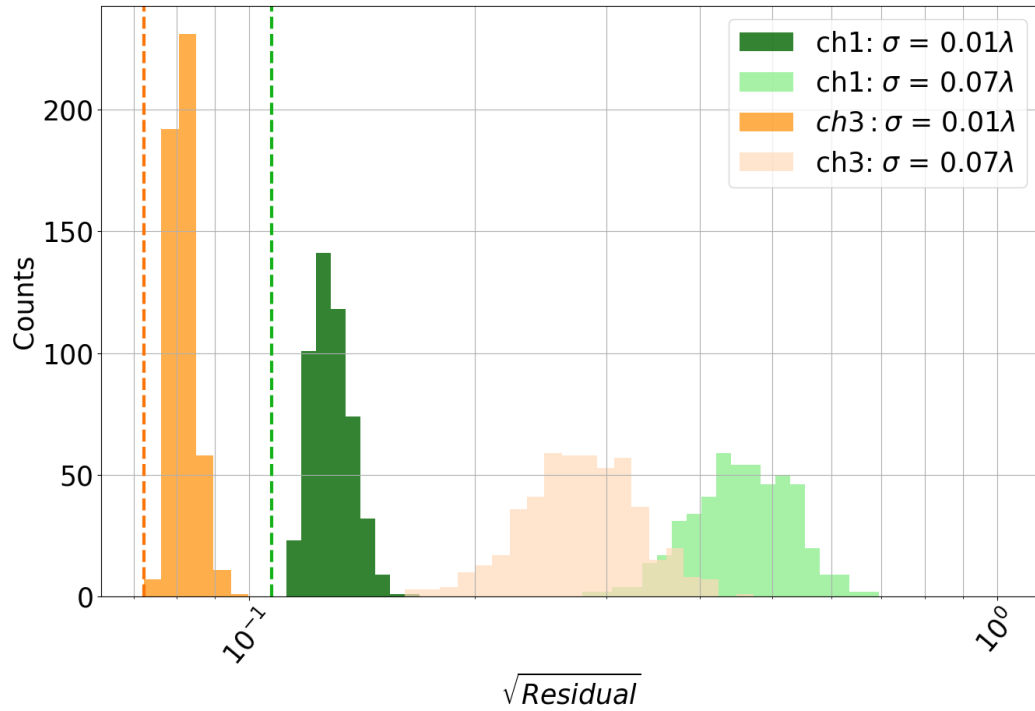


Figure 7.6: The histograms show the variability of the residual functions for an underground array with  $N = 15$  seismometers (single and three-axis) and  $\text{SNR} = 15$  when the optimized array coordinates are shifted with random values extracted by a Gaussian distribution with standard deviation  $\sigma$ . The two vertical dashed lines show the residuals for the optimized coordinates.

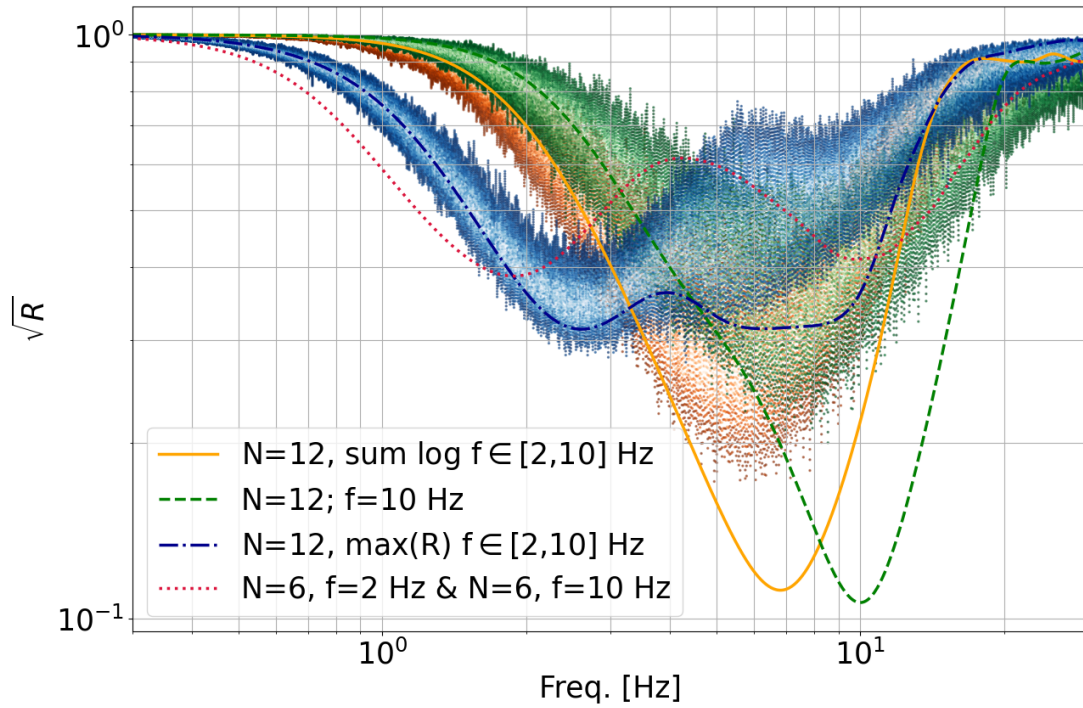


Figure 7.7: Broadband optimization of cancellation performance also including histograms of residuals when all sensor coordinates are shifted randomly of values drawn from a Gaussian with standard deviation of 50 m (which corresponds to about  $0.08\lambda$  at 10 Hz). The curve  $N = 6 + 6$  is plotted without histogram.

of various attempts to achieve broadband-optimized cancellation. The dashed curve shows the NN reduction using an array with 12 seismometers optimized at 10 Hz. In this case, NN reduction at 2 Hz is minor. Similar performance is obtained when minimizing the sum of residuals between 2 Hz and 10 Hz using 12 seismometers, as shown by the solid curve. The dotted curve results from merging two arrays with 6 seismometers each, one optimized for 2 Hz, the other for 10 Hz. Good suppression can be achieved at low and high frequencies, but the performance is not uniform over the entire NN band. The best solution was found by minimizing the maximum residual over the band 2 Hz to 10 Hz (dot-dashed):

$$\mathcal{L} = \max_{\forall \omega \in \omega_i} \{R(\omega)\} \quad (7.5)$$

Of course, better other cost functions could be found, in future, to yield even better broadband results.

The optimization results presented in this work are only indicative of course. In reality, the seismic field is neither isotropic nor homogeneous. Nonetheless, isotropic fields pose a greater challenge to NN cancellation designs than anisotropic fields [18], and since inhomogeneities are caused by the presence of local sources or strong scattering of seismic waves, it is possible to adapt the array provided that the location of local sources and scattering centres are known. An important result from subsection 7.3.2 is that seismometer positions do not need to exactly match the optimal positions (see Figure 7.6). Even strongly degraded configurations with respect to the optimum can still achieve a factor 3 of NN reduction in our analysis. We therefore conclude that reduction of NN in ET by a factor 10 using coherent cancellation of body-wave NN would be feasible. Clearly, it remains a significant effort since boreholes for about 15 seismometers per test mass need to be drilled and a site-characterization campaign is required to obtain two-point spatial correlations of the seismic field. It should also be mentioned that the cancellation can be achieved with already existing commercial seismometers, which have instrumental noise below the seismic global low-noise model up to 10 Hz.

## 7.4 Conclusion

In this work, published in 2019 [17], we have analysed the performance of optimized seismometer arrays for the cancellation of body-wave NN using Wiener filters. We found that about 15 sensors are required to reduce NN by a factor 10 (in amplitude) when 1/3 of the spectral density of the seismic field is in compressional waves (the rest being in shear waves). The optimal array configurations were determined for isotropic, homogeneous fields. The cancellation performance

## 7. OPTIMIZED ARRAYS FOR UNDERGROUND NN CANCELLATION

---

is mainly limited by the array's ability to disentangle shear from compressional waves. In contrast, cancellation performance is limited by the seismometer noise if only one wave polarization (either compressional or shear) is present in the seismic field.

We then found that for a well performing array, the seismometer locations do not have to match the optimal locations precisely. This is true for Rayleigh-wave and body-wave NN cancellation given the respective NN suppression targets in future detectors.

Cancellation of NN will likely be required to achieve ET sensitivity (according to the reference sensitivity ET-D). Our results lead us to the conclusion that NN cancellation is feasible for underground detectors. Neither the required number of seismometers, nor their sensitivity, nor the required accuracy of their positioning in boreholes is prohibitive. We therefore propose coherent cancellation of NN using Wiener filters as technique in the third-generation GW detector Einstein Telescope.

Finally, we discuss the role of the various assumptions made in this paper. The assumption of an isotropic and homogeneous field is of course a great simplification. However, something we know from previous work [18] is that anisotropy does not have a big impact on cancellation performance, and it can even be beneficial, e.g., you only need one seismometer if waves always come from a single direction. However, concerning homogeneity, one cannot be sure that our analysis is robust when introducing heterogeneities. This is a complicated matter since there are different reasons for which a field can be inhomogeneous (scattering, nearby seismic sources, coupling to other fields such as sound, . . .). We expect that body-wave fields should have a high degree of homogeneity, since dominant sources of body waves are typically distant, and since body waves are so fast and therefore long that the wave field is less disturbed by scattering, also considering that an underground environment is geologically more homogeneous than near-surface soil. Nevertheless, in the case of strong underground seismic sources, as often present in underground array measurements (e.g., anthropogenic noise from ventilation and pumps), this assumption might not hold. In this case, it is important to know the local underground seismic sources to adapt the seismic array accordingly, and we cannot exclude that the number of sensors required in this case needs to be higher. However, in Chapter 9 we showed that the seismic noise from infrastructures is not a big concern from the point of view of the seismic and the Newtonian noises.

For what concerns the assumption of a spherically shaped cavern, simple arguments can be used to conclude that the shape and size of the cavern is not so important for NN and its cancellation. The main point is that the seismic waves are much longer than the diameter of the cavern [136]. Newtonian noise

## 7. OPTIMIZED ARRAYS FOR UNDERGROUND NN CANCELLATION

---

is therefore almost the same if one considers a cavity of 5 m radius and one of 50 m. Both numbers are a small fraction of the length of body waves even at a frequency as high as 10 Hz. For the same reason, the effect of scattering on NN can be neglected [52] (see section 6.5 ), and it follows that the shape of the cavern has no significant effect either. It does not even matter where the test mass is located inside the cavity since the position can only vary by a small fraction of the length of a seismic wave.

The last assumption made is that P and S waves are in average uncorrelated. We know that this is likely not the case since an incoming body wave, when reflected from the surface, is partially converted into other polarizations. How much average correlation this produces between P and S is not known to us, and it will be important to estimate this effect in future work. It might well have a significant impact on optimal array configurations.



## 7. OPTIMIZED ARRAYS FOR UNDERGROUND NN CANCELLATION

---

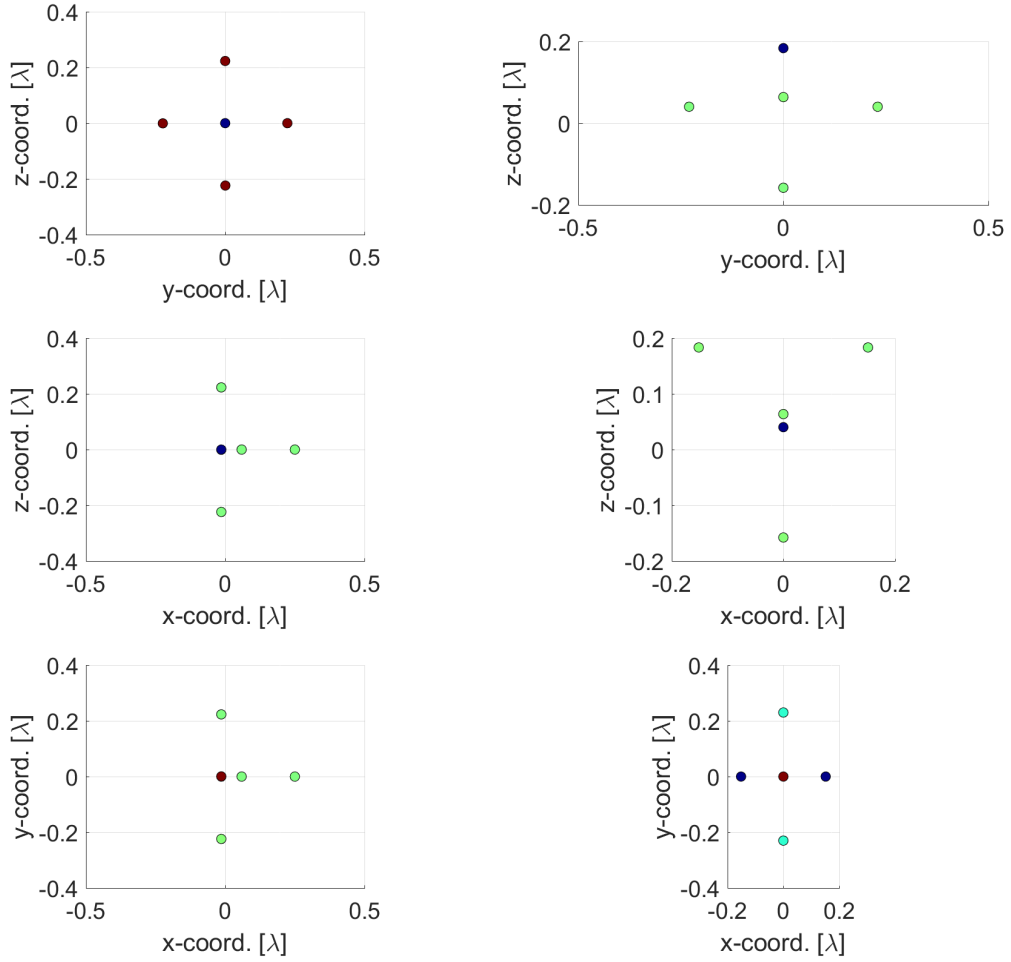


Figure 7.8: Optimal array configurations for  $N = 6$  and  $p = 1/3$  (coordinates listed in Table 7.1). Difference in marker colors indicates different values of the coordinate along the projection direction.

## 7. OPTIMIZED ARRAYS FOR UNDERGROUND NN CANCELLATION

# 8 ARRAY SEISMOMETER OPTIMIZATION FOR ADV

## Contents

---

8.1	Introduction	116
8.2	Instruments and positioning	119
8.3	Surrogate model of the Wiener filter	120
8.4	Array optimization	125
8.5	Conclusion	132

---

The work presented in this chapter was published in 2020 [124].

## 8.1 Introduction

For Virgo detector, the dominant contributions to NN are predicted to come from seismic and acoustic fields [137, 51]. Low-frequency noise, including Newtonian noise, will have significant impact on parameter estimation of compact-binary GW signals [138, 139, 140], and it can also significantly influence the signal-to-noise ratio, especially of intermediate-mass black-holes visible mostly through their harmonics excited during the merger [141]. Mitigation of NN, therefore, will have an important impact on the science that could be done with GW observations.

New methods to lower environmental noise are being developed and implemented. One approach is to lower disturbances in the environment, which is possible whenever the sources are under human control like pumps and ventilation systems. Another method is the so-called offline subtraction of noise, where data from environmental sensors are passed through filters and subtracted from the detector data [142, 107]. This method has been implemented successfully in LIGO and Virgo, for example, to reduce noise from vibrations of optical tables causing laser-beam jitter [11].

A combination of these two methods is also being considered to mitigate NN at Virgo as part of the AdV+ detector upgrade.

Extensive seismic studies were carried out to characterize the field in terms of its spatial and temporal properties [19]. The goal was to understand from the observed properties of the seismic field, especially its two-point correlations, how to deploy the seismometers. In order to implement the NN offline subtraction [134, 131] which will be ready for O4, the results of this work will be used to deploy a total of 120 sensors inside the three main experimental halls of the Virgo detector.

Optimization of array configurations for NN cancellation has been a difficult challenge, and so far, it was only possible to calculate optimal arrays for simple fields where seismic correlations and the gravity perturbation have a known analytic expression [111, 18]. The main challenges are:

- The optimization involves a large number of variables (2 coordinates per seismometer).
- Real seismic fields, especially those at Virgo site where local seismic sources dominate and seismic waves interact with a complex infrastructure [19, 137], cannot be represented by analytic models.

## 8. ARRAY SEISMOMETER OPTIMIZATION FOR ADV

---

- Information about the seismic field obtained by site-characterization measurements with arrays is incomplete [143].
- How to systematically and optimally use information about the seismic field for the design of a NN cancellation system has been an open problem so far.

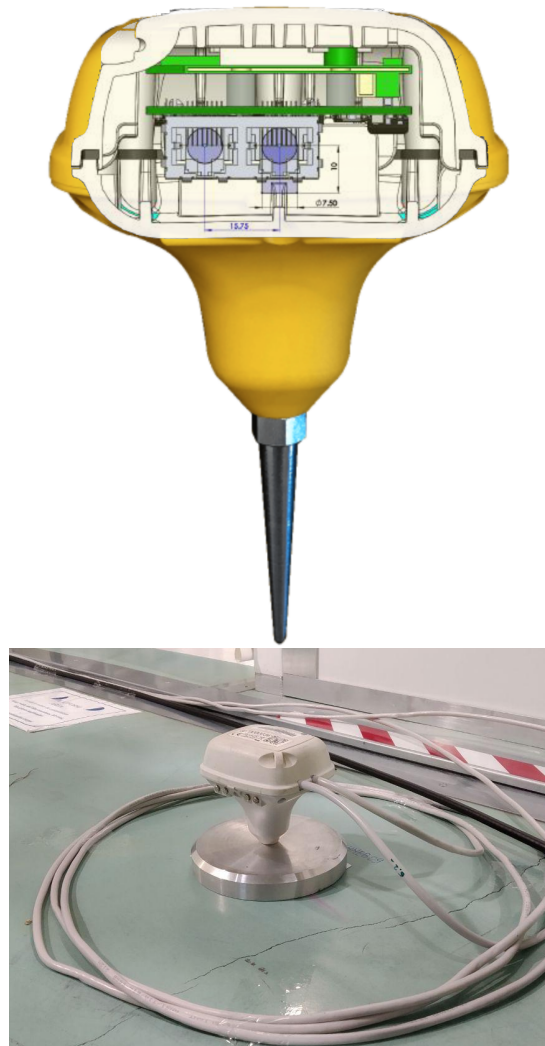


Figure 8.1: InnoSeis sensor used to record data. The mount was modified by Nikhef in order to be used indoors. The cables were twisted around the sensors in order to reduce as much as possible the vibrational coupling with the instrument.

In this work, I present an efficient approach to the optimal design of a NN cancellation system based on observed two-point spatial correlations between the

## 8. ARRAY SEISMOMETER OPTIMIZATION FOR ADV

seismometers deployed in the array (see also subsection 6.8.4). The solution takes the form of a surrogate Wiener filter with seismometers as input channels, and whose output constitutes an estimate of the gravity fluctuation produced by the seismic field. It can be calculated for an arbitrary number of seismometers with arbitrary positions on the surface. The method incorporates kriging [102, 103] (as Gaussian process regression is sometimes called when spatial correlations are involved) and a simple interpolation, and it is devised to address computational limitations (the optimization procedure still requires a computer cluster to obtain robust optimization results).

A summary of the seismic experiment at Virgo whose data were used to calculate the surrogate model is given in section 8.2. In section 8.3, I describe the construction of the Wiener-filter surrogate model and some of its properties. The results about the optimization of the seismometer locations are presented in section 8.4.

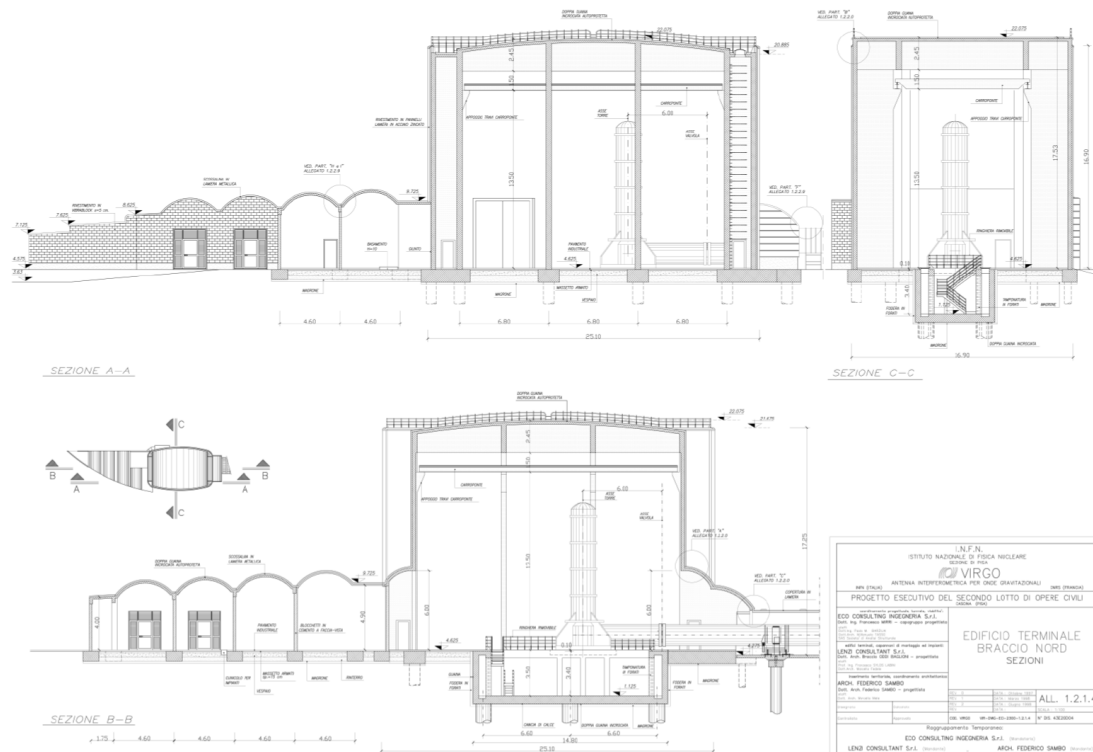


Figure 8.2: Blueprint of the end building of Virgo.

## 8.2 Instruments and positioning

In this work I used the data collected with 38 seismometers (5 Hz *geophones*) placed in the Virgo West-End Building (WEB) [19].

The seismometers (geophon type) were manufactured by InnoSeis [144]. A geophone is a transducer of the seismic motion (velocity) into voltage, the working principle exploits the inductance law. The sensors were placed on the ground and were mounted on a heavy metal plate attached to the ground by means of a double-sided adhesive tape (see Figure 8.1). The data used here were taken during one hour between the 00:00 and the 01:00 of February 5, 2018, i.e., a time without human activity in the building and therefore representative of the situation during Virgo observation runs. The WEB hosts one of Virgo's sus-

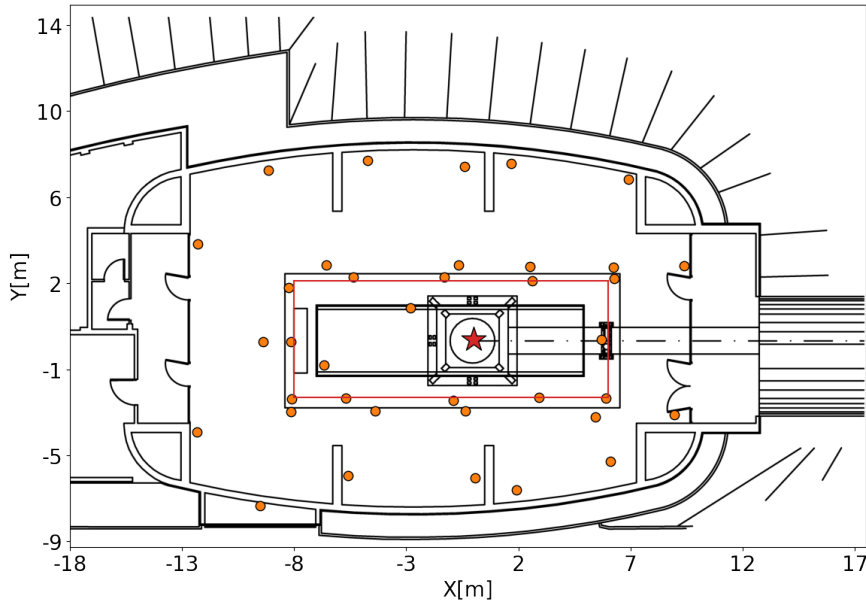


Figure 8.3: Plan of the WEB seismic array.

ended test masses (red star in Figure 8.3 and in all our plots); we can see from Figure 8.2 that it has a complicated structure: the ground is not homogeneous and consists of a basement placed under the test mass whose floor is 3.5 m below the surface (horizontal extent of the recess will be marked by a red rectangle in our plots). The ceiling and the walls of the basement are disconnected by a thin gap (5 cm) from the main building floor. The entire structure supported by the basement is called *tower platform* and it is anchored with 52 m deep pillars to a more stable gravel layer beneath the clay (there are many gravel layers, which alternate with clay in the substrate of soil beneath Virgo [145]). These pillars

are meant to prevent the sinking of the platform. This is important since the platform carries the vacuum chamber of the seismic isolation and the test-mass suspension system [45].

I placed the origin of our coordinate system at the surface level, right below the test mass. The basement extends from -8 m to 6 m along  $x$ , and  $\pm 2.6$  m along  $y$  (see Singha et al for more details [137]). Of the 38 seismometers placed in the WEB, 15 were placed on the tower platform (of which, only two were on the floor of the basement) and 23 on the building floor. One seismometer was discarded since it was deployed on a metal sheet that forms part of the ceiling of the basement, and whose vibrations are uncorrelated with the seismic field. Also, the metal sheet is too thin to contribute significantly to NN.

### 8.3 Surrogate model of the Wiener filter

For the noise cancellation, data from witness sensors is passed through a filter and its output is subtracted from a target channel [146, 133, 147]. Normally, the goal is to reduce the variance of the target time series. For the cancellation of stationary noise, the Wiener filter (see section 5.3) is known to minimize the variance of the residual data [146], and they were therefore proposed for NN cancellation in GW detectors [134].

When the source of disturbance is an entire field, as for NN, then effective monitoring of the field becomes the main challenge in the design of a noise-cancellation system. Effective monitoring can be achieved by choosing effective types of seismic sensors [148], and by optimal sensor positioning [111, 18, 17]. Until now, determining the optimal sensor locations based on correlation measurements of the seismic field has been an open problem.

For this work, observations of vertical seismic surface displacement,  $\xi$ , were considered and for the optimization the same cost function as Chapter 7 was used. I recall that the noise residual of Equation 7.2 depends on the cross-spectral density matrix between all the seismometers,  $\bar{\mathbf{C}}_{SS}$  and the cross correlations between the  $N$  seismometers and the test-mass,  $\mathbf{C}_{SN}$ . While  $\mathbf{C}_{SN}$  is a function of two parameters per seismometer (its two horizontal coordinates),  $\bar{\mathbf{C}}_{SS}$  depends on the coordinates of a pair seismometers, and so it is a four dimensional function.

The Wiener filter minimizes the residual noise  $R(\omega)$  for a given configuration of the seismic array and it is related to the NN power spectral density (PSD)  $C_{NN}$  of the test mass. For reasons that will be clear later we express Equation 7.2 as:

$$R(\omega) = 1 - \frac{\hat{C}_{NN}(\omega)}{C_{NN}(\omega)} \quad (8.1)$$



Where  $\hat{C}_{\text{NN}}$  is the Wiener filter estimation of the PSD of the NN:  $\hat{C}_{\text{NN}} = \mathbf{C}_{\text{SN}}^\dagger(\omega) \cdot (\bar{\mathbf{C}}_{\text{SS}}(\omega))^{-1} \cdot \mathbf{C}_{\text{SN}}(\omega)$ . The aim is now to minimize  $R(\omega)$  by finding the optimal locations of the  $N$  seismometers. This can be achieved by maximizing the numerator in Equation 7.2, indeed  $C_{\text{NN}}$  is just a constant. In past studies (like the one of Chapter 7), analytic models were used for  $\mathbf{C}_{\text{SN}}$  and  $\bar{\mathbf{C}}_{\text{SS}}$  representing simplified, i.e., isotropic, homogeneous seismic fields. The field observed in Virgo is very complicated and cannot be represented by any analytic model [19]. The question arises how to make best use of the information we have about the seismic field to estimate the optimal array configuration and how to evaluate Equation 8.1.

The approach taken here is to construct a surrogate model of the Wiener filter for an arbitrary number of seismometers, and to use it for the calculation of the optimal array. While we can obtain  $\bar{\mathbf{C}}_{\text{SS}}$  from the data by means of regression methods (see section 8.4) we cannot do the same for  $\mathbf{C}_{\text{SN}}$  since Virgo's sensitivity is not yet good enough to observe NN. We need then to provide a model for  $\mathbf{C}_{\text{SN}}$ . Assuming that the dominant seismic displacement is produced by Rayleigh waves, or more generally, that NN contributions from surface displacement are dominating over contributions from (de)compression of the ground medium, we can use the model of Equation 6.56. Here we must consider that the tower basement  $h$  has two values: 1.5 m and 5 m, for points on the main building floor and on the basement floor, respectively. The kernel  $\mathcal{K}$  of Equation 6.56 links the seismic correlations with the NN from Rayleigh waves or surface displacement. Its values are shown in Figure 8.5. I point out that contributions from the normal displacement of basement walls, despite the fact that they can be included in Equation 6.56, cannot be considered in our analysis since no sensors were installed on the basement walls.

In order to perform the optimization over  $R(\omega)$  to find the optimal configuration of the seismometer array we need a way to evaluate  $R(\omega)$  in every possible configuration. In subsection 6.8.4, we have seen that this simply translates in having the values of  $\bar{\mathbf{C}}_{\text{SS}}$  for every possible position of the  $N$  sensors. The collected data cannot, of course, cover all the possible combinations of sensors locations, but only very few of them. For this reason, we need to use the collected data to infer the underlying model for  $\bar{\mathbf{C}}_{\text{SS}}$ . This, in principle, could be done with a simple interpolation (spline or linear, for example) of the CPSDs that we can calculate from the 37 seismometers deployed in the WEB. However, we can achieve much better results with a Bayesian approach, i.e., Gaussian-process regression (GPR) that was discussed in section 5.2. The GPR approach makes it also possible to extend the analysis to a region beyond the convex envelope of the deployed array, this last point is convenient for technical reasons, since it let the possibility of

## 8. ARRAY SEISMOMETER OPTIMIZATION FOR ADV

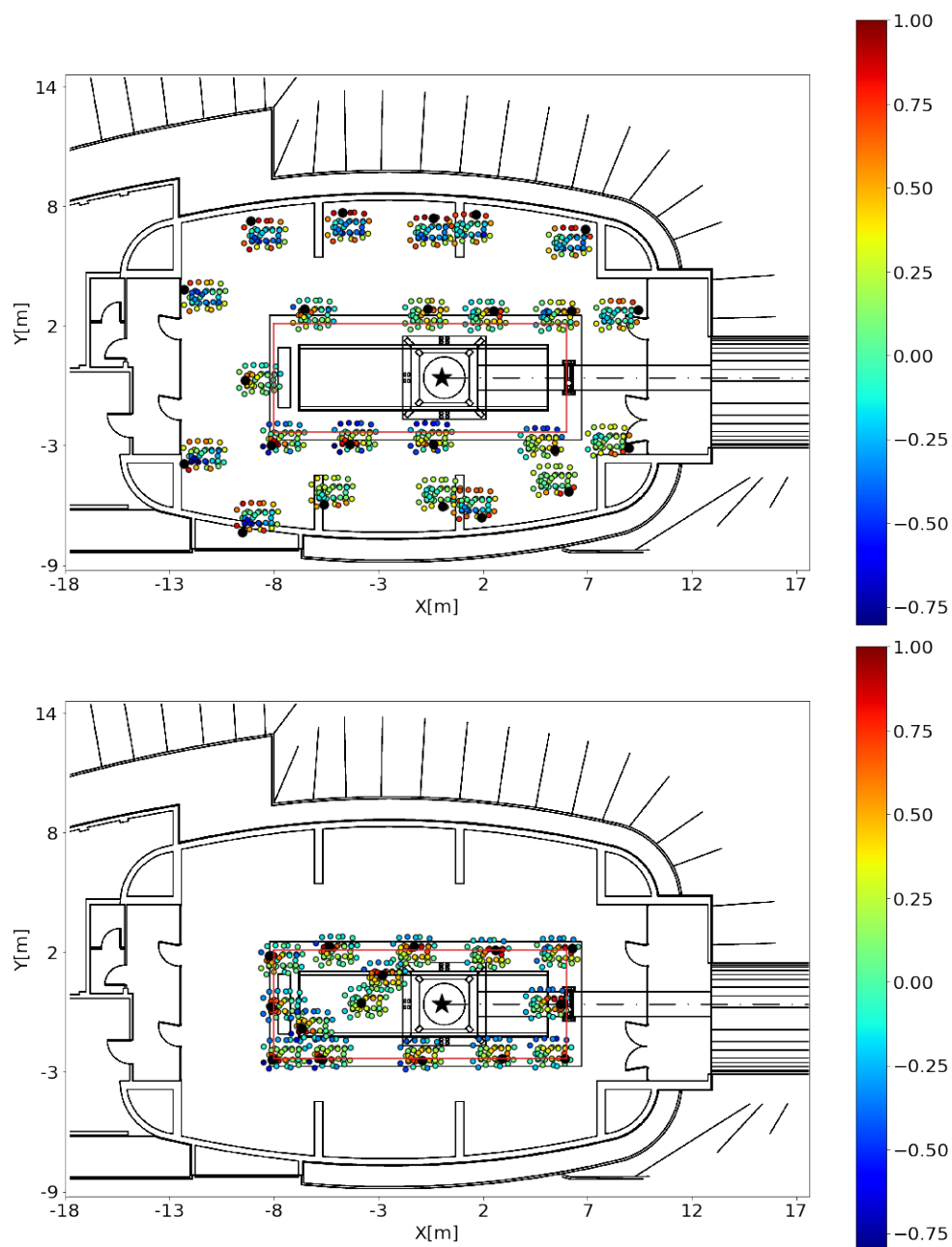


Figure 8.4: Normalized cross-spectral densities (coherence) between all possible pairs of seismometers at 15 Hz. The correlation values are shown in a down-scaled array configuration where the reference seismometer is marked as black dot. *Top*: reference sensors on main building floor. *Bottom*: reference sensors on tower platform.

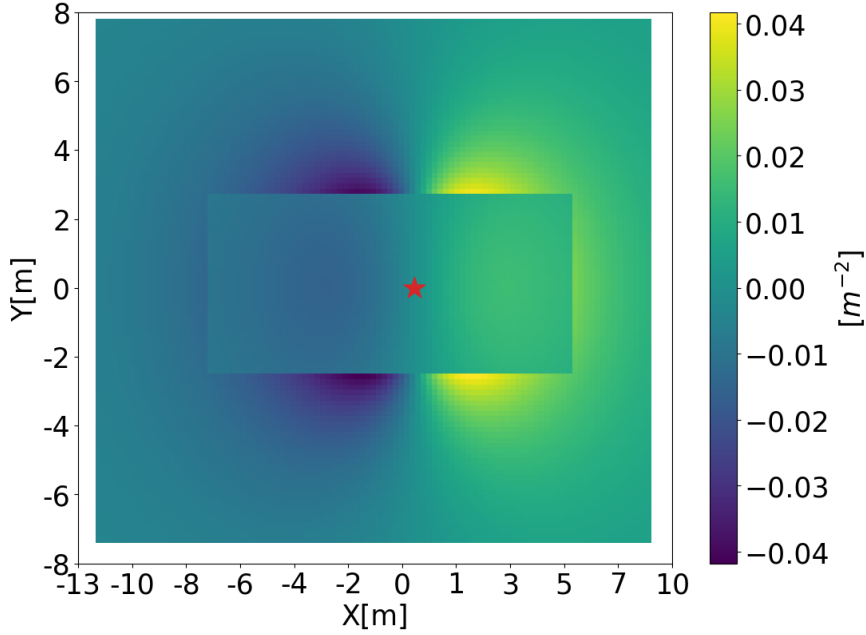


Figure 8.5: Kernel of gravitational coupling between seismic field and NN from Rayleigh waves or surface displacement.

using a rectangular area for our analysis.

The main problem that arises here is that the elements of  $\bar{\mathbf{C}}_{SS}$  are obtained by a function defined in the 4D space:  $C_{SS}(x_i, y_i, x_j, y_j, \omega) : \mathbb{R}^2 \times \mathbb{R}^2$ , where  $x_i, y_i, x_j, y_j$  are the  $x, y$  coordinates of the  $i^{\text{th}}$  and  $j^{\text{th}}$  sensors taken into consideration. The GPR should then in principle infer a 4D function starting from the CPSDs obtained by the 37 sensors' data, i.e.,  $37^2$  total training points. This poses two main challenges: the first is that the GPR regression requires to invert a matrix that is  $37^2 \times 37^2$ , which requires huge computational efforts. The second thing concerns the *curse of the dimensionality* [149]. Indeed, it turns out that we have not enough density of data to infer with sufficient accuracy the values of  $\bar{\mathbf{C}}_{SS}$ . To demonstrate that the density of data points in the 4D space is not good, we can compare it with the density of data points in the 2D space: to make them comparable we need to define a dimensionless density of points. I will define, then, the density of points as follows:

$$\rho_{nD} = \frac{M_{\text{data.points}} * V_n}{V_{\text{tot}}} \quad (8.2)$$

Where  $\rho_{nD}$  represents the dimensionless density of the  $M$  data points that we have in the  $nD$  space.  $V_{\text{tot}}$  represents the minimum (hyper)rectangle containing

## 8. ARRAY SEISMOMETER OPTIMIZATION FOR ADV

---

all the 37 seismometers' coordinates. In the 2D space it will have volume:  $L_1 L_2$ , with  $L_1$  and  $L_2$  the long and the short side, while in the 4D space  $V_{\text{tot}}$  will be:  $(L_1 L_2)^2$ .  $V_n$ , instead, is the volume of hyperspheres of unitary radius centred on the data points and used here to make the densities dimensionless and then comparable:

$$V_n(R) = \frac{\pi^{\frac{n}{2}}}{\Gamma\left(\frac{n}{2} + 1\right)} R^n \quad (8.3)$$

Where  $\Gamma\left(\frac{n}{2} + 1\right)$  is the Gamma function and  $n$  represents the dimensions of the space.

With the actual values of  $L_1 = 16.36 \text{ m}$  and  $L_2 = 22.72 \text{ m}$  we can see that:  $\rho_{2D} = 0.31$  and  $\rho_{4D} = 0.05$ . So, for the GPR it would be better to use a 2D space with 37 data points, rather than a 4D space with  $37^2$  data points. This is the main point of this work: we can infer the 4D  $C_{SS}$  function by simply switching to a lower dimensional space: the 2D space. This is made possible by the Fourier convolution theorem. If we apply the theorem to  $C_{SS}(x_i, y_i, x_j, y_j, \omega)$  we can see that it is enough to have the Fourier amplitudes,  $\tilde{\xi}_i(\omega)$ , defined in every point of the 2D space:

$$C_{SS}(x_i, y_i, x_j, y_j, \omega) = \frac{1}{T} \langle \tilde{\xi}_i(\omega) \tilde{\xi}_j^*(\omega) \rangle, \quad (8.4)$$

where  $\tilde{\xi}_i$ ,  $\tilde{\xi}_j$  are the Fourier amplitudes at the points  $(x_i, y_i)$  and  $(x_j, y_j)$  and  $\langle \cdot \rangle$  represents the ensemble average. This allows us to perform the GPR on the 2D space, where the density of data points is higher and the inversion of the matrix in the GPR is easier (because it is smaller since we have only 37 data points). So, for a fixed frequency  $\omega$  and for any couple of sensor's locations,  $(x_i, y_i)$  and  $(x_j, y_j)$ , we are now able to evaluate  $C_{SS}(x_i, y_i, x_j, y_j, \omega)$  using a surrogate model. In the optimization process this would be enough: we have everything we need since we can already evaluate  $\mathbf{C}_{SS}$  in every possible couple of locations. However, calculating  $\mathbf{C}_{SS}$  using eq. 8.4 for each point explored in the optimization process, becomes too expensive from the computational point of view. So, to avoid this problem, I added a further step before the evaluation of  $C_{SS}$  for the optimization. This consists in evaluating with the preceding method only  $N^4$  elements of  $C_{SS}(x_i, y_i, x_j, y_j, \omega)$  over a *regular* 4D grid and then performing a linear interpolation (it is faster if the points are on a regular grid). During the optimization, the evaluation of  $C_{SS}(x_i, y_i, x_j, y_j, \omega)$  was calculated from the linear interpolation instead that evaluating every time Equation 8.4.

This allows us to have a very precise, but fast, evaluation of  $C_{SS}$  for every possible point in the 4D space. In this specific case, I used a 4D grid of  $N = 30$  points that allowed us to construct a 4D density of points  $\rho_{4D.\text{linear}} = 28.9$ , which is even one order of magnitude bigger than the density we had for the 2D GPR of

the Fourier amplitudes. Thus, introducing this middle step linear interpolation with so many points, we do not spoil the final evaluation of  $C_{SS}(x_i, y_i, x_j, y_j, \omega)$  with respect to the one that we would obtain using Equation 8.4.

This method was the key point which allowed me to perform an optimization of this kind in feasible times (two weeks for the optimization with 15 seismometers) and with much more precision than using the GPR directly on the  $37^2$  data points in the  $4D$  space.

## 8.4 Array optimization

As stated in section 8.3, I used a coarse-grained representation of the seismic correlations obtained by GPR and then performed a regular grid linear interpolation to evaluate  $C_{SS}$  at arbitrary points, as requested by the integration in Equation 6.56 and by the optimization algorithm.

For the evaluation of the 2D integral of  $\mathbf{C}_{SN}$  (Equation 6.56), I used Simpson's method [150]. For what concerns the optimization process, I chose the Particle Swarm Optimization algorithm [99] (see also subsection 5.1.3). Some of the results were also compared with the Differential Evolution algorithm [96] (subsection 5.1.2) to check their consistency.

In Figure 8.6, I present results for optimizations at 10 Hz, 15 Hz, and 20 Hz. Each plot contains optimal arrays with 2, 5, and 10 seismometers. It is interesting to observe that the most efficient placements of seismometers starts around the edge of the tower platform in extension of the arm, and only with 10 seismometers the array starts to occupy space closer to the test mass. This can be explained by the fact that most of the dominant seismic sources in the NN band are located in a part of the building that lies towards negative  $X$  values, beyond the plotted range. This means that the seismic displacement is significantly stronger closer to these sources. This was also shown by Tringali et al. [19]. However, one might still wonder whether placing several sensors close to each other, as seen in these optimal arrays, is an effective strategy for NN cancellation. We will be able to explain why this is the case in the following. However, it should also be pointed out that, as seen in subsection 5.3.3, the Wiener filter averages the self noise of the sensors, so having more sensors close one to another means that the overall SNR is improved also improving the cancellation performances.

Few important features of the obtained optimized arrays need to be considered. We can see that, up to 10, the sensors are all located near the edge of the tower platform. It also seems very unlikely that sensors outside the building will be required for NN cancellation, which was an important open question for the design of the NN cancellation system at Virgo. The solutions also indicate that

## 8. ARRAY SEISMOMETER OPTIMIZATION FOR ADV

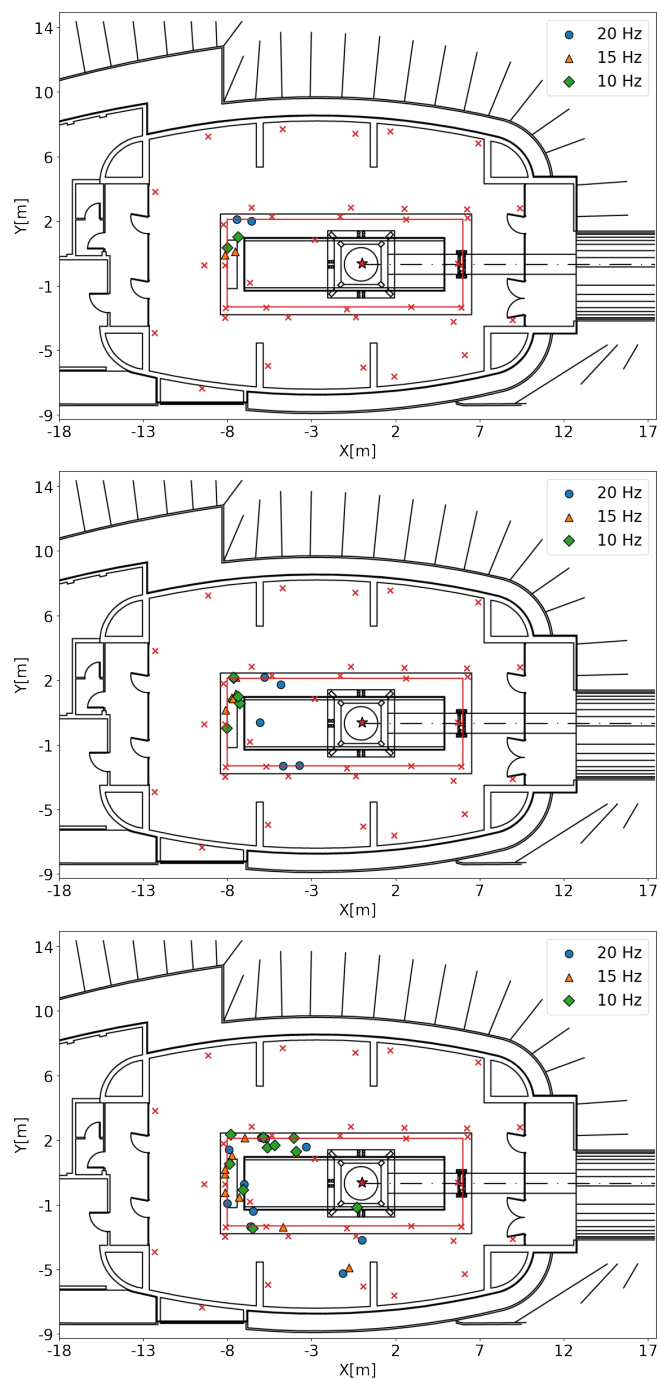


Figure 8.6: Sample of optimal arrays with 2 (*top*), 5 (*center*), 10 (*bottom*) seismometers at 10, 15 and 20 Hz

## 8. ARRAY SEISMOMETER OPTIMIZATION FOR ADV

---

deployment of sensors on the basement floor might be advantageous. It should be noted, though, that only two seismometers used to take data were deployed on the basement floor (most seismometers within the red rectangle, which marks the edge of the tower platform, were deployed at surface level, on the ceiling of the basement), which means that the basement contribution to the integral in Equation 6.56 might be biased towards greater values (because the PSD is, on average, stronger on the ceiling).

One important observation about all the 100 optimizations that I run is that, with many more than 5 sensors, I never found two equal optimal configurations (albeit they were very similar). This indicates that I might not have found the global minimum of the residual noise, but just many local minima. This is not a problem for the design of the NN cancellation system because the performances of the Wiener filter were practically the same. This is also consistent with the result found by Choromanska et al [151], which states that in large neural networks most local minima are equivalent and lead to similar performances on a test set. Comparing with our method, this is of course to be taken with a grain of salt, since they demonstrated it for a multilayered neural network, which is something very different from what we have, but it could be a symptom of the high-dimensional optimization problems.

At first sight, the optimization results seem inconsistent with the estimated correlation  $C_{SN}$  of Equation 6.56 shown in Figure 8.7. For example, the 10 Hz plot in Figure 8.7 shows that there is strong correlation between NN and ground motion near the edge of the tower platform towards positive  $X$ . Why then do optimal arrays never include sensors located there? The answer is that the seismic displacements at the two ends of the tower platform are partially correlated, which can be verified by close inspection of the two plots in Figure 8.4 for 15 Hz. This means that placing a seismometer at one end, it is possible to cancel NN originating from seismic displacements at both ends. The negative  $X$  side of the tower platform is then favored, because the part of the seismic field uncorrelated between the two ends is stronger there. This is true at 10 Hz and 15 Hz. In contrast, only one end of the tower platform shows significant correlation with NN at 20 Hz. The most likely explanation for this is, as reported in [19], that seismic waves originating from the machine rooms beyond  $X = -13$  m are reflected from the tower platform and never make it (with significant amplitude) to the other side of the tower platform. The key here, is that the waves at 20 Hz are sufficiently short to be strongly affected by the tower platform.

Finally, in Figure 8.8, I show the Wiener-filter performances. There, I plotted the estimation of the PSD of the NN ( $\hat{C}_{NN}$ ) that we can obtain with the

## 8. ARRAY SEISMOMETER OPTIMIZATION FOR ADV

---

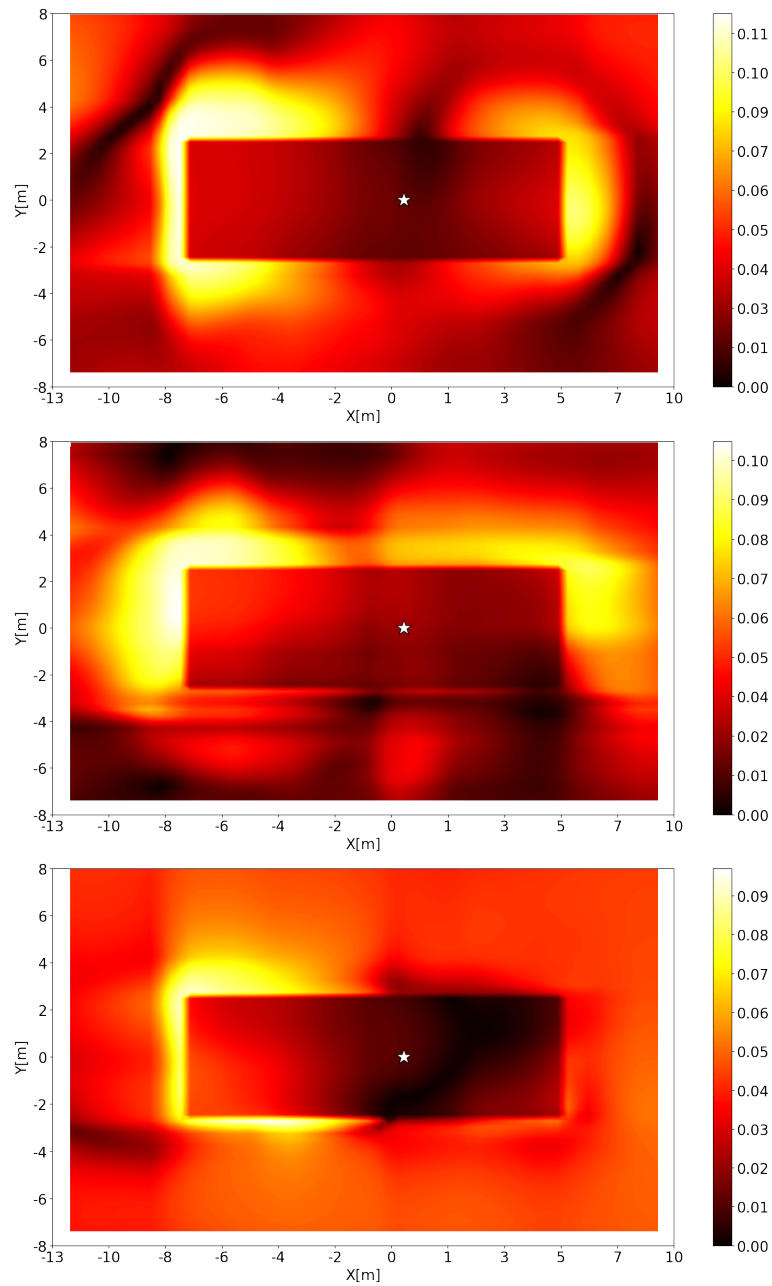


Figure 8.7: Fraction of NN cancelled ( $1 - R$ ) by deploying a single seismometer as a function of seismometer position. *top*: 10 Hz, *center*: 15 Hz and *bottom*: 20 Hz.

optimized array as a function of the number of seismometers and at different frequencies.  $\hat{C}_{\text{NN}}$  was then normalized by an estimate of the NN at infinite to show



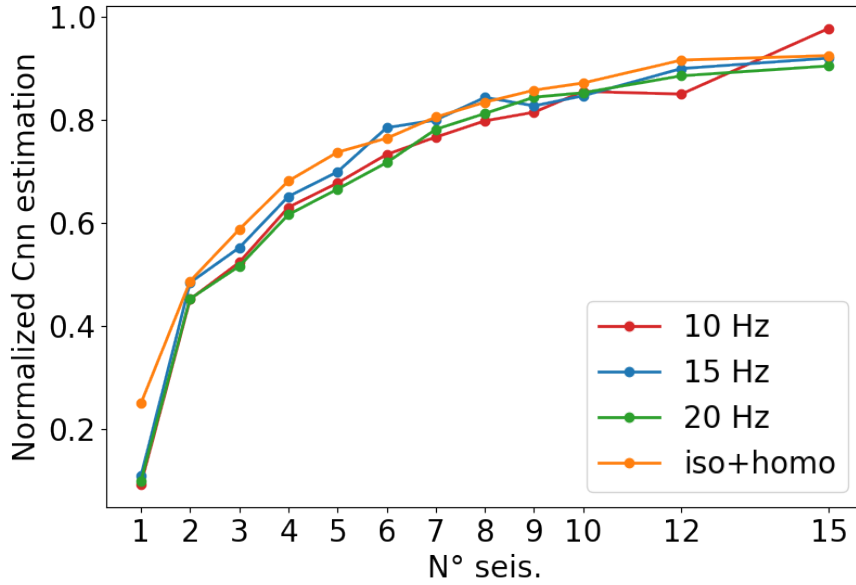


Figure 8.8: Wiener-filter performance (1 being the maximum) as a function of number of seismometers in optimized arrays. For comparison, a theoretical performance curve is shown for the isotropic, homogeneous Rayleigh field.

the relative cancellation performance. To obtain the NN estimate at infinite for a given frequency, I performed a fit over the values of  $\hat{C}_{NN}$  and then took the limit for an infinite number of sensors:  $N \rightarrow \infty$ . The fit was calculated for the function:

$$c(N) = a \left( 1 - \frac{1}{bN} \right) \quad (8.5)$$

The parameter  $a$  is the NN estimate that we are searching for. It is first of all surprising that all the curves follow this model. This was indeed expected to hold only for sensor-noise limited performances and to depend on properties of the seismic field [17]. Seismic correlations at 10 Hz, 15 Hz, and 20 Hz are qualitatively different at the WEB, and certainly different from the correlations in an isotropic, homogeneous Rayleigh-wave field (which for comparison was also plotted in Figure 8.8). This means that if Wiener-filter performances depend on properties of the seismic field, then the curves should look differently. This points to a yet-to-be understood universality of Wiener-filter performances in Rayleigh-wave fields, but, certainly, comparisons with array measurements at other sites are necessary to verify that universality holds in all cases.

The value taken by  $a$  in the fitting function also provides a NN estimate that takes into account the observed seismic correlations, as well as the presence of the basement. These values are listed in Table 8.1 and compared with a theoretical

## 8. ARRAY SEISMOMETER OPTIMIZATION FOR ADV

---

model of NN in units of strain from a single test mass assuming a flat surface and isotropic, homogeneous Rayleigh field [52]

$$C_{\text{NN}}^{\text{iso}}(\omega) = \left( \frac{1}{L\omega^2} \right)^2 (2\pi G\rho_0 e^{-h\omega/c}\gamma)^2 \frac{1}{2} S(\xi_z; \omega), \quad (8.6)$$

where  $G$  is the gravitational constant,  $\rho = 2500 \text{ kg/m}^3$  is the density of a homogeneous medium,  $\gamma = 0.8$  accounts for the suppression of NN due to sub-surface (de)compression of soil by Rayleigh waves,  $c = 300 \text{ m/s}$  is the speed of Rayleigh waves, and  $S(\xi_z; \omega)$  is the PSD of the vertical surface displacement. For the value of the test mass height above the ground I used  $h = 1.5 \text{ m}$ , which would be its height if the surface at WEB was flat, i.e., without basement. Here, the best guesses of parameter values were used, since we do not have precise knowledge of average density of the ground, speed of Rayleigh waves at WEB, and the Rayleigh-NN reduction  $\gamma$ , which also depends on ground properties. While there

Frequency	$\sqrt{C_{\text{NN}}^{\text{iso}}}$	$\sqrt{a}$
10 Hz	$1.33 \cdot 10^{-23} \text{ 1}/\sqrt{\text{Hz}}$	$4.04 \cdot 10^{-23} \text{ 1}/\sqrt{\text{Hz}}$
15 Hz	$7.21 \cdot 10^{-24} \text{ 1}/\sqrt{\text{Hz}}$	$1.04 \cdot 10^{-23} \text{ 1}/\sqrt{\text{Hz}}$
20 Hz	$4.34 \cdot 10^{-24} \text{ 1}/\sqrt{\text{Hz}}$	$4.44 \cdot 10^{-24} \text{ 1}/\sqrt{\text{Hz}}$

Table 8.1: Comparison between a theoretical model of an isotropic, homogeneous seismic field and the square root of the estimated NN PSD ( $a$ ) in Equation 8.5.

is a significant mismatch between our predictions and the ones obtained from a simple theoretical model, the estimated NN values  $\sqrt{a}$  are in accordance with results from a finite-element simulation of an isotropic Rayleigh-wave field when including the basement (see top, right plot in figure 4 of [137]).

Now, with the NN estimate  $C_{\text{NN}} = a$ , we can evaluate the relative residual in Equation 8.1. The results are summarized in Table 8.2. Accordingly, we can predict that up to a factor 10-50 reduction of NN can be achieved with an optimized array of 15 seismometers. However, one needs to keep in mind that these reductions are achieved by optimizing the array configuration at the respective frequencies. The last column shows that if we assume the same array of 15 seismometers (optimized at 15 Hz) for the cancellation at 10 Hz and 20 Hz, then NN is reduced only by about a factor 2-3. This might still be sufficient for AdV+, but it is clear that we need to refine the technique if we target a factor 10 reduction throughout the entire NN band. A broadband optimization is then required.

## 8. ARRAY SEISMOMETER OPTIMIZATION FOR ADV

	$\sqrt{\vec{C}_{\text{SN}}^\dagger(\omega) \cdot (\mathbf{C}_{\text{SS}}(\omega))^{-1} \cdot \vec{C}_{\text{SN}}(\omega)}$	Relative residual	Relative residual; 15 Hz optimized
10 Hz	$3.95 \cdot 10^{-23} \text{ } 1/\sqrt{\text{Hz}}$	0.02	0.39
15 Hz	$9.60 \cdot 10^{-24} \text{ } 1/\sqrt{\text{Hz}}$	0.08	0.08
20 Hz	$4.01 \cdot 10^{-24} \text{ } 1/\sqrt{\text{Hz}}$	0.09	0.47

Table 8.2: The second column corresponds to the PSD of the Wiener-filter output with 15 seismometers. The third column shows the corresponding relative residuals  $R$ . The fourth column shows the relative residual achieved with an array optimized at 15 Hz.

This is done by combining the single-frequency cost function of Equation 8.1 at different frequencies  $\omega_i$ . In Chapter 7, I found that a good cost function  $\mathcal{L}$  is given by Equation 7.5. I performed such an optimization using three frequencies:  $\omega_i = 10, 15, 20$  Hz. In Figure 8.10, the values of the residual obtained with the broadband optimization and calculated at those three frequencies are compared with the single-frequency optimization. Here, we first notice that, looking at a specific frequency, the broadband optimization performs worse compared to the single-frequency optimization (around 80% of the reduction factor that we get with the single-frequency optimization is achieved). We also see that the broadband optimization gives best cancellation performances at 15 Hz, while the 10 Hz NN reduction is significantly less than at the other two frequencies. It is not surprising that one frequency has a significantly higher residual than the others in the broadband optimization. Indeed, minimizing the broadband cost function means to find a trade-off configuration that reconciles the requirements of the optimal array needed at each of the three considered frequencies. The result in Figure 8.10 means that the broadband configuration is at a local minimum for  $R(\omega)$  at 10 Hz: this was the largest residual between the three and the optimization tried to push down its value, without caring about the other two since they were lower. Given that  $\mathcal{L}$  is defined in such a way that it does not constrain the residuals at 15 Hz and 20 Hz, these residuals should not be expected to be at their local minimum. Figure 8.9 shows the array configurations for 3, 5 and 10 seismometers obtained with the broadband optimization.

We do not have a theoretical model for the broadband-minimized residuals (like Equation 5.30), thus, it is difficult to extrapolate the results to higher number of sensors. Using polynomial and exponential fits, I can obtain residuals of  $R = 0.1$  and less with at least 20 seismometers, which means a bit more than a factor 3

reduction of NN amplitude. Of course, from Table 8.2 we know that no more than  $3 \times 15$  seismometers are required to achieve  $R < 0.1$  at all three frequencies.

## 8.5 Conclusion

I have developed a surrogate Wiener filter to make the best use of seismic correlation measurements at the Virgo detector for the estimation of Newtonian noise and to calculate optimal array configurations for Newtonian-noise cancellation. The approach was to use Gaussian Process Regression in combination with simple interpolation techniques. The technique is an important milestone for the design of Newtonian-noise cancellation systems of current and future GW detectors, where array configurations are to be chosen using available information of the seismic field from previous site-characterization measurements.

The method requires correlations between ground motion and GW data. This correlations are provided by a model based on purely gravitational coupling determined by the field of seismic correlations. This model is accurate for arbitrarily complex surface displacements, but it does not consider contributions of sub-surface compression of the ground medium by body waves. As soon as Newtonian noise will be observed (or any other linear ground-to-test-mass coupling [131, 108]), the coupling model in Equation 6.56 can be substituted by correlation measurements between seismometers and GW data, which makes the optimized array configuration fully model independent.

I found that there is a universal dependence of the noise residuals on the number of seismometers used for Newtonian-noise cancellation, i.e., weakly dependent on the properties of the seismic field. Its origin should be investigated since it could be used to greatly simplify the prediction of Wiener-filter performance with optimized arrays in future detectors.

I calculated arrays with up to 15 seismometers optimized for Newtonian-noise reduction at a single frequency, which yielded a reduction by a factor 3-7 in noise amplitude depending on frequency. A broadband optimization with up to 6 seismometers showed that reduction by almost a factor 2 can be achieved in amplitude. Here, extrapolation to larger numbers of sensors would not give reliable estimates since we do not have a model of the broadband residuals as a function of the number of sensors, and extrapolation depends strongly on the chosen fitting function. The results obtained with this work were used to deploy the seismic array that will be used for the NN cancellation subsystem in O4:

## 8. ARRAY SEISMOMETER OPTIMIZATION FOR ADV

---

30 sensors were deployed in the WEB, other 30 in the NEB and, finally, 60 will be installed in the CEB. In Figure 8.11 we can see the positions of the sensors deployed in the WEB. Since the optimized array covered only specific frequencies and its cancellation performances degrade for other frequencies values, the arrays were placed following only the main results:

- On the left side the noise is stronger and the covered area needs to be larger (Figure 8.7) and with more sensors.
- The space around the edges of the platform is very important and need to be covered by many sensors.
- No sensors were placed in the basement since optimization results only weakly indicated the necessity of basement sensors. In comparison, the seismometers at the surface level were showing stronger contributions with respect to the basement ones.

Finally, this optimization method can be applied to all current and future gravitational-wave detectors located at the surface. Moreover, it can be extended to the case of an underground detector. In this case, it would be enough to change the step regarding the 2D Gaussian process regression into a 3D Gaussian process regression (in an underground detector we should place seismometers all around the test masses). In the underground detector case,  $C_{SS}$  would depend on 6 coordinates instead of 4. These modifications would lead to a much bigger computational effort. At the same time, it might also be more challenging to provide enough underground seismic data for the inference of  $C_{SS}$ , but this strongly depends on the properties of body-wave fields, of which little is known. One way to mitigate the scarcity of underground data would be to perform a fully Bayesian GPR combined with numerical simulations of the seismic field [143].

As a final remark, I would like to bring the attention on Equation 6.57: in principle, one might think that this equation is enough general to allow to properly estimate the NN at the test mass. So we could think of observing data for a very long time, evaluating Equation 6.57 and then taking the inverse discrete Fourier transform to obtain the time series that will be subtracted from the data stream. This could work in principle, but in reality we need to consider various things: firstly Equation 6.57 is valid for a general Rayleigh wave field propagating in a flat half space. So, any deviation from flatness would spoil the NN estimate (this is true as well for Equation 6.57 used in the residual evaluation). Moreover, to perform a precise integration, we need to scan very well the seismic field and have a very precise value of the test mass heigh. All of this, summed with the fact that such an integral could lead to numerical errors, makes this way

## 8. ARRAY SEISMOMETER OPTIMIZATION FOR ADV

---

too complicated with respect to implement a Wiener filter in the way explained so far.

## 8. ARRAY SEISMOMETER OPTIMIZATION FOR ADV

---

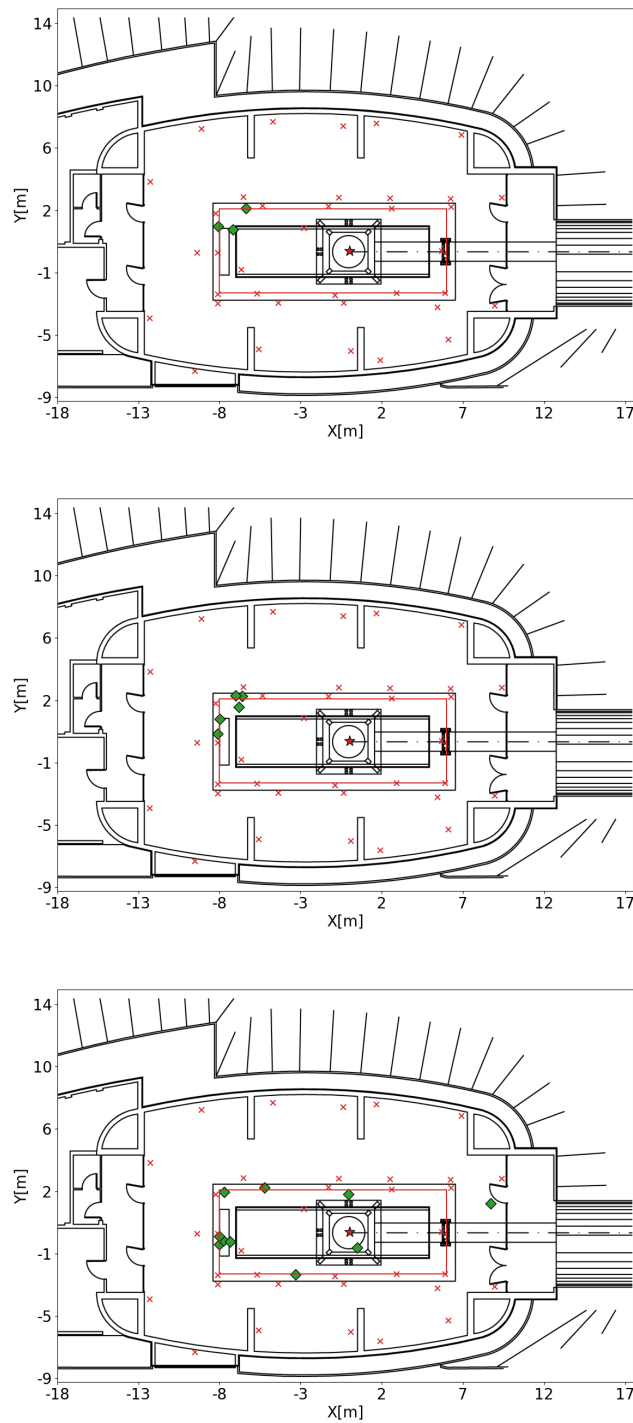


Figure 8.9: Array configurations for 3,5 and 10 seismometers obtained with the broadband optimization.

## 8. ARRAY SEISMOMETER OPTIMIZATION FOR ADV

---

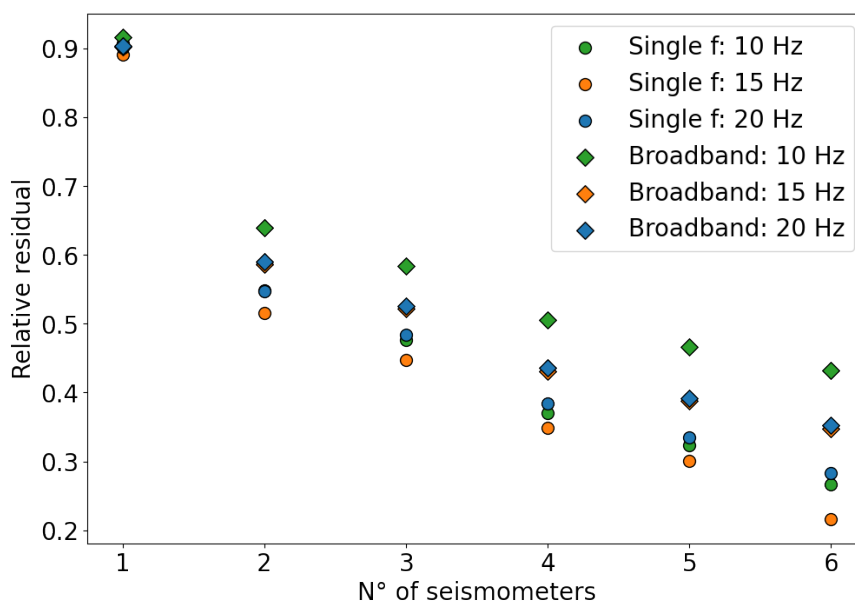


Figure 8.10: Relative residual  $R$  obtained from the broadband optimization (diamond) compared with the one obtained from the single-frequency optimization (circle).

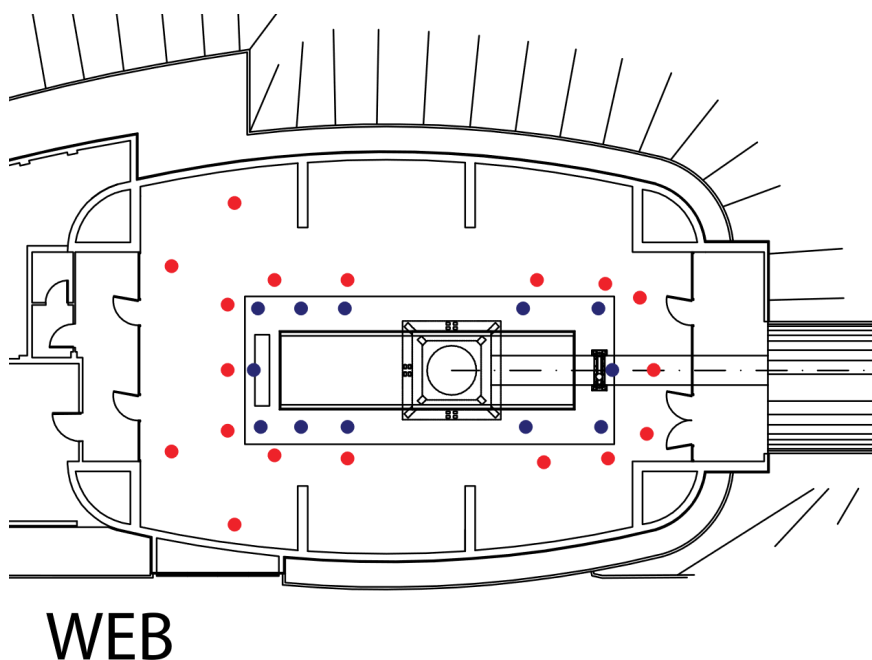


Figure 8.11: Sensors installed in the WEB in sight of the NN cancellation system for O4.



# SEISMIC AND NEWTONIAN NOISE ESTIMATES AT KAGRA

## Contents

---

9.1	KAGRA mine as a probe for 3rd generation underground detectors	138
9.2	Instrumentation and measurements	138
9.3	Underground seismic noise	140
9.4	Seismic array processing	141
	<i>9.4.1 Introduction to the method</i>	141
	<i>9.4.2 Velocity estimation in KAGRA</i>	145
9.5	NN estimate in KAGRA	149

---

## 9.1 KAGRA mine as a probe for 3rd generation underground detectors

KAGRA is an L-shaped gravitational-wave detector, just like Virgo and LIGO are, but there are two main differences with respect to them. Firstly, KAGRA is constructed underground, in order to reduce the seismic noise (it is in the Ikenoyama mountain, close to Kamioka mine, where also the super-Kamiokande and kamLAND neutrino detectors are hosted). Secondly, its test masses are made of sapphire and are designed to work at cryogenic temperatures ( $\sim 20K$ ) to reduce the thermal noise [3].

Third generation gravitational-wave detectors could as well be constructed underground to reduce the seismic noise and its consequent Newtonian noise. These detectors (like for example ET, see sec. section 4.2) will be very complicated instruments that will need many components, including vacuum pumps, water pumps, cryotrap, cryostats, ventilation systems and so on. This infrastructure might produce a lot of seismic and acoustic noise, which could make it pointless going underground. It is then important to look at the already existing KAGRA detector, which is already built underground: this will allow us to assess the importance of these noises.

With this purpose, some measurements of the seismic field were performed at KAGRA in order to assess the impact of the infrastructure and to estimate the NN in an underground detector.

## 9.2 Instrumentation and measurements

We used one compact Trillium seismometer 20s to acquire seismic data of the corner station of KAGRA (where the BS and the input test masses are hosted) and inside the arms  $X$  and  $Y$ . The reason for that was to check how the seismic noise produced in the corner station would propagate along the arms to the end test masses. Measuring the spectra was not the only goal: we initially wanted to measure also the seismic correlations between the Trillium and another seismometer already installed in the mine. For that reason, it was important to synchronize the Trillium with the other seismometer. Unfortunately, the synchronization by means of a GPS was not feasible being that we were hundreds of meters underground. KAGRA, on the other hand, can synchronize all the equipment by means of a GPS located outside the mine and connected via long cables to all the instrumentation. Of course, the time delay caused by the cables is compensated in such a way that everything is well synchronized with a negligible delay [152]. We took data with the movable seismometer in the corner



Figure 9.1: Two Trillium compact seismometers. One was connected to KAGRA’s acquisition system, while for the other one this was not possible, so it was just deployed close to the first one in order to synchronize them.

station and along the two arms of the interferometer, see Figure 9.2 for details. Since we could not synchronize our Trillium with KAGRA seismometer by means of a GPS, we chose to use the KAGRA seismometer as a reference clock. The reference seismometer was located close to the input test mass, in the  $X$  arm (IXC). Data were taken during 6 days for about 24 h in each position. The sample rate was 250 Hz.

The method used to synchronize the mobile seismometer with the one installed in the mine was simple in principle: beating strong hits in proximity of the two seismometers placed close to each other. In this way it was possible to extract the time shift between the internal clock of the mobile seismometer with respect to the GPS time of the installed seismometer. With the assumption that the time shift was changing linearly, the measure was only performed three times, one at the beginning and twice at the end of the the 6 days data acquisition (we did it twice at the end because there were some problems with the reference seismometer).

The reason for having synchronized seismometer was to use their data to extract some information about the apparent velocity of the seismic waves. However, we concluded that, if one aims to perform this kind of measure, this synchronization method is not good.

Indeed, to measure seismic wave speeds it is necessary to measure the difference in the time travel between two seismometers (this is only a rough method though, since it would be more appropriate using an array of seismometers [153, 154, 155]), so we need a very precise synchronization between them. Let assume that the seismic wave speed we are trying to measure is of the order of  $10^3$  m/s

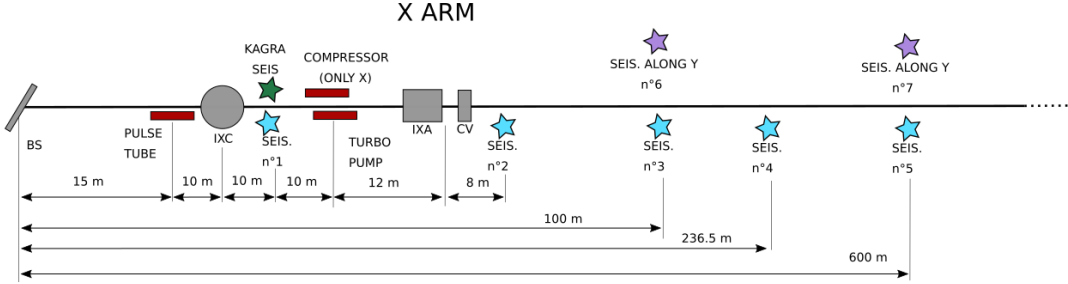


Figure 9.2: Positions where we measured the seismic noise by moving the Trillium day by day and a representation of the  $X$  arm with the noise sources (red rectangles). *Green star*: KAGRA seismometer used as reference clock. *Light blue stars*: positions relative to the  $x$  arm. *Lilac stars*: positions relative to the  $Y$  arm.

(this is a very conservative assumption) and that the two seismometers are separated by 500 m. In this case, the travel time difference will be of the order of:  $\Delta\tau = 0.5$  s (or less, depending on the incidence angle of the seismic wave). This means that, if the clock drift is not perfectly linear as we assumed, then any deviation from linearity must be  $\ll 0.5$  s, which was not the case with our sensors. Indeed, thanks to the third measurement of the time shift, we measured fluctuations of about 0.9 s. This means that it is not possible to extract any useful information about seismic speed using that couple of seismometers.

We used the data collected with the Trillium to estimate the NN and the seismic noise induced by the infrastructure. For estimating the velocities we instead asked for seismic data from the already installed seismometers at KAGRA: one in the cave hosting the BS and the other two in the caves of the ending test masses. In this way, it has been possible to extract speed information and directions of the seismic field (although a seismic array of only 3 seismometers can provide very low quality information). As a final step, we also used some data from the F-net seismograph network, in Japan, in order to estimate the NN impact of the surface Rayleigh waves. Indeed, at low frequencies, they propagate underground with a damping factor of  $e^{-hk}$  (where  $h$  is the depth and  $k$  is the horizontal seismic wave vector).

### 9.3 Underground seismic noise

We firstly investigated the seismic noise in the mine moving the Trillium from the corner station, where many noisy instruments are collocated, along the  $X$

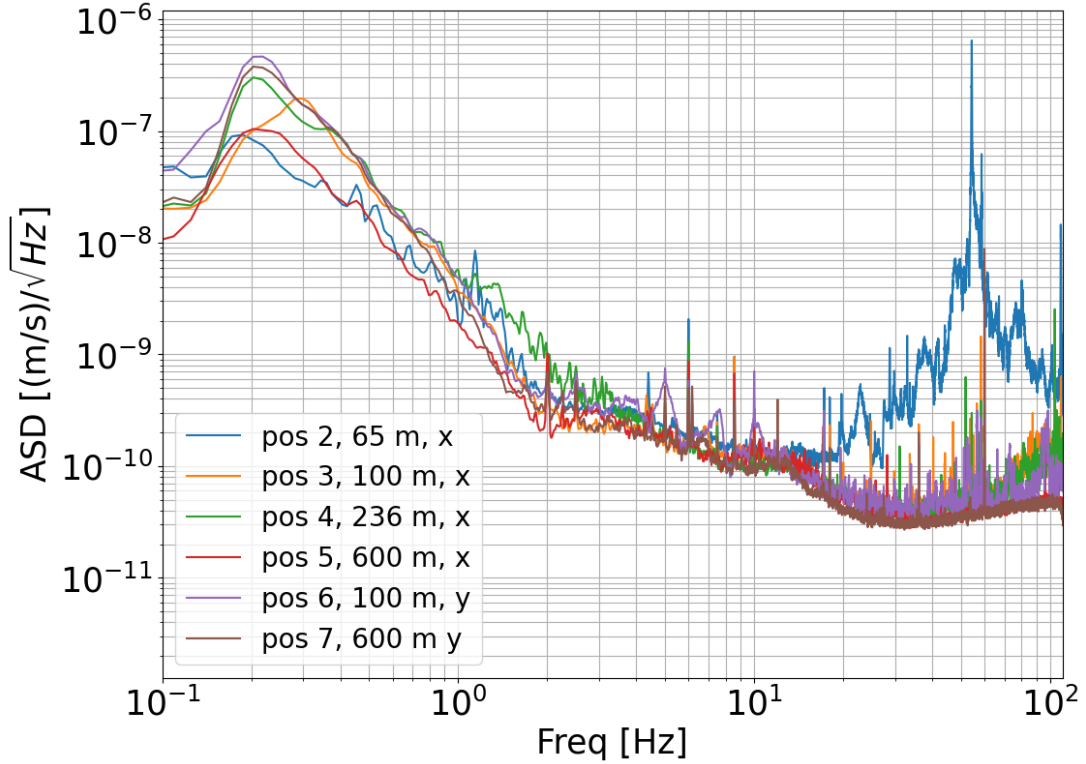


Figure 9.3: ASD of the seismic noise as measured along the interferometer arm (see Figure 9.2 for position references). Distances are taken from the BS.

and Y arm. These measurements are useful to understand the impact of the infrastructure on the seismic noise and how it can propagate. In particular, the data taken in the position number 2 (Figure 9.2) are interesting from this point of view. Indeed, as we can see in Figure 9.3, the infrastructure noise starts to be important only above 10 Hz, where the suspensions system starts to suppress the seismic noise [156]. This means that the underground detector infrastructure do not pose a limitation to the seismic noise, nor to the NN.

In Figure 9.4 spectrograms of the seismic noise relative to all the positions in which we placed the Trillium are shown.

## 9.4 Seismic array processing

### 9.4.1 Introduction to the method

The simplest way to measure the velocity of a seismic wave would be that of measuring its propagation time along its direction of arrival (DOA). We generally

## 9. SEISMIC AND NEWTONIAN NOISE ESTIMATES AT KAGRA

---

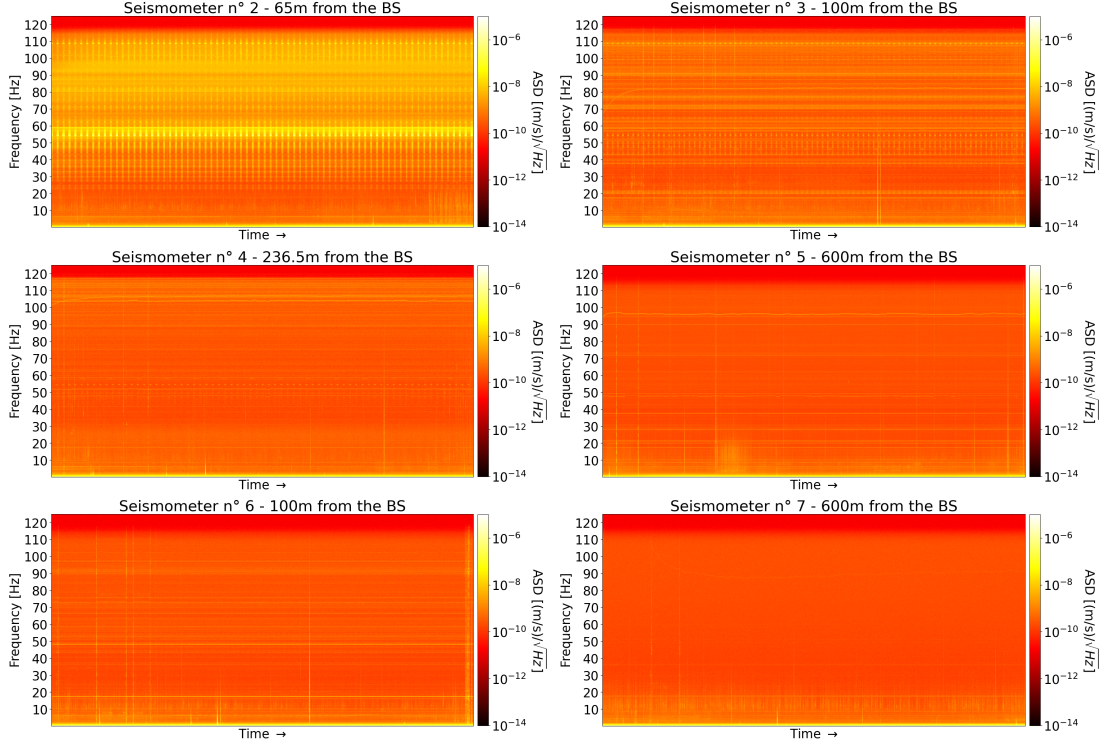


Figure 9.4: Spectrograms relative to the different locations at which the Trillium was set (see Figure 9.2).

do not know the DOA, but we can exploit the information gathered by multiple sensors in order to infer both the DOA and the velocity of the wave. In this case we would use an array of seismometers.

Let us assume that we have an array of  $M$  sensors and an incoming signal:

$$E(t, \mathbf{r}) = A(t - r/c)e^{j(\omega t - \mathbf{k} \cdot \mathbf{r})} \quad (9.1)$$

where  $r$  is the distance between the source and a sensor,  $\mathbf{k}$  is the wave vector and  $c$  is the phase velocity:  $k = \omega/c$ . We consider valid the so-called narrowband assumption for which it holds:  $A(t - r_m/c) = A(t - r/c)$ , where  $r_m$  is the distance of the  $m^{\text{th}}$  sensor from the source and  $r$  is the distance of the origin of the array from the source (it can be placed on one particular sensor). This means that  $A(t)$  does not vary too much compared to the carrier  $e^{j\omega t}$  and that its frequency content will be at very low frequency, so the signal  $E(t, \mathbf{r})$  will have a spectrum peaked on  $\omega$  with a very narrow frequency band. This assumption is important since it allows us to assume that the signal recorded at each seismometer will be:  $x_m(t) = s(t)e^{-j\mathbf{k} \cdot \mathbf{r}_m}$ , with:  $s(t) = A(t - r/c)e^{j\omega t}$  being the signal recorded in the origin; in this way each seismometer output will differ from the origin only by a

## 9. SEISMIC AND NEWTONIAN NOISE ESTIMATES AT KAGRA

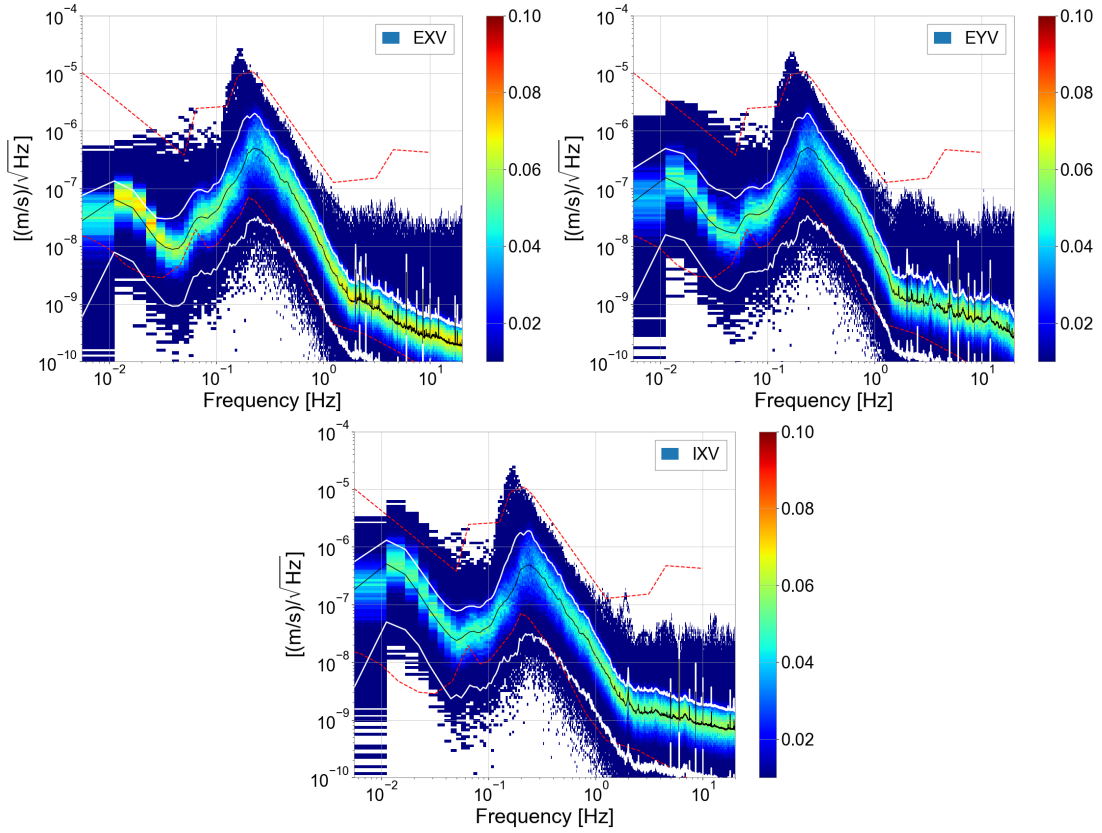


Figure 9.5: Above each test mass in KAGRA, at 13 m of height, there are additional caves which host the upper part of the suspension systems and where the seismometers we used are also hosted. We show here their ASD variations (over a year of quiet times) together with the NHNM and the NLNM (red dashed lines) [116] and the 10<sup>th</sup>, 90<sup>th</sup> (white lines) and 50<sup>th</sup> (black line) quantiles. We used these three seismometers as an array to measure seismic velocities. *Upper left*: Seismometer in the X end mass upper cave, *Upper right*: Seismometer in the Y end mass upper cave, *Bottom*: Seismometer in the X input mass upper cave.

phase shift.

For some applications the narrowband assumption is not suitable: for example, when we want to extract speed information using the ambient seismic noise (as far as we work in the time domain). This can be overcome by taking the Fourier transform of Equation 9.1 (after demodulation, i.e. after removing the carrier), in this way the output at each seismometer would still be affected only by a phase shift:  $X_m(\omega) = S(\omega)e^{-\mathbf{k}\cdot\mathbf{r}_m}$ . We can define the array output as:

$\mathbf{X}(\omega) = [X_1(\omega), X_2(\omega), \dots, X_M(\omega)]$ , that would read:

$$\mathbf{X}(\omega) = \mathbf{a}(\mathbf{k})S(\omega) + \mathbf{n}(\omega) \quad (9.2)$$

Where  $\mathbf{a}(\mathbf{k}) = [e^{\mathbf{k}\cdot\mathbf{r}_1}, e^{\mathbf{k}\cdot\mathbf{r}_2}, \dots, e^{\mathbf{k}\cdot\mathbf{r}_M}]$  is called steering vector (or array response vector) and  $\mathbf{n}(\omega)$  was introduced to account for some injected sensor noise.

The problem of finding the velocity of the incoming seismic wave can be solved by exploiting the array output to find the  $\mathbf{k}$  of the seismic wave. The easiest way to do that is to "steer" the array to find for which  $\mathbf{k}$  the power of its output will be maximised. With this purpose, we can use a linear combination of the outputs of each sensor:

$$Y(\omega) = \sum_{m=1}^M W_m X_m(\omega) = \mathbf{W} \cdot \mathbf{X}_m \quad (9.3)$$

If we search for the values of  $W_m$  that maximise the power of  $Y(\omega)$  we are constructing a spatial filter that "steers" the array until the maximum power is reached. This operation means that the  $W_m$  weights bring again the  $m^{th}$  output in phase with all the others, and so the weights  $W_m$  are those that carry the information about the  $\mathbf{k}$  of the signal.

This technique is called beamforming and different beamformings correspond to different ways of weighting the outputs. The conventional one, the Bartlett beamforming, is obtained by maximizing the power of Equation 9.3. If we search for the  $W_m$  which maximize Equation 9.3 we obtain that the power of  $Y(\omega)$  can be written as a function of  $\mathbf{k}$ :

$$P_Y(\mathbf{k}) = \frac{\mathbf{a}^H(\mathbf{k})\hat{\mathbf{R}}\mathbf{a}(\mathbf{k})}{\mathbf{a}^H(\mathbf{k})\mathbf{a}(\mathbf{k})} \quad (9.4)$$

Where  $\hat{\mathbf{R}}$  is the  $(M \times M)$  matrix of the cross correlations between the sensors. At this point, if we want to find the  $\mathbf{k}$  of the incoming seismic wave, it will be enough to run an optimization and find for which  $\mathbf{k}$  Equation 9.4 will be maximized, that  $\mathbf{k}$  will correspond to the signal's one [157].

We should consider the fact that measuring a signal with an array of sensors means sampling the signal in the space. As it happens when sampling in the time domain, we can measure signals without falling into aliasing up to frequencies lower than  $\pi/\Delta$ , where  $\Delta$  is the maximum distance between the sensors. The larger  $\Delta$  will be, the better will be the resolution of the array, that is, the ability of distinguish between different  $\mathbf{k}$ . Aliasing is not the only way where ambiguities can arise: the less the sensors in the array, the more the  $\mathbf{k}$  compatible with the observed signal (see Figure 9.6). The best thing would then be constructing an array with large  $\Delta$  and many sensors.



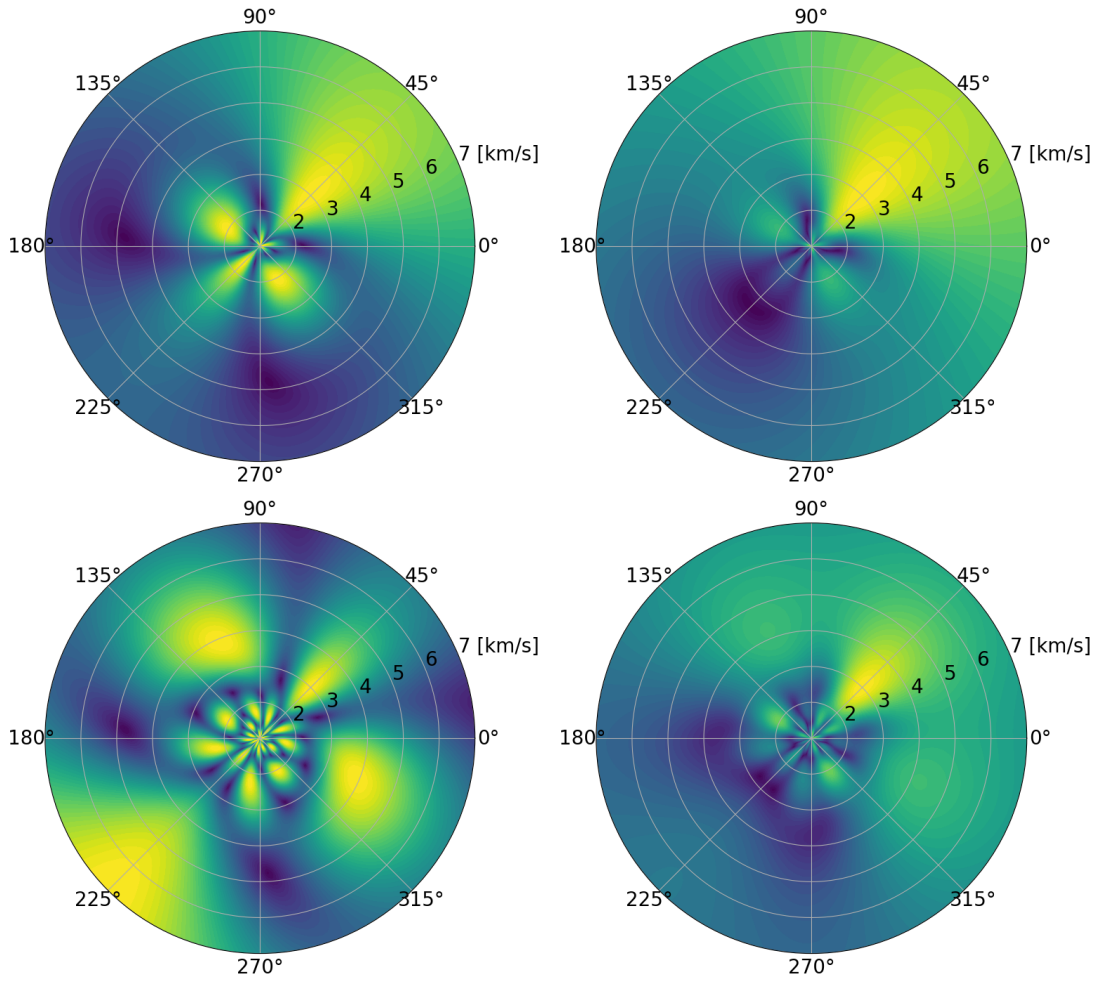


Figure 9.6: Array response  $|\mathbf{a}^H(\mathbf{k}_0)\mathbf{a}(\mathbf{k})|$  of different arrays relative to a monochromatic wave with wave vector  $\mathbf{k}_0$  at 0.5 Hz from a DOA of  $\pi/4$  and  $v = 3$  km/s. *Upper left*: array with 3 seismometers located in  $(0,0)$ ;  $(0,L)$ ;  $(L,0)$ . *Upper right*: array with 5 seismometers located in  $(0,0)$ ;  $(0,L)$ ;  $(L,0)$ ;  $(0,L/2)$ ;  $(L/2,0)$ . *Bottom left*: array with 3 seismometers located in  $(0,0)$ ;  $(0,2L)$ ;  $(2L,0)$ . *Bottom right*: array with 7 seismometers located in  $(0,0)$ ;  $(0,L/2)$ ;  $(L/2,0)$ ;  $(0,L)$ ;  $(L,0)$ ;  $(0,2L)$ ;  $(2L,0)$ . With  $L = 3$  km.

### 9.4.2 Velocity estimation in KAGRA

In this section it will be explained how the velocities of the seismic waves were estimated using a small array composed by only three sensors.

We used data collected during 100 quiet periods sampled along one entire year and lasting one hour each. The data were taken with three seismometers placed

one in the corner station (which will be taken as the origin of the array) and two at the end of the interferometer arms. The arm length is  $L = 3$  km and this gives us a very poor resolution along the  $x$  and  $y$  directions:  $k_r = \pi/L \sim 10^{-3} \text{ m}^{-1}$ . With only three seismometers, not only is the resolution poor, but also it is difficult to understand which is the peak in  $k$ -space relative to the physical signal and which ones are the aliased peaks (see Figure 9.6). We searched for all the

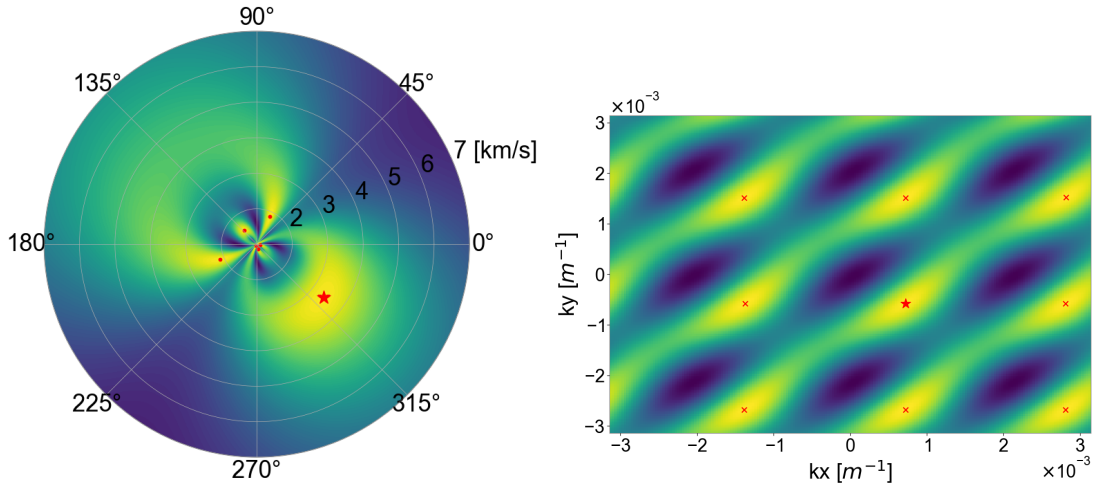


Figure 9.7: The 9 peaks in the portion of the wave vector space analysed at 0.5 Hz. They are represented both in the polar plane (*left*) and in the Cartesian plane (*right*).

peaks contained in the wave vector space with  $k_x, k_y \in [-3k_r, +3k_r]$  and then we ranked them by velocity values in descending order. We can assume indeed that the physical peaks in the wave vector space are those that are closer to the origin (recalling that  $v \propto 1/k$ ), the others being produced by the aliasing effect. For a given frequency we searched for the  $\mathbf{k}$  that maximized Equation 9.4 and this was done for each one of the 100 pieces of data we had. In Figure 9.8 I plotted the median values found for the 9 ranked velocities (in the analysed portion of  $k$ -space,  $[-3k_r, +3k_r]$ , there is space for 9 peaks, so 9 values of velocities). If we look at the median velocity produced with the first peak (the one closer to the origin in the  $k$ -space), we can see that after 0.6 Hz there is an increase in the velocity values. This is very likely due the fact that the first peak does not correspond any more to the physical one. If now we look at the median values of the velocities produced with the other ranked peaks, we can notice that after 0.6 Hz the median values obtained with the peaks from 4 to 9 follow a linear trend: this suggests that they are the result of aliased peaks. Indeed, an aliased

mode can be written as:

$$k_{x,y} = k_{0_{x,y}} + \frac{2\pi N}{\Delta_{x,y}} \quad (9.5)$$

where  $\Delta_{x,y}$  is the largest distance along the  $x$  or  $y$  direction,  $k_{0_{x,y}}$  is the physical mode that we are searching for and  $k_{x,y}$  is the  $x$  or  $y$  component of the peak located in  $\mathbf{k}$ . This means that the velocity is

$$v = \frac{\omega}{\sqrt{k_x^2 + k_y^2}} = \frac{\omega}{\sqrt{(k_{0_x} + 2\pi N/L)^2 + (k_{0_y} + 2\pi N/L)^2}} \quad (9.6)$$

and if  $2\pi N/L$  is large compared to  $k_{0_{x,y}}$  the velocities will have a linear trend with respect to the frequency  $\omega$ :  $v = \omega L / (2\sqrt{2}\pi N)$ . We want then to discard velocities obtained from the peaks 4 to 9. After 0.6 Hz we need to understand which peak between 2 and 3 is the correct one. At this regard we should look at the plot of the DOA (Figure 9.8). Here we can notice that up to 0.6 Hz the DOA is the same for all the frequencies, while after 0.6 Hz it changes a lot from one frequency to another. This is probably due to the fact that the wavelength of that waves starts to have the sizes of the mountain and scattering can arise. For the analyses we used the vertical displacement that should contain only the Rayleigh wave contribution. Indeed, it is true that underground Rayleigh waves are suppressed, but at frequencies below 1 Hz this does not hold any more [125]. Here Rayleigh waves should dominate the spectrum. If we take into account also the horizontal displacement we can get some hint about the DOA of the seismic waves. With this purpose we calculated the PSD of the horizontal channels along  $x$  and  $y$  and then took the arctan of  $|\text{PSD}_y|/|\text{PSD}_x|$ . This is done in the assumption that the spectrum is Rayleigh-dominated and so, since Rayleigh waves produce horizontal displacement only along their DOA, the horizontal  $x$  and  $y$  PSD should contain more or less signal depending on the DOA. The direction so calculated is only defined between 0 and  $\pi/2$  rad so we cannot distinguish between directions that differ for  $\pm\pi/2$  or  $+\pi$ . In Figure 9.9 we can see the four indistinguishable directions (red) along with the DOA that were calculated from the first three ranked peaks (blue, green, orange). After 0.6 Hz, excluding the DOA from the first peak, we can see that the one from the third peak better follows the red lines, so we are led to believe that the velocities from the third peak correspond to physical values. In Figure 9.10 I plotted the median velocities obtained using the first peak (up to 0.6 Hz) and the third one (beyond 0.6 Hz).

Below 0.2 Hz we cannot say anything because in this case the resolution is not good enough to correctly estimate the velocity. Indeed, at those frequencies wavelengths start to be very large, and therefore  $k$  will be very small. It is then not possible to find the right  $\mathbf{k}$ . Indeed, if we suppose to have a Gaussian

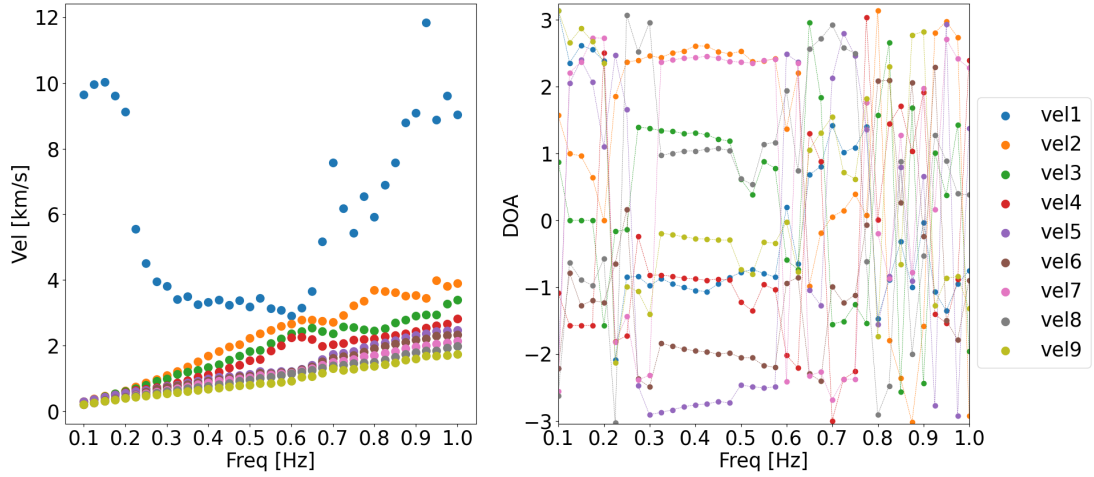


Figure 9.8: Values of the 9 median ranked velocities (*left*) and their corresponding DOA (*right*) at different frequencies.

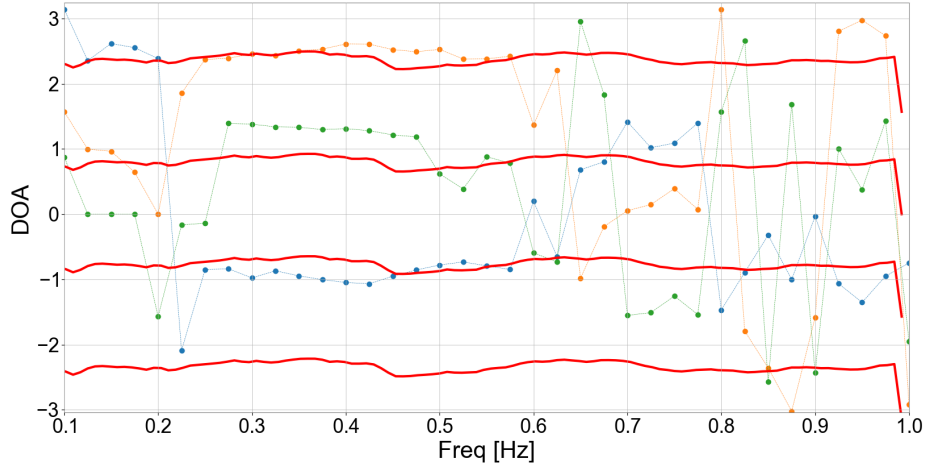


Figure 9.9: Comparison of the DOA from the first three peaks (blue: first peak, orange: second peak and green: third peak) with the DOA inferred from the horizontal channels (red line). See in the text to further explanations.

shaped peak in the  $k$ -space, with  $3\sigma = \pi/L \text{ m}^{-1}$  then  $\sigma = 3.5 \cdot 10^{-4} \text{ m}^{-1}$  with the peak that will fall inside:  $[-\sigma, +\sigma]$ . This means that the spatial frequency corresponding to  $k = 1\sigma$  will be:  $f = kv/(2\pi) = 0.2 \text{ Hz}$  with  $v = 4 \text{ km/s}$ . With this simple reasoning we can find that 0.2 Hz is the lower frequency limit that we can reach with the resolution allowed by our simple array.

In Figure 9.10 we can see that from 0.2 Hz to 0.6 Hz velocities diminish with

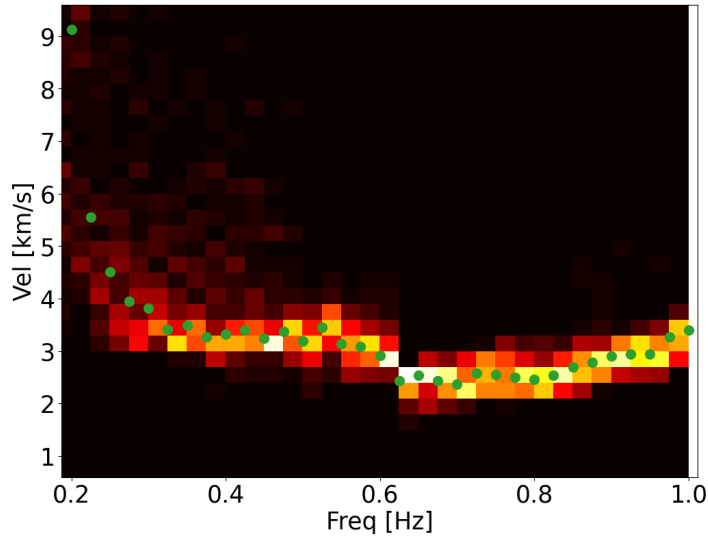


Figure 9.10: Median of velocities given by the first ranked peak (up to 0.6 Hz) and by the third one (from 0.6 Hz to 1 Hz).

the increasing of the frequency. This is in agreement with some other studies where we can see this trend [158]. Moreover, the velocities that we found are phase velocities of Rayleigh waves propagating from the surface deep into the mountain. This is reasonable since we know that the microseism below 1 Hz consists mainly of fundamental mode of the Rayleigh waves [125]. We can also see that, if we consider a depth of  $\sim 200$  m [152], at 0.5 Hz and with a seismic velocity  $v = 3$  km/s (Figure 9.10), the attenuation factor of the Rayleigh waves is only  $e^{-hk} \sim 0.8$ , so it is reasonable to assume that Rayleigh waves at frequencies  $< 1$  Hz are also present underground.

## 9.5 NN estimate in KAGRA

Interferometers like KAGRA are constructed underground for one main reason: limiting the seismic noise and consequently also the NN. This helps to improve the sensitivity but also to have a more stable interferometer, which means less troubles in the control systems. We can see in Figure 9.11 that at 10 Hz the measured ASD at KAGRA is 2 orders of magnitude smaller than that measured at Virgo. At the surface we can indeed assume that the Rayleigh contribution to the seismic noise is stronger and dominates all the others (even if it depends a lot on the soil and on the noise properties) [125]. Surface waves are also composed by Love waves (horizontal spectrum), but their contribution to the NN can be neglected compared to that of the Rayleigh waves, which instead dominates

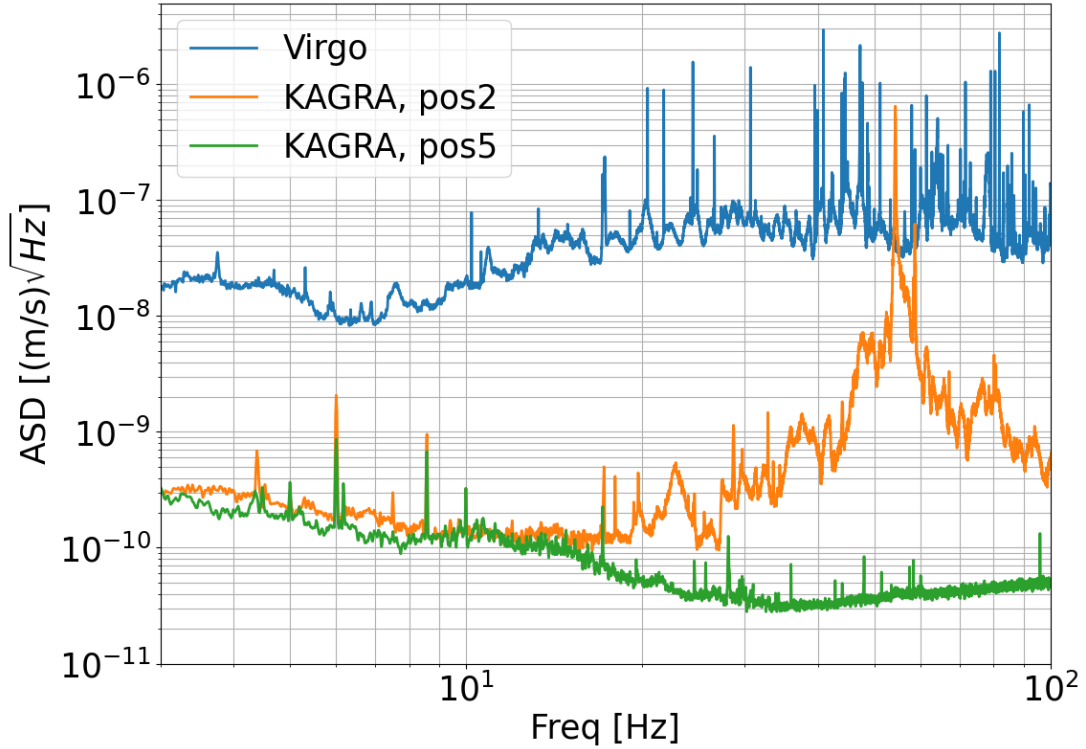


Figure 9.11: Comparison between the ASD of the average seismic noise at KAGRA (position 2 and 5 of Figure 9.2) and Virgo.

the spectrum (the vertical one in particular, see section 6.2). Surface waves are characterized by an exponential decay  $e^{-h\omega/v}$  that reduces their amplitude going deep in the ground, especially at higher frequencies. Going underground helps to greatly reduce the NN from surface seismic contribution, but the NN contribution from the body waves still remains (see Figure 6.3). It is then important to understand how much NN is still present in these kind of detectors.

To estimate the body wave NN budget, we can use the data taken inside the arm's tunnel, in particular, we used the data taken in the position number 5, see Figure 9.2. From Figure 9.3 we already know that the impact of the instrumentation over the NN is not a problem: the noise in position 2 starts indeed to rise above the noise recorded in the other positions only after 10 Hz, and up to 30 Hz the NN budget in position 2 is the same as that in the other positions showed in Figure 9.14. To estimate the NN from body waves, we can consider Equation 6.13 in the limit  $a \rightarrow 0$ , which is valid in an infinite and homogeneous space filled by a P wave seismic field. Using only the P contribution is of course an approximation given by the fact that we do not know the relative spectrum of P and S waves (that could be disentangled by a strainmeter though) and that in

the bulk (i.e. without cavity) only P waves contribute to the NN (at most we will overestimate the NN). Moreover, we have to remember that the NN contribution needs to be multiplied by 2 since we consider uncorrelated NN between the two end test masses. We also need to consider that, even if KAGRA is hosted inside a cave, we can still neglect its small dimensions, that, compared to the considered wavelengths, are negligible [52] (section 6.5).

For completeness, we can also check the Rayleigh waves contribution to the NN by using Equation 6.18 and the data taken from the F-net seismometer network, in Japan. Given that Equation 6.18 has been calculated with a model valid only for test masses located *above* the surface and not *below*, we are probably slightly underestimating or overestimating the NN. However, in the frequency band of interest for KAGRA, Rayleigh waves are negligible, so we can still use Equation 6.18 without introducing too much error. In ET the dimensions of the cavities will be instead bigger, and therefore in Figure 6.3 it has been used a model which also takes this into account.

In Figure 9.12 the NN budget coming from Rayleigh and body waves is shown, while in Figure 9.13 represents their comparison. We can see that Rayleigh-wave NN is always lower than body-wave NN, even if close to 3 Hz they start to be similar. I did not plot the contribution to the NN below 1 Hz because there Rayleigh waves should dominate and so the body-wave model loses its validity without a method to disentangle body from surface waves.

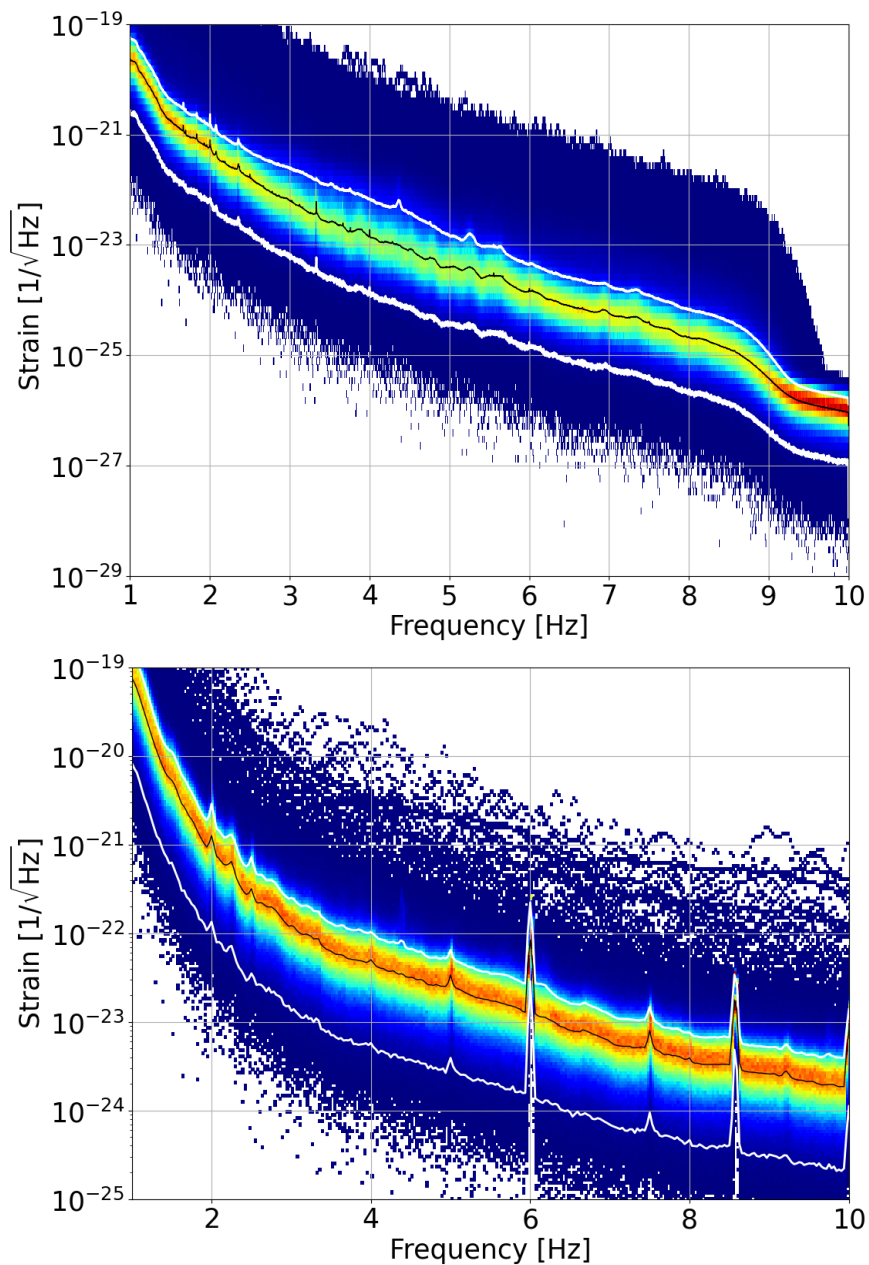


Figure 9.12: NN estimate from surface Rayleigh waves (*top*) and from body waves (*bottom*), the black line is the 50<sup>th</sup> quantile, the white lines represent the 10<sup>th</sup> and the 90<sup>th</sup> quantiles.



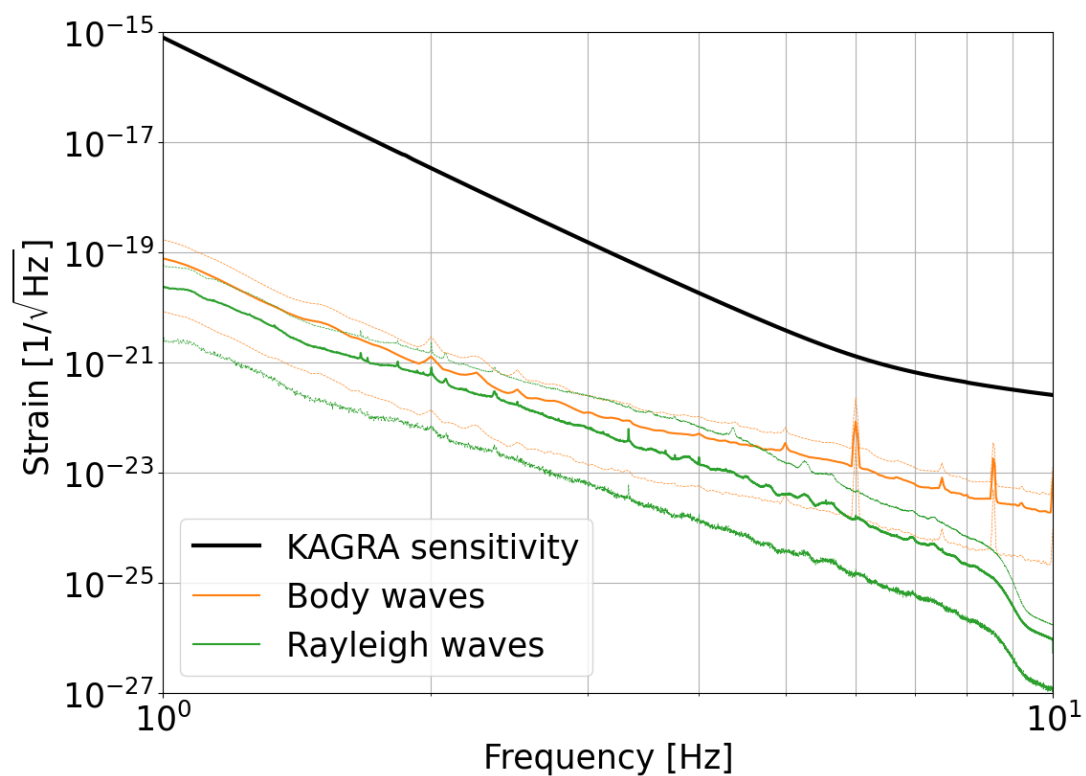


Figure 9.13: Comparison of the NN generated from body waves and the NN generated by Rayleigh waves at a depth of 200 m. The NN from body waves was estimated using seismic data from position 2 (see Figure 9.2) while the NN from Rayleigh waves was estimated with seismic data taken from the SRN station of the F-net seismic network, Japan.

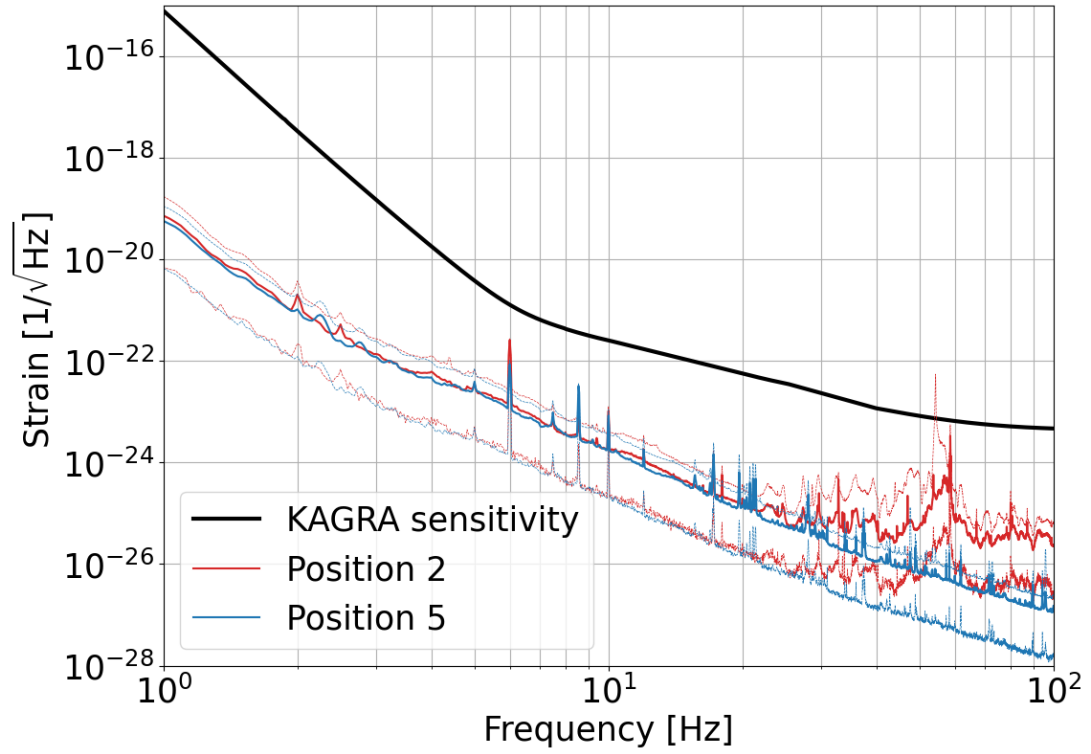


Figure 9.14: Comparison of the NN budget inside the cave (position 2) and in the arm of the interferometer (position 5). The thinner lines represent the 10<sup>th</sup> and the 90<sup>th</sup> quantiles (the thickest being the 50<sup>th</sup> quantile instead).

# 10

CONCLUSION

## 10. CONCLUSION

---

This thesis work fits in the Newtonian noise (NN) cancellation framework for gravitational-wave (GW) detectors of 2<sup>nd</sup> and 3<sup>rd</sup> generation. In particular, I focus on the optimization of the seismic array that, together with a Wiener filter, will be used to develop the NN cancellation system. The optimization is a very important task because it allows us to maximize the performances of the Wiener filter.

The state of the art for underground seismic array optimization was still in the embryonal phase of a 2D step wise optimization [52] (where sensors are added one after the other at the best location). It is clear that the optimization should be done in 3D and using a global approach, that is, exploiting a global optimization algorithm. However, a global optimization requires a huge computational effort: for this reason, before this work, this task was not yet accomplished. To optimize the positions of  $N$  sensors in a 3D space we need to find the global minimum of a cost function –typically the noise residual– in a  $3N$ -dimensional space. In order to find the global minimum for the residual function, the global optimization algorithm searches all over the phase space of the array for the best configuration. It is then clear that with  $3N$  dimensions this task is computationally very expensive.

To construct the cost function to be used in the (global) optimization I make a few assumptions, considering the seismic field as composed only by body waves and neglecting every possible contribution from surface waves (which is reasonable at the frequencies where 3<sup>rd</sup> generation detectors will work). Moreover, I assume the seismic field homogeneous and isotropic: since we do not yet know the future location for ET, nor we have underground seismic data, this is the most reasonable assumption we can make (any inhomogeneity and anisotropy would be characteristic of the specific chosen site). I also neglect the dimensions of the cavity and the scattering of the seismic field from the cavity walls. In order to test the results, I run two different global optimization algorithms (100 times each) on a computer cluster. They both reached the same optimal configurations. With this work I am able to assess the feasibility of active NN reduction in underground detectors and the possibility of reaching a factor 10 of reduction (at 10 Hz) by deploying only 15 sensors. In 2019 I published the above results in the Classical Quantum Gravity peer-reviewed journal [17].

The second work I did during my PhD was conceptually similar to the previous one but very different in the approach needed to solve it. The complex structure of the buildings hosting Virgo’s test masses do not allow to describe the seismic field with an isotropic and homogeneous field, nor with an analytical model. The best way to proceed in this case is to characterize the seismic field by means of sensor’s array data and use them to evaluate the cost function (the residual). It is possible to demonstrate that the residual can be described only by two-

## 10. CONCLUSION

---

point seismic correlations between the sensors of the array. Here lies the biggest problem: we need a continuous two-point seismic correlation function. A simple interpolation on the available data is not enough: in reality, the two-point seismic correlation function is defined in the 4D space and the data are too sparse to allow an informative interpolation of the seismic field. What I do is circumventing this problem exploiting the convolution theorem. I perform a Gaussian process regression on the 2-dimensional space of the Fourier amplitudes of the recorded signals and then I calculate the two-point seismic correlation with the above mentioned theorem. This allows me to construct a *surrogate model* of the Wiener filter but at the cost of introducing more computational complexity. In order to reduce the computational effort, I introduce a further step in which the two-point seismic correlation function is sampled over a dense grid of points in the 4D space. This lets me to perform a 4D linear interpolation, which is faster, while keeping intact the information about the seismic field. The global optimization algorithm is then run 100 times in order to statistically prove the global minimum, exactly as it was done in the previous work on the underground optimization. As a result, I find that the deployment of an array of 15 seismometers should be able to achieve a NN reduction by a factor of 3 to 7. This is enough for the aimed sensitivity of O4. Moreover, there seems to be some universal dependence of performances of the Wiener filter with respect to the characteristics of the seismic field. This is a point that I did not investigate further, but that might be worth being deepened. The results of this work were used to set the array for the NN cancellation system in AdV+.

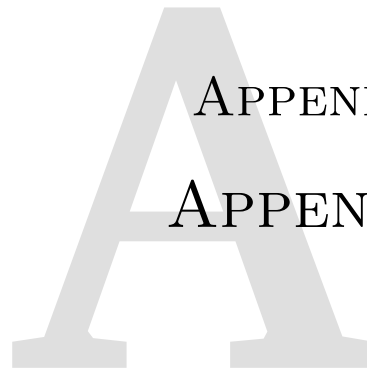
In 2020, I also published the above results on the peer-reviewed journal *Classical Quantum Gravity*. Moreover, this approach will be probably useful in the future, when seismic data will be available to perform the more computationally expensive optimization for underground seismic arrays.

Finally, I use seismic data collected in the Kamioka mine (where the gravitational-wave detector KAGRA is hosted) to investigate the seismic noise caused by the presence of noisy infrastructure and also the NN budget. These are important aspects that need to be assessed in view of the 3<sup>rd</sup> generation gravitational-wave detectors, like the Einstein Telescope. Seismic data show that the infrastructure noise becomes relevant above 10 Hz, where the NN reduces its impact on the detector and the seismic isolation system suppresses the seismic vibrations. Moreover, I use the data from three seismometers to perform a beamforming analysis of the velocities and the main directions of the seismic waves. The extracted values serve as a reference for the velocity in the NN estimation. For completeness, I also estimate the contribution of surface Rayleigh waves to the NN budget. For this task I exploit the data of the F-net network, in Japan. Finally, I show that both the NN from surface waves and the one from body

## 10. CONCLUSION

---

waves can be neglected in KAGRA.



APPENDIX  
APPENDIX

**Contents**

---

A.1	Bessel functions	160
A.2	Calculations of Equation 6.53	160
A.3	Calculations of Equation 6.56 and Equation 6.57	161

---

## A.1 Bessel functions

We introduce here some relations useful to the resolution of integrals reported in this thesis.

$$\begin{aligned} J_n(x) &= \frac{1}{2\pi} \int_{-\pi}^{+\pi} e^{i(x \sin(\phi) - n\pi)} = \\ &= \frac{1}{2\pi} \int_{-\pi}^{+\pi} e^{i(x \cos(\phi) - n(\pi/2 - \phi))} \end{aligned} \quad (\text{A.1})$$

From which follows:

$$J_1(x) = \frac{1}{2\pi i} \int_{-\pi}^{+\pi} e^{ix \cos(\phi)} \cos(\phi) \quad (\text{A.2})$$

This can be also recovered in a more elegant way, exploiting the relation:

$$-\partial_x J_0(x) = J_1(x) \quad (\text{A.3})$$

## A.2 Calculations of Equation 6.53

We start from Equation 6.31 where instead of calculating  $C(\delta a_x; \boldsymbol{\varrho}, \omega) = \langle \delta a_x^*(\mathbf{0}, \omega) \delta a_x(\boldsymbol{\varrho}, \omega) \rangle$  we calculate:  $C(\delta a_x; \boldsymbol{\varrho}_0, \omega) = \langle \delta a_x^*(\mathbf{0}, \omega) \xi_z(\boldsymbol{\varrho}_0, \omega) \rangle$ , where  $\boldsymbol{\varrho}_0$  is the sensor position on the surface and the integrals are performed in 2D:

$$\begin{aligned} C(\delta a_x, \xi_z; \boldsymbol{\varrho}_0, \omega) &= 2\pi i G \rho_0 \gamma(\nu) \int d\Delta r d\theta \Delta r \int \frac{dk d\alpha k}{(2\pi)^2} \\ &C(\xi_z, \omega) J_0(k^R \Delta r) e^{-hk^R} e^{ik^R \varrho_0 \cos(\alpha)} e^{k\Delta r \cos(\theta)} \cos(\beta) \end{aligned} \quad (\text{A.4})$$

Where  $\beta$  is the angle formed by  $\mathbf{k}$  with the  $x$ -axis. Integrating over  $d\theta$  we get a  $J_0(k\Delta r)$  and integrating over  $d\Delta r$  we get a  $\delta(k - k^R)/k^R$  where we used:

$$\int d\Delta r \Delta r J_0(k\Delta r) J_0(k^R \Delta r) = \frac{\delta(k - k^R)}{k^R} \quad (\text{A.5})$$

So that the integral A.4 becomes:

$$C(\delta a_x, \xi_z; \boldsymbol{\varrho}_0, \omega) = 2\pi i G \rho_0 \gamma(\nu) \int \frac{d\alpha}{(2\pi)} C(\xi_z, \omega) e^{-hk^R} e^{ik^R \varrho_0 \cos(\alpha)} \cos(\beta) \quad (\text{A.6})$$

We still have to integrate over  $\alpha$ , which means integrating all over the directions of  $\mathbf{k}^R$ . We see that  $\beta$  depends too from  $\alpha$ :  $\beta = \alpha + \phi$  where  $\phi$  is the angle



between  $\boldsymbol{\varrho}_0$  and the  $x$ -axis. So,  $\cos(\beta) = \cos(\alpha)\cos(\phi) - \sin(\alpha)\sin(\phi)$  and then the integral with  $\sin(\alpha)\sin(\phi)$  goes to zero and Equation A.4 becomes:

$$\boxed{C(\delta a_x, \xi_z; \boldsymbol{\varrho}_0, \omega) = 2\pi G \rho_0 \gamma(\nu) C(\xi_z, \omega) e^{-hk^R} J_0(k^R \varrho_0) \cos(\phi)} \quad (\text{A.7})$$

Where we used that:

$$\int d\alpha e^{ik^R \Delta r \cos(\alpha)} i \cos(\alpha) = 2\pi J_0(k^R \Delta r) \quad (\text{A.8})$$

### A.3 Calculations of Equation 6.56 and Equation 6.57

$$C(\delta a_x, \xi; \boldsymbol{\varrho}_0, \boldsymbol{\varrho}, \omega) = 2\pi G \rho_0 \gamma(\nu) \int d^2 \mathbf{r}' \int d^2 \mathbf{r}'' \int \frac{d^2 \mathbf{k}}{(2\pi)^2} \int \frac{d^2 \mathbf{k}'}{(2\pi)^2} \quad (\text{A.9})$$

$$C(\xi_z; \mathbf{r}', \mathbf{r}'', \omega) e^{hk} i \cos(\alpha) e^{i\mathbf{k} \cdot (\boldsymbol{\varrho}_0 - \mathbf{r}')} e^{i\mathbf{k}' \cdot (\boldsymbol{\varrho} - \mathbf{r}'')}$$

Integrating over  $d^2 \mathbf{k}'$  we obtain a  $\delta(\varrho - \mathbf{r}'')$ , integrating over  $d^2 \mathbf{r}''$  we get:

$$C(\delta a_x, \xi; \boldsymbol{\varrho}_0, \boldsymbol{\varrho}, \omega) = 2\pi G \rho_0 \gamma(\nu) \int d^2 \mathbf{r}' \int \frac{d^2 \mathbf{k}}{(2\pi)^2} C(\xi_z; \mathbf{r}', \boldsymbol{\varrho}, \omega) e^{-hk} i \cos(\alpha) e^{i\mathbf{k} \cdot \boldsymbol{\varrho}_0 - \mathbf{r}' \cos \phi} \quad (\text{A.10})$$

Again, we can see that  $\phi$  depends also from  $\alpha$ :  $\beta = \alpha + \phi$  where  $\phi$  is the angle between  $\boldsymbol{\varrho}_0$  and the  $x$ -axis. So,  $\cos(\beta) = \cos(\alpha)\cos(\phi) - \sin(\alpha)\sin(\phi)$  and then the integral with  $\sin(\alpha)\sin(\phi)$  goes to zero and using Equation A.2 and the Hankel transform:

$$\int k dk J_1(k|\boldsymbol{\varrho}_0 - \mathbf{r}'|) e^{-hk} = \frac{2|\boldsymbol{\varrho}_0 - \mathbf{r}'| \Gamma(3/2)}{(|\boldsymbol{\varrho}_0 - \mathbf{r}'|^2 + h^2)^{3/2} \sqrt{\pi}} \quad (\text{A.11})$$

And we finally get:

$$\boxed{C(\delta a_x, \xi; \boldsymbol{\varrho}_0, \boldsymbol{\varrho}, \omega) = 2\pi G \rho_0 \gamma(\nu) \int d^2 \mathbf{r}' C(\xi_z; \mathbf{r}', \boldsymbol{\varrho}, \omega) \frac{x_0 - x'}{(|\boldsymbol{\varrho}_0 - \mathbf{r}'|^2 + h^2)^{3/2}}} \quad (\text{A.12})$$

Where  $x_0 - x' = \cos(\beta)|\boldsymbol{\varrho}_0 - \mathbf{r}'|$  and  $\Gamma(3/2) = \sqrt{\pi}/2$ . With similar passages we can easily obtain also Equation 6.57.



# B

APPENDIX  
APPENDIX

## Contents

---

B.1 Reduced SNR for sum of incoherent signals

164

---

## B.1 Reduced SNR for sum of incoherent signals

Let us assume to have an array of sensors that have record two different signals plus some noise,  $\epsilon$ :

$$Y_i(\omega) = X_1(\omega) + X_2(\omega) + \epsilon_i(\omega) \quad (\text{B.1})$$

Thus, with the definition of  $\text{SNR}_X^2 = C_{XX}/C_{\epsilon\epsilon}$ , the total SNR will be:

$$\text{SNR}_{\text{tot}_i}^2 = 1 + \frac{C_{X_1X_1} + C_{X_2X_2}}{C_{\epsilon\epsilon}} + 2c \frac{\sqrt{C_{X_1X_1}C_{X_2X_2}}}{C_{\epsilon\epsilon}} \quad (\text{B.2})$$

With:

$$c = \frac{\Re\{C_{X_1X_2}\}}{\sqrt{C_{X_1X_1}C_{X_2X_2}}} \quad (\text{B.3})$$

the Pearson's correlation coefficient:  $-1 \leq c \leq 1$ . We can then see that:

$$\text{for } c = 1 \text{ then: } \text{SNR}_{\text{tot}_i} = 1 + (\text{SNR}_{X_1} + \text{SNR}_{X_2})^2$$

$$\text{for } c = 0 \text{ then: } \text{SNR}_{\text{tot}_i} = 1 + (\text{SNR}_{X_1} + \text{SNR}_{X_2})^2 - 2\text{SNR}_{X_1}\text{SNR}_{X_2}$$

$$\text{for } c = -1 \text{ then: } \text{SNR}_{\text{tot}_i} = 1 + (\text{SNR}_{X_1} + \text{SNR}_{X_2})^2 - 4\text{SNR}_{X_1}\text{SNR}_{X_2}$$

So any difference in the phase of  $X_1$  and  $X_2$  will lead to a decrease of the SNR in the  $i^{\text{th}}$  sensor.

# BIBLIOGRAPHY

- [1] LIGO SCIENTIFIC COLLABORATION. “Instrument Science White Paper 2019, LIGO-T1900409–v3”. In: (2019).
- [2] F Acernese et al. “Advanced Virgo: a second-generation interferometric gravitational wave detector”. In: *Classical and Quantum Gravity* 32.2 (2015), p. 024001. DOI: 10.1088/0264-9381/32/2/024001. URL: <http://stacks.iop.org/0264-9381/32/i=2/a=024001>.
- [3] T. Akutsu et al. “KAGRA: 2.5 Generation Interferometric Gravitational Wave Detector”. In: *Nature Astronomy* 3.1 (2019), pp. 35–40. DOI: 10.1038/s41550-018-0658-y.
- [4] C. S. UNNIKRISHNAN. “IndIGO AND LIGO-INDIA: SCOPE AND PLANS FOR GRAVITATIONAL WAVE RESEARCH AND PRECISION METROLOGY IN INDIA”. In: *International Journal of Modern Physics D* 22.01 (Jan. 2013), p. 1341010. DOI: 10.1142/s0218271813410101. URL: <https://doi.org/10.1142/s0218271813410101>.
- [5] B. P. Abbott et al. “Observation of Gravitational Waves from a Binary Black Hole Merger”. In: *Physical Review Letters* 116.6 (Feb. 2016). <https://doi.org/10.1103/physrevlett.116.061102>. DOI: 10.1103/physrevlett.116.061102.
- [6] B. P. Abbott et al. “Multi-messenger Observations of a Binary Neutron Star Merger”. In: *The Astrophysical Journal* 848.2 (Oct. 2017). <https://doi.org/10.3847/2041-8213/aa91c9>, p. L12. DOI: 10.3847/2041-8213/aa91c9.
- [7] R Abbott et al. “GWTC-2: Compact Binary Coalescences Observed by LIGO and Virgo During the First Half of the Third Observing Run”. In: *arXiv preprint arXiv:2010.14527* (2020).

## BIBLIOGRAPHY

---

- [8] B P Abbott et al. “A guide to LIGO–Virgo detector noise and extraction of transient gravitational-wave signals”. In: *Classical and Quantum Gravity* 37.5 (Feb. 2020), p. 055002. DOI: 10.1088/1361-6382/ab685e. URL: <https://doi.org/10.1088/1361-6382/ab685e>.
- [9] Scott A. Hughes and Kip S. Thorne. “Seismic gravity-gradient noise in interferometric gravitational-wave detectors”. In: *Physical Review D* 58.12 (Nov. 1998). DOI: 10.1103/physrevd.58.122002. URL: <https://doi.org/10.1103/physrevd.58.122002>.
- [10] Jan Harms and Stefan Hild. “Passive Newtonian noise suppression for gravitational-wave observatories based on shaping of the local topography”. In: *Classical and Quantum Gravity* 31.18 (Aug. 2014), p. 185011. DOI: 10.1088/0264-9381/31/18/185011. URL: <https://doi.org/10.1088/0264-9381/31/18/185011>.
- [11] J. C. Driggers et al. “Improving astrophysical parameter estimation via offline noise subtraction for Advanced LIGO”. In: *Physical Review D* 99.4 (Feb. 2019). DOI: 10.1103/physrevd.99.042001. URL: <https://doi.org/10.1103/physrevd.99.042001>.
- [12] Ryan DeRosa et al. “Global feed-forward vibration isolation in a km scale interferometer”. In: *Classical and Quantum Gravity* 29.21 (Oct. 2012), p. 215008. DOI: 10.1088/0264-9381/29/21/215008. URL: <https://doi.org/10.1088/0264-9381/29/21/215008>.
- [13] Jennifer C. Driggers et al. “Active noise cancellation in a suspended interferometer”. In: *Review of Scientific Instruments* 83.2 (Feb. 2012), p. 024501. DOI: 10.1063/1.3675891. URL: <https://doi.org/10.1063/1.3675891>.
- [14] J. A. Giaime et al. “Feedforward reduction of the microseism disturbance in a long-base-line interferometric gravitational-wave detector”. In: *Review of Scientific Instruments* 74.1 (Jan. 2003), pp. 218–224. DOI: 10.1063/1.1524717. URL: <https://doi.org/10.1063/1.1524717>.
- [15] M Beccaria et al. “Relevance of Newtonian seismic noise for the VIRGO interferometer sensitivity”. In: *Classical and Quantum Gravity* 15.11 (1998), p. 3339.
- [16] M Punturo et al. “The Einstein Telescope: a third-generation gravitational wave observatory”. In: *Classical and Quantum Gravity* 27.19 (Sept. 2010), p. 194002. DOI: 10.1088/0264-9381/27/19/194002. URL: <https://doi.org/10.1088/0264-9381/27/19/194002>.

## BIBLIOGRAPHY

---

- [17] F Badaracco and J Harms. “Optimization of seismometer arrays for the cancellation of Newtonian noise from seismic body waves”. In: *Classical and Quantum Gravity* 36.14 (2019), p. 145006. DOI: 10.1088/1361-6382/ab28c1. URL: <https://doi.org/10.1088/1361-6382/ab28c1>.
- [18] M Coughlin et al. “Towards a first design of a Newtonian-noise cancellation system for Advanced LIGO”. In: *Classical and Quantum Gravity* 33.24 (2016), p. 244001. URL: <http://stacks.iop.org/0264-9381/33/i=24/a=244001>.
- [19] Maria C Tringali et al. “Seismic array measurements at Virgo’s west end building for the configuration of a Newtonian-noise cancellation system”. In: *Classical and Quantum Gravity* 37.2 (Dec. 2019), p. 025005. DOI: 10.1088/1361-6382/ab5c43. URL: <https://doi.org/10.1088/1361-6382/ab5c43>.
- [20] Tony Rothman. “The Secret History of Gravitational Waves”. In: *American Scientist* 106.2 (2018), p. 96. DOI: 10.1511/2018.106.2.96. URL: <https://doi.org/10.1511/2018.106.2.96>.
- [21] “VIII. A dynamical theory of the electromagnetic field”. In: *Philosophical Transactions of the Royal Society of London* 155 (Dec. 1865). <https://doi.org/10.1098/rstl.1865.0008>, pp. 459–512. DOI: 10.1098/rstl.1865.0008.
- [22] F. A. E. Pirani. “Invariant Formulation of Gravitational Radiation Theory”. In: *Physical Review* 105.3 (Feb. 1957). <https://doi.org/10.1103/physrev.105.1089>, pp. 1089–1099. DOI: 10.1103/physrev.105.1089.
- [23] Kip S Thorne, Charles W Misner, and John Archibald Wheeler. *Gravitation*. Freeman, 2000.
- [24] Hermann Bondi, Félix AE Pirani, and Ivor Robinson. “Gravitational waves in general relativity III. Exact plane waves”. In: *Proceedings of the Royal Society of London. Series A. Mathematical and Physical Sciences* 251.1267 (1959), pp. 519–533.
- [25] Andrzej Trautman. “Radiation and Boundary Conditions in the Theory of Gravitation”. In: *Bull. Acad. Pol. Sci. Ser. Sci. Math. Astron. Phys.* 6.6 (1958), pp. 407–412. arXiv: 1604.03145 [gr-qc].
- [26] Pustovoit Gertsenshtein. “On the detection of low frequency gravitational waves”. In: *soviet physics jetp* 16.2 (1963).
- [27] Robert L. Forward. “Wideband laser-interferometer graviational-radiation experiment”. In: *Physical Review D* 17.2 (Jan. 1978), pp. 379–390. DOI: 10.1103/physrevd.17.379. URL: <https://doi.org/10.1103/physrevd.17.379>.

## BIBLIOGRAPHY

---

- [28] Weiss. “Electromagnetically coupled broadband gravitational antenna”. In: *Final Quarterly Report, MIT Research Laboratory of Electronics* (1972).
- [29] A. Giazotto, A. Brillet, et al. “The Virgo project”. In: *Proposal for the construction of a large interferometer to detect Gravitational Waves* (1989).
- [30] J. H. Taylor and J. M. Weisberg. “A new test of general relativity - Gravitational radiation and the binary pulsar PSR 1913+16”. In: *The Astrophysical Journal* 253 (Feb. 1982), p. 908. DOI: 10.1086/159690. URL: <https://doi.org/10.1086/159690>.
- [31] B. P. Abbott et al. “GW170817: Observation of Gravitational Waves from a Binary Neutron Star Inspiral”. In: *Physical Review Letters* 119.16 (Oct. 2017). <https://doi.org/10.1103/physrevlett.119.161101>. DOI: 10.1103/physrevlett.119.161101.
- [32] B. P. Abbott et al. “Multi-messenger Observations of a Binary Neutron Star Merger”. In: *The Astrophysical Journal* 848.2 (Oct. 2017). <https://doi.org/10.3847/2041-8213/aa91c9>, p. L12. DOI: 10.3847/2041-8213/aa91c9.
- [33] B. P. Abbott et al. “Gravitational Waves and Gamma-Rays from a Binary Neutron Star Merger: GW170817 and GRB 170817A”. In: *The Astrophysical Journal* 848.2 (Oct. 2017). <https://doi.org/10.3847/2041-8213/aa920c>, p. L13. DOI: 10.3847/2041-8213/aa920c.
- [34] R. Abbott et al. “GW190521: A Binary Black Hole Merger with a Total Mass of  $150 M_{\odot}$ ”. In: *Physical Review Letters* 125.10 (Sept. 2020). DOI: 10.1103/physrevlett.125.101102. URL: <https://doi.org/10.1103/physrevlett.125.101102>.
- [35] Steven Weinberg. *Gravitation and cosmology: principles and applications of the general theory of relativity*. 1972.
- [36] Michael Paul Hobson, George P Efstathiou, and Anthony N Lasenby. *General relativity: an introduction for physicists*. Cambridge University Press, 2006.
- [37] Michele Maggiore. *Gravitational waves: Volume 1: Theory and experiments*. Vol. 1. Oxford university press, 2008.
- [38] Bernard F Schutz. “Gravitational wave astronomy”. In: *Classical and Quantum Gravity* 16.12A (1999), A131.
- [39] A. A. Michelson and E. W. Morley. “On the relative motion of the Earth and the luminiferous ether”. In: *American Journal of Science* s3-34.203 (Nov. 1887), pp. 333–345. DOI: 10.2475/ajs.s3-34.203.333. URL: <https://doi.org/10.2475/ajs.s3-34.203.333>.



## BIBLIOGRAPHY

---

- [40] Peter R. Saulson. “If light waves are stretched by gravitational waves, how can we use light as a ruler to detect gravitational waves?” In: *American Journal of Physics* 65.6 (June 1997). <https://doi.org/10.1119/1.18578>, pp. 501–505. DOI: 10.1119/1.18578.
- [41] Arkadiusz Blaut. “Angular and frequency response of the gravitational wave interferometers in the metric theories of gravity”. In: *Physical Review D* 85.4 (Feb. 2012). DOI: 10.1103/physrevd.85.043005. URL: <https://doi.org/10.1103/physrevd.85.043005>.
- [42] Andreas Freise and Kenneth Strain. “Interferometer Techniques for Gravitational-Wave Detection”. In: *Living Reviews in Relativity* 13.1 (Feb. 2010). DOI: 10.12942/lrr-2010-1. URL: <https://doi.org/10.12942/lrr-2010-1>.
- [43] Malik Rakhmanov. “Response of test masses to gravitational waves in the local Lorentz gauge”. In: *Physical Review D* 71.8 (Apr. 2005). <https://doi.org/10.1103/physrevd.71.084003>. DOI: 10.1103/physrevd.71.084003.
- [44] Stephen W Hawking and Werner Israel. *Three hundred years of gravitation*. Cambridge University Press, 1989. Chap. Gravitational radiation-Detection of gravitational waves.
- [45] T Accadia et al. “Virgo: a laser interferometer to detect gravitational waves”. In: *Journal of Instrumentation* 7.03 (Mar. 2012), P03012–P03012. DOI: 10.1088/1748-0221/7/03/p03012. URL: <https://doi.org/10.1088/1748-0221/7/03/p03012>.
- [46] Massimo Bassan. “Advanced interferometers and the search for gravitational waves”. In: *Astrophysics and Space Science Library* 404 (2014), pp. 275–290.
- [47] F. Acernese et al. “Increasing the Astrophysical Reach of the Advanced Virgo Detector via the Application of Squeezed Vacuum States of Light”. In: *Physical Review Letters* 123.23 (Dec. 2019). DOI: 10.1103/physrevlett.123.231108. URL: <https://doi.org/10.1103/physrevlett.123.231108>.
- [48] F. Acernese et al. “Lock acquisition of the Virgo gravitational wave detector”. In: *Astroparticle Physics* 30.1 (Aug. 2008), pp. 29–38. DOI: 10.1016/j.astropartphys.2008.06.005. URL: <https://doi.org/10.1016/j.astropartphys.2008.06.005>.

## BIBLIOGRAPHY

---

- [49] T Accadia et al. “Reconstruction of the gravitational wave signal  $h(t)$  during the Virgo science runs and independent validation with a photon calibrator”. In: *Classical and Quantum Gravity* 31.16 (Aug. 2014), p. 165013. DOI: 10.1088/0264-9381/31/16/165013. URL: <https://doi.org/10.1088/0264-9381/31/16/165013>.
- [50] S Hild et al. “DC-readout of a signal-recycled gravitational wave detector”. In: *Classical and Quantum Gravity* 26.5 (Feb. 2009), p. 055012. DOI: 10.1088/0264-9381/26/5/055012. URL: <https://doi.org/10.1088/0264-9381/26/5/055012>.
- [51] Donatella Fiorucci et al. “Impact of infrasound atmospheric noise on gravity detectors used for astrophysical and geophysical applications”. In: *Phys. Rev. D* 97 (6 2018), p. 062003. DOI: 10.1103/PhysRevD.97.062003. URL: <https://link.aps.org/doi/10.1103/PhysRevD.97.062003>.
- [52] Jan Harms. “Terrestrial gravity fluctuations”. In: *Living Reviews in Relativity* 22.1 (Oct. 2019). DOI: 10.1007/s41114-019-0022-2. URL: <https://doi.org/10.1007/s41114-019-0022-2>.
- [53] Peter R. Saulson. “Thermal noise in mechanical experiments”. In: *Physical Review D* 42.8 (Oct. 1990), pp. 2437–2445. DOI: 10.1103/physrevd.42.2437. URL: <https://doi.org/10.1103/physrevd.42.2437>.
- [54] François Bondu, Patrice Hello, and Jean-Yves Vinet. “Thermal noise in mirrors of interferometric gravitational wave antennas”. In: *Physics Letters A* 246.3-4 (Sept. 1998), pp. 227–236. DOI: 10.1016/s0375-9601(98)00450-2. URL: [https://doi.org/10.1016/s0375-9601\(98\)00450-2](https://doi.org/10.1016/s0375-9601(98)00450-2).
- [55] P Amico et al. “Thermal noise limit in the Virgo mirror suspension”. In: *Nuclear Instruments and Methods in Physics Research Section A: Accelerators, Spectrometers, Detectors and Associated Equipment* 461.1-3 (2001), pp. 297–299.
- [56] Carlton M. Caves. “Quantum-mechanical noise in an interferometer”. In: *Physical Review D* 23.8 (Apr. 1981), pp. 1693–1708. DOI: 10.1103/physrevd.23.1693. URL: <https://doi.org/10.1103/physrevd.23.1693>.
- [57] Stefan L. Danilishin and Farid Ya. Khalili. “Quantum Measurement Theory in Gravitational-Wave Detectors”. In: *Living Reviews in Relativity* 15.1 (Apr. 2012). DOI: 10.12942/lrr-2012-5. URL: <https://doi.org/10.12942/lrr-2012-5>.

## BIBLIOGRAPHY

---

- [58] J. Aasi et al. “Enhanced sensitivity of the LIGO gravitational wave detector by using squeezed states of light”. In: *Nature Photonics* 7.8 (July 2013), pp. 613–619. DOI: 10.1038/nphoton.2013.177. URL: <https://doi.org/10.1038/nphoton.2013.177>.
- [59] Haocun Yu et al. “Quantum correlations between light and the kilogram-mass mirrors of LIGO”. In: *Nature* 583.7814 (July 2020), pp. 43–47. DOI: 10.1038/s41586-020-2420-8. URL: <https://doi.org/10.1038/s41586-020-2420-8>.
- [60] Stefan Hild. “A Basic Introduction to Quantum Noise and Quantum-Non-Demolition Techniques”. In: *Advanced Interferometers and the Search for Gravitational Waves*. Springer International Publishing, 2014, pp. 291–314. DOI: 10.1007/978-3-319-03792-9\_11. URL: [https://doi.org/10.1007/978-3-319-03792-9\\_11](https://doi.org/10.1007/978-3-319-03792-9_11).
- [61] H. J. Kimble et al. “Conversion of conventional gravitational-wave interferometers into quantum nondemolition interferometers by modifying their input and/or output optics”. In: *Physical Review D* 65.2 (Dec. 2001). DOI: 10.1103/physrevd.65.022002. URL: <https://doi.org/10.1103/physrevd.65.022002>.
- [62] L. McCuller et al. “Frequency-Dependent Squeezing for Advanced LIGO”. In: *Physical Review Letters* 124.17 (Apr. 2020). DOI: 10.1103/physrevlett.124.171102. URL: <https://doi.org/10.1103/physrevlett.124.171102>.
- [63] S Hild et al. “Sensitivity studies for third-generation gravitational wave observatories”. In: *Classical and Quantum Gravity* 28.9 (2011), p. 094013. URL: <http://stacks.iop.org/0264-9381/28/i=9/a=094013>.
- [64] Stefan Grimm and Jan Harms. “Multiband gravitational-wave parameter estimation: A study of future detectors”. In: *Physical Review D* 102.2 (July 2020). DOI: 10.1103/physrevd.102.022007. URL: <https://doi.org/10.1103/physrevd.102.022007>.
- [65] Maximiliano Isi et al. “Detecting beyond-Einstein polarizations of continuous gravitational waves”. In: *Physical Review D* 91.8 (Apr. 2015). DOI: 10.1103/physrevd.91.082002. URL: <https://doi.org/10.1103/physrevd.91.082002>.
- [66] David Reitze et al. “Cosmic Explorer: The U.S. Contribution to Gravitational-Wave Astronomy beyond LIGO”. In: *Bulletin of the AAS* 51.7 (Sept. 30, 2019). <https://baas.aas.org/pub/2020n7i035>. URL: <https://baas.aas.org/pub/2020n7i035>.

## BIBLIOGRAPHY

---

- [67] Jan Harms et al. “Low-frequency terrestrial gravitational-wave detectors”. In: *Physical Review D* 88.12 (Dec. 2013). DOI: 10.1103/physrevd.88.122003. URL: <https://doi.org/10.1103/physrevd.88.122003>.
- [68] B Sathyaprakash et al. “Scientific objectives of Einstein Telescope”. In: *Classical and Quantum Gravity* 29.12 (June 2012), p. 124013. DOI: 10.1088/0264-9381/29/12/124013. URL: <https://doi.org/10.1088/0264-9381/29/12/124013>.
- [69] ET Steering Committee Editorial Team. “Design report update 2020”. In: (2020).
- [70] Stefan Hild et al. “A xylophone configuration for a third-generation gravitational wave detector”. In: *Classical and Quantum Gravity* 27.1 (2009), p. 015003.
- [71] Matthew Abernathy, F Acernese, P Ajith, et al. “Einstein gravitational wave Telescope conceptual design study. available from European Gravitational Observatory, document number ET-0106C-10, 2011”. In: *Accessed on 31.07* (2017).
- [72] A Freise et al. “Triple Michelson interferometer for a third-generation gravitational wave detector”. In: *Classical and Quantum Gravity* 26.8 (Apr. 2009), p. 085012. DOI: 10.1088/0264-9381/26/8/085012. URL: <https://doi.org/10.1088/0264-9381/26/8/085012>.
- [73] Karsten Danzmann et al. “LISA Laser Interferometer Space Antenna—A proposal in response to the ESA call for L3 mission concepts”. In: *Albert Einstein Inst. Hanover, Leibniz Univ. Hanover, Max Planck Inst. Gravitational Phys., Hannover, Germany, Tech. Rep* (2017).
- [74] TA Prince et al. “LISA: Probing the Universe with Gravitational waves”. In: *2007 AAS/AAPT Joint Meeting*. Vol. 38. AAS publications. 2007, p. 990.
- [75] Benjamin Canuel et al. “ELGAR - a European Laboratory for Gravitation and Atom-interferometric Research”. In: *Classical and Quantum Gravity* (July 2020). DOI: 10.1088/1361-6382/aba80e. URL: <https://doi.org/10.1088/1361-6382/aba80e>.
- [76] B Canuel et al. “Technologies for the ELGAR large scale atom interferometer array”. In: *arXiv preprint arXiv:2007.04014* (2020).
- [77] Masaki Ando et al. “Torsion-Bar Antenna for Low-Frequency Gravitational-Wave Observations”. In: *Physical Review Letters* 105.16 (Oct. 2010). DOI: 10.1103/physrevlett.105.161101. URL: <https://doi.org/10.1103/physrevlett.105.161101>.

## BIBLIOGRAPHY

---

- [78] Ho Jung Paik et al. “Low-frequency terrestrial tensor gravitational-wave detector”. In: *Classical and Quantum Gravity* 33.7 (Mar. 2016), p. 075003. DOI: 10.1088/0264-9381/33/7/075003. URL: <https://doi.org/10.1088/0264-9381/33/7/075003>.
- [79] Ayaka Shoda et al. “Ground-based low-frequency gravitational-wave detector with multiple outputs”. In: *Physical Review D* 95.8 (Apr. 2017). DOI: 10.1103/physrevd.95.082004. URL: <https://doi.org/10.1103/physrevd.95.082004>.
- [80] Ho Jung Paik. “SOGRO (Superconducting Omni-directional Gravitational Radiation Observatory)”. In: *EPJ Web of Conferences* 168 (2018). Ed. by B. Gwak et al., p. 01005. DOI: 10.1051/epjconf/201816801005. URL: <https://doi.org/10.1051/epjconf/201816801005>.
- [81] Harms J. et al. “Lunar Gravitational-Wave Antenna”. In: *ArXiv preprint arXiv:2010.13726* (2020).
- [82] Harvey Leifert. “Seismic noise in the moon”. In: *Physics Today* 58.10 (Oct. 2005), pp. 9–9. DOI: 10.1063/1.4796767. URL: <https://doi.org/10.1063/1.4796767>.
- [83] Ho Jung Paik and Krishna Yethadka Venkateswara. “Gravitational wave detection on the Moon and the moons of Mars”. In: *Advances in Space Research* 43.1 (Jan. 2009), pp. 167–170. DOI: 10.1016/j.asr.2008.04.010. URL: <https://doi.org/10.1016/j.asr.2008.04.010>.
- [84] Warren W. Johnson. “The moon as a gravitational wave detector, using seismometers”. In: *AIP Conference Proceedings*. AIP, 1990. DOI: 10.1063/1.39102. URL: <https://doi.org/10.1063/1.39102>.
- [85] J. V. van Heijningen, A. Bertolini, and J. F. J. van den Brand. “A novel interferometrically read out inertial sensor for future gravitational wave detectors”. In: *2018 IEEE Sensors Applications Symposium (SAS)*. 2018, pp. 1–5. DOI: 10.1109/SAS.2018.8336722.
- [86] J.V. van Heijningen. “A fifty-fold improvement of thermal noise limited inertial sensitivity by operating at cryogenic temperatures”. In: *Journal of Instrumentation* 15.06 (June 2020), P06034–P06034. DOI: 10.1088/1748-0221/15/06/p06034. URL: <https://doi.org/10.1088/1748-0221/15/06/p06034>.
- [87] Fausto Acernese et al. “A Michelson interferometer for seismic wave measurement: theoretical analysis and system performances”. In: *Remote Sensing for Environmental Monitoring, GIS Applications, and Geology VI*. Ed. by Manfred Ehlers and Ulrich Michel. SPIE, Sept. 2006. DOI: 10.1117/12.687907. URL: <https://doi.org/10.1117/12.687907>.

## BIBLIOGRAPHY

---

- [88] John M. Goodkind. “The superconducting gravimeter”. In: *Review of Scientific Instruments* 70.11 (Nov. 1999), pp. 4131–4152. DOI: 10.1063/1.1150092. URL: <https://doi.org/10.1063/1.1150092>.
- [89] Brian Olson et al. “Basin Hopping as a General and Versatile Optimization Framework for the Characterization of Biological Macromolecules”. In: *Advances in Artificial Intelligence 2012* (2012), pp. 1–19. DOI: 10.1155/2012/674832. URL: <https://doi.org/10.1155/2012/674832>.
- [90] David J. Wales and Jonathan P. K. Doye. “Global Optimization by Basin-Hopping and the Lowest Energy Structures of Lennard-Jones Clusters Containing up to 110 Atoms”. In: *The Journal of Physical Chemistry A* 101.28 (1997), pp. 5111–5116. DOI: 10.1021/jp970984n. URL: <https://doi.org/10.1021/jp970984n>.
- [91] David Wales et al. *Energy landscapes: Applications to clusters, biomolecules and glasses*. Cambridge University Press, 2003.
- [92] David J Wales and Harold A Scheraga. “Global optimization of clusters, crystals, and biomolecules”. In: *Science* 285.5432 (1999), pp. 1368–1372.
- [93] Z. Li and H. A. Scheraga. “Monte Carlo-minimization approach to the multiple-minima problem in protein folding.” In: *Proceedings of the National Academy of Sciences* 84.19 (1987), pp. 6611–6615. DOI: 10.1073/pnas.84.19.6611. URL: <https://doi.org/10.1073/pnas.84.19.6611>.
- [94] P. A. Vikhar. “Evolutionary algorithms: A critical review and its future prospects”. In: *2016 International Conference on Global Trends in Signal Processing, Information Computing and Communication (ICGTSPICC)*. 2016, pp. 261–265.
- [95] A.E. Eiben and J.E. Smith. *Introduction to Evolutionary Computing*. Springer Berlin Heidelberg, 2015. DOI: 10.1007/978-3-662-44874-8. URL: <https://doi.org/10.1007/978-3-662-44874-8>.
- [96] Rainer Storn and Kenneth Price. “Differential evolution—a simple and efficient heuristic for global optimization over continuous spaces”. In: *Journal of global optimization* 11.4 (1997), pp. 341–359.
- [97] S. Das and P. N. Suganthan. “Differential Evolution: A Survey of the State-of-the-Art”. In: *IEEE Transactions on Evolutionary Computation* 15.1 (2011), pp. 4–31. DOI: 10.1109/TEVC.2010.2059031.
- [98] James Kennedy. “The particle swarm: social adaptation of knowledge”. In: *Proceedings of 1997 IEEE International Conference on Evolutionary Computation (ICEC'97)*. IEEE. 1997, pp. 303–308.

## BIBLIOGRAPHY

---

- [99] James Kennedy and Russell Eberhart. “Particle swarm optimization”. In: *Proceedings of ICNN’95-International Conference on Neural Networks*. Vol. 4. IEEE. 1995, pp. 1942–1948.
- [100] Christopher KI Williams and Carl Edward Rasmussen. *Gaussian processes for machine learning*. Vol. 2. 3. MIT press Cambridge, MA, 2006.
- [101] Hyun-Chul Kim and Jaewook Lee. “Clustering Based on Gaussian Processes”. In: *Neural Computation* 19.11 (Nov. 2007), pp. 3088–3107. DOI: 10.1162/neco.2007.19.11.3088. URL: <https://doi.org/10.1162/neco.2007.19.11.3088>.
- [102] Donald R Jones. “A taxonomy of global optimization methods based on response surfaces”. In: *Journal of global optimization* 21.4 (2001), pp. 345–383.
- [103] Alexander Forrester, Andras Sobester, and Andy Keane. *Engineering design via surrogate modelling: a practical guide*. John Wiley & Sons, 2008.
- [104] Fernando Perez-Cruz et al. “Gaussian Processes for Nonlinear Signal Processing: An Overview of Recent Advances”. In: *IEEE Signal Processing Magazine* 30.4 (July 2013), pp. 40–50. DOI: 10.1109/msp.2013.2250352. URL: <https://doi.org/10.1109/msp.2013.2250352>.
- [105] Norbert Wiener. *Extrapolation, interpolation, and smoothing of stationary time series, vol. 2*. 1949.
- [106] R.B. Burckel Reinhold Remmert. *Theory of Complex Functions*. Graduate Texts in Mathematics / Readings in Mathematics v. 122. Springer, 1990. ISBN: 9780387971957,0387971955.
- [107] M Coughlin et al. “Wiener filtering with a seismic underground array at the Sanford Underground Research Facility”. In: *Classical and Quantum Gravity* 31.21 (2014), p. 215003. DOI: 10.1088/0264-9381/31/21/215003. URL: <https://doi.org/10.1088/0264-9381/31/21/215003>.
- [108] J. Harms et al. “Observation of a potential future sensitivity limitation from ground motion at LIGO Hanford”. In: *Phys. Rev. D* 101 (10 2020), p. 102002. DOI: 10.1103/PhysRevD.101.102002. URL: <https://link.aps.org/doi/10.1103/PhysRevD.101.102002>.
- [109] Jan Harms. *Terrestrial gravity fluctuations as fundamental sensitivity limit of GW detectors*. Youtube. URL: <https://www.youtube.com/watch?v=cY3qtATATHA>.
- [110] Freeman J. Dyson. “Seismic Response of the Earth to a Gravitational Wave in the 1-Hz Band”. In: *The Astrophysical Journal* 156 (May 1969), p. 529. DOI: 10.1086/149986. URL: <https://doi.org/10.1086/149986>.

## BIBLIOGRAPHY

---

- [111] Jennifer C. Driggers, Jan Harms, and Rana X. Adhikari. “Subtraction of Newtonian noise using optimized sensor arrays”. In: *Phys. Rev. D* 86 (10 2012), p. 102001. DOI: 10.1103/PhysRevD.86.102001. URL: <http://link.aps.org/doi/10.1103/PhysRevD.86.102001>.
- [112] F Acernese et al. “Properties of seismic noise at the Virgo site”. In: *Classical and Quantum Gravity* 21.5 (Feb. 2004), S433–S440. DOI: 10.1088/0264-9381/21/5/008. URL: <https://doi.org/10.1088/0264-9381/21/5/008>.
- [113] Peter R. Saulson. “Terrestrial gravitational noise on a gravitational wave antenna”. In: *Phys. Rev. D* 30 (4 1984), pp. 732–736. DOI: 10.1103/PhysRevD.30.732. URL: <http://link.aps.org/doi/10.1103/PhysRevD.30.732>.
- [114] K. Aki and P. G. Richards. *Quantitative Seismology, 2nd edition*. University Science Books, 2009.
- [115] Oldrich Novotny. “Seismic surface waves”. In: *Bahia, Salvador: Instituto de Geociencias* 61 (1999).
- [116] J. Peterson. “Observation and modeling of seismic background noise”. In: *Open-file report* 93-322 (1993).
- [117] T Tanimoto and K Heki. “4.16-Interaction of Solid Earth, Atmosphere and Ionosphere”. In: *Treatise on Geophysics* (2015), pp. 421–443.
- [118] M.S Longuet-Higgins. “A theory of the origin of microseisms”. In: *Philosophical Transactions of the Royal Society of London. Series A, Mathematical and Physical Sciences* 243.857 (Sept. 1950), pp. 1–35. DOI: 10.1098/rsta.1950.0012. URL: <https://doi.org/10.1098/rsta.1950.0012>.
- [119] Tatsuhiko Saito. “Love-wave excitation due to the interaction between a propagating ocean wave and the sea-bottom topography”. In: *Geophysical Journal International* 182.3 (July 2010), pp. 1515–1523. DOI: 10.1111/j.1365-246x.2010.04695.x. URL: <https://doi.org/10.1111/j.1365-246x.2010.04695.x>.
- [120] Spahr C. Webb. “19 Seismic noise on land and on the sea floor”. In: *International Geophysics*. Elsevier, 2002, pp. 305–318. DOI: 10.1016/s0074-6142(02)80222-4. URL: [https://doi.org/10.1016/s0074-6142\(02\)80222-4](https://doi.org/10.1016/s0074-6142(02)80222-4).
- [121] H Bungum, S Mykkeltveit, and T Kvaerna. “Seismic noise in Fennoscandia, with emphasis on high frequencies”. In: *Bulletin of the Seismological Society of America* 75.6 (1985), pp. 1489–1513.



## BIBLIOGRAPHY

---

- [122] M.G. Beker et al. “Improving the sensitivity of future GW observatories in the 1 - 10Hz band: Newtonian and seismic noise”. English. In: *General Relativity and Gravitation* 43.2 (2011), pp. 623–656. ISSN: 0001-7701. DOI: 10.1007/s10714-010-1011-7. URL: <http://dx.doi.org/10.1007/s10714-010-1011-7>.
- [123] F Amann et al. “Site-selection criteria for the Einstein Telescope”. In: *arXiv preprint arXiv:2003.03434* (2020).
- [124] F Badaracco et al. “Machine learning for gravitational-wave detection: surrogate Wiener filtering for the prediction and optimized cancellation of Newtonian noise at Virgo”. In: *Classical and Quantum Gravity* 37.19 (Sept. 2020), p. 195016. DOI: 10.1088/1361-6382/abab64. URL: <https://doi.org/10.1088/1361-6382/abab64>.
- [125] Sylvette Bonnefoy-Claudet, Fabrice Cotton, and Pierre-Yves Bard. “The nature of noise wavefield and its applications for site effects studies”. In: *Earth-Science Reviews* 79.3-4 (Dec. 2006), pp. 205–227. DOI: 10.1016/j.earscirev.2006.07.004. URL: <https://doi.org/10.1016/j.earscirev.2006.07.004>.
- [126] S Mykkeltveit et al. “Seismic array configuration optimization”. In: *Bulletin of the Seismological Society of America* 73.1 (1983), pp. 173–186.
- [127] Valeri A Korneev and Lane R Johnson. “Scattering of elastic waves by a spherical inclusion—I. Theory and numerical results”. In: *Geophysical Journal International* 115.1 (1993), pp. 230–250.
- [128] Soumen Koley et al. “S-wave Velocity Model Estimation using Ambient Seismic Noise at Virgo, Italy”. In: *SEG Technical Program Expanded Abstracts 2017*. Society of Exploration Geophysicists, Aug. 2017. DOI: 10.1190/segam2017-17681951.1. URL: <https://doi.org/10.1190/segam2017-17681951.1>.
- [129] Waled Hassan and Peter B. Nagy. “Simplified expressions for the displacements and stresses produced by the Rayleigh wave”. In: *The Journal of the Acoustical Society of America* 104.5 (Nov. 1998), pp. 3107–3110. DOI: 10.1121/1.423901. URL: <https://doi.org/10.1121/1.423901>.
- [130] Toshiaki Yokoi and Sos Margaryan. “Consistency of the spatial autocorrelation method with seismic interferometry and its consequence”. In: *Geophysical Prospecting* 56.3 (May 2008), pp. 435–451. DOI: 10.1111/j.1365-2478.2008.00709.x. URL: <https://doi.org/10.1111/j.1365-2478.2008.00709.x>.

## BIBLIOGRAPHY

---

- [131] M. W. Coughlin et al. “Implications of Dedicated Seismometer Measurements on Newtonian-Noise Cancellation for Advanced LIGO”. In: *Phys. Rev. Lett.* 121 (22 2018), p. 221104. DOI: 10.1103/PhysRevLett.121.221104. URL: <https://link.aps.org/doi/10.1103/PhysRevLett.121.221104>.
- [132] M Punturo et al. “The third generation of gravitational wave observatories and their science reach”. In: *Classical and Quantum Gravity* 27.8 (2010), p. 084007. URL: <http://stacks.iop.org/0264-9381/27/i=8/a=084007>.
- [133] Saeed V. Vaseghi. “Wiener Filters”. In: *Advanced Digital Signal Processing and Noise Reduction*. John Wiley & Sons, Ltd, 2001, pp. 178–204. ISBN: 9780470841624.
- [134] G. Cella. “Off-Line Subtraction of Seismic Newtonian Noise”. English. In: (2000). Ed. by B. Casciaro et al., pp. 495–503. DOI: 10.1007/978-88-470-2113-6\\_44. URL: [http://dx.doi.org/10.1007/978-88-470-2113-6\\\_44](http://dx.doi.org/10.1007/978-88-470-2113-6\_44).
- [135] Rainer Storn and Kenneth Price. In: *Journal of Global Optimization* 11.4 (1997), pp. 341–359. DOI: 10.1023/a:1008202821328. URL: <https://doi.org/10.1023/a:1008202821328>.
- [136] J. Harms et al. “Gravity-Gradient Subtraction in 3rd Generation Underground Gravitational-Wave Detectors in Homogeneous Media”. In: (2009). arXiv: 0910.2774 [gr-qc].
- [137] Ayatri Singha, Stefan Hild, and Jan Harms. “Newtonian-noise reassessment for the Virgo gravitational-wave observatory including local recess structures”. In: *Classical and Quantum Gravity* 37.10 (Apr. 2020), p. 105007. DOI: 10.1088/1361-6382/ab81cb. URL: <https://doi.org/10.1088/1361-6382/ab81cb>.
- [138] Ryan Lynch et al. “Effect of squeezing on parameter estimation of gravitational waves emitted by compact binary systems”. In: *Phys. Rev. D* 91 (4 2015), p. 044032. DOI: 10.1103/PhysRevD.91.044032. URL: <https://link.aps.org/doi/10.1103/PhysRevD.91.044032>.
- [139] Salvatore Vitale and Matthew Evans. “Parameter estimation for binary black holes with networks of third-generation gravitational-wave detectors”. In: *Phys. Rev. D* 95 (6 2017), p. 064052. DOI: 10.1103/PhysRevD.95.064052. URL: <https://link.aps.org/doi/10.1103/PhysRevD.95.064052>.

## BIBLIOGRAPHY

---

- [140] Evan D Hall and Matthew Evans. “Metrics for next-generation gravitational-wave detectors”. In: *Classical and Quantum Gravity* 36.22 (2019), p. 225002. DOI: 10.1088/1361-6382/ab41d6. URL: <https://doi.org/10.1088/1361-6382/ab41d6>.
- [141] Chris Van Den Broeck and Anand S Sengupta. “Binary black hole spectroscopy”. In: *Classical and Quantum Gravity* 24.5 (2007), pp. 1089–1113. DOI: 10.1088/0264-9381/24/5/005. URL: <https://doi.org/10.1088/0264-9381/24/5/005>.
- [142] Jennifer C Driggers, Andrew Lundgren, et al. “Offline noise subtraction for Advanced LIGO”. In: *Technical Document LIGO-P1700260 (2017)* ().
- [143] Tomislav Andric and Jan Harms. “Simulations of Gravitoelastic Correlations for the Sardinian Candidate Site of the Einstein Telescope”. In: *Journal of Geophysical Research: Solid Earth* 125.10 (Oct. 2020). DOI: 10.1029/2020jb020401. URL: <https://doi.org/10.1029/2020jb020401>.
- [144] Mark Beker et al. “Innovations in seismic sensors driven by the search for gravitational waves”. In: *The Leading Edge* 35.7 (July 2016), pp. 590–593. DOI: 10.1190/tle35070590.1. URL: <https://doi.org/10.1190/tle35070590.1>.
- [145] BRUNO Della Rocca, RENZO Mazzanti, and ENZO Pranzini. “Studio geomorfologico della pianura di Pisa”. In: *Geografia Fisica e Dinamica Quaternaria* 10.1987 (1987), pp. 56–84.
- [146] Jacob Benesty, Yiteng(Arden) Huang, and Jingdong Chen. “Wiener and Adaptive Filters”. English. In: *Springer Handbook of Speech Processing*. Ed. by Jacob Benesty, M.Mohan Sondhi, and Yiteng(Arden) Huang. Springer Berlin Heidelberg, 2008, pp. 103–120. ISBN: 978-3-540-49125-5. DOI: 10.1007/978-3-540-49127-9\_6. URL: [http://dx.doi.org/10.1007/978-3-540-49127-9\\_6](http://dx.doi.org/10.1007/978-3-540-49127-9_6).
- [147] Wang J., Tilmann F. J., White R. S., Soosalu H., and Bordoni P. “Application of Multi-channel Wiener Filters to the Suppression of Ambient Seismic Noise in Passive Seismic Arrays”. In: *Leading Edge* 27.2 (2008), pp. 232–238.
- [148] Jan Harms and Krishna Venkateswara. “Newtonian-noise cancellation in large-scale interferometric GW detectors using seismic tiltmeters”. In: *Classical and Quantum Gravity* 33.23 (2016), p. 234001. URL: <http://stacks.iop.org/0264-9381/33/i=23/a=234001>.
- [149] Trevor Hastie, Robert Tibshirani, and Jerome Friedman. *The elements of statistical learning: data mining, inference, and prediction*. Springer Science & Business Media, 2009.

## BIBLIOGRAPHY

---

- [150] William H Press et al. *Numerical recipes 3rd edition: The art of scientific computing*. Cambridge university press, 2007.
- [151] Anna Choromanska et al. “The loss surfaces of multilayer networks”. English (US). In: *Journal of Machine Learning Research* 38 (2015), pp. 192–204. ISSN: 1532-4435.
- [152] T Akutsu et al. “Construction of KAGRA: an underground gravitational-wave observatory”. In: *Progress of Theoretical and Experimental Physics* 2018.1 (Jan. 2018). DOI: 10.1093/ptep/ptx180. URL: <https://doi.org/10.1093/ptep/ptx180>.
- [153] Sebastian Rost. “Array seismology: Methods and applications”. In: *Reviews of Geophysics* 40.3 (2002). DOI: 10.1029/2000rg000100. URL: <https://doi.org/10.1029/2000rg000100>.
- [154] Johannes Schweitzer et al. “Seismic Arrays”. eng. In: *New Manual of Seismological Observatory Practice 2 (NMSOP2)* (2012). DOI: 10.2312/GFZ.NMSOP-2\_CH9. URL: <http://gfzpublic.gfz-potsdam.de/pubman/item/escidoc:43213>.
- [155] Soumen Koley et al. “Rayleigh wave phase velocity models for gravitational wave detectors using an array of nodal sensors”. In: *First Break* 35.6 (2017).
- [156] Okutomi Koki. “Development of 13.5-meter-tall Vibration Isolation System for the Main Mirrors in KAGRA”. In: *PhD thesis, SOKENDAI, The Graduate University for Advanced Studies, 2019* ().
- [157] H. Krim and M. Viberg. “Two decades of array signal processing research: the parametric approach”. In: *IEEE Signal Processing Magazine* 13.4 (July 1996), pp. 67–94. DOI: 10.1109/79.526899. URL: <https://doi.org/10.1109/79.526899>.
- [158] K. Nishida, H. Kawakatsu, and K. Obara. “Three-dimensional crustal-Swave velocity structure in Japan using microseismic data recorded by Hi-net tiltmeters”. In: *Journal of Geophysical Research* 113.B10 (Oct. 2008). DOI: 10.1029/2007jb005395. URL: <https://doi.org/10.1029/2007jb005395>.

## Acknowledgement

These three years spent at GSSI within a wonderful group of research have come to an end in a blink of an eye, but despite the time spent here seemed so short to me, I learnt many many things that (hopefully) will make me a researcher able to face new problems.

This has been possible thanks to the scientifically rich environment that I found in GSSI, but especially to my super-supervisor: Jan Harms. It should go without saying that none of this work would have been possible without your infinite patience... I know that I can be veery annoying when I decide that I have-to-understand-that. So, thank you for answering in great detail the tons of daily emails that I sent to you and for finding the time to meet me when I was in desperate need of help. Thank you also for teaching me to critically check all my results in order to find the errors that I invariably spread here and there. I hope that one day I will be able to catch them at a glance like you do (or just stop doing them). And thank you also for giving me the opportunity of working on a such interesting topic.

Luca: a big big big thank must also go to you. You helped me to deal with CNAF resources other than teaching me a lot of things and being a good friend. You are the only person that somehow was present both during my master and during my PhD!

Let's go on with the thanks: a great one goes to Marica (and to all the great women in GSSI) who proves to us, young girl PhD students, that we can do it: I hope to develop at least one tenth of your strength and determination.

Gor and Marco: with you it is impossible to be sad: you made me laugh so much and I will miss you two a lot!

Then, I should thank all the GSSI GW group: Jan, Marica, Diego&Damian, Marco, Gor, Elena, Eleonora, Nandita, Tomislav, Nandini, Samuele, Ashish, Stefan, Simone, Odysse and Matteo (but also Donatella even if she went away). I have spent with all of you many good dinners (when it was allowed of course) and nice coffee breaks: I promise all of you that "in two weeks I will be back".  
cit.

Thanks to all my PhD mates with whom I shared the struggles of the PhD life: Alessia, Luca, Antonio, Nandita, Valentina, Silvia, Ambra, Stefan, Ashish, Austin, Anna and Eirini. In particular thank you Eirini: during my lonely quarantine you kept me company with long calls and later, when it was possible, with walks around the empty town.

Nandita! Now it's your turn: despite our little fights I will miss very much you and our long chats: I am very happy to have shared the house with you. Thank you for enlightening me with your wisdom and your delicious Indian food when

## BIBLIOGRAPHY

---

I was miserable and desperate. I wish you to find what you are searching for. Many thanks also to my friends at home: Marti, Vitta, Nanna, Ronca, Alby, Campo, Davide. An even bigger thanks to whom of you who made me that nice surprise in Rome!

My whole family always cheers for me and gives me a lot of support: this made my PhD much easier from a human point of view. So thank you mum and dad, Antonella, Gilberto and Tommaso to make my life better.

Thank you also to Marina, Peppi and Ida for making me feel always at home, especially thank you Ida, you are for me like the grandma I never had.

Finally, a super-mega-giga-estra-peta big thanks to Alessio: you really support me in literally everything: if I hold on, it is also thanks to you who, when I sometimes lose my determination, push me to go on and on. Moreover, you are the only person who understands me at a 100% level: with you I can even discuss my scientific results!